UNIVERSIDADE DE BRASÍLIA – UNB

CAMPUS UNB GAMA: FACULDADE DE CIÊNCIAS E TECNOLOGIAS EM ENGENHARIA

PROGRAMA DE PÓS-GRADUAÇÃO EM INTEGRIDADE DE MATERIAIS DA ENGENHARIA

COMPARATIVE ANALYSIS OF DIFFERENT SEMI-ACTIVE SUSPENSION CONTROL TECHNIQUES APPLIED ON REAL WORLD MR DAMPERS

LEONARDO DA COSTA RODRIGUES FERREIRA

ADVISOR: PROF. DR. MARCUS VINÍCIUS GIRÃO DE MORAIS

UNIVERSIDADE DE BRASÍLIA – UNB
CAMPUS UNB GAMA: FACULDADE DE CIÊNCIAS E TECNOLOGIAS EM ENGENHARIA

COMPARATIVE ANALYSIS OF DIFFERENT SEMI-ACTIVE SUSPENSION CONTROL TECHNIQUES APPLIED ON REAL WORLD MR DAMPERS

LEONARDO DA COSTA RODRIGUES FERREIRA

ADVISOR: PROF. DR. MARCUS VINÍCIUS GIRÃO DE MORAIS

MASTER'S THESIS IN INTEGRITY OF ENGINEERING MATERIALS
ISSUE: 116A/2025

BRASÍLIA/DF, ABRIL DE 2025

UNIVERSIDADE DE BRASÍLIA – UNB
FACULDADE DE CIÊNCIAS E TECNOLOGIAS EM ENGENHARIA
PROGRAMA DE PÓS-GRADUAÇÃO EM INTEGRIDADE DE MATERIAIS DA ENGENHARIA

COMPARATIVE ANALYSIS OF DIFFERENT SEMI-ACTIVE SUSPENSION CONTROL TECHNIQUES APPLIED ON REAL WORLD MR DAMPERS

LEONARDO DA COSTA RODRIGUES FERREIRA

MASTER'S THESIS SUBMITTED TO THE POSTGRADUATE PROGRAM IN INTEGRITY OF ENGINEERING MATERIALS AT UNIVERSITY OF BRASILIA, AS PART OF THE REQUIREMENTS FOR OBTAINING A MASTER'S DEGREE.

APPROVED BY:

PROF. DR. MARCUS VINÍCIUS GIRÃO DE MORAIS
ADVISOR

PROF. DR. SUZANA MOREIRA ÁVILA
EXAMINER - FCTE/UNB

PROF. DR. ANDRÉ MURILO DE ALMEIDA PINTO
EXAMINER - EENG/UFLA

Relatório (ata) de defesa de dissertação assinado eletronicamente pela banca avaliadora, via Sistema Eletrônico de Informações - SEI, documento 12589202, processo 23106.021439/2025-50.

BRASÍLIA/DF, ABRIL DE 2025

CATALOGRAPHIC CARD

FERREIRA, LEONARDO DA COSTA RODRIGUES
Comparative analysis of different semi-active suspension control techniques applied on real world MR dampers
[Distrito Federal], 2025.
205p., 210 × 297 mm (FCTE/UnB Gama, Master's in Integrity of Engineering Materials, 2025).
Master's Thesis - University de Brasília. Faculdade de Ciências e Tecnologias em Engenharia. FCTE

1. Vehicular Dynamics
2. Vibration control
3. Semi-active damper
4. Magnetorheological damper

I. ENC/FT/UnB.
II. Title (Series)

REFERENCE

FERREIRA, LEONARDO DA COSTA RODRIGUES (2025). Comparative analysis of different semi-active suspension control techniques applied on real world MR dampers. Master's Thesis in Integrity of Engineering Materials, Publication 116A/2025, Postgraduate Program, Faculty of Technology, University of Brasília, Brasília, DF, 205p.

ASSIGNMENT OF RIGHTS

AUTHOR: Leonardo da Costa Rodrigues Ferreira

TITLE: Comparative analysis of different semi-active suspension control techniques applied on real world MR dampers

DEGREE: Master's

YEAR: 2025

ferreira.ldcr@gmail.com

Brasília, DF – Brazil

ACKNOWLEDGMENTS

I'd like to thank my family for supporting me through the whole process of developing the Thesis and acquiring the Degree.

I'd like to thank Marcus Vinicius Girão de Morais, for providing me his insightful guidance through the writing process and for teaching me how to execute my ideas in a reliable manner.

I'd like to thank Davi Mathias Dutra, for providing the experimental data of the MR damper used in the numerical fitting procedures.

I'd like to thank Aravind Seshari for freely providing the Matlab routine for the NSGA-II algorithm.

I'd like to acknowledge and thank the financial support granted by the CAPES foundation. This study was financed in part by the Coordenação de Aperfeiçoamento de Pessoal de Nível Superior - Brasil (CAPES) – Finance Code 001.

ANÁLISE COMPARATIVA DE DIFERENTES TÉCNICAS DE CONTROLE DE SUSPENSÕES SEMIATIVAS APLICADAS A AMORTECEDORES MR DO MUNDO REAL

RESUMO

Suspensões veiculares são centrais na resposta dinâmica do veículo a pertubações de estrada, tendo papel importante no conforto e estabilidade veiculares. Há um limite no que pode ser alcançado com suspensões passivas. Suspensões semiativas, e especialmente suspensões magneto-reológicas (MR), são uma opção estudada na indústria para superar essas limitações a um custo acessível, mas sua performance depende da estratégia de controle empregada.

Com base nesses fatores, essa dissertação busca avaliar computacionalmente o desempenho de diferentes estratégias de controle de suspensões semiativas em maximizar o conforto e da segurança de sistemas veiculares dotados de suspensões com amortecedores MR de comportamento realista.

Objetivando analisar o desempenho de diversos controladores em uma planta veicular realista, muitos modelos de amortecedor MR foram contemplados. Quatro diferentes propostas foram testadas em Simulink: O modelo de corpo de Bingham, o modelo Bouc-wen assimétrico, um modelo Sigmoide Duplo denominado modelo Wang e uma nova forma modificada do modelo Wang com base na equação logística. Os parâmetros dos modelos foram otimizados com um algoritmo genético e classificados com base na capacidade de replicar resultados experimentais. O modelo Wang modificado proposto na tese teve o melhor desempenho, e foi utilizado nas simulações de veículo.

As simulações de veículo focaram no estudo de diferentes técnicas de controle em conjunto com o amortecedor MR. As estratégias de controle avaliadas foram a Híbrida Skyhook-Groundhook (Hybridhook), a LQR e a State Dependent Riccati Equation (SDRE). Os controladores foram aplicados em modelos 1/4 e 1/2 de veículo no ambiente Simulink. O NSGA-II foi utilizado para fazer uma otimização multiobjetivo dos modelos de 1/4 de veículos. Parâmetros da suspensão e do controlador foram otimizados em conjunto para ter melhor performance em segurança (deslocamento dinâmico da roda) e conforto (aceleração RMS do chassi). Soluções específicas dos resultados foram escolhidas para estudos mais aprofundados e testes em perfis de estrada determinísticos (quebra-molas e meio-fio). No geral, todos controladores superaram seus equivalentes passivos. O LQR teve a melhor performance média e o SDRE a pior. Os estudos de caso foram replicados em 1/2 veículo, mas não se fez uma nova otimização. Utilizou-se os parâmetros resultantes da otimização em 1/4 de veículo no lugar. Eles atenuaram vibrações em menor grau quando empregados no 1/2 veículo. Novamente, o LQR teve os melhores resultados, seguido do Hybridhook. O SDRE falhou em prover melhorias consistentemente, mas demonstrou grande potencial.

Palavras-chave: Dinâmica veicular, Controle de vibrações, Amortecedor semiativo, Amortecedor Magneto-reológico, Otimização genética.

COMPARATIVE ANALYSIS OF DIFFERENT SEMI-ACTIVE SUSPENSION CONTROL TECHNIQUES APPLIED ON REAL WORLD MR DAMPERS

ABSTRACT

Vehicular suspensions are central to the dynamic response of a vehicle to road perturbations, having an important role in the vehicle's comfort and stability. There are limits to what can be obtained with passive suspensions. Semi-active suspensions, and specially magnetorheological (MR) suspensions, are an alternative studied by the industry for overcoming these limitations at an accessible cost, but its performance is dependent on the control strategy employed.

Based on these factors, this thesis aims to use simulations for evaluating the performance of different semi-active suspensions control strategies at maximizing the comfort and safety of vehicle systems equipped with MR dampers with realistic behaviors.

With the objective of evaluating the performance of diverse controllers in a realistic vehicle plant, many MR damper models were considered. Four different proposals were evaluated in Simulink: The Bingham body model, the asymmetric Bouc-wen model, a high performance Double Sigmoid model referred to as the Wang model, and a novel modified form of the Wang model based on the logistic equation. Each model parameters were optimized by a genetic algorithm and ranked according to how well they fit experimental data. The modified Wang model proposed in the thesis performed best, and was utilized in the vehicle simulations.

The vehicle simulations focused on study of different control techniques coupled to the MR damper. The evaluated control strategies were the Hybrid Skyhook-Groundhook (Hybridhook), LQR and the State Dependent Riccati Equation (SDRE). The controllers were applied on 1/4 vehicle and 1/2 vehicle models in Simulink. The NSGA-II was used to perform a multi-objective optimization of the 1/4 vehicle models. Suspension and controller parameters were jointly optimized for performance in two competing parameters of safety (dynamic wheel displacement) and comfort (chassis acceleration RMS). A few results were chosen for in depth studies and tests under deterministic road excitations (bump and linear rise). All schemes outperformed their passive equivalent in general. The LQR showed the best performance overall, and the SDRE the worst. The case studies were repeated on the 1/2 vehicle, but no additional optimization was performed and the suspension parameters from the 1/4 vehicle optimization were used instead. They reduced vibrations on the 1/2 vehicle to a lesser degree. Once again, the LQR performed best, followed by the Hybridhook. The SDRE failed to provide consistent improvements, but showed great potential.

Keywords: Vehicular Dynamics, Vibration control, Semi-active damper, Magnetorheological damper, Genetic optimization.

Contents

List of Tables

List of Figures

LIST OF NOMENCLATURES AND ABBREVIATIONS

Abs	Absolute
Cnt	Continuous
ER	Electro-rheological
GWN	Gaussian White Noise
HBH	Hybridhook
MR	Magnetorheological
LQR	Linear-quadratic regulator
LWBD	Lower body displacement
N/A	Not Available
PID	Proportional-derivative-integral
PSD	Power spectral density
RMS	Root mean square
SAS	Semi-active suspension
SDRE	State-Dependent Ricatti Equation
UPBD	Upper body displacement
UPBA	Upper body acceleration
UPBR	Upper body angular displacement
UPBRA	Upper body angular acceleration

LIST OF SYMBOLS AND SUBSCRIPTS

SYMBOLS

k_{cl}, O, η_p, η_n, a_0, a_1, a_2, a_3, a_4, k_0, k_{1c}, k_{1e}, k_2, k_3, k_4, k_5, k_6, I_0, I_1 f_0, f_c, λ, n, α, δ, γ, β, μ	Rheological model parameters
A	State matrix.
B	Input matrix.
C, c	1. Constant: Damper constant (N/s). 2. Matrix: Excitation matrix.
D	Damping matrix.
d	Distance (m).
d_x	Horizontal displacement (m).
F	Force (N).
f	Time derivative of damper model force (N/s).
G()	Gain function.
H()	Frequency domain representation. Also denotes a Fourier Transform if variable is in time domain.
H_a	Hamiltonian function.
H_2	1. Function: Euclidean norm. 2. Variable: RMS value of the upper body acceleration gain.
H_∞	1. Function: Chebyshev norm. 2. Variable: Peak value of the unsprung body displacement gain.
J	1. Constant: Moment of Inertia constant. ($kg.m^2$) 2. Function: Cost function.
K, k	1. Constant: Spring constant (N/m). 2. Matrix: Stiffness matrix.

L	1. Function: Laplace Transform. 2. Matrix: Control matrix.
M, m	Mass constant (kg).
O	Optimal control terminal error cost weight matrix.
P, P(x)	Riccati equation solution matrix.
Q, Q(x), Q_0**,** $Q_1(x)$	Optimal control error cost weight matrix.
R, R(x), R_0**,** $R_1(x)$	Optimal control control cost weight matrix.
S()	Constraints function.
T()	Transfer function.
t	Time (s).
U	Cholesky decomposition of Optimal control weight matrix Q.
u**,** $u(t)$	Control vector.
v	Velocity (m/s).
v	Relative displacement between damper terminals (m).
ω**,** f	Frequency (Cycles/s or Rads/s).
Ψ	Road profile displacement PSD.
x**,** $x(t)$	State vector.
X	State vector Fourier Transform.
z	Excitation vector.

SUBSCRIPTS

f	Pertaining to the front body.
r	Pertaining to the rear body.
s	Pertaining to the sprung body.
θ	Pertaining to the sprung body rotation.
u	Pertaining to the unsprung body.
0	Pertaining to the initial value or the value at the origin.
$4gdl$	Pertaining to the 1/2 vehicle model.

1 INTRODUCTION

It is not an overstatement to claim that the automobile has revolutionized the human way of life. From logistics to leisure, wheeled vehicles such as cars, motorcycles and trucks have shaped much of the 20th and 21st century. As society progresses, so do its demands from vehicles. They are required to be safer, more efficient and comfortable, all while maintaining their costs as low as possible. To overcome these challenges, a diversity of solutions have been employed, ranging from direct improvements in aerodynamics, engines, suspensions and materials to changes in the surrounding infrastructure, legislation and norms.

In Brazil, the importance of this constant innovative process was recognized in the forms of the law 13.755/2018, of 10/12/18 (Brasil, 2018), also known as the Rota 2030 programme, and the provisional law 1.205 of 30/12/23, MOVER programme, which took its place. Both aimed strengthening the national automobile industry taking into account the present and future necessities of the sector and society. Chapter II, section 1 of the law 13.755/2018 contains the following articles concerning the program directives, which have been translated:

- 7th Article - The Program Rota 2030 - Mobility and Logistics is hereby instituted, with the objective of supporting the technological development, competitiveness, innovation, vehicular safety, environmental friendliness, energetic efficiency and quality of automobiles, trucks, busses, motorized chassis and auto parts.
- 8th article, section III - Stimulate the production of new technologies and innovations, in line with the global technological tendencies.

These necessities from society are vehicles that improve the collective well being. Vehicles that preserve human life, either by being less accident prone or by inducing less long term health effects, are one way to achieve that. One of the key systems in a vehicle that impacts all these factors is the suspension, being important for the comfort, long-term health consequences and safety of a passenger in a vehicle.

The manner by which the suspension determines the comfort and health impact of a vehicle is through control of road induced chassis vibration and, by extension, passenger vibration. This is because vibrations are both a source of discomfort and health hazard, depending on the magnitude, frequency and exposure time. ISO (1997) defines a series of detrimental effects that exposure to vibration can cause beyond human comfort, ranging from immediate effects such as motion sickness and impairments in perception to long term health effects. It also defines the tolerance limits for the frequency-weighted acceleration exposure, which tends to fall with

logarithm of the exposure time, displayed in Figure 1.1. Excessive vibrations at any level pose an accident risk, being specially critical for those in jobs such as truck or taxi drivers, which require continuous driving thought the day.

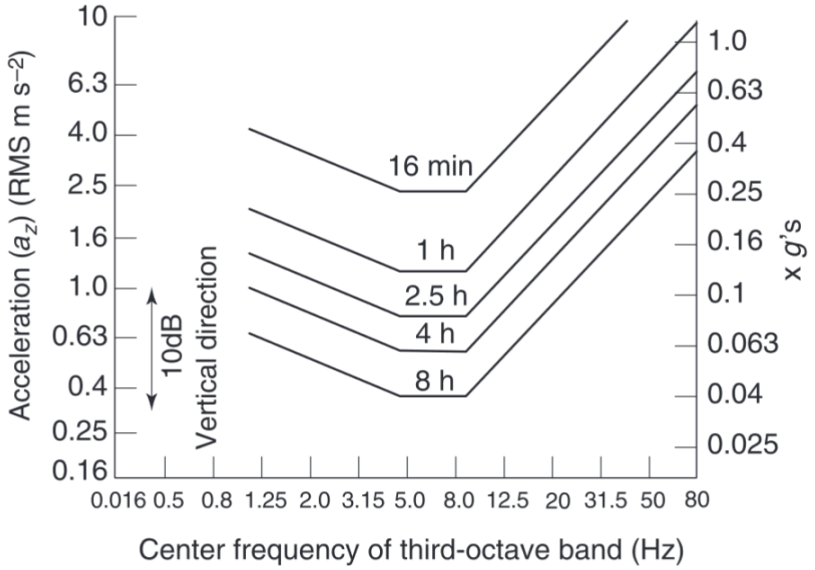

Figure 1.1. Maximum allowed vibration exposure time based on the frequency (x axis) and acceleration (y axis). Reproduced from ISO (1997).

The suspension impacts the safety of a vehicle by determining the reliability of a vehicle under high risk situations, such as a sudden stop or a tight curve (Mazzilli *et al.*, 2021). This is due to its influence on the tire-road normal contact force, which if too low allows the tire to slide over the road and sharply decreases tire friction. When this happens, it becomes significantly harder to do things such as braking and steering, as they depend on the exchange of forces between the tire and the road to provide the respective decelerating and centripetal forces. Slipping will increase braking distance and cause a vehicle to understeer in a curve, and as such a reliable contact pressure can be the difference between an accident occurring or not. While systems such as the ABS (Anti-lock breaking system) ensure no slipping occurs by keeping the friction forces lower than the allowed by the maximum contact forces, the suspension can directly increase the maximum contact force, permitting the maneuvers to occur in even more stringent situations. This is done by actions like increasing the downward force on the wheel, decreasing the contact force amplitude and decreasing the wheel displacement relative to the ground, all of which decreases the likelihood of slipping under different scenarios.

While both the safety and comfort aspects of a vehicle are very important, traditional suspension technologies offer a limited compromise between comfort and safety aspects (Tener, 2004; Els *et al.*, 2007). This is because, in a very broad manner, safety is usually achieved by increasing the damping in a suspension, while comfort comes from decreasing it. Furthermore, there's a limit to their performance regardless of the trade-off performed. Controllable suspensions, on the other hand, can not only outperform traditional passive suspension systems in individual aspects but also break this trade-off and do so in both criteria simultaneously (Gillespie, 2021; Yu *et al.*, 2023).

Controllable suspensions are an old technology. In the 70's, several authors (Karnopp, 1995; M. Valášek and M. Novák, 1996) were already proposing semi-active suspension systems for vehicles. The advent of advanced micro controllers (Çimen, 2010) further allowed the technology to come into play. These suspensions enable rides that are more comfortable and safer for those inside and outside the vehicle, as they increase a vehicle cornering and stopping capabilities with far less drawbacks than traditional systems. Often, they manage to outperform passive systems on both fronts. Slowly but steadily, controlled suspensions have been garnering more adoption as shown in (Soliman and Kaldas, 2021) and reproduced in Figure 1.2.

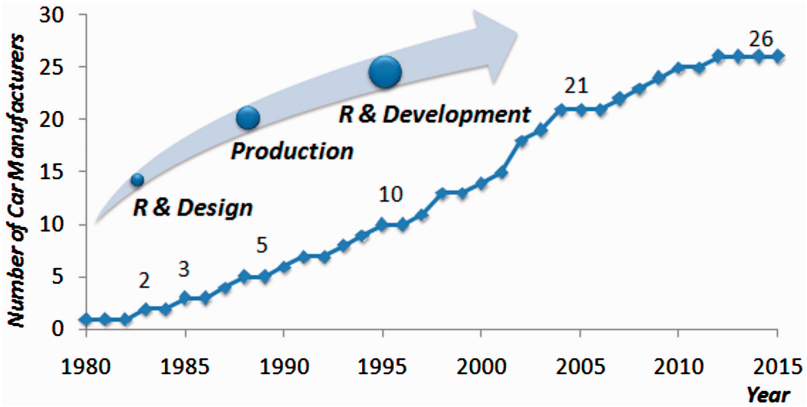

Figure 1.2. Controllable suspension adoption by manufacturers over the years. Reproduced from Soliman and Kaldas (2021).

The main drawbacks of controllable suspensions, and the reason why they haven't seen widespread adoption, are their higher costs, power draw and added weight (Yu *et al.*, 2023; Soliman and Kaldas, 2021; Gillespie, 2021). These limitations have kept them from reaching the mainstream adoption enjoyed by traditional systems. The technology that has seen the most adoption out of all controllable suspensions, however, is the semi-active suspension. The use of semi-active suspensions instead of active ones can decrease cost, weight and power draw, at the price of an inability to exert arbitrary control forces. While this decreases performance compared to an active suspension, the degree of performance loss, as well as their ultimate overall performance, is dependent on the control rule utilized. This means that, with the correct control schemes, semi-active suspensions could potentially provide improvements in ride quality comparable to an active suspension at a much lower price, making them a promising field of study in the search for an improved suspension system viable for mass market adoption.

Among the technologies used to realize the semi-active suspensions, the Magnetorheological (MR) damper has been given the most attention in recent years. This is due to its greater reliability, safety and cost parameters compared to its main competitors (Yoon *et al.*, 2021; Wang *et al.*, 2024; Soliman and Kaldas, 2021). An additional challenge it brings is that its behavior is heavily non-linear, requiring a dedicated model to describe it (Soltane *et al.*, 2015; Kwok *et al.*, 2007; Wang *et al.*, 2004; Xiong *et al.*, 2024). The real world effectiveness of a controller might not match simulations if the model is not precise enough. Non-linearities can also make linear controllers struggle. The selection of a control scheme, then, becomes coupled to the MR damper modeling.

1.1 OBJECTIVES

The general objective of this graduate thesis is to computationally evaluate the effectiveness of different semi-active suspension control schemes applied on realistically modeled MR dampers at controlling the road induced vibrations which impact the comfort and safety of a typical passenger vehicle under steady-state conditions.

The specific objectives of the present dissertation are:

- Quantitatively determining the comfort and safety performance of the vehicle for a typical passenger car equipped with an MR damper operating under four different control techniques: Groundhook, Skyhook, Linear-quadratic regulator (LQR) and State-Dependent Ricatti Equation (SDRE);
- Ensuring the MR damper mathematical model behaves as close as possible to reality given the available data;
- Ensuring the control schemes parameters are adequate, even if not optimal;

1.2 METHODOLOGY

The objectives have been laid out in the prior section, and are the main topic of Chapter 1. The work begins with a bibliographical revision of the topics relevant to the proposed object of study in Chapter 2. Upon sufficient material being analyzed, a strategy for the methodology is laid out in Chapter 3. It determines what parameters, tools and models will be used, as well as what steps will be executed given the information collected in the bibliography. If the need for a new process is identified at this stage, a bibliographical revision is performed on the subject and the methodology is revised. The identified needs were:

- Develop code for simulating the chosen MR damper models (Bingham, Bouc-wen, Wang, Wang-II). Assert the best suited damper model for the computational simulation of MR dampers in a vehicle under random excitations. This model must receive a combination of constants and vehicle state parameters and return the damper force.
- Develop code for simulating the 1/4 and a 1/2 vehicle model under white noise road excitations. Develop code for calculating the Upper body displacement (UPBD) Root mean square (RMS) metric of a given vehicle model for purposes of comfort measurement and the Road-hold metric of a given vehicle model for purposes of safety measurement.
- Evaluate the effectiveness of the Skyhook and Groundhook control schemes at controlling the vibration of a 1/4 and a 1/2 vehicle model. Evaluate the effectiveness of the LQR and SDRE control schemes at controlling the vibration of a 1/4 vehicle model. Compare the results of the 1/4 vehicle model to the 1/2 vehicle model and determine whether the results on the simpler model are in line with the results obtained on the more complex model.

If the proposed investigation cycle is deemed viable from start to finish, the work proceeds to the creation of computational routines in Chapter 4. This is the step in which Simulink or Matlab scripts are created to execute the steps determined in the methodology. The routines are then executed, and the results are collected and interpreted in Chapter 5. If relevant, the results from a simulation step are fed into the next. Once all simulations have been completed, the question of whether all the objectives laid out in the beginning have been reached is performed. If not, the work regresses to the methodology layout stage and the short comings are evaluated to determine how they can be averted. If they have, then the conclusions are stated in Chapter 6, important findings from the dissertation are discussed and suggestion for follow up works are made based on the findings.

A simplified view of the methodology used for developing this work is present in Figure 1.3. The full methodology can be seen in the dedicated Methodology chapter as Figure 3.1.

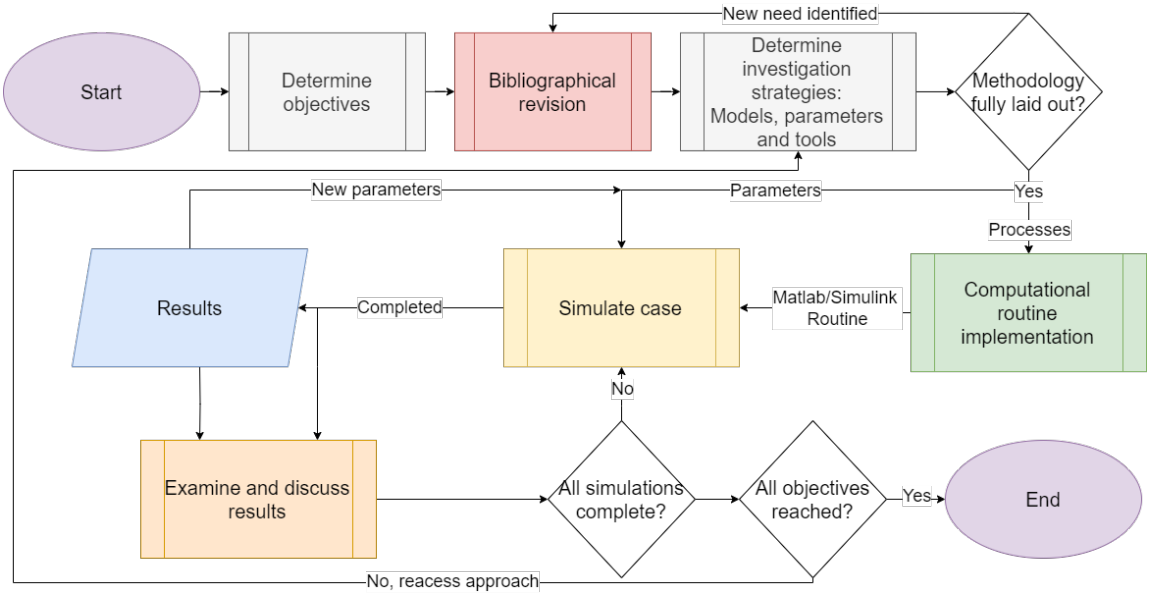

Figure 1.3. Simplified methodology employed in the development of the present work.

1.2.1 Scope and limitations

The present work is purely computational. The majority of the studied vehicular systems use the 1/4 vehicle model, which is capable of detecting simple vertical modes. It trades off the precision and mode detection capabilities of a full vehicle model for model simplicity and computational lightness. The 1/2 vehicle model is also used, presenting the same trade-offs but to a lesser degree. It can detect more vertical modes, including pitching movements. The only source of excitation was the road represent by a Gaussian White Noise (GWN), which presents constant power across the frequency spectrum. Real world roads are usually described by colored noises. Sources such originating from but not limited to the passengers, aerodynamics and engines weren't taken into account.

The damper models employed have their behavior based on experimental data. None perfectly replicates the experimental behavior. They also cannot take into account damper

phenomena that they do not model, nor can they have their parameters fit to behavior that doesn't appear under test bench circumstances. While the models seem to agree with the data to a reasonable degree, it cannot be determined how representative of real world situations the test bench data is.

The precision of the results is also dependent on the numerical parameters used. A finer time discretization provides more accurate solutions of the system dynamics, while a longer simulation time provides finer frequency domain results, both at the cost of computational time and resource demands. A compromise was reached based on the barest precision that could be mathematically guaranteed compared to that was necessary. Genetic algorithms were used for optimization procedures. More individuals and generations achieve more optimal results at the cost of greater computational resource demands and time. Due to the heuristic and random nature of the algorithm family, it was not possible to determine the exact parameters needed for a certain result to be guaranteed. Instead, the compromise reached was based off the parameters observed in similar works from the literature, experience, iterative trial and error based on the analysis of the results regarding solution convergence, computational limitations and time available.

The metrics optimized are all of vertical behavior. Lateral and longitudinal dynamics and metrics were not optimized, and the pitch behavior was only evaluated in select cases.

1.3 GRADUATE THESIS LAYOUT

The graduate thesis has been sectioned in the following manner:

Chapter 2 - Theoretical fundamentals This chapter aims to review and present all the theoretical fundamentals relevant to this work. This includes: numerical models for vehicles, road excitation models, controllable suspensions types, MR damper models, optimization techniques, computational simulation techniques, the Hook class of controllers and the Optimal control class of controllers. The chapter is concluded with a state-of-the-art review.

Chapter 3 - Methodology This chapter seeks to describe all the computational techniques used in the paper, as well as justify all choices made. It contains all parameters used.

Chapter 4 - Computational implementation This chapter has the objective of describing in depth all the computational routines elaborated for the purpose of this graduate thesis, as well as make their reproduction by a third party viable.

Chapter 5 - Results and discussion This chapter aims to showcase all results obtained from the application of the routines described in Chapter 4 and techniques described in Chapter 5 for the purposes described in the Objectives section, as well as comment and interpret their results.

Chapter 6 - Conclusions This chapter seeks to review and comment the conclusions of all the results obtained in the graduate Thesis, as well as suggest how this work may be

continued in the future.

1.4 PUBLISHED LITERATURE

During the development of this thesis, several of its partial results were or will be published as stand-alone articles. The published articles so far are Ferreira *et al.* (2023) and Ferreira and Morais (2023). Ferreira *et al.* (2025) has been sent to the journal "*Vehicle system dynamics*", and is currently under peer review.

- Ferreira, L. D. C. R., Morais, M., e Silva, D. M. (2023). Modelling MR dampers under non-harmonic excitations through logistic curve models. In Proc. of the XLIV Ibero-Latin American Congress on Computational Methods in Engineering.
  Ferreira *et al.* (2023) contains the procedures and results performed for the parametric identification and validation of damper models, with the results displayed in Section 5.1.

- Ferreira, L. D. C. R. e Morais, M. (2023). Optimization of the lqr and sdre control scheme for a non-linear semi-active MR damper on a quarter vehicle model. In Proc. of the 27th International Congress of Mechanical Engineering.
  Ferreira and Morais (2023) contains the optimization of a clipped optimal control on a quarter vehicle model with an MR suspension. Its results have been superseded by the following article, and have not been included in the thesis.

- Ferreira, L. D. C. R., Morais, M. V. G., e Avila, S. M. (2025). LQR semi-active control and optimization of quarter vehicle model with a Sigmoid model of magnetorheological damper. Under review for Vehicle System Dynamics.
  Ferreira *et al.* (2025) contains the procedures and results for the combined simultaneous optimization of a clipped LQR controller parameters, its passive suspension parameters and its MR suspension parameters on a quarter vehicle model with an MR Semi-active suspension (SAS). Its results are displayed in Section 5.2.4.

2 THEORETICAL FUNDAMENTALS

The present chapter showcases fundamental results sourced from the literature which have relevance to the procedures carried out in this work and the results obtained from them. This includes information about suspension modeling, controllable suspensions, MR dampers, vehicle models, road profile modeling, performance metrics, control schemes applied to vehicular vibration attenuation and parametric optimization.

2.1 SUSPENSION SYSTEMS

The vehicular suspension system is the component in a vehicle that mediates the load transfer between the chassis and the wheels and, therefore, the road. It is basic composition is that of a damper, a spring and a set of mechanical elements that ensure the unsprung and sprung masses are linked (Savaresi *et al.*, 2010; Yu *et al.*, 2023).

Besides ensuring the vehicle chassis is connected to its wheels, Gillespie (2021) mentions the suspension system has many other primary functions, including isolating the chassis from the road roughness, ensuring the wheels have the desired steer and camber attitudes for a given road, reacting to all three-dimensional forces and momentum the tire is subject to originating from both the vehicle and the road, and keeping the tires in contact with the road while minimizing the variations in its load.

There are many ways to physically realize the suspension, with Gillespie (2021) dividing them in two main categories: the independent and solid axle suspensions. Solid axle suspensions have laterally opposing wheels connected to each other by a rigid element, which imposes kinematic conditions that transmit the movement on one wheel to the other. Independent suspensions, on the other hand, permit the wheels to have independent movement from each other. Solid axle configurations are mostly found in the rear suspension of vehicles specialized for load-carrying tasks such as trucks and SUVs, while the independent suspension is the most prevalent in passenger vehicles in general.

A few types of independent suspension are (Gillespie, 2021):

- Trailing arm suspension
- SLA front suspension
- MacPherson strut
- Multi-link rear suspension

- Trailing-arm rear suspension
- Semi-trailing arm
- Swing axle

Example illustrations of an idealized suspension, the MacPherson suspension and the trailing arm suspension can be found in Figure 2.1. All these suspensions have their advantages and disadvantages, such as cost and behavior trade-offs, which won't be explored in depth here. Because this work focuses on passenger vehicles, the use of an independent suspension system will be assumed when relevant.

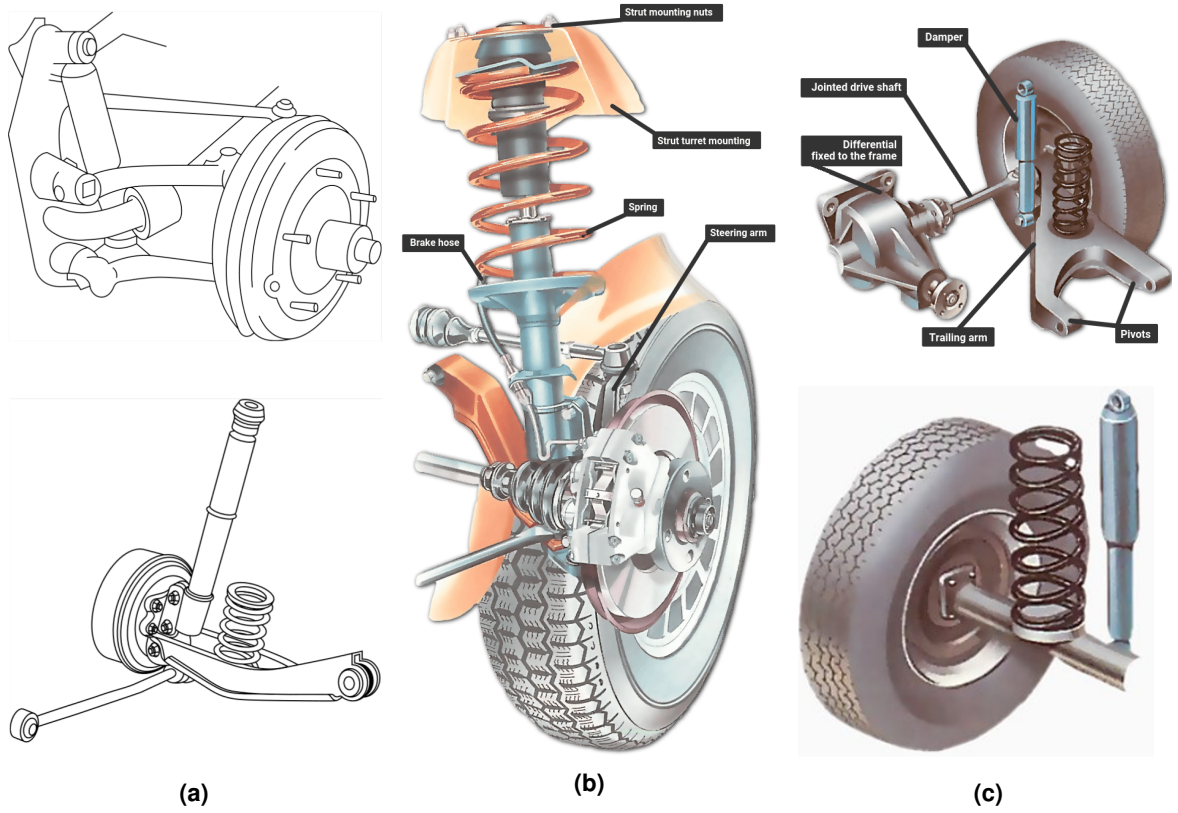

Figure 2.1. Example of representation of suspensions. a) Suspension diagrams for a Trailing arm (top) and Macpherson (bottom). Source: Adapted from Gillespie (2021). b)-c): Illustrations for a MacPherson (right), Trailing arm (top) and idealized (bottom) suspensions. Source: Alex Muir from "How a Car Works".

2.1.1 Passive and controllable suspensions

There are many ways to categorize suspensions. From the viewpoint of vibration control, an useful classification is the one between active, semi-active and passive suspensions. They differ from each other by the extent to which they can be made to react to the dynamical conditions of the vehicle and of disturbances like the road.

The passive suspension is a sub-type of suspensions systems characterized by the lack of controllable elements, having its static and dynamic parameters at a specific operating condition

fixed unless one of its elements is substituted. This contrasts with active and semi-active suspension systems, also known as controlled suspension systems (Soliman and Kaldas, 2021). In those, one or more parameters of the suspension may be controlled without direct component substitution. The difference between the active and semi-active suspension is what parameters can be affected: while the semi-active suspension can only control the damping coefficient, the active suspension can directly apply arbitrary forces instead.

The passive suspension configuration is currently the most employed in passenger vehicles. This is due to a combination of characteristics which currently make it the most cost-effective option.

The lower cost relative to controllable suspensions (Soliman and Kaldas, 2021; Gillespie, 2021) is one of its key aspects. Controllable dampers need electronics to measure and control the behavior of the system, as well as a robust power source in the case of active suspensions (Soliman and Kaldas, 2021). Furthermore, because said systems are an additional point of failure in controllable suspensions, passive alternatives enjoy higher reliability (Gillespie, 2021; Soliman and Kaldas, 2021). The lack of all these additional elements and a simpler overall construction also lead to lower masses (Gillespie, 2021).

It does, however, possess some short comings. The main drawback of a passive suspension system is that it has limits to the extent with which it can satisfy competing safety and comfort requirements compared to controllable suspensions (Gillespie, 2021; Ahmadian, 2017; Savaresi *et al.*, 2010; Yu *et al.*, 2023). These differences are exemplified in Figure 2.2, while the Table 2.1 provides an overview of the issue. Some data was classified as Not Available (N/A) in the original table. While mentioned in the table, self-leveling suspensions are not of interest to the present work and will not be discussed in depth.

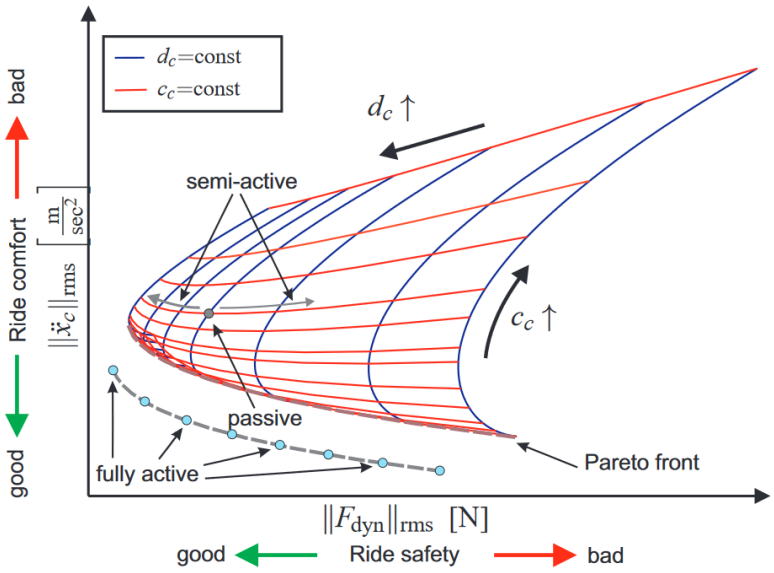

Figure 2.2. Trade-off between safety and comfort performance for an active, on-off semi-active and passive suspension. Reproduced from Koch (2011).

Table 2.1. Comparison between different suspension types. Adapted from Gillespie (2021).

	Performance mode					
Suspension Type	Ride	Height	Roll	Dive	Squat	Road-holding
Passive	Performance is a compromise between all modes					
Self-leveling	High	High	N/A	N/A	N/A	N/A
Semi-active	Medium	N/A	Low	Low	Low	Medium
Full-active	High	High	High	High	High	High

While inferior to the active suspension in performance, the semi-active damper offers the best performance-cost compromise out of the controllable suspensions (Soliman and Kaldas, 2021).

2.1.2 Semi-active suspension

Semi-active suspensions are suspensions equipped with controllable dampers which can alter the energy they dissipate, but cannot apply arbitrary controllable forces to the vehicle. Control strategies for semi-active dampers can either account for this discrepancy in its mathematical development or use the clipped control approach. In the clipped control, the control action is calculated as if the system were active, and if the value is impossible for the semi-active damper the closest possible value is instead assumed (Koch, 2011).

A semi-active damper may vary either continuously or discretely. Discrete varying dampers are able to assume a finite number of states, and can be so either through construction, such as a solenoid valve that controls whether a damper has 2 or 3 working orifices, or through control, such as an on-off controller. Continuously varying dampers, on the other hand, can theoretically assume a continuum of states. While only able to assume a finite number in practice due to digital controller limitations, this difference is not relevant for the results of the application.

As described in (Soliman and Kaldas, 2021), there are three main types of semi-active damper technologies: Servo or solenoid valve actuator, MR or Electro-rheological (ER) fluid and electromagnetic. Furthermore, the solenoid valve actuator and MR fluid dampers are the ones that see the most commercial use, due to cost and certain advantages.

Both solenoid valve and MR fluid dampers are able to be used in continuously varying dampers. However, there are far fewer studies done on continuous solenoid valve dampers owing to their recency. As this work aims to use continuous control schemes, focus will be given to the MR damper.

2.1.3 MR damper

A MR damper is catch all term for dampers infused with a magnetically active fluid, which allows their properties to be altered by the application of a magnetic field. Ahmadian (2017) mentions that there are three main operation modes for the MR damper, but the Valve mode, in which the MR fluid flows through an orifice which may have a magnetic field around it, is the

one most commonly employed. This mode is illustrated in Figure 2.3.

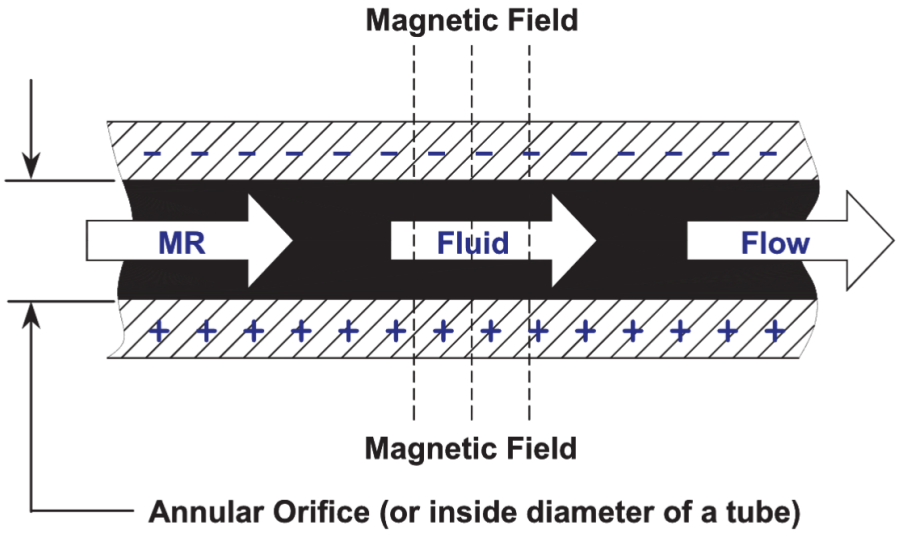

Figure 2.3. MR damper with the MR fluid in Valve mode. Reproduced from Ahmadian (2017).

MR dampers work on the principle of embedding magnetic particles on a fluid, which alter its rheological behavior. When a magnetic field is applied, these magnetic particles align with the field lines, creating a film like structure which further alters the rheological behavior. This is demonstrated in Figure 2.4. As the damper uses the Valve mode, the film structures formed by the magnetic particles are formed perpendicular to the flow direction, increasing the resistance.

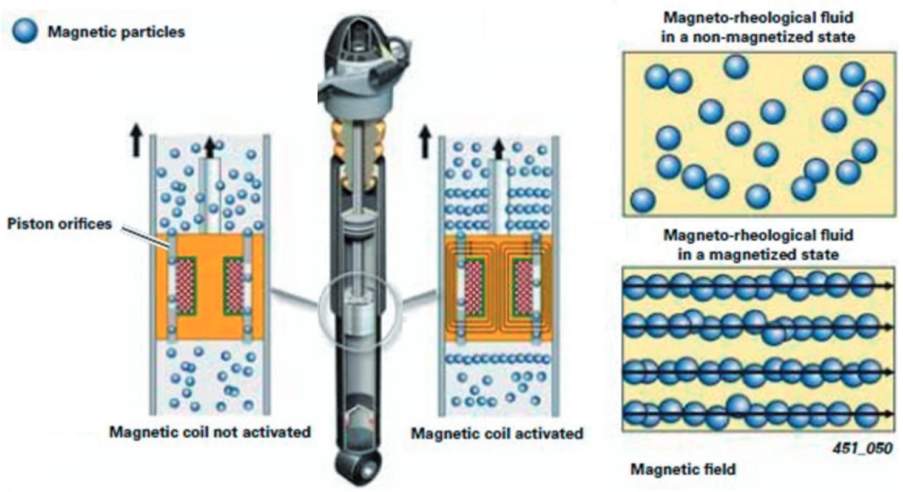

Figure 2.4. MR damper working principle. Adapted from Soliman and Kaldas (2021).

All these characteristics creates a very peculiar relationship between the velocity and force of the damper. As depicted in Figure 2.5, the force-velocity curve exhibits a highly non-linear behavior, including:

- Hysteresis
- Non-linear velocity rise

- Asymmetric velocity relationship
- Non-zero force at zero speed
- Non-linear change of non-linear parameters with application of magnetic field

Given all these properties, there have been attempts to model the MR damper relationship based on its velocity and electric current of applied magnetic field.

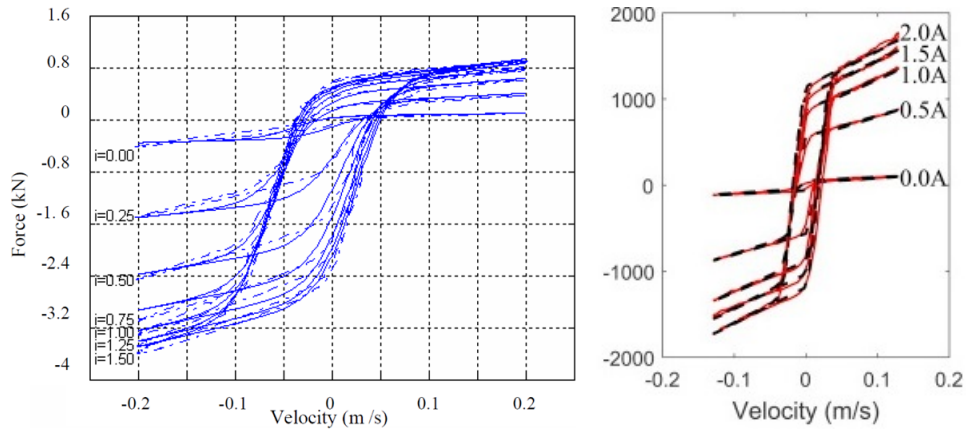

Figure 2.5. Some example of the force-velocity MR damper relationship. Comparison between model and experimental data. a) Model (continuous), experimental (dashed). Reproduced from Wang *et al.* (2004); b) Model (dashed), experimental (continuous). Adapted from Kwok *et al.* (2007).

The modeling of the MR damper force-velocity behavior can be accomplished with many models. According to Abdul Aziz *et al.* (2022), there are many parameters that affect the characteristics of MR dampers, such as the properties of its coils, valves and power specification. They can, however, be broadly classified into either monotube or twin-tube and double or single-ended. Given this classification, Abdul Aziz *et al.* (2022) demonstrates the use of different mathematical models for different dampers. Santade (2017) perform additional tests. Ismail *et al.* (2009) performs a review on the uses of the Bouc-wen model. This information is condensed at Table 2.2.

From the table, it can be seen that the Bouc-wen and Bingham family of models are the most versatile and often employed for the representation of MR dampers, followed by the double Sigmoid model. Furthermore, there are fewer double ended monotube applications in the literature, and even fewer of the twin-tube.

In Santade (2017) it was concluded that the double Sigmoid model was better suited to represent the damper used compared to the Nth-power model. The experimental data in (Silva *et al.*, 2022) was also successfully matched to a double Sigmoid model, and the damper used in both works were almost the same, with Santade using the short stroke and Dutra using the long stroke variation.

Given the information collected, there's interest in the description of three damper models:

Table 2.2. Models mentioned and showcased uses in Abdul Aziz *et al.* (2022), Santade (2017) and Ismail *et al.* (2009).

Damper model	Monotube		Twin tube	
Mathematical model	Single ended	Double ended	Single ended	Double ended
Bingham	Yes	Yes	Yes	N/A
Maxwell Nonlinear Slider	Yes	N/A	N/A	N/A
Nth-power	Yes	N/A	N/A	N/A
Hyperbolic tangent	Yes	N/A	N/A	N/A
Bouc-wen	Yes	Yes	N/A	Yes
Dahl friction	N/A	Yes	N/A	N/A
Herschel-Bulky	N/A	Yes	N/A	N/A
Double Sigmoid	Yes	Yes	N/A	N/A

the Bingham, Bouc-wen and Double Sigmoid.

2.1.3.1 Bingham body

The Bingham family of models has many variations in the literature. The Bingham plastic is the simplest model, which is a damper in parallel with a dry friction element. It lacks hysteresis and a small displacement force. Santade (2017) provides two additional variants which are often used for MR damper modeling: Bingham body model and Gamota-Filisko model. The Bingham body model variant adds a stiffness element in series, giving it a low speed force component. The Gamota-Filisko model adds a parallel damping-stiffness element in series with the Bingham body, creating plastic viscosity (low velocity force) and flow stress.

The equations for the Bingham plastic model are (Santade, 2017):

$$F = C\dot{v} + f_c \, sgn(\dot{v}) + f_0 \tag{2.1}$$

where v is the displacement of the terminals, C is the linear damper constant, f_0 is a residual force and f_c is the dry friction force and F is the resulting damper force. The model is in Figure 2.6.

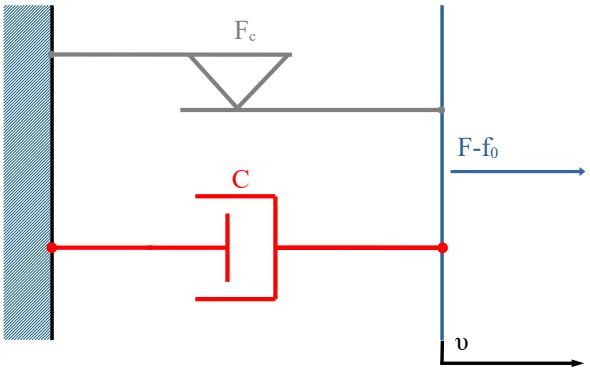

Figure 2.6. Discrete rheological diagram of the Bingham plastic model. Reproduced from Ferreira *et al.* (2023).

The equations for the Bingham body model are (Sapiński and Filuś, 2003):

$$\begin{cases} F = K(\upsilon_2 - \upsilon_1) + f_0 & if\ |F| \leq f_c \\ F = C\dot{\upsilon}_2 + f_c\ sgn(\dot{\upsilon}_1) + f_0 & if\ |F| > f_c \end{cases} \tag{2.2}$$

where υ_1 and υ_2 are the displacement of the terminals, K is the linear spring constant, C is the linear damper constant, f_0 is a residual force, f_c is the dry friction force and F is the resulting damper force. The model is in Figure 2.7.

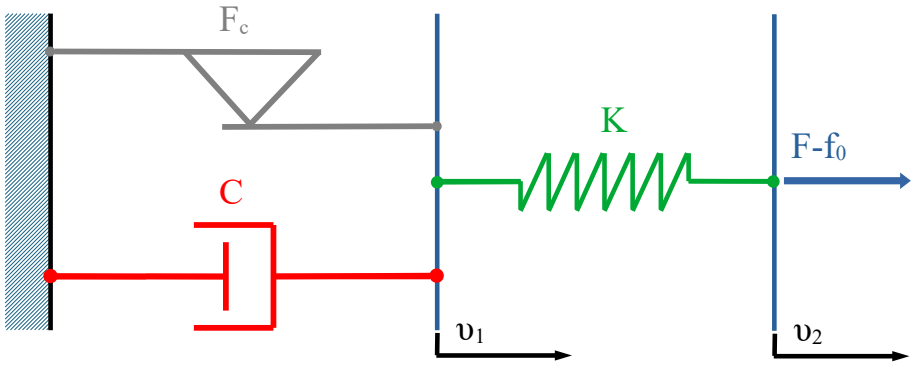

Figure 2.7. Discrete rheological diagram of the Bingham body model. Adapted from Ferreira *et al.* (2023).

The Gamota-Filisko model structure is present in Figure 2.8.

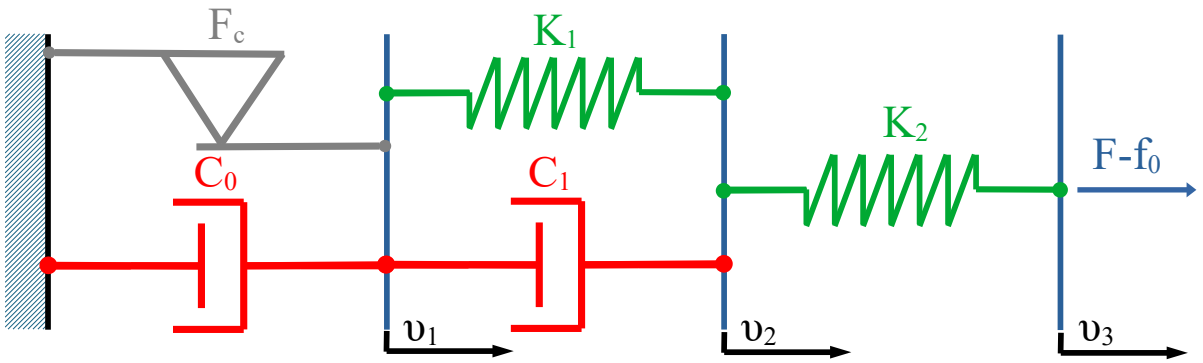

Figure 2.8. Discrete rheological diagram of the Gamota-Filisko formulation. Adapted from Ferreira *et al.* (2023).

The equations for the Gamota-Filisko model are (Sapiński and Filuś, 2003):

$$F = \begin{cases} K_2(\upsilon_3 - \upsilon_2) + f_0 = K_1(\upsilon_2 - \upsilon_1) + C_1\dot{\upsilon}_2 + f_0 & if\ |F| \leq f_c; \\ K_2(\upsilon_3 - \upsilon_2) + f_0 = K_1(\upsilon_2 - \upsilon_1) + C_1\dot{\upsilon}_2 + f_0 & \\ = C_0\dot{\upsilon}_1 + f_c sgn(\dot{u}_1) + f_0 & if\ |F| > f_c; \end{cases} \tag{2.3}$$

where υ_1, υ_2 and υ_3 are the displacement of the terminals, K_1 and K_2 are the linear spring constants for the first and second stages respectively, C_1 and C_2 are the linear damper constant for the first and second stages respectively, f_0 is a residual force, F_c is the dry friction force and F is the resulting damper force. It requires solving a partial differential equation for the values of

$\dot{v}_1$, $\dot{v}_2$, v_1 and v_2, or integrating an equivalent system of ordinary differential equations for $\ddot{v}_1$, $\ddot{v}_2$, $\dot{v}_1$ and $\dot{v}_2$.

The Bingham plastic force may be solved directly, while the Bingham body is directly solved after evaluating an if loop. The Gamota-Filisko model needs to be numerically integrated as well.

2.1.3.2 Bouc-wen model

The Bouc-wen model is composed by a Bouc-wen hysteresis term in parallel with a stiffness and a damping element. This can be observed in Figure 2.9.

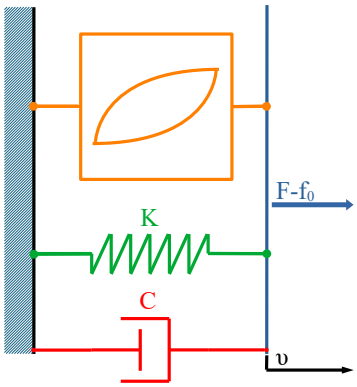

Figure 2.9. Bouc-wen model. Adapted from Ferreira *et al.* (2023).

Ismail *et al.* (2009) gives many formulations from the literature for the Bouc-wen hysteresis, with the following being the most elementary one:

$$F = c\dot{v} + kv + \alpha z - f_0 \tag{2.4}$$

where v is the terminals' relative displacement, f_0 is a residual force, c is the linear damping, k is the linear stiffness of the model and z is the hysteresis variable given by

$$\dot{z} = (\delta - \beta|\dot{z}|^n - \gamma\dot{z}|\dot{z}|^{n-1})\dot{v} \tag{2.5}$$

with n, α, δ, γ and β being the hysteresis loop constants.

The most promising model is the one in (Kwok *et al.*, 2007). It gives the formulation for the forces in a non-symmetric MR damper as well as the hysteretic component the same as equation (2.4), but has a slight variation for equation (2.5). It describes it as

$$\dot{z} = (\delta - \beta|\dot{z}|^n - \gamma sgn(zv_\mu)|\dot{z}|^n)v_\mu \tag{2.6}$$

$$v_\mu = (\dot{v} - \mu\, sgn(v)) \tag{2.7}$$

where μ is an additional hysteresis loop constant, which creates a force asymmetry with relation to $\dot{v}$. In other words, this allows for a non-zero force at zero velocity, which is desirable when modeling an MR damper.

The variation of the model with the current has been done in a few different ways, such as the more explicit model in (Dominguez *et al.*, 2008), the curve fitting method in (Xiaoliang *et al.*, 2022; Abebaw *et al.*, 2020) or the exponential curve fitting method in (Zhu *et al.*, 2019). The advantage of the fit methods is that they are much simpler to model, while their disadvantage is that their precision depends heavily on the number of tests performed.

Erlicher and Point (2004) also gives three constraints,

$$\begin{cases} n > 0 \\ \beta > 0 \\ -\beta \leq \gamma \leq \beta \end{cases} \tag{2.8}$$

which guarantee the model obeys the second law of thermodynamics.

2.1.3.3 Double Sigmoid

The double Sigmoid model is named so because it contains two Sigmoid curves dividing each other. The general expression for the curve is given (RICHARDS, 1959) as

$$y_{lgi}(k_{cl}, K, \gamma, O, B, t, \eta) = k_{cl} + \frac{K - k_{cl}}{(\gamma + Oe^{-Bt})^{\frac{1}{\eta}}} \tag{2.9}$$

in which k_{cl}, K, γ, O, B, and η are curve parameters and t is the independent variable. Meanwhile, the basic double Sigmoid model is described in (Abdul Aziz *et al.*, 2022) as

$$F(\dot{v}) = F_c \frac{1 - e^{a(\dot{v} - x_v sign(v))}}{1 + e^{a(\dot{v} - u_v sign(v))}} + C_i \dot{v} \tag{2.10}$$

where F is the damper force for velocity $\dot{v}$, F_c is the Coulomb damper force, x_v is the zero-force velocity, a is the Coulomb force velocity coefficient and C_i is the linear damping constant. This model lacks some of the features present in Wang's model, such as direct parametrization of the damper response to current.

Wang's model is part of the double Sigmoid family of models, developed in a pair of articles (Wang *et al.*, 2004; Ma *et al.*, 2002). Its current form is

$$F(\dot{v}) = f_t \left(\frac{1 - e^{F_1(\dot{v})}}{1 + e^{F_1(\dot{v})}} - k_5 \right) (1 + F_2(\dot{v})) \tag{2.11}$$

where f_t is the function described in equation (2.12), F_1 is the Sigmoid curve hysteresis term laid out in equation (2.13) and F_2 is the high-low velocity rise term described in equation (2.15):

$$f_t = f_0(1 + e^{a_1 v_m}) \left(1 + \frac{k_2}{1 + e^{-a_2(i + I_0)}} - \frac{k_2}{1 + e^{-a_2(I_0)}} \right) \tag{2.12}$$

$$F_1(\dot{v}) = -\frac{a_0}{1 + k_0 v_m} \left((\dot{v}) + sgn(\ddot{v}) k_4 v_m (1 + \frac{k_3}{1 + e^{-a_3(i + I_1)}} - \frac{k_3}{1 + e^{-a_3(I_1)}}) + k_6 v_m \right) \tag{2.13}$$

$$v_m = \sqrt{\dot{v}^2 - \ddot{v}\ v} \tag{2.14}$$

$$F_2(\dot{v}) = |(\dot{v})|e^{-a_4 v_m}\left(\frac{1 + sgn_2(\dot{v})}{2}k_{1c} + \frac{1 - sgn_2(\dot{v})}{2}k_{1e}\right) \tag{2.15}$$

where a_0, a_1, a_2, a_3, a_4, k_0, k_{1c}, k_{1e}, k_2, k_3, k_4, k_5, k_6, I_0, I_1 and f_0 are model constants, with an applied current i and a peak velocity v_m. By employing the function $sgn_2(\dot{v})$[1], it is possible to avoid any evaluations of "if" loops for the model.

2.1.4 Modified Wang model

During preliminary testings, divergence issues were detected with the Wang model. Upon further analysis, these stability issues were traced back to a single term, the v_m term. This happened because the v_m term is inherently self-amplifying at an exponential degree.

Mathematically, this can be seen by observing that the expression for v_m presented in the literature, equation (2.14), is proportional to the instantaneous velocity, acceleration and position. However, $\ddot{x}$ is proportional to, among other terms, $f_0\ exp\ (\alpha_1\ v_m)$. This means that, whenever v_m becomes big enough, it dominates the expression and becomes the most influential factor in $\ddot{x}$. Because it is proportional to the exponential of itself, it quickly diverges, regardless of the integration scheme.

Logically, this can be explained as occurring because the expression for v_m is dependent on the future maximum velocity. Since this future maximum velocity also depends on the acceleration, if the acceleration becomes big enough, this maximum velocity follows suit. The future maximum velocity retroactively depends on what it predicts itself to be, with its magnitude increasing based on its own prediction. This is not always stable, clearly violating energy conservation when it becomes an exponential force growth.

Under test bench conditions, this maximum velocity is determined a priori, and the force exerted by the damper is compensated by the testing machine so as to apply the desired test conditions into the damper. The acceleration and velocity never depend on the damper, and this issue never surfaces. When placed in a suspension, however, the damper is a key part of the evolution of the x variable over time. This becomes even more pronounced with random excitations, as they can produced very high $\ddot{v}$ values due to their nature allowing for big and sudden variations in the $K \cdot x_u$ term. This creates high $\ddot{v}$ values that can allow the v_m value to go overboard.

To solve this while maintaining compatibility with the results from the literature, a new expression that only depends on past excitation history is proposed for the v_m term. Instead of the maximum future velocity, the maximum past velocity is proposed as the v_m value. This means that the damper hysteresis loop is dictated by its history, consistent with the hypothesis of hysteresis.

Equation (2.16) is proposed as the new formulation for the v_m term, which states that

[1] $sgn_2(\dot{v})$ is a a modified Signum function whose value at $\dot{v}$ = 0 is 1.

$$v_m = \begin{cases} max(\dot{v}(t), max(v_m)) & if \quad \ddot{v} \leq 0 \\ min(\dot{v}(t), min(v_m)) & if \quad \ddot{v} > 0. \end{cases} \tag{2.16}$$

In this equation, the peak velocity is determined by either the past peak velocity or the present velocity, if it surpasses the past recorded peak. The peak velocity can be either positive or negative, depending on whether the damper terminals are accelerating or decelerating. This allows for the upper hysteresis loop to be separated from the lower. Because past and future maximum excitations are the same for harmonic excitations under steady state, equations (2.14) and (2.16) are the same for said cases. This guarantees the formula is still valid for results in the literature using harmonic excitations.

In order to show that this formulation was truly equal for harmonic excitations and has better stability under random excitations, a test will be carried out. This test will be performed on a modified test bench condition in which a Wang damper element will be associated in series to a mass followed by spring, in the manner displayed in Figure 2.10. The purpose of this modified setup is to allow for the dynamical feedback conditions needed for the purported stability issues with the original v_m formulation to occur.

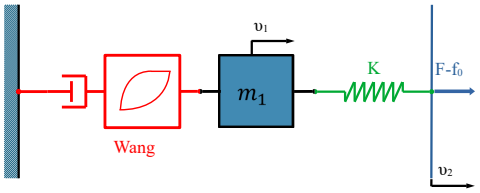

Figure 2.10. Example of Wang's damper under a different load condition. Adapted from Ferreira *et al.* (2023).

Tho ensure the modification actually corrects the problem and retains compatibility with the results in the literature, the two models will then be loaded with two inputs: a sine excitation and a fixed-seed GWN excitation. The results between the Wang damper with the original and new v_m formulation will be compared. The results are presented in Section 5.1.

2.1.5 The Wang-II formulation

The Wang model is, in general terms, a combination of a linear damper with a general Sigmoid curve expression. However, the Sigmoid element in the model can be expressed in an even more general manner as seen in equation (2.9). As such, an extension of the model can be proposed by adding the remaining degree of freedom into the Sigmoid part of the Wang model.

To show how this can be done, it is first necessary to show that the expression in equation (2.17) is the sum of two scaled versions of the logistic curve y_{logi} from equation (2.9). This

means that

$$\begin{aligned}\left(a\frac{C-Oe^{-Bt}}{(C+Oe^{-Bt})^{\frac{1}{\eta}}}+z\right)=-a\left(\frac{C+Oe^{-Bt}-2C}{(C+Oe^{-Bt})^{\frac{1}{\eta}}}-z\right)=\\ -a\frac{1}{(C+Oe^{-Bt})^{\frac{1}{\eta}-1}}+2aC\frac{1}{(C+Oe^{-Bt})^{\frac{1}{\eta}}}+az\\ =y_{lgi}(az,-a(1-z),C,O,B,t,\frac{\eta}{1-\eta})+y_{lgi}(0,2aC,C,O,B,t,\eta)=y_{lgi_1}+y_{lgi_2}\end{aligned} \tag{2.17}$$

We also show that, if we consider Bt as equal to $F_1(\dot{v})$ and η, O and C as equal to 1, the same is true for expression

$$\begin{aligned}f_t\left(\frac{1-e^{F_1(\dot{v})}}{1+e^{F_1(\dot{v})}}-k_5\right)=-f_t\left(\frac{e^{-F_1(\dot{v})}-1}{1+e^{-F_1(\dot{v})}}-k_5\right)=-f_t\left(\frac{1+e^{-F_1(\dot{v})}-2}{1+e^{-F_1(\dot{v})}}-k_5\right)=\\ -f_t(1-k_5)+2f_t\frac{1}{1+e^{-F_1(\dot{v})}}=y_{lgi}(-f_t(1-k_5),f_t(1+k_5),1,1,\frac{F(\dot{v})}{\dot{v}},\dot{v},1).\end{aligned} \tag{2.18}$$

Finally, it can also be shown expression (2.18) is a specific case of (2.17), as well as of (2.9), where a equals f_t, z equals k_5, C, O and η equals 1, B equals $\frac{F(\dot{v})}{\dot{v}}$ and t equals $\dot{v}$:

$$\begin{aligned}y_{lgi}(-f_t(1-k_5),f_t(1+k_5),1,1,\frac{F(\dot{v})}{\dot{v}},\dot{v},1)=\\ y_{lgi}(f_tk_5,-f_t(1-k_5),C,O,B,t,1)+y_{lgi}(0,2f_t,1,1,\frac{F(\dot{v})}{\dot{v}},\dot{v},1)=\\ y_{lgi}(az,-a(1-z),C,O,B,t,\frac{\eta}{1-\eta})+y_{lgi}(0,2aC,C,O,B,t,\eta)=y_{lgi_1}+y_{lgi_2}\end{aligned} \tag{2.19}$$

We can then generalize (2.11) into

$$\frac{F_{wang}(\dot{v})}{(1+F_2(\dot{v}))}=f_t\left(\frac{1-e^{-F_1(\dot{v})}}{1+e^{-F_1(\dot{v})}}-k_5\right)=f_t\left(\frac{C-Oe^{-F_1(\dot{v})}}{\left(C+Oe^{-F_1(\dot{v})}\right)^{\frac{1}{\eta}}}-k_5\right). \tag{2.20}$$

The exact correspondence between the terms of the generalized logistic curve and the Wang formulation is determined by analyzing the expressions. The terms O, k_{cl}, γ and η are originally hidden in the unmodified Wang model by being set to either $\pm$ 1 or 0. By allowing them to take any value, the curve gain additional freedom to shape itself in any manner. The η coefficient was further split into η_n and η_p so as to allow for a asymmetric curve behavior regarding speed.

The formulation in equation (2.12) can, then, be modified to the following form proposed

$$F(\dot{v})=f_t\left(\frac{\gamma-Oe^{F_1(\dot{v})}}{\left(\gamma+Oe^{F_1(\dot{v})}\right)^{F_4(v)}}-k_5\right)(1+F_2(\dot{v}))+k_{cl_2}\dot{v} \tag{2.21}$$

where

$$F_4(v)=\left(\frac{1+sgn_2(\dot{v})}{2}\eta_p+\frac{1-sgn_2(\dot{v})}{2}\eta_n\right)^{-1}. \tag{2.22}$$

One deviation from the original Richard's curve is that the term k_{cl} is originally just a constant.

However, it was decided to make it a function of $\dot{v}$ so as to behave as a linear damping term instead. Furthermore, it was originally supposed to be added to the term f_t, but it was opted not to so as to separate the influence of the terms. Another way of looking at it is that f_t actually equals $(K - k_{cl2})$ and the $k_{cl}\dot{v}$ term is just an added linear damping term unrelated to the logistic expression. This extended formulation was denominated the Wang-II model.

To assert whether this modification improves the model, this modified model was compared to other models with respect to how well it could reproduce experimental data. This procedure is described in Section 3.2 and the results are presented in Section 5.1.

2.1.6 Transient considerations

A problem came to light after performing the procedures described in the previous section. The presented v_m model is inadequate for modeling systems under transient excitations. Its main issue is the permanent hysteresis, which occur because once v_m has reached a certain magnitude, it has no mechanism to climb down. This is not a concern for steady state models, which are expected to have nearly constant values of v_m over time, but transient oscillations can create phenomena such as a permanent damper displacement under no excitation. To enable the study of damper behavior under obstacles such as speed bumps, a second v_m formulation was proposed:

$$v_m = \sqrt{abs(|L^{-1}\{L\{\dot{v}^2\}T(s)\}|)} \tag{2.23}$$

$$T(s) = \frac{C_3}{sC_2 + C_1} \tag{2.24}$$

where $L(s)$ is the Laplace transform operator, s is the Laplace transform variable and C_1, C_2 and C_3 are model constants. This formulation sought to meet three criteria:

- Be as simple as possible while still being accurate;
- Only depend on past excitations;
- Have a decay mechanism.

This formulation was obtained through an iterative process of trial and error, where the procedures performed for fitting the v_m formulation of the Modified Wang model were repeated with different candidates. This formulation was chosen as the one that had the best performance, with simpler formulations being preferred for similar performance levels. The full procedure is also described in Section 3.2 and the results are presented in Section 5.1.

Additionally, a few minor issues were also identified with the previous formulation. They weren't the main driving force behind the new formulation being proposed, but also affect the behavior fidelity of the formulation.

First, because the v_m term affects the force equilibrium displacement, this also causes the model equilibrium point to be dependent upon the v_m value and to tend to grow as time goes

on. As the vehicle with equipped with an MR damper is a chaotic system (Boreiry *et al.*, 2019), this means that the equilibrium point is meta-stable sometimes.

Second, the presented formulation also causes the value of v_m to be more extreme than it otherwise would. A model with permanent memory will always be proportional to its most extreme event in the time window considered, while a model with limited memory will be proportional to the most extremes event in its finite window. Once the model with permanent memory has been subjected to a time frame longer than the finite model's window, it is picking its value from a bigger pool of possible values, naturally allowing greater quantities to be reached.

2.2 VEHICLE MODELING

A vehicle may be modeled through more direct representations such as multi body dynamic simulation, or through simplifications that focus on the vibrational dynamics. Of note are the vehicle simplifications into mass, spring and damper elements, such as the 1/4 vehicle, the 1/2 vehicle and the full vehicle model. They are exemplified in Figure 2.11.

The full vehicle model can measure all metrics, including the lateral roll dynamics, as well as provide the most complete picture of the vehicle dynamical behavior regarding said metrics. Due to its great performance coming at the cost of the highest model complexity, it has moderate presence in the topics of ride quality evaluation (Abdelkareem *et al.*, 2018; Widner *et al.*, 2022), MR damper behavior analysis (Xu and Ahmadian, 2013) and controllable suspension performance investigation (Fleps-Dezasse and Brembeck, 2016; Kim *et al.*, 2023). The passenger and seat may be included in the model (Shirahatti *et al.*, 2008; Mitra *et al.*, 2016). This increases the complexity of the vehicle model as well as the precision of the results.

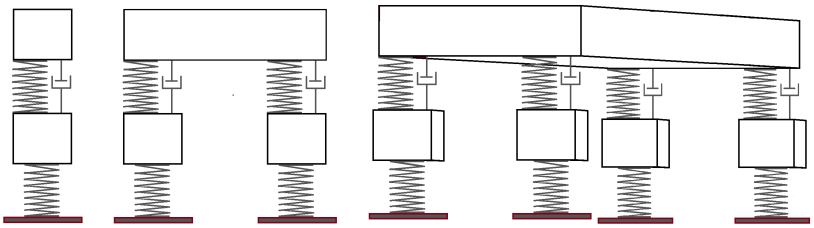

Figure 2.11. Example of quarter, half and full vehicle models.

All these models work by representing the suspension as simply connecting two masses. Some works use more complex suspension configurations, such as the MacPherson suspension (Nagarkar and Vikhe, 2016; Hong *et al.*, 2000). While this does model the vehicle with greater accuracy if it uses said suspension, it loses some generality. It also introduces non-linearities which may be undesirable, as well as makes the model more complex.

Most tire models are a linear stiffness element or occasionally a parallel assemble of linear damping and stiffness elements (Wang *et al.*, 2004). Gillespie (2021) explains that the damping element may be added to represent the tire inherent visco-elastic nature.

The generic shape of the 1/4, 1/2 and full vehicle model systems is

$$\boldsymbol{M}\ddot{\boldsymbol{x}} + \boldsymbol{D}\dot{\boldsymbol{x}} + \boldsymbol{K}\boldsymbol{x} + \boldsymbol{B}\boldsymbol{u} = \boldsymbol{C}\boldsymbol{z} \tag{2.25}$$

where $\boldsymbol{C}$ is the excitation matrix, $\boldsymbol{z}$ is the excitation vector, $\boldsymbol{M}$ is the mass matrix, $\boldsymbol{D}$ is the damping matrix, $\boldsymbol{K}$ is the stiffness matrix, $\boldsymbol{x}$ is the system coordinates, $\boldsymbol{B}$ is the Input matrix and $\boldsymbol{u}$ is the control action. This equation is valid for all the models as long as the appropriate matrices are used.

The vehicle models discussed are all linear. Real world vehicles are subject to non-linearities borne from varied causes. Some of these phenomena will be discussed in other sections.

2.2.1 State space

The equation system in 2.25 is a partial differential equation, but it may be represented into its state-space equivalent (Ogata, 2010), which transforms it into a more complex system of ordinary differential equations. This is useful because, while more complex, it is easier to numerically solve the ordinary differential equations. It can be expressed as

$$\begin{bmatrix} \dot{\boldsymbol{x}} \\ \ddot{\boldsymbol{x}} \end{bmatrix} = \begin{bmatrix} 0 & \boldsymbol{I} \\ \boldsymbol{K}\boldsymbol{M}^{-1} & \boldsymbol{D}\boldsymbol{M}^{-1} \end{bmatrix} \begin{bmatrix} \boldsymbol{x} \\ \dot{\boldsymbol{x}} \end{bmatrix} + \begin{bmatrix} 0 \\ \boldsymbol{B}\boldsymbol{M}^{-1} \end{bmatrix} \begin{bmatrix} 0 \\ \boldsymbol{u} \end{bmatrix} + \begin{bmatrix} 0 \\ \boldsymbol{C}\boldsymbol{M}^{-1} \end{bmatrix} \begin{bmatrix} 0 \\ \boldsymbol{z} \end{bmatrix} \tag{2.26}$$

where $\boldsymbol{I}$ is the identity matrix. The generic compact representation of the state space is of the form

$$\dot{\boldsymbol{x}} = \boldsymbol{A}\boldsymbol{x} + \boldsymbol{B}\boldsymbol{u} + \boldsymbol{C}\boldsymbol{z} \tag{2.27}$$

where $\boldsymbol{A}$ is the space-state linear matrix terms and $\boldsymbol{B}$, $\boldsymbol{C}$, $\boldsymbol{x}$, $\boldsymbol{u}$ and $\boldsymbol{z}$ are their state space equivalents.

2.2.2 Quarter vehicle

The 1/4 vehicle is used in many works for purposes including, but not limited to, ride quality evaluation (Gillespie, 2021; Ferreira *et al.*, 2022; Rill and Castro, 2020), MR damper behavior analysis (Jamadar *et al.*, 2021; Majdoub *et al.*, 2013; Ferreira and Morais, 2023; Li *et al.*, 2021) and controllable suspension performance investigation (Koch, 2011; Karnopp *et al.*, 1974; Melo, 2017; Karnopp, 1995; Chen *et al.*, 2014; Ahmadian, 2017). It is widespread use occurs because of it provides good approximations of the real vehicle dynamics while being very simple (Gillespie, 2021). More specifically, as explained by (Savaresi *et al.*, 2010), the 1/4 vehicle can analyze two important safety and comfort metrics, the Road-hold and UPBD RMS respectively, discussed in Section 2.4. Model examples are demonstrated in Figure 2.12.

Using a notation where subscript s denotes the upper body (the upper mass and the suspension) and the subscript u denotes unsprung body (the tire), the basic 1/4 vehicle model

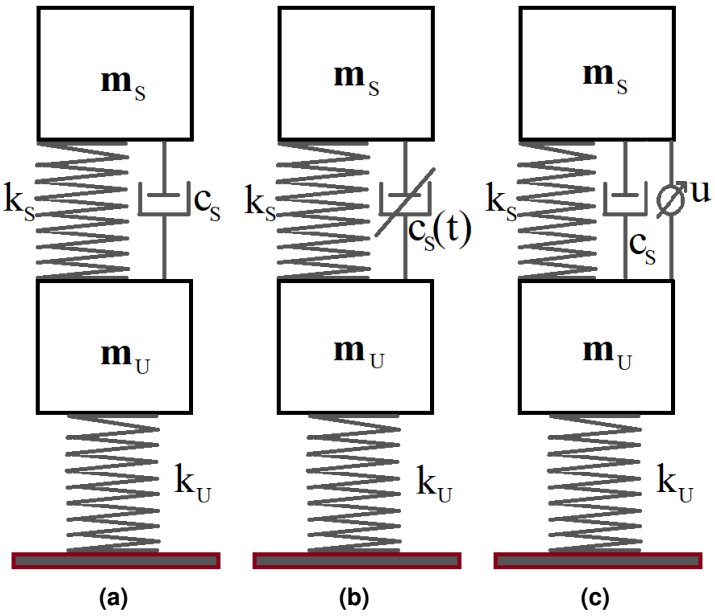

Figure 2.12. Quarter vehicle models representations for different types of suspensions: a) Passive, b) Semi-active, c) Active. Variables are explained in equation (2.29).

is given as

$$\begin{aligned} m_s\ddot{x}_s &= k_s(x_s - x_u) + c_s(\dot{x}_s - x_u) - u \\ m_u\ddot{x}_u &= k_u(x_u - x_s + z) + c_s(\dot{x}_u - \dot{x}_s + \dot{z}) + u, \end{aligned} \tag{2.28}$$

which can be represented in matrix form as the systems of equations

$$\begin{bmatrix} m_s & 0 \\ 0 & m_u \end{bmatrix} \begin{bmatrix} \ddot{x}_s \\ \ddot{x}_u \end{bmatrix} + \begin{bmatrix} c_s & -c_s \\ -c_s & c_s \end{bmatrix} \begin{bmatrix} \dot{x}_s \\ \dot{x}_u \end{bmatrix} + \begin{bmatrix} k_s & -k_s \\ -k_s & k_s + k_u \end{bmatrix} \begin{bmatrix} x_s \\ x_u \end{bmatrix} = \begin{bmatrix} 0 \\ k_u \end{bmatrix} z + \begin{bmatrix} B_{E1} \\ B_{E2} \end{bmatrix}, \tag{2.29}$$

where k_s and k_u are the stiffness of suspension and tires respectively, c_s is the suspension damper coefficient, m_s and m_u are the sprung and unsprung masses, respectively, B_{E1} and B_{E2} are the control forces on the sprung and unsprung bodies (which absorb the u term), z is the road excitation and x are the vehicle coordinates.

2.2.2.1 Input matrix B

The term **B** can vary depending on which model is being used. The general form of a controller on a 1/4 vehicle model will be

$$\begin{bmatrix} B_{E1} \\ B_{E2} \end{bmatrix} = \begin{bmatrix} B_1 & B_2 & 0 \\ 0 & -B_2 & B_3 \end{bmatrix} \begin{bmatrix} u_1 \\ u_2 \\ u_3 \end{bmatrix} \tag{2.30}$$

where u_1 and B_1 are the control terms which exert force only on the upper body, u_2 and B_2 are the control terms which exert force between the upper and lower body, and u_3 and B_3 are the

control terms which exert force only on the lower body. In general, it is not feasible to attach an actuator solely in the upper or lower body, and the only term that is not 0 is B_2. For the active and semi-active suspensions, the $\boldsymbol{B}$ term is given by

$$\begin{bmatrix} B_{E1} \\ B_{E2} \end{bmatrix} = \begin{bmatrix} B_2 \\ -B_2 \end{bmatrix} u_2 \tag{2.31}$$

while a passive system will have $\boldsymbol{B}$ equal to 0, as there is no controller force u_2 either. The main difference between an active and semi-active system comes from the fact that u_2 is more limited in its values, being only able to assume values with the same sign as $(\dot{x}_s - \dot{x}_u)$. The value of B_2 itself is usually 1.

2.2.2.2 System solutions

The frequency domain results of these equations can be solved for in two manners: directly in the frequency domain, or indirectly in the time domain and then using a tool such as the Fourier transform to cast the results into the frequency domain. Numerical solutions are preferred because they can better capture non-linear behavior. These linearities can arise from the suspension, tires, the road or from control actions.

To obtain the time domain solution the state space representation in (2.27) is applied on the 1/4 vehicle model, which results in

$$\begin{bmatrix} \dot{x}_s \\ \dot{x}_u \\ \ddot{x}_s \\ \ddot{x}_u \end{bmatrix} = \begin{bmatrix} 0 & 0 & 1 & 0 \\ 0 & 0 & 0 & 1 \\ -\frac{k_s}{m_s} & \frac{k_s}{m_s} & -\frac{c_s}{m_s} & \frac{c_s}{m_s} \\ \frac{k_s}{m_u} & -\frac{k_s+k_u}{m_u} & \frac{c_s}{m_u} & -\frac{c_s}{m_u} \end{bmatrix} \begin{bmatrix} x_s \\ x_u \\ \dot{x}_s \\ \dot{x}_u \end{bmatrix} + \begin{bmatrix} 0 \\ 0 \\ 0 \\ \frac{K_u}{m_u} \end{bmatrix} z + \begin{bmatrix} 0 \\ 0 \\ \frac{1}{m_s} \\ \frac{1}{m_u} \end{bmatrix} u. \tag{2.32}$$

It is then numerically integrated with a suitable algorithm to obtain the variables in the time domain. Common algorithms used include the forward Euler, the Backwards Euler, the Crank-Nicholson, the Runge-Kutta of n-th order and the adaptative Runge-Kutta of n-th/m-th order. The Matlab software offers the adaptative 4th/5th order Runge-Kutta algorithm ('RK45') as its the standard solution method, which has shown good performance in prior works by the author. The Backwards Euler and Crank-Nicholson also showed success when coupled with Matlab's numerical equation solver, but were ultimately outperformed. The forward Euler and non-adaptative n-th order Runge-Kutta did not perform well, diverging too often.

The second method is to analytically solve it. Assuming no controller term, the analytical frequency domain model is obtained by applying the Fourier transform on (2.29). The frequency domain representation $H(x_i)$ of a variable x_i can be obtained by its Fourier transform as such (Proakis and Manolakis, 2014):

$$H(x_i, \omega) \int_{-\infty}^{\infty} x_i(t) e^{-jt\omega} dt \tag{2.33}$$

where ω is the evaluated frequency in rads and j is the imaginary unit $\sqrt{-1}$. The transform of a

matrix with a time varying term is given by

$$H\left(N \cdot \frac{d^n\, x(t)}{d\, t^n}, \omega\right) = N \cdot X(\omega)(-j\omega)^n \tag{2.34}$$

where $\boldsymbol{N}$ is an arbitrary constant matrix and $\boldsymbol{X}(\omega)$ is the Fourier transform H of $\boldsymbol{x}$(t). By performing this operation on (2.29), its obtained

$$\left(-\omega^2 \begin{bmatrix} 1 & 0 \\ 0 & \chi \end{bmatrix} + j\omega \begin{bmatrix} c & -c \\ -c & c \end{bmatrix} + \begin{bmatrix} K_s & -K_s \\ -K_s & K_s + K_u \end{bmatrix}\right) \begin{bmatrix} X_s(\omega) \\ X_u(\omega) \end{bmatrix} = \begin{bmatrix} 0 \\ K_u \end{bmatrix} Z(\omega) \tag{2.35}$$

where χ is the mass ratio $\frac{m_u}{m_s}$, c, K_s and K_u are $\frac{c_s}{m_s}$, $\frac{k_s}{m_s}$ and $\frac{k_u}{m_s}$ respectively, and $X_s(\omega)$, $X_u(\omega)$ and $Z(\omega)$ are the frequency domain vehicle coordinates and excitation respectively.

The gain variables, which are $H_s(\omega) = \frac{X_s(\omega)}{Z(\omega)}$ and $H_u(\omega) = \frac{X_u(\omega)}{Z(\omega)}$, can then be obtained by first creating the system's matrix $\boldsymbol{S_{sys}}(\omega)$

$$\left(\begin{bmatrix} j\omega c + K_s - \omega^2 & -j\omega c - K_s \\ -j\omega c - K_s & j\omega c + K_s + K_u - \omega^2\chi \end{bmatrix}\right) \begin{bmatrix} X_s(\omega) \\ X_u(\omega) \end{bmatrix} = \boldsymbol{S_{sys}(\omega)} \begin{bmatrix} X_s(\omega) \\ X_u(\omega) \end{bmatrix} \tag{2.36}$$

and substituting it back into equation (2.35)

$$\boldsymbol{S_{sys}}(\omega) \begin{bmatrix} X_s(\omega) \\ X_u(\omega) \end{bmatrix} = \begin{bmatrix} 0 \\ K_u \end{bmatrix} Z(\omega), \tag{2.37}$$

followed by reorganizing the terms as

$$\boldsymbol{S_{sys}}^{-1}(\omega)\boldsymbol{S_{sys}}(\omega) \begin{bmatrix} X_s(\omega) \\ X_u(\omega) \end{bmatrix} Z(\omega)^{-1} = \boldsymbol{S_{sys}}^{-1}(\omega) \begin{bmatrix} 0 \\ K_u \end{bmatrix} Z(\omega)Z(\omega)^{-1} \tag{2.38}$$

and using the matrix inverse property

$$\boldsymbol{A}^{-1} = \frac{1}{|\boldsymbol{A}|} adj(\boldsymbol{A}) \tag{2.39}$$

where $adj(\boldsymbol{A})$ is the matrix A adjoint to obtain

$$\begin{bmatrix} X_s(\omega)Z(\omega)^{-1} \\ X_u(\omega)Z(\omega)^{-1} \end{bmatrix} = \frac{1}{|\boldsymbol{S_{sys}}(\omega)|} adj(\boldsymbol{S_{sys}}(\omega)) \begin{bmatrix} 0 \\ K_u \end{bmatrix} \tag{2.40}$$

which results in the matrix expression for the gains

$$\begin{bmatrix} H_s(\omega) \\ H_u(\omega) \end{bmatrix} = \frac{1}{|\boldsymbol{S_{sys}}(\omega)|} \left(\begin{bmatrix} (-j\omega c - K_s)K_u \\ (j\omega c + K_s - \omega^2)K_u \end{bmatrix}\right). \tag{2.41}$$

The closed expressions for the gains then are

$$H_s(\omega) = \frac{K_s K_u + j(K_u c\omega)}{|\boldsymbol{S_{sys}}(\omega)|} \tag{2.42}$$

and

$$H_u(\omega) = \frac{K_s K_u + j(K_u c\omega) - \omega^2 K_u}{|\boldsymbol{S_{sys}}(\omega)|} \tag{2.43}$$

where $|\boldsymbol{S_{sys}}(\omega)|$ is

$$|\boldsymbol{S_{sys}}(\omega)| = \chi\omega^4 - (k_u + k_s\chi + k_s)\omega^2 + k_s k_u + j(k_u c\omega - (1+\chi)c\omega^3) \tag{2.44}$$

To solve these systems when a control is applied, the solution depends on the structure of the controller. Some controllers have straightforward representations in the frequency domain, and the Laplace domain method can also be solved if a solution in time is desired. However, complex controllers might need specific methods, and non-linear controllers might not be solvable.

2.2.3 Half vehicle

The 1/2 vehicle model can refer to a half vehicle approximation that considers the separate behavior of either the front and back wheels or the left and right wheels. The front-back model is the most relevant for the present work, and all future mentions of the half vehicle model will refer to it unless otherwise specified. It also sees plenty of use in topics such as ride quality evaluation (Otkur *et al.*, 2022; Ferreira, 2022; de Lima *et al.*, 2012), MR damper behavior analysis (Pang *et al.*, 2018; Prabakar *et al.*, 2009) and controllable suspension performance investigation (Khan *et al.*, 2020; Prabakar *et al.*, 2016). It can analyze more ride qualities such as the rotational UPBD RMS, provide more accurate data of the Road-hold and vertical UPBD RMS and measure the longitudinal metrics of Dive and Squat under conditions of change of speed. It is more complex than the 1/4 vehicle, however. Its system for a passive vehicle is shown in Figure 2.13.

Using the notation that the subscript f represents the front elements, r the rear elements, θ the chassis rotation, u the wheels, s the chassis vertical displacement and suspension, the 1/2 vehicle model force equations are given by

$$\begin{aligned} m_{f,u}\ddot{x}_f + (c_{f,u} + c_{f,s})\dot{x}_f - c_{f,s}\dot{x}_s + c_{f,s}d_r\dot{x}_\theta + \\ (k_{f,u} + k_{f,s})x_f - k_{f,s}x_s + k_{f,s}d_r x_\theta = Z_f k_{f,u} + B_{f,s}u_{f,s} \end{aligned} \tag{2.45}$$

$$\begin{aligned} m_{r,u}\ddot{x}_f + (c_{r,u} + c_{r,s})\dot{x}_r - c_{r,s}\dot{x}_s - c_{r,s}d_f\dot{x}_\theta + \\ (k_{r,u} + k_{r,s})x_r - k_{r,s}\dot{x}_s - k_{r,s}d_f x_\theta = Z_t k_{r,u} + B_{r,s}u_{r,s} \end{aligned} \tag{2.46}$$

$$\begin{aligned} m_s\ddot{x}_s - c_{f,s}\dot{x}_f - c_{r,s}\dot{x}_r + (c_{f,s} + c_{r,s})\dot{x}_s + (c_{f,s}d_r - c_{r,s}d_f)\dot{x}_\theta \\ -k_{f,s}x_f - k_{r,s}x_r + (k_{f,s} + k_{r,s})\dot{x}_s + (k_{f,s}d_r - k_{r,s}d_f)x_\theta = -B_{f,s}u_{f,s} - B_{r,s}u_{r,s} \end{aligned} \tag{2.47}$$

$$\begin{aligned} J\ddot{x}_\theta - c_{f,s}d_r\dot{x}_f + c_{r,s}d_f\dot{x}_r + (c_{f,s}d_r - c_{r,s}d_f)\dot{x}_s + (c_{f,s}d_r^2 + c_{r,s}d_f^2)\dot{x}_\theta - k_{f,s}d_r x_f + \\ k_{r,s}d_f x_r + (k_{f,s}d_r - k_{r,s}d_f)\dot{x}_s + (k_{f,s}d_r^2 + k_{r,s}d_f^2)x_\theta = B_{f,s}u_{f,s}d_f - B_{r,s}u_{r,s}d_r \end{aligned} \tag{2.48}$$

where $k_{f,s}$ and $k_{r,s}$ are the suspension stiffness, $c_{f,s}$ and $c_{r,s}$ are the suspension damping

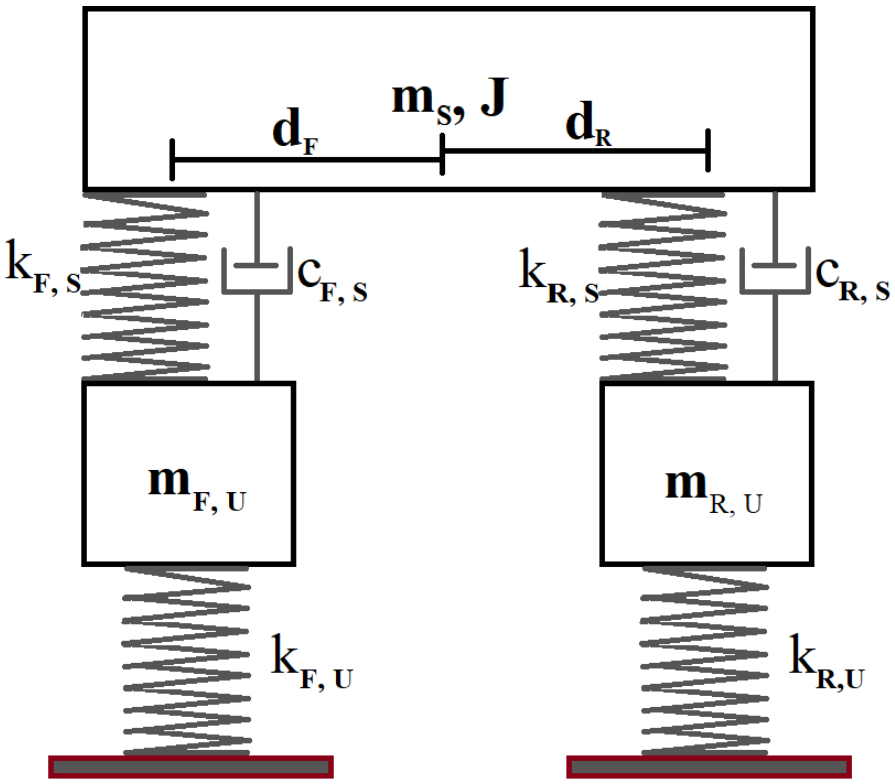

Figure 2.13. Visual representation a passive 1/2 vehicle system.

coefficients, $k_{f,u}$ and $k_{r,u}$ are the tire stiffnesses, and $m_{f,s}$ and $m_{r,s}$ are the tire mass of the front and rear wheels respectively for all the mentioned terms; J is the chassis moment of inertia, m_s is the chassis mass, $u_{f,s}$ and $u_{f,s}$ are the control actions, $B_{f,s}$ and $B_{r,s}$ are the control terms, Z_f and Z_t are the road excitations, $x_{f,u}$ and $x_{r,u}$ are the wheel coordinates and d_f and d_r are the distances from the vehicle's center of gravity of the front and rear wheels respectively for all the mentioned terms; x_θ and x_s are the chassis rotational displacement and vertical displacement coordinates.

This system of equations can, like the 1/4 vehicle, also be simplified by representing the system in matrix form, which yields

$$\boldsymbol{M_{4gdl}}\begin{bmatrix}\ddot{x}_f\\ \ddot{x}_r\\ \ddot{x}_s\\ \ddot{x}_\theta\end{bmatrix}+\boldsymbol{D_{4gdl}}\begin{bmatrix}\dot{x}_f\\ \dot{x}_r\\ \dot{x}_s\\ \dot{x}_\theta\end{bmatrix}+\boldsymbol{K_{4gdl}}\begin{bmatrix}x_f\\ x_r\\ x_s\\ x_\theta\end{bmatrix}=\boldsymbol{C_{4gdl}}\begin{bmatrix}Z_f\\ Z_t\end{bmatrix}+\boldsymbol{B_{4gdl}}\begin{bmatrix}u_{f,s}\\ u_{r,s}\end{bmatrix} \tag{2.49}$$

where $\boldsymbol{M_{4gdl}}$, $\boldsymbol{D_{4gdl}}$ and $\boldsymbol{K_{4gdl}}$ are mass, damping and stiffness matrices represented by

$$\boldsymbol{M_{4gdl}}=\begin{bmatrix}m_{f,u} & 0 & 0 & 0\\ 0 & m_{r,u} & 0 & 0\\ 0 & 0 & m_s & 0\\ 0 & 0 & 0 & J\end{bmatrix} \tag{2.50}$$

$$\boldsymbol{D_{4gdl}} = \begin{bmatrix} c_{f,u} + c_{f,s} & 0 & -c_{f,s} & c_{f,s}d_r \\ 0 & c_{r,u} + c_{r,s} & -c_{r,s} & -c_{r,s}d_f \\ -c_{f,s} & -c_{r,s} & c_{f,s} + c_{r,s} & c_{f,s}d_r - c_{r,s}d_f \\ -c_{f,s}d_r & c_{r,s}d_f & c_{f,s}d_r + c_{r,s}d_f & c_{f,s}d_r^2 + c_{r,s}d_f^2 \end{bmatrix} \tag{2.51}$$

$$\boldsymbol{K_{4gdl}} = \begin{bmatrix} k_{f,u} + k_{f,s} & 0 & -k_{f,s} & k_{f,s}d_r \\ 0 & k_{r,u} + k_{r,s} & -k_{r,s} & -k_{r,s}d_f \\ -k_{f,s} & -k_{r,s} & k_{f,s} + k_{r,s} & k_{f,s}d_r - k_{r,s}d_f \\ -k_{f,s}d_r & k_{r,s}d_f & k_{f,s}d_r + k_{r,s}d_f & k_{f,s}d_r^2 + k_{r,s}d_f^2 \end{bmatrix} \tag{2.52}$$

and $\boldsymbol{C_{4gdl}}$ and $\boldsymbol{B_{4gdl}}$ are the road and control matrices represented by

$$\boldsymbol{C_{4gdl}} = \begin{bmatrix} k_{f,u} & 0 \\ 0 & k_{r,u} \\ 0 & 0 \\ 0 & 0 \end{bmatrix} \tag{2.53}$$

$$\boldsymbol{B_{4gdl}} = \begin{bmatrix} B_{f,s} & 0 \\ 0 & B_{r,s} \\ -B_{f,s} & -B_{r,s} \\ B_{f,s}d_f & -B_{r,s}d_r \end{bmatrix} \tag{2.54}$$

The solution of this system can be carried out much in the same manner as the 1/4 vehicle: either transform it into the state space form in equation (2.26) and numerically integrate it or solve it analytically by taking its Fourier Transform and isolating its response. This will result in two gains, one for each road excitation.

2.2.4 Alternative tire models

The usual tire model is a spring, sometimes in parallel to a damper. More complex tire models exist, such as the magic formula model (Bakker *et al.*, 1987; Pacejka and Bakker, 1992), which accounts for the tire behavior more in-depth. However, such models are far more complex while not necessarily adding to the simulation. According to Ružinskas and Sivilevičius (2017), for example, the model is mostly used when fitting experimental slip data to numerical models. This is very useful when predicting behavior on non-standard terrain or tire conditions, specially on critical tire load maneuvers such as braking or turning. However, the vehicle model used must also be able to capture longitudinal and/or lateral dynamics, as otherwise the added tire dynamics won't be exposed to the conditions were they make the most difference.

While advanced tire models mainly affect maneuvers such as cornering and braking (Gillespie, 2021), some works have explored their effect on vertical dynamics (Min and Wei, 2024; Gong, 1993). The approach used seems to account for the tire's vibrational modes by modeling it as an elastic ring structure, which cause the stiffness to be displacement dependent. This approach is rare however.

Nonetheless, as evident by its widespread usage, the standard tire model adequately

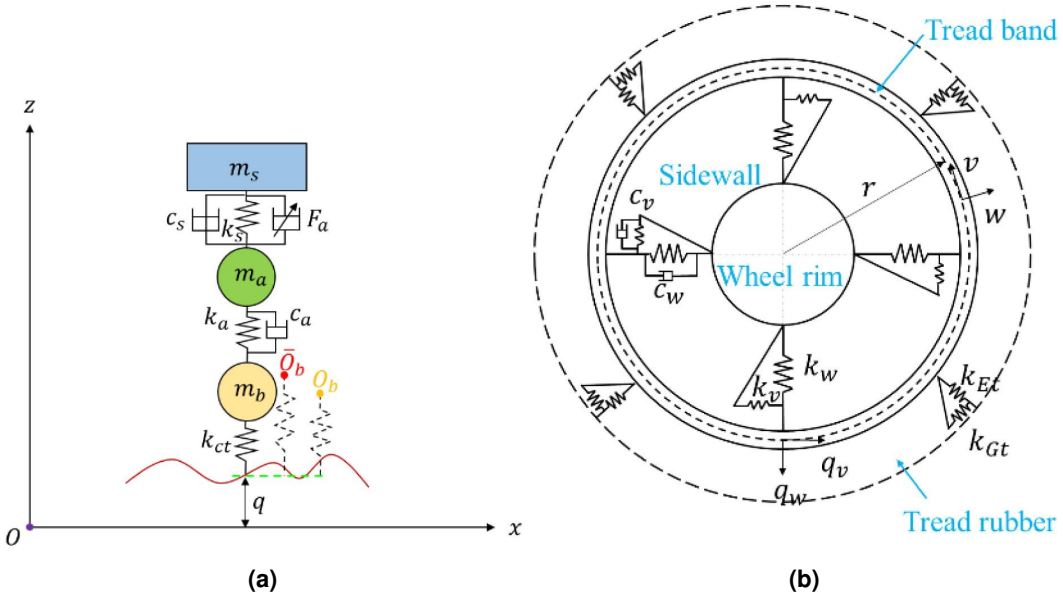

Figure 2.14. Examples of alternative tire models. Source: (Min and Wei, 2024). a) Rigid ring tire model on a quarter vehicle model. b) Flexible ring tire model.

represents the vehicular dynamics in everyday circumstances.

2.2.5 Suspension mathematical modeling

When considering the suspension, many elements can be non-linear. Figure 2.15 shows how a leaf suspension exhibits hysteresis behavior on its load cycle. A coil spring stiffness coefficient is valid only in the range its coils haven't made contact (Norton, 2006). Models like the MacPherson strut are inherently non-linear due to their arrangement.

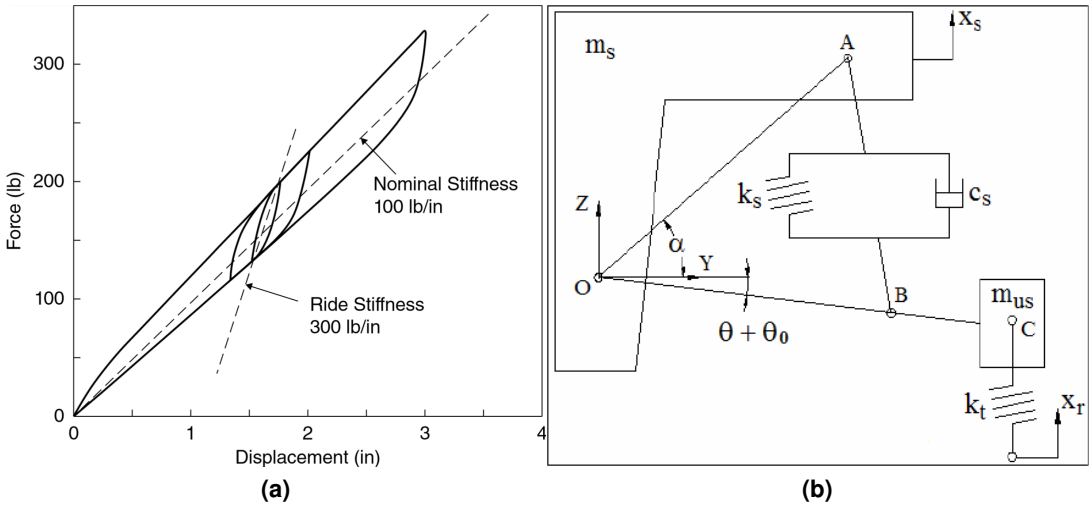

Figure 2.15. Examples of non-linearities which may be present in a suspension. a) Non-linearity of hysteresis on a leaf suspension. Source: (Gillespie, 2021). b) MacPherson strut model. Source: (Nagarkar and Vikhe, 2016).

As with the alternative tire models, the main drawback of such models is that the added

complexity is not necessarily worth the added precision. These non-linearities might not have big influences on the behavior of the vehicle. Furthermore, the results obtained for such models are less generalizable to other suspension models which don't have such property, and using specific models limits the works to which a result can be compared.

The most relevant suspension model for this study is the MR damper semi-active suspension model. The MR damper has many non-linearities. It exhibits behaviors of hysteresis, non-zero force at zero velocity and speed dependent damping coefficient, all of which are current dependent. This has been discussed in depth at Section 2.1.3.

Ideal controllable suspensions can be modeled as parts of the $\boldsymbol{Bu}$ term in equation (2.25). An ideal semi-active suspension can be modeled as an active suspension whose control action is bound, a technique known as the clipped approach:

$$u(t) = \begin{cases} f_{min} & f_{min} > u_a(t) \\ u_a(t) & f_{min} < u_a(t) < f_{max} \\ f_{max} & u_a(t) > f_{max} \end{cases} \tag{2.55}$$

where f_{min} and f_{max} are the lower and upper semi-active damping forces.

Another way to model a semi-active suspension is to represent it as a controllable damping term, such that

$$c_s(t) = c_0 + c_c(t) \tag{2.56}$$

where c_0 is the linear suspension term and $c_c(t)$ is the controllable damping term, which must always be positive.

The MR damper has additional terms which are not controllable, and which are non-linear. The main drawback of using a controllable damping term is that the damping alone cannot represent a zero velocity force, which the MR damper has due to its hysteresis. Another issue is the asymmetrical MR damper curve would sometimes require a negative damper term. These detail favors representing it with a clipped approach. Still, a mixed strategy can also be employed, where the linear terms are considered part of the linear damping, the non-linear and controllable terms are considered part of the force boundaries in the controller.

2.3 ROAD MODELING

When being used, vehicles are in constant contact with the ground. A perfectly flat terrain is nearly impossible to produce, as well as undesirable because it would remove all wheel traction. This means that the contact with the ground provides a constant source of excitations to the vehicle. Then, to model vehicle behavior, it is necessary to provide an excitation that matches the characteristics of the road profile. This is done through road models.

In (Koch, 2011), road disturbances are classified into two groups: stochastic and deterministic. These model, roughly speaking, steady state road conditions and singular events such as holes or speed bumps.

2.3.1 Deterministic models

To model a known profile, all that is necessary is to uniquely define the geometry of interest. Not all road conditions can be meaningfully studied by a deterministic shape, but elements like speed bumps, sudden elevations and long size periodic waves represent some of the realistic conditions a vehicle might find on the road that have a deterministic shape. These models are often used in conjunction with stochastic models to characterize a vehicle's functionality across multiple conditions.

2.3.1.1 Sinusoidal excitations

To periodic vibrations may be used to obtain the response of a vehicle to road conditions or to harmonic excitations at a certain frequency. They might be used to simulate long period oscillations such as surface waves (Kim *et al.*, 2023), to simulate a specially rough road as a combination of discrete sinusoidal waves (Pang *et al.*, 2018), or to obtain the system behavior at a certain frequency (Majdoub *et al.*, 2013; Nguyen, 2023). The latter case is more common when performing heave sweep tests. The gain obtained in a Heave sweep is representative of the gain for said frequency when more oscillations are added in the case of linear systems, which makes it an useful tool for analysis, but this is not a guarantee for non-linear systems (Savaresi *et al.*, 2010). The general form of single harmonic excitation is

$$E(d_x) = I\ sin(\omega\ d_x + p) + I_b \tag{2.57}$$

where I is the oscillation amplitude, ω is the frequency, d_x is the independent variable, p is the phase and I_b is the bias. The variable x is usually either the time itself or the spatial coordinate, with the frequency f being the number of cycles per second or cycles per meter respectively. Sines and cosines can be easily equated by the application of a 90º phase angle.

2.3.1.2 Bump

The profile of a speed bump is often represented through a sudden, short elevation up to a smooth peak with a mirroring descent. Its function is described in the literature in different ways. Fleps-Dezasse and Brembeck (2016) defines it as an impulse function, which has the characteristic of having a constant, finite area under its curve as its maximum goes to infinity. Oke *et al.* (2007) defines rectangular and conical bumps of both positive and negative peaks, the latter which is the case of a sudden descent followed by an elevation instead. García-Pozuelo *et al.* (2015) created a bump generating tool for Matlab in which the bump profile. The most common profile is the sinusoidal based (Khan *et al.*, 2020; Majdoub *et al.*, 2013; Pang *et al.*, 2018; Kilicaslan, 2022), while other approximations include is the parabolic profile (Otkur *et al.*, 2022), the rectangular rise (Kim *et al.*, 2023; Fleps-Dezasse and Brembeck, 2016; Oke *et al.*, 2007; Jamadar *et al.*, 2021), the triangular raise and the circular perimeter (Fleps-Dezasse and Brembeck, 2016).

For the sinusoidal raise, Majdoub *et al.* (2013) defines it as

$$E(t) = \begin{cases} \frac{I}{2}(1 - cos\left(2\pi \frac{t-T_1}{T_2-T_1}\right)) & T_1 <= t <= T_2 \\ 0 & Otherwise; \end{cases} \tag{2.58}$$

where I is the bump height, T_1 is the time where the vehicle first touches the Bump, T_2 is the time where the vehicle finishes contact, and t is the overall time. This results in a geometry with base $(T_2 - T_1)v$, where v is the velocity.

The semi-spherical bump in (García-Pozuelo *et al.*, 2015) can be defined as

$$E(d_x) = \begin{cases} R\left(1 - cos\left(arcsin\left(\frac{w-2(d_x-d_{x_1})}{2R}\right)\right)\right) & d_{x_1} <= d_x <= d_{x_1} + w \\ 0 & Otherwise; \end{cases} \tag{2.59}$$

in which I is the bump height, d_x is the spatial coordinate, d_{x_1} is the bump starting point, w is the bump length and R is a design constant which represents the radius of the base bump circle and controls how sudden the elevation is. Alternatively, R may be defined in terms of a design angle as

$$\alpha = arcsin\left(\frac{R}{2w}\right) \tag{2.60}$$

where α is the control variable instead. These parameters are made explicit in Figure 2.16.

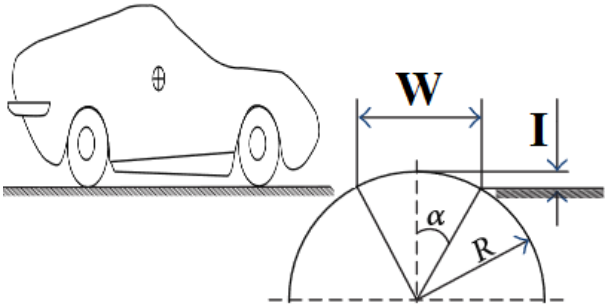

Figure 2.16. Geometric parameters of the circular formulation. Adapted from García-Pozuelo *et al.* (2015).

The formula for the rectangular bump is

$$E(d_x) = \begin{cases} I & d_{x_1} <= d_x <= d_{x_1} + W \\ 0 & Otherwise; \end{cases}, \tag{2.61}$$

and for the triangular bump is

$$E(d_x) = \begin{cases} I\frac{2(d_x-d_{x_1})}{W} & d_{x_1} <= d_x <= d_{x_1} + W/2 \\ I\left(1 - \frac{2(d_x-d_{x_1})}{W}\right) & d_{x_1} + W/2 <= d_x <= d_{x_1} + W \\ 0 & Otherwise \end{cases}. \tag{2.62}$$

The Brazilian Traffic Signaling Manual (CONTRAN, 2022) specifies two standard dimensions

for speed bumps, dubbed type A and type B. The type A variety seeks to enforce a maximum vehicle speed of 30 km/h, while type B is designed for a maximum vehicle speed of 20 km/h and has a smaller profile with smaller peaks but a higher spatial frequency due to its shorter base. Its dimensions are specified in Table 2.3.

Type	Height	Length	Max speed
A	8 to 10 cm	370 cm	30 km/h
B	6 to 8 cm	150 cm	20 km/h

Table 2.3. Speed bump dimensions according to the Brazilian Traffic Signaling Manual (CONTRAN, 2022).

2.3.1.3 Linear rise or Step

A similar case to the bump is the linear rise or step function, used to represent a sudden permanent raise, as opposed to sudden transient raise. This can effectively represent small discontinuities such as a change from one road to another, or big discontinuities such as passing through a curb. The same formulas used for the bump can be adapted to the curb by simply changing their profile to not decrease after reaching the peak height I, as in

$$E(d_x) = \begin{cases} 0 & d_x <= d_{x_1} \\ Bump & d_{x_1} <= d_x <= d_{x_1} + W/2 \\ I & d_{x_1} + W <= d_x \end{cases} \tag{2.63}$$

where "Bump" is the bump function valid in the interval d_{x_1} to $d_{x_1} + W$. The most common step function representation is the simple raise (Nassar and Al-Ghanim, 2018), which is simply

$$E(d_x) = \begin{cases} 0 & d_x <= d_{x_1} \\ I & d_{x_1} < d_x \end{cases}. \tag{2.64}$$

This function is sometimes defined as valued $I/2$ at $d_x = d_{x_1}$, becoming the Heaviside function in that case. Another relevant function is the triangular bump equivalent (Melo, 2017; Majdoub *et al.*, 2013), called the ramp function:

$$E(d_x) = \begin{cases} 0 & d_x <= d_{x_1} \\ I\frac{2(d_x - d_{x_1})}{L} & d_{x_1} <= d_x <= d_{x_1} + W \\ I & d_{x_1} + W <= d_x \end{cases} \tag{2.65}$$

in which W is the ramp length, equal to half the triangular bump length. It should be noted that, sometimes, step functions are also referred to as bumps.

2.3.2 Stochastic models

A stochastic model is a model that is inherently random. This kind of model is useful for describing road conditions because often the road profile's main source of disturbance comes from small scale variations in its surface, such as defects and natural roughness inherent to all surfaces (Aghababaei *et al.*, 2022; Dagnall, 1986). Dagnall (1986) also differentiates between roughness and waviness: waviness refers to larger scale oscillations, and while waviness can also be modeled by stochastic functions, it is not formed through the same processes nor is can only be represented by stochastic functions. This difference is illustrated in Figure 2.17.

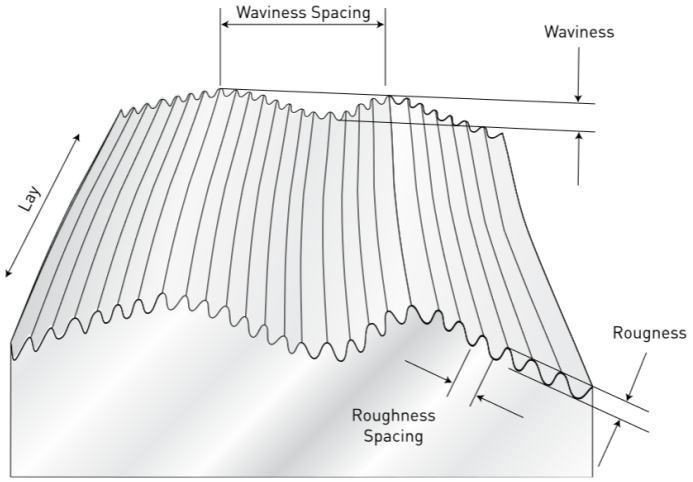

Figure 2.17. Illustration of surface roughness and waviness. Source: (Dagnall, 1986).

There are many possible terrains, such as asphalt, dirt, concrete and ice, each with their own roughness characteristics (Ružinskas and Sivilevičius, 2017). In ISO (2016) it is required that at least the information about the type of surface material, its maintenance condition, its grade (longitudinal slope), its cross-fall (lateral slope) and, if any, the curve radius all be provided. This is because all these factors can affect the nature of the road analyzed. When an adequate road profile curve for the desired simulation conditions has been obtained, it can then be used to simulate a vehicle. This is done by substituting the profile data as the excitation term in equation (2.25), as Figure 2.18 indicates.

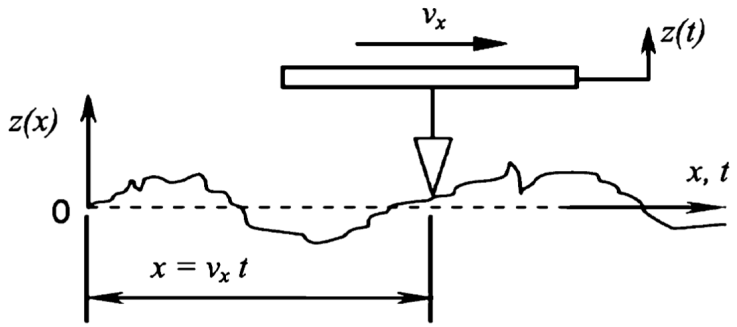

Figure 2.18. Example of surface roughness being used to excite a vehicle model. Source: (Dharankar *et al.*, 2016).

For a simulation performed in the time domain, the profile must also be described temporally.

However, when describing the roughness and oscillations of a certain road profile, the most common approach is to do so by its Power spectral density (PSD) (Dharankar *et al.*, 2016). The road profile PSD data must be used for creating the spatial profile.

2.3.2.1 Power Spectral Density

The PSD of a function is defined as the Fourier transform of its autocorrelation (Inman, 2013). In more tangible terms, the PSD consists of a diagram or data series describing the distribution of excitation energy across the wave frequencies, either spatial or temporal, of said function. This data allows for the creation of a time profile with the same characteristics through procedures such summing pure sine waves of adequate power with a random phase, also known as the method of superposition of harmonics (Dharankar *et al.*, 2016; Buhari and Seblan, 2022), or through a white noise filtration process (Dharankar *et al.*, 2016; Lenkutis *et al.*, 2020). The function itself can be either the road displacement or slope velocity (ISO, 2016).

A typical description of a road profile is one which follows a power law as

$$\Psi(\omega) = \phi_0 \left(\frac{\omega_0}{\omega}\right)^w \tag{2.66}$$

where $\Psi(\omega)$ is the road profile displacement PSD, ω is the frequency, ϕ_0 is the desired variance at the reference frequency ω_0 and w is the waviness number, typically between 1.75 to 2.25, with 2 being the average value (Schiehlen, 2006a). For road profiles its common to use the spatial frequency, which has units of cycles/m or rads/m. The value of ϕ_0 is a free variable, and defines how rough the road is at the reference frequency ω_0.

The power law model is usually determined as valid in only a finite frequency range. This is because the model has two problems: First, its PSD goes to infinity as the frequency goes to 0. Second, this makes the wave have infinite power. This characteristic is not seen in real road profiles, and as such other models exist that are valid in the whole domain.

As per Schiehlen (2006a), there two main ways to approximate a road profile displacement PSD so it has finite variance, the first order approximation and second order approximation. Their PSD are given by

$$\Psi(\omega) = \frac{2\alpha\sigma^2}{\pi} \frac{1}{\alpha^2 + \omega^2} \tag{2.67}$$

for the 1st order approximation and by

$$\Psi(\omega) = \frac{2\alpha\sigma^2}{\pi} \frac{\omega^2 + \alpha^2 + \beta^2}{(\omega^2 - \alpha^2 - \beta^2)^2 + 4\alpha^2\omega^2} \tag{2.68}$$

for the second order approximation, where σ is the white noise variance and α and β are the frequency cut-off constants. The PSD are plotted for an ISO grade B road in Figure 2.19. Minor differences can be seen between the models for a low β, while a high value of β produces more noticeable differences. The difference between the ISO profile and the model approximations in the linear section is because the σ was calculated using the approximation in equation (2.79) instead of the more exact value in (2.80).

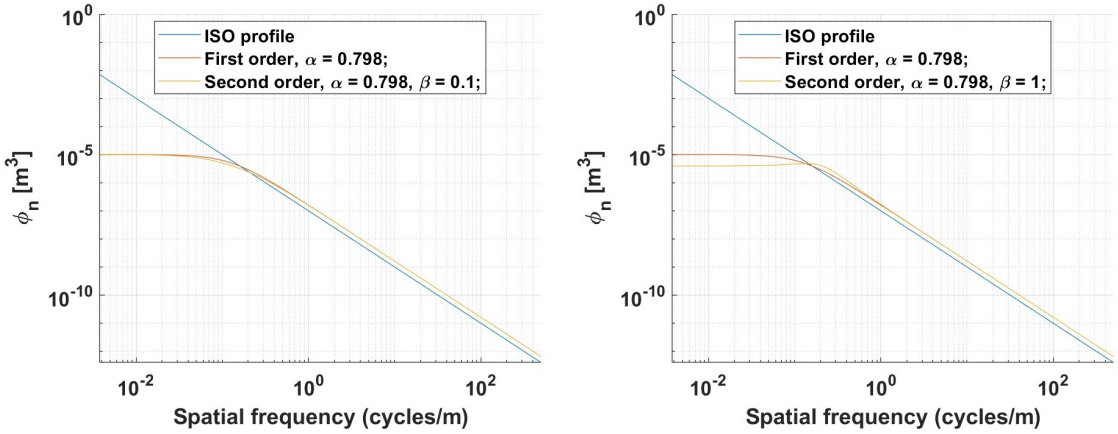

Figure 2.19. Comparison of the PSD generated with the linear, 1st and 2nd order approximations for a variance of 0.004, α of 0.798 and β of a) 0.1 and b) 1.

The low frequency cut-off constant is described by α, and it determines the lowest spatial frequency whose PSD value increases as the ω decreases. It is given as 0.127 rads/m in the literature (Tyan *et al.*, 2009), and depends solely on road conditions and not the road class. The term β is less described, and its effect is to add periodic oscillations to Ψ. This can be observed in their spatial correlation functions

$$C(\xi) = \sigma^2 e^{-\alpha|\xi|} \tag{2.69}$$

for the 1st order model and

$$C(\xi) = \sigma^2 e^{-\alpha|\xi|} cos(\beta\xi) \tag{2.70}$$

for the 2nd order model, where ξ is the distance (Schiehlen, 2006a). This can be observed in Figure 2.20, where the value of β has been purposefully exaggerated for easier visualization.

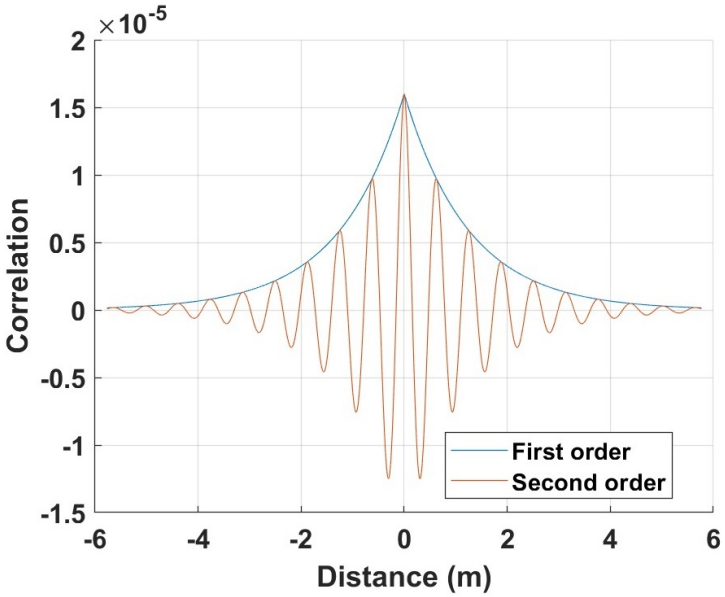

Figure 2.20. Spatial correlation functions for the 1st and 2nd order models. α = 0.798, β = 10, σ = 0.004.

There are many ways a PSD can be obtained. Typically, oscillation data is collected from a road of interest with a special purpose vehicle, which is then used to generate the PSD of that specific road (Dharankar *et al.*, 2016; ISO, 2016). This PSD is already a valid source for profile information, with some works taking this approach (Koch, 2011). However, there are also generic PSD in the literature representative of certain road conditions.

An example is the set of standards put forth by ISO (2016), which determines a series of road PSD profiles for varying road conditions ranging from A (smoothest) to H (roughest). This profile is commonly used in works due to its normative value (Nagarkar and Vikhe, 2016; Abdelkareem *et al.*, 2018; Ergin and Yatak, 2023). It has the following relationship for its road classes (ISO, 2016):

$$\phi_0(N) = 4^N 10^{-6} \tag{2.71}$$

where N is the road class. The lower the value of N, the better the road class, with a grade 'A' road having N equal to 0, a 'B' grade road having N equal to 1, etc. This standard has a reference frequency of 1 rad/m. Another example is available in Ahmed (2001), in which both realistic profiles and their approximations are available, and another in Sevin and Pilkey (1971). These profiles are exemplified in Figure 2.21.

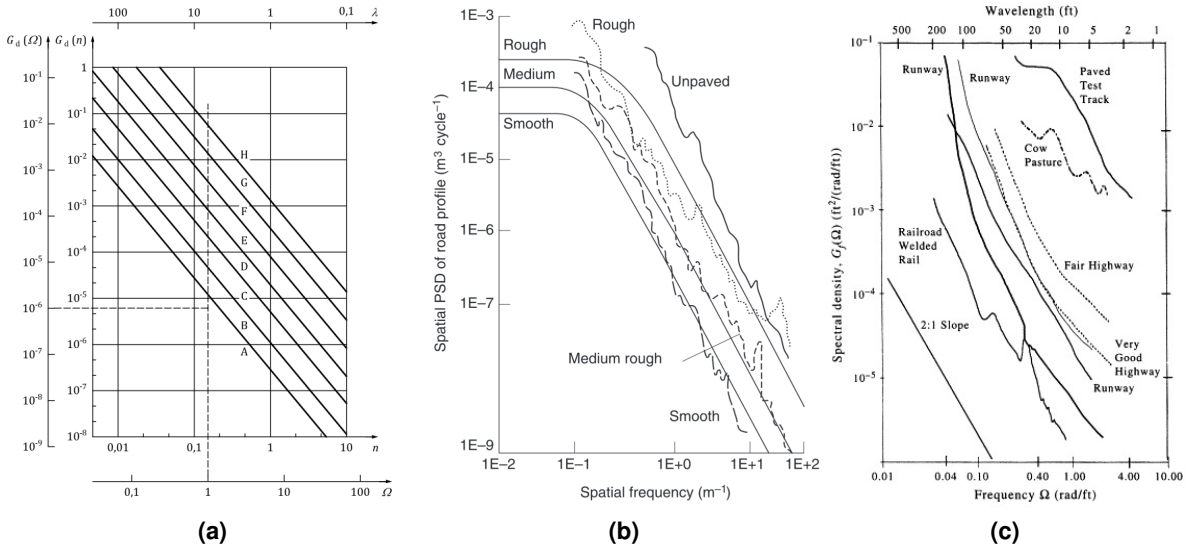

Figure 2.21. Examples of road profile's PSD in the literature. a) Source: (ISO, 2016). b) Source: (Ahmed, 2001). c) Source: (Sevin and Pilkey, 1971)

The lines on a PSD diagram can be given names based on their inclination (ANSI, 2011), which correspond to the waviness number in equation (2.66). This is called colored noise. From the diagrams in Figure 2.21, it is possible to see they all have negative curvature, decreasing in power as frequency increases. This contrasts with white noise, which has 0 inclination and constant power over all frequency bands. While white noise might seem like a poor representation of a road profile, its can be used as an excitation in vehicle simulations because it simplifies the process of obtaining the frequency gain of a system (Schiehlen, 2006b). While the gain in non-linear systems is not just a function of frequency, but also of the excitation magnitude (Gillespie, 2021), this method is still used and encouraged in the literature (Savaresi

et al., 2010; Koch *et al.*, 2010). White noise can be used directly as the excitation, but is more commonly used as the profile velocity curve in processes such as equation (2.67) or (2.68). It is use is extremely common (Prabakar *et al.*, 2009; Kilicaslan, 2022; Nguyen, 2023; Pang *et al.*, 2018; Fleps-Dezasse and Brembeck, 2016).

Special attention must be given to what convention is being followed in the reported data, as different publications might use different standards of what exactly constitutes the PSD function (Davis and Thompson, 2001). In this work, the convention of a single sided PSD is assumed unless otherwise stated. It is related to the double-sided PSD Ψ_2 as

$$\Psi(\omega) = \begin{cases} 2\Psi_2(\omega) & \omega >= 0 \\ 0 & \omega < \quad 0 \end{cases} \tag{2.72}$$

2.3.2.2 Profile generation techniques

A road profile compliant with a PSD can be generated through different procedures. The superposition of sines method and the filtration method will be discussed.

For the superposition of sines method, one must first approximate the PSD by dividing it into discrete frequency bands. Then, sine curves are generated for each of those bands, having constant frequencies and a random phase component. These sines are then weighted according to the magnitude of their frequency in the PSD and summed. The exact method for choosing the frequencies, band sizes and weighting function has been the subject of debate, as it can influence the number of sine functions needed for the simulated PSD to convergence to the target PSD (Shinozuka, 1972). Shinozuka (1972) gives the functions

$$z(x) = \sum_{i=0}^{N} \delta_i sin(\Omega_i x + \phi_i) \tag{2.73}$$

$$\delta_i = \sqrt{2S(\Omega_i)\delta\Omega} \tag{2.74}$$

where N is the number of frequency bands, Ω_i is the frequency of the i-th band, ϕ_i is the random phase of the i-th band, δ_i is the weight function, $S(\Omega_i)$ is the value of the PSD for Ω_i and $\Delta\Omega_i$ is the i-th frequency band amplitude. In this method, Ω_i is the band's upper frequency value, and the interval with 0 frequency value is omitted to avoid changes in the mean value.

For the filtration method, a filter is applied to the PSD signal. Dharankar *et al.* (2016) shows two implementations, a first order filter with and without a low-frequencies. Adopting the model constant g as 1, which removes it from the equations, the expression for generating their road profiles are

$$\dot{z}(t) = \alpha v z(t) + \eta(T) \tag{2.75}$$

for the 1st order model and

$$\begin{bmatrix} \dot{z}_1(t) \\ \dot{z}_2(t) \end{bmatrix} = \begin{bmatrix} 0 & 1 \\ -v^2(\alpha^2 + \beta^2) & -2\alpha v \end{bmatrix} \begin{bmatrix} z_1(t) \\ z_2(t) \end{bmatrix} + \begin{bmatrix} 0 \\ 1 \end{bmatrix} \eta(t) \tag{2.76}$$

for the 2nd order model (Schiehlen, 2006a), where $\eta(T)$ is a GWN variable. For equation (2.76), the value of z(t) is obtained through the expression

$$z(t) = z_1(t)v\sqrt{(\alpha^2 + \beta^2)} + z_2(t). \tag{2.77}$$

The variance value does not appear directly in the equation, but is important for calculating the properties of the $\eta(t)$ variable. According to Dharankar *et al.* (2016), the one-sided PSD value in cycles/m of the white noise variable subject to the filtration is given as

$$\phi = \frac{\phi_0 v}{2\pi} \tag{2.78}$$

while σ can be expressed by the relationship

$$\sigma = \sqrt{\frac{\phi(\omega_0)}{2\pi}\left(\frac{1}{\omega_0} - \frac{1}{\omega_{max}}\right)} \tag{2.79}$$

where ω_0 is the lowest frequency evaluated, dependent on the observation window, and ω_{max} is the highest frequency evaluated, dependent on the domain discretization. According to Tyan *et al.* (2009), however, this value is approximated in most of the literature as

$$\sigma = \sqrt{4\phi_0}. \tag{2.80}$$

Given some quantities may be defined in terms of the total power and others in terms of the variance, the relationship between the power and the variance is sometimes useful. It is defined as

$$P(x) = \sigma(x) = \int_{-\infty}^{+\infty} |x(a)|^2 da \tag{2.81}$$

where σ is the variance of the variable x, equal to its power P.

2.4 VEHICULAR VERTICAL DYNAMICS METRIC

The two most widely recognized metrics for vertical vehicular dynamics are the Road-hold and the RMS of one of the upper body's measures, often shortened to simply RMS (Gillespie, 2021). This is because they are simple metrics for measurement of a vehicle's safety and comfort parameters, being both easy to measure and possible to do so on simple models such as the 1/4 vehicle.

2.4.1 Frequency representation, RMS, and Gain

Three important concepts to mathematically define are the frequency representation of a variable, the RMS and gain.

2.4.1.1 Frequency representation

Recalling equation (2.33), a time dependent variable variable x_i can be represented in the frequency domain by its Fourier transform $H(x_i, \omega)$. This is usually computed with the fast Fourier transform algorithm in digital systems. It is also obtained if directly solving in the frequency domain as in equations (2.42) and (2.43).

For systems that are discrete in time, it is important to pay attention to the requisites of the Nyquist frequency for aliasing and frequency resolution requirements (Proakis and Manolakis, 2014). The Nyquist frequency states that, in order to evaluate the transform of a variable x_i at frequency ω, it is necessary to have a sampling frequency of at least 2ω, otherwise aliasing occurs. The frequency resolution requirement is that, for a resolution of $\delta\omega$ to be achievable in the transform, the variable must be observed for a period T of at least $\frac{1}{2\delta\omega}$. This is also valid when performing an windowing process for frequency estimation, where the observation period T is now the window length. If this is not observed and a greater resolution is attempted, power leakage as in Figure 2.22 occurs.

2.4.1.2 RMS

The RMS of a metric refers to the procedure of calculating the root mean square average of the Absolute (Abs) of said variable, which is done in the frequency domain as (ISO, 1997)

$$RMS(H(x_i)) = \sqrt{\int_0^\infty |H(x_i, \omega)|^2 d\omega} \tag{2.82}$$

for the frequency representation and in time domain as (Žáček *et al.*, 2022)

$$RMS(x_i) = \lim_{T\to\infty} \sqrt{\frac{1}{T}\int_0^T |x_i(t)|^2} \tag{2.83}$$

where T is the analysis time. The RMS is also known as the H_2 measure (Gawronski, 2004), being the mean distance in a Euclidian sense. ISO (1997) also defines an Alternative formula with frequency weighting coefficients, which won't be covered here. The RMS can be applied to whichever variable one would like.

2.4.1.3 Gain

The variable denominated gain, also known as the system's transfer function, is the ratio between a variable and its disturbance. It is defined as

$$G(x_i, \omega) = \frac{H(x_i, \omega)}{H(z_i, \omega)} \tag{2.84}$$

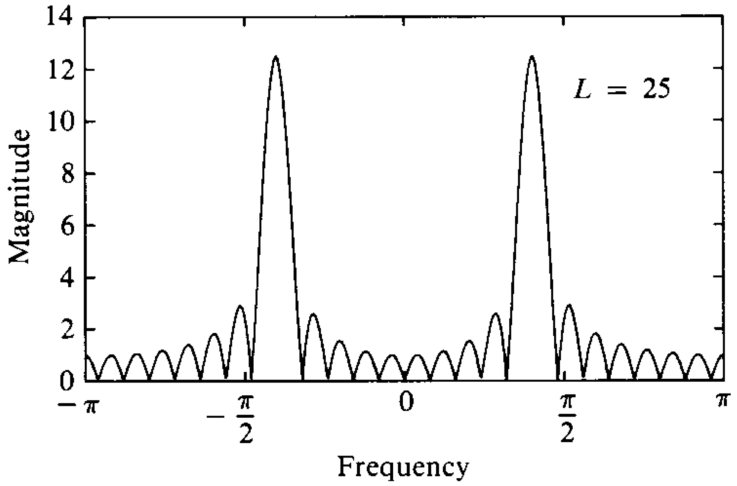

Figure 2.22. Power leakage phenomena due to improper frequency resolution for observation time. Adapted from Proakis and Manolakis (2014).

for the frequency domain and

$$G(x_i) = \frac{x_i(t)}{z_(t)} \tag{2.85}$$

for the time domain, where n is the degree of the derivative, z_i(t) is the excitation and $H(z_i)$ is its representation in the frequency domain. The excitation is the system excitation, not the excitation directly applied to the measured variable, but they must be of the same degree of time derivation - an acceleration variable must be compared to the acceleration of the excitation.

2.4.2 Upper body RMS and comfort

The RMS of an upper body variable, usually the vertical acceleration, is often used to measure comfort. For the upper body acceleration $\ddot{x}_s$, this results in

$$H_2(G(\ddot{x}_s)) = \sqrt{\int_0^\infty \left| \frac{H(\ddot{x}_s, \omega)}{H(\ddot{z}, \omega)} \right|^2 d\omega} \tag{2.86}$$

for the frequency domain and

$$H_2(G(\ddot{x}_s), T) = \lim_{T \to \infty} \sqrt{\frac{1}{T} \int_0^T \left| \frac{\ddot{x}_s(t)}{\ddot{z}(t)} \right|^2} \tag{2.87}$$

for the time domain. This metric is the chief metric used in this work for evaluating comfort.

This is not the only variable that is relevant for comfort, with metrics such as the UPBD RMS also being mentioned as sources of discomfort in cases were there's a difference between seat and steering wheel, for example (Gillespie, 2021). Many works also evaluate the peak displacement or the displacement in time (Prabakar *et al.*, 2009; Otkur *et al.*, 2022). Due to this usage, the UPBD RMS metric is also chosen for use in this work as the comfort metrics, being

defined as

$$H_2(G(x_s)) = \sqrt{\int_0^\infty \left| \frac{H(x_s, \omega)}{H(z, \omega)} \right|^2 d\omega} \tag{2.88}$$

for the frequency domain and

$$H_2(G(x_s)) = \lim_{T \to \infty} \sqrt{\frac{1}{T} \int_0^T \left| \frac{x_s(t)}{z(t)} \right|^2} \tag{2.89}$$

in the time domain. One thing of note is that, for linear systems excited by a white noise process, the relationship in the frequency domain can be simplified to

$$H_2(G(\ddot{x}_s)) = \sqrt{\frac{1}{P} \int_0^\infty |H(\ddot{x}_s, \omega)|^2 \, d\omega} \tag{2.90}$$

where P is the total power in the white noise process that served as input.

2.4.3 Road-holding and safety

The Road-holding property is a measure of the relative displacement of the wheel in relative to and in proportion with the excitation magnitude (Gomes *et al.*, 2023; Gillespie, 2021). This makes it a measurement of safety, as a relative proportional displacement grater than 0 means that, normalized by the excitation, the tire has risen up more than the road itself, implying a loss of contact. A loss of contact, or even a reduced force, can cause loss of performance and command authority over the vehicle longitudinal and latitudinal behavior, increasing the chances of an accident. The Road-hold is given in the frequency domain as

$$rh(x_u) = max\left(\frac{H(x_u, \omega) - H(z, \omega)}{H(z, \omega)} \right) = max(G(x_u, \omega) - 1) \tag{2.91}$$

and in the time domain as

$$rh(G_u) = max(\frac{x_u - z}{z}) \tag{2.92}$$

where the maximum of H is also known as the H_∞ metric of that quantity, being the distance in a Chebyshev norm sense.

2.4.4 Metric dependence on vehicle model

Some metrics are not not obtainable on the 1/4 vehicle model, instead requiring the 1/2 vehicle model. Other metrics become ambiguous once there is more than one lower mass. Finally, the precision of the calculated metrics is dependent on the model accuracy, with higher order models trading complexity for precision. However, it is accepted that 1/4 vehicle results are generally a good indicator of the vehicle's real oscillation (Gillespie, 2021).

On a half-vehicle model, the RMS of the pitch angle x_θ is also relevant, being calculated as

$$H_2(G(\ddot{x}_\theta)) = \sqrt{\int_0^\infty \left| \frac{H(\ddot{x}_\theta, \omega)}{H(\ddot{z}, \omega)} \right|^2 d\omega} \tag{2.93}$$

for the frequency domain and

$$H_2(G(\ddot{x}_\theta), T) = \lim_{T \to \infty} \sqrt{\frac{1}{T} \int_0^T \left| \frac{\ddot{x}_\theta(t)}{\ddot{z}(t)} \right|^2} \tag{2.94}$$

for the time domain. This is used in some works to further measure comfort (Otkur *et al.*, 2022; Khan *et al.*, 2020; Pang *et al.*, 2018).

The Road-holding of a vehicle is split into two metrics for the half-vehicle model. To deal with the new data the multiple tires bring, there are many approaches: to report the mean of the front and rear tire's H_∞ (Abdelkareem *et al.*, 2018; Khan *et al.*, 2020), to report the highest H_∞ between the front and rear tire, to report the sum of the rear and front tire's H_∞ (Prabakar *et al.*, 2009), and to report both rear and front tire's H_∞ separately. The mean is more commonly used. The same logic can be applied when calculating any individual metric for multiple bodies.

2.5 CONTROL STRATEGIES

An overview of control techniques for vehicular suspensions usually yields a few techniques of note. They are the LQR, Skyhook/Groundhook, Proportional-derivative-integral (PID), Model Predictive, Sliding modes, Linear Parameter Varying, Neural Networks and Fuzzy controllers (Mazzilli *et al.*, 2021; Valdivieso-Soto *et al.*, 2023; Theunissen *et al.*, 2021). More complex controllers like Neural Networks and Sliding Modes are noted for being more robust, adaptable and offer better performance on non-linear problems, while simpler controllers like the Skyhook are easier to implement.

A through analysis is carried out in Section 2.7. Based on the available information, it was decided to tackle the Hook and Optimal family of controllers. The Hybridhook was chosen due to being the more general out of the simple Hook controllers. The LQR and SDRE were chosen from the Optimal family. The LQR was also chosen due to being the simpler out of the available controllers, while the SDRE was chosen for being a more complex controller able to deal with non-linearities. It was picked over the MPC technique because a gap in the literature for its usage was noticed.

2.5.1 Optimal control

The Optimal control family contains the set of controllers derived from the Optimal control theory, namely the Linear-quadratic regulator (LQR) and State-Dependent Ricatti Equation (SDRE) techniques.

The basic control of an algorithm in the family is based on solving for the control action

which minimizes a quadratic cost function given the current system state and the chosen cost matrices. The LQR algorithm is the simplest one, but has poor performance if the system linear properties deviate too much from the value for which it was calculated. The ”quadratic” comes from the quadratic terms in the cost function, and the ”linear” comes from the linear state equation. The SDRE system is more complex and computationally expensive, but allows for non-linear state-dependent behavior to be accounted for.

The general problem for an Optimal control problem is to, given a system state variable x, a control action u and a quadratic cost function J, find the control matrix **L** which minimizes J in the time frame t_0 to t_1 (Khamis *et al.*, 2014).

$$J(x,u,t) = \frac{1}{2}x(t_1)^T O(t_1)x(t_1) + \frac{1}{2}\int_{t_0}^{t_1} x(t)^T Q(t)x(t) + u(t)^T R(t)u(t)\ dt \tag{2.95}$$

$$u(t) = -L(t)x(t) \tag{2.96}$$

where **Q**(t) is a positive-definite symmetric cost matrix for the square of the state vector, **R**(t) is a positive-definite symmetric cost matrix for the square of the control action vector and **o** is a cost matrix for the final condition of the square of x. The solution proposed by Pontryagm along diverse works (Fuller, 1963) was to employ the instantaneous version of the Lagrange multiplier method, also known as the control theory Hamiltonian (not to be confused with the general concept of a Hamiltonian), which was proven as a necessary condition for the optimality of the solution. Given a cost function J and a set of constraints S, the Hamiltonian H_a is

$$H_a(x,u,t) = J(x,u,t) + S(x,u,t)^T\lambda(t) \tag{2.97}$$

where $\lambda(t)$ is the instantaneous Lagrange multiplier, also known as the co-state variable. For a system with arbitrary variations with time, the set of constraints S is given by

$$S(x,u,t) = A(t)x(t) + B(t)u(t), \tag{2.98}$$

where **A**(t) is the state matrix and **B**(t) is the control matrix at time t. For the vehicle system, the terms **A** and **B** are the same as the ones in equation (2.26). The optimal control is the one that satisfies the condition

$$\frac{\partial H_a(x,u,t)}{\partial u} = 0, \tag{2.99}$$

as this condition indicate a minima of the system's Hamiltonian with respect to the control action. Assuming no constraints with regards to the system's linearity or time dependence, the expression obtained for L is

$$L = R(t)^{-1}B(t)^T P(t), \tag{2.100}$$

where $\boldsymbol{P}$ is the matrix that solves the problem's associated Riccati differential equation:

$$\begin{aligned} -\dot{P}(t) - x(t)^t\nabla A(t)^T P(t) - \frac{\partial(u(x(t))^T B(t)^T)}{\partial x}P(t) - \frac{\partial(u(x(t))^T R(t)^T u(x(t)))}{\partial x}P(t) \\ -\frac{\partial(x(t)^T Q(t)^T x(t))}{\partial x}P(t) = P(t)A(x) + A(x)^T P(t) + L(t)^T R(t)L(t) + Q \end{aligned} \tag{2.101}$$

with the terminal condition

$$P(t_1) = O(t_1). \tag{2.102}$$

The full derivation of how to obtain equation (2.101) from equation (2.99) is demonstrated in Appendix B.

However, because not all systems are non-linear, nor are their variations arbitrary in time, simpler solutions can be obtained for those systems. Two less general optimal control formulations are of interest: the LQR and the SDRE formulations with infinite time horizons.

2.5.1.1 Finite and infinite horizon

As time progresses, the system reaches steady-state. Two phenomena happen under this condition: $\boldsymbol{x}$(t) goes to 0, also bringing the gradient terms to 0, and the term $\dot{\boldsymbol{P}}$ goes to 0 due to $\boldsymbol{P}$ becoming constant. This is denominated the infinite horizon solution of the Optimal controller, and is the origin of the steady-state optimal problem solution, given by the now algebraic Riccati equation

$$A(t)^T P + PA(t) - PB(t)R^{-1}B(t)^T P + Q = 0 \tag{2.103}$$

Another consequence is term $\boldsymbol{O}$, which refers to the terminal condition, becomes insignificant and is dropped out of the equation. This results in the infinite horizon cost function (Gawronski, 2004)

$$J = \int_0^\infty x(t)^T Q(t)x(t) + u(t)^t R(t)u(t)\ dt. \tag{2.104}$$

In this formulation, the values of $\boldsymbol{P}$ and $\boldsymbol{L}$ can be solved once at before the plant is deployed and their values are constant for the rest of the plant's lifespan. This means the control is very cheap to calculate, and could even be executed by passive elements depending on the real plant. However, this is also the technique's weak point - if the values of $\boldsymbol{A}$ and $\boldsymbol{B}$ change over time, such as when representing a non-linear system with matrices, the solution for $\boldsymbol{L}$ and $\boldsymbol{P}$ obtained at the start might no longer be valid. This causes the system to behave in unintended and unpredictable ways.

A simplified associated problem in which the gradient terms are not taken into account is often used even for the non steady-state solution, called the sub-optimal solution. This results in a Riccati ordinary differential equation associated to the problem given as:

$$A(t)^T P(t) + P(t)A(t) - P(t)B(t)R^T B(t)^T P(t) + Q = -\dot{P}(t) \tag{2.105}$$

which has the boundary condition $\boldsymbol{P}(t_1) = O(t_1)$ and $\boldsymbol{A}$ is the system's state matrix described in equation (2.26).

2.5.1.2 LQR formulation

The LQR formulation is the simplification obtained when all matrices are considered as constant in time. As such, equations (2.95), (2.96), (2.97) and 2.98 respectively become

$$J = \frac{1}{2}x(t_1)^T O x(t_1) + \frac{1}{2}\int_{t_0}^{t_1} x(t)^T Q x(t) + u(x(t))^T R u(t)\ dt \tag{2.106}$$

$$u(x(t)) = -Lx(t) \tag{2.107}$$

$$S(x, u, t) = Ax(t) + Bu(t). \tag{2.108}$$

This parametrization is adequate when the system is linear or doesn't stray too far from the linearization point, which is why they are often used near equilibrium points in non-linear systems. This is results in the most common Optimal control problem, known as the LQR:

$$A^T P + PA - PBR^{-1}B^T P + Q = 0. \tag{2.109}$$

An important detail is that equation (2.109) can have more than one matrix $\boldsymbol{P}$ which solves it. The desired solution, and the one which makes $\boldsymbol{P}$ unique, is the positive definite $\boldsymbol{P}$ (Kučera, 2011). This is also known as the stabilizing solution.

Another relevant detail is that, in order for $\boldsymbol{J}$ to have a minimum value which is finite, $\boldsymbol{Q}$ must be positive semidefinite while $\boldsymbol{R}$ must be positive definite.

There are different ways of solving for $\boldsymbol{P}$. The Invariant Subspace method with Schur's factorization is discussed in Appendix B.

2.5.1.3 SDRE formulation

The SDRE formulation has the system in which the all time-dependent matrices are parameterized as functions of x instead, thus becoming dependent on the state instead of time. As such, equations (2.95), (2.96), (2.97) and (2.98) become, respectively,

$$J = \frac{1}{2}x(t_1)^T O(x(t_1))x(t_1) + \frac{1}{2}\int_{t_0}^{t_1} x(t)^T Q(x(t))x(t) + u(x(t))^T R(x(t))u(t)\ dt \tag{2.110}$$

$$u(x(t)) = -L(x(t))x(t) \tag{2.111}$$

$$S(x, u, t) = A(x(t))x(t) + B(x(t))u(t). \tag{2.112}$$

Due to this parametrization, this method is far more suited to control non-linear systems than the standard LQR formulation (Çimen, 2010). The formulation for the system at **x** = **x**(t) and **O**(**x**(t_1)) = 0 becomes:

$$\begin{aligned} &-(\dot{P}(x) + x^t \nabla A(x)^T P(x) + \frac{\partial(u(x)^T B(x)^T)}{\partial(x)} P(x)) = \\ &P(x)A(x) + A(x)^T P(x) + L(x)^T B(x)^T P(x) + Q(x). \end{aligned} \tag{2.113}$$

This equation can be further simplified by assuming an infinite horizon, which leads to

$$J = \frac{1}{2}\int_0^\infty x(t)^T Q(x(t))x(t) + u(t)^T R(x(t))u(t)\ dt \tag{2.114}$$

and

$$P(x)A(x) + A(x)^T P(x) + L(x)^T B(x)^T P(x) + Q(x) = 0. \tag{2.115}$$

A key aspect of the SDRE method is the parametrization of the variables. The variables **A**(**x**) and **B**(**x**) are split into a linear and non-linear portion, as

$$A(x)x = (A_c + v(x)) \begin{bmatrix} x_s \\ x_u \\ \dot{x}_s \\ \dot{x}_u \end{bmatrix} \tag{2.116}$$

where A_c is the constant part of **A**(**x**) and **v**(**x**) is a non-linear matrix term which makes the equality valid. As per (Çimen, 2010), the parametrization must define the matrix **A**(**x**), but it doesn't need to be unique. In fact, there are infinite valid parametrizations for most cases. An example of such parametrization for the case of the **A** matrix in the space-state system described in equation (2.32) can be created by taking the linear damping term c and substituting it by the non-linear damping force derivative $f(x)$. In the following case, the matrix has been split into a constant parcel with the linear spring and system evolution terms and an **x** dependent parcel containing the non-linear damping:

$$A(x)\ x = \left(\begin{bmatrix} 0 & 0 & 1 & 0 \\ 0 & 0 & 0 & 1 \\ -\frac{K_s}{m_s} & \frac{K_s}{m_s} & 0 & 0 \\ \frac{K_s}{m_u} & -\frac{K_s+K_u}{m_u} & 0 & 0 \end{bmatrix} + \begin{bmatrix} 0 & 0 & 0 & 0 \\ 0 & 0 & 0 & 0 \\ 0 & 0 & -\frac{f(\dot{x})}{m_s} & \frac{f(\dot{x})}{m_s} \\ 0 & 0 & \frac{f(\dot{x})}{m_u} & -\frac{f(\dot{x})}{m_u} \end{bmatrix} \right) \begin{bmatrix} x_s \\ x_u \\ \dot{x}_s \\ \dot{x}_u \end{bmatrix}. \tag{2.117}$$

The matrices Q and R are design choices, and their value greatly affects the resulting solution. It is a choice with no general analytical solution, often done through trial and error (Gawronski, 2004). Optimization procedures are also commonly employed (Ferreira and Morais, 2023).

2.5.2 Hook based controllers

Hook based controllers are a set of control algorithms which determine the desired system response using an idealized, "hooked" version of the real system as a behavior target. The "hooking" refers to the coupling of a body in the idealized system to a displacement reference surface by means of a damper element.

The first description of such systems was by Karnopp et al (Karnopp *et al.*, 1974). In it, the Skyhook system was postulated. The motivation for its inception was to be a control scheme which would have an acceptable performance on a semi-active device when compared to an active suspension implementation. This was shown to be the case through computational models.

Further hook controllers were later proposed, with the most notorious ones being the Groundhook and Hybridhook controllers. The concept of the Groundhook system was proposed in M. Valášek and M. Novák (1996), with the same authors further postulating the concept of the hybrid hook controller in Novák and Valášek (1996) under the name of ”Combined Groundhook and Skyhook”.

For quarter vehicle models, if only the upper mass vibration is controlled, the scheme is called ”Skyhook”, and if only the lower mass vibration is controlled the scheme is called ”Groundhook”. If both are hooked the system is called ”Hybridhook”, and the result is a linear combination of both the Skyhook and Groundhook controllers. For more complex vehicle systems or systems in general, the term ”Groundhook” may be used for bodies in contact with the ground, like wheels or tracks, and ”Skyhook” for all other bodies. There's no formal convention on the terminology, however.

One of the strengths of the hook model is that, as put by Ahmadian (2017), it eliminates the usual trade-off between high-frequency isolation and resonance peak that passive vehicle dampers have. This is because, as explained by Karnopp *et al.* (1974), passive dampers force depend on the relative velocity while the hook damper acts on the body's absolute velocity. The relative velocity is greater at higher frequencies, which leads to an increase in suspension stiffness proportional to the damping coefficient. This is not present in systems with the Skyhook controller, as shown in Figure 2.23.

Valášek *et al.* (1997) mentions that one of the main weaknesses found in the Groundhook and Hybridhook applications was that, despite good performance under harmonic loads, it had issues with bump excitations. The article proposes a solution which takes into account the tire deformation when calculating the equivalent force.

2.5.2.1 Physical motivation and mathematical modelling

The mathematical modeling of the hook controller is based on calculating the force application needed so the target body has the same acceleration as its idealized system counterpart.

First, a choice is made regarding which body will be ”hooked”. For example, on a quarter vehicle, this can be either the wheel or the chassis. Such arrangement is displayed in Figure 2.24.

Then, the forces that such body would feel were there a damper connecting it to a inertial referential are calculated. By equating the free body diagram of both bodies the real and idealized systems are linked, providing the information of what force the actuator should exert. Thus, the expression in (2.118) is obtained. In equation (2.118), the actuator is between the

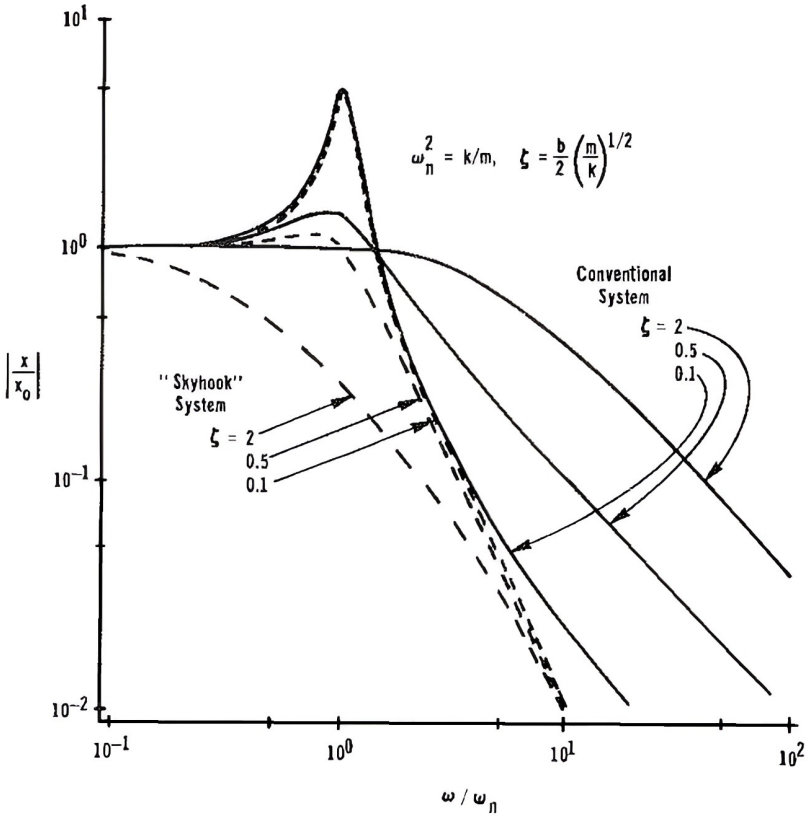

Figure 2.23. Comparison between the gains of conventional and Skyhook systems as a function of frequency and damping coefficient. Adapted from Karnopp *et al.* (1974).

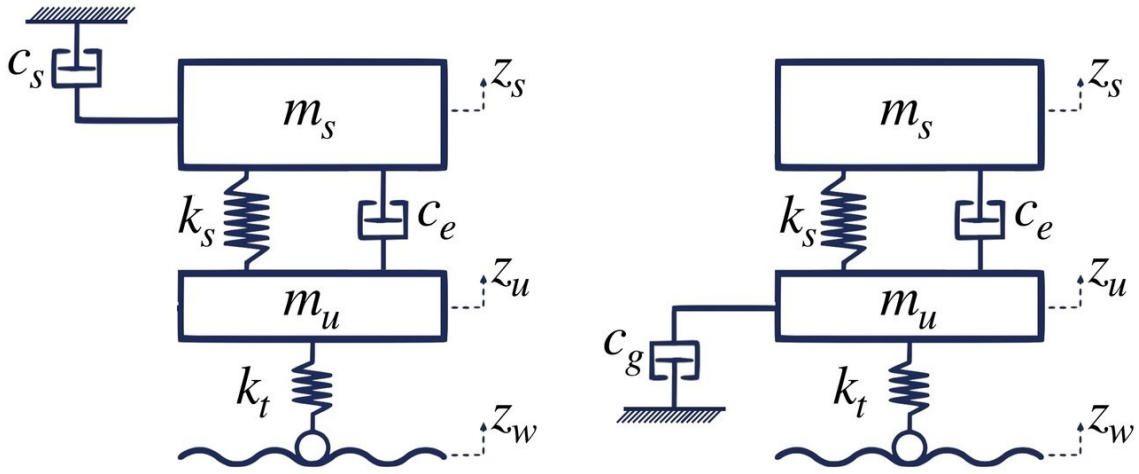

(a) Skyhook **(b)** Groundhook

Figure 2.24. Idealized Skyhook and Groundhook systems for quarter vehicle models. Adapted from Aljarbouh and Fayaz (2020).

bodies with displacement x_1 and x_2. $C_{controllable}$ is the controllable damper damping coefficient, and C_{ideal} is the idealized system damper's damping coefficient. $\dot{x}_{reference}$ is the speed of the reference surface which the hook is attached to.

$$F = C_{controllable}\ (\dot{x}_1 - \dot{x}_2) = C_{ideal}\ (\dot{x}_1 - \dot{x}_{reference}). \tag{2.118}$$

Such process increases the stability of the target body, usually at the cost of decreasing the stability of the connected body. This is because those forces are obtained with no regard towards the stability of the connected body.

For many works, the formula for the force is given instead of the coefficient. Expression (2.118) can be rearranged to obtain a way of expressing any description of damper force as a description of the desired controllable damper damping coefficient, as per equation (2.119).

$$C_{controllable} = \frac{F}{(\dot{x}_1 - \dot{x}_2)} = C_{ideal} \left(\frac{\dot{x}_1 - \dot{x}_{reference}}{\dot{x}_1 - \dot{x}_2} \right). \tag{2.119}$$

This formulation has some advantages. First, in many works, there are activation conditions regarding the value of $\dot{x}_1 - \dot{x}_2$. This form makes it clearer why such conditions are necessary, as in general controllable dampers are not able to have negative damping constants. Second, it explicitly returns the value the controllable damper must be at, which is useful for dampers explicitly defined through their constant. However, in cases which the damper characteristics are described by a force-speed diagram, the force can be easily obtained by removing the $(\dot{x}_1 - \dot{x}_2)$ term.

In this section, all works in which a force expression is given, an equivalent expression for the controllable damping coefficient is instead provided. It is done so under the premise that the real damper is in a quarter vehicle between the upper and lower mass. The controllable damping constant is referred to as either simply "C" or "$C_{skyhook}$/$C_{groundhook}$where the distinction is necessary, while the ideal damping constant of the system is referred to as either "C_{sky}" or "C_{ground}".

2.5.2.2 Alternative implementations

The original formulation given by Karnopp *et al.* (1974) for the Skyhook damping is in equation (2.120).

$$C = C_{sky} \left(\frac{\dot{x}_s}{\dot{x}_s - \dot{x}_u} \right) \tag{2.120}$$

For the Groundhook formulation, different forms may be taken. M. Valášek and M. Novák (1996) originally proposes a formulation that takes into account the ground velocity, being a more proper "Groundhook" and leading to equation (2.122). Žáček *et al.* (2022) explains that such form is often impractical, as measuring the relatives wheel and ground velocities is complicated. Soliman and Kaldas (2021) demonstrates a form dependent only on wheel velocity, as per equation (2.121).

$$C = C_{ground} \left(\frac{\dot{x}_u}{\dot{x}_u - \dot{x}_s} \right) \tag{2.121}$$

$$C = C_{ground} \left(\frac{\dot{x}_u - \dot{z}}{\dot{x}_u - \dot{x}_s} \right) \tag{2.122}$$

Valášek *et al.* (1997) further proposes a modification to the Groundhook formulation that takes into account tire and suspension deformation to improve performance in bump excitations. This

formulation is laid out in equation (2.123).

$$C = \frac{C_{ground}\left(\dot{x}_u - \dot{z}\right) + K_u\left(x_u - z\right) - K_s\left(x_u - x_s\right)}{\dot{x}_u - \dot{x}_s} \tag{2.123}$$

Žáček *et al.* (2022) uses a formulation based on the unsprung mass acceleration instead of the relative wheel velocity, as per equation (2.124).

$$C = C_{ground}\left(\frac{\ddot{x}_u}{\dot{x}_u - \dot{x}_s}\right) \tag{2.124}$$

The Hybridhook formulation is

$$C = C_{hybrid}(\alpha\, C_{skyhook} + (1-\alpha)\, C_{groundhook}), \tag{2.125}$$

where $C_{skyhook}$ is the value of C calculated by applying the Skyhook formula in (2.120) with $C_{sky} = 1$, $C_{groundhook}$ is the value of C obtained from using one of the many Groundhook formulations, such as equations (2.121), (2.122) or (2.123) with $C_{ground} = 1$, α is an arbitrary constant chosen by the designer which determines the weight between the Skyhook and Groundhook approaches, and C_{hybrid} is the damping constant for the Hybridhook formulation.

The calculated equivalent damping can then be applied to an actuator. This application can be done in many ways. The first method is the on-off switch. This technique uses the hook damping coefficient if a certain condition is met, and the damper inactive state coefficient otherwise. According to (Soliman and Kaldas, 2021) is the most common method of implementing the control technique. The second method is the continuous variation technique. In it, as long as the calculated force value is feasible for the damper to exert, such value is assumed. This is also known as the clipped approach (Hrovat *et al.*, 1983).

2.6 OPTIMIZATION

When designing a car suspension, many combinations of properties can yield physically attainable solutions. However, some solutions produce dynamical behaviors that are more desirable than others. This is, thus, an optimization problem: find the best solution withing a space of possible parameters.

With the intent of not only finding a singular solution, but finding the best solution amongst all possible choices that satisfy the given conditions, optimization algorithms are employed. When picking an optimization algorithm, many characteristics are considered such as its computational load, convergence speed, how often it converges to global optimums as opposed to local optimums, implementation difficulty, capacity for multi-objective optimization and whether it has a deterministic or stochastic behavior.

2.6.1 Genetic algorithm

While many techniques are used, the genetic algorithm is an extremely popular optimization technique for vehicular suspension, both for optimizing the control (Fleps-Dezasse and Brembeck, 2016; Nagarkar and Vikhe, 2016; Han *et al.*, 2024; Do *et al.*, 2011; Mitra *et al.*, 2016) and the parametric identification of suspension models (Xue *et al.*, 2010; Abebaw *et al.*, 2020; Yu *et al.*, 2017; Kwok *et al.*, 2007; Ferreira *et al.*, 2023). This popularity is due to algorithm capacity to optimize problems that:

- Have many variables
- Have complex non-linearities
- Have many optimization objectives
- Don't have an explicit gradient defined for its objective(s) function(s)

The genetic algorithm is a biologically inspired algorithm that finds an optimal solution or set of solutions by employing evolutionary concepts to its heuristic search. In it, a group of initial solutions is initially generated called a ""population". Each variable is represented as a "pair" inside a "chromosome"", which represents a complete set of variables. The carrier of the chromosome is the "individual". The performance of each individual in the population is evaluated, and the better performing solutions generate "offspring" and "survive". To "survive" is to be retained for the next "generations", while to "reproduced" is to have part of its bases in its chromosome combined with another individual's to generate a new individual for the next "generation". A "generation" is a round of population evaluations.

To make avoid having only the initial population values for bases represented, as well as to avoid local minima, some surviving individuals produce a "mutated" copy instead of an offspring, which is an individual with a copy of its chromosomes but with some values randomly altered. The general process of a genetic algorithm is described in Figure 2.25. Katoch *et al.* (2021) states that the choice of parameters such as population size, mutation and survival rates are one of the main challenges of a genetic algorithm implementation, as a suboptimal choice can slow down convergence or lead the solution to false global optimums.

2.6.1.1 NSGA-II

Deb *et al.* (2002) posits of one the most famous genetic algorithms in the field, the NSGA-II algorithm. It is very famous for its capacity to handle complex multi-objective problems in an efficient manner, due to its implementation of the survival criteria of elitism, where the best individuals that survive are selected from successive Pareto fronts which are dominated only by the already accounted for fronts.

The NSGA-II works, at its core, like any other genetic algorithm. It takes a population, acts on it based on reproductive fitness principles, and returns a new population. Its advantage lies in how it selects the new population's parents.

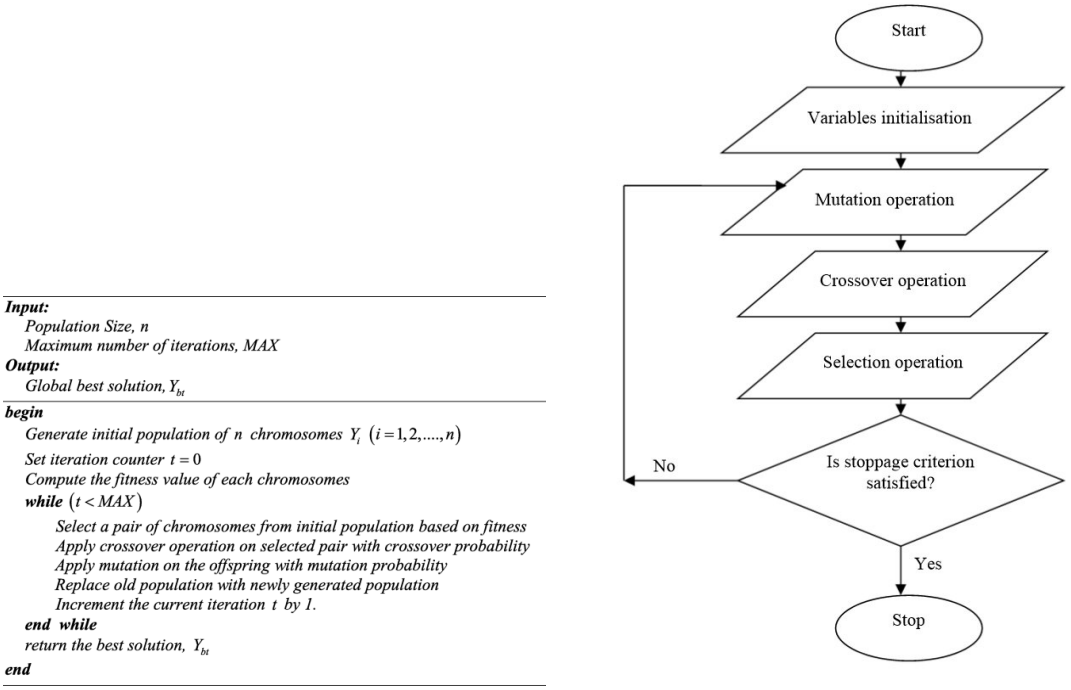

(a) Pseudo-code **(b)** Flowchart

Figure 2.25. Algorithms for generic genetic algorithms. Reproduced from (a) Katoch *et al.* (2021) and (b) Ighravwe and Oke (2015).

The algorithm starts by taking in the initial population and evaluating its fitness. Each individual in the population is ranked based on their dominance. Dominance is when all the fitness metrics of an individual are better than another. A set of individuals which don't dominate each other is called a front, with the front that dominates all the others being called the Pareto front. Another metric, Crowding Distance, is also calculated. It measures how relatively dense in solutions a region in the Pareto front is, so later on individuals which provide a more unique solution can be prioritized.

The individuals are then selected for reproduction through a random selection that favors high ranking individuals. The original NSGA-II paper (Deb *et al.*, 2002) uses a Tournament selection, in which a small number of individuals are randomly picked from the population and are pitted against each other. The winner is the most dominant individual in the tournament, with individuals of equal dominance being selected based on the one with the highest crowding distance (i.e., the most unique). This is done until enough winners are picked to fill the reproductive pool.

A new set of individuals is created from the population in the reproductive pool. There are two mechanisms for generating new individual: crossover and mutation. Crossover, or recombination as its called in the original article, takes two individuals as parents and creates two offspring. The offspring chromosomes are created by taking their parents' chromosomes and combining their bases with each other according to a Crossover operator. For real variables in (Deb *et al.*, 2002), the Crossover operator used was the Simulated Binary Crossover, which simulates a single-point binary Crossover event for real coded variables (Deb *et al.*, 1995). In

this case, the Crossover Distribution Index determines how similar the offspring will be to their parents, with higher values leading to less changes. Mutation produces offspring from a single individual, also through a Mutation operator whose effect is controlled by a Mutation Distribution index. In Deb *et al.* (2002), a polynomial mutation operator was used (Deb and Deb, 2014).

Once enough offspring are generated, this intermediary population has its fitness evaluated. Then, the original and offspring population are combined, and the population is ranked again for dominance and crowding distance. The next generation is composed of the highest ranking individuals dominance-wise up to the population size. If including an additional front would cause the next generation population to exceed this limit, the individuals of the last front are sorted based on crowding distance and included up to the population size.

By sorting its population based on dominance, the algorithm emphasizes convergence, while by using the crowding distance as an internal ranking inside the fronts, the algorithm incentives solution diversity. This combination makes the NSGA-II a very powerful optimization tool. Its does have some shortcomings, as the algorithm suffers from premature convergence and lack of diversity for problems with too many objective variables (Katoch *et al.*, 2021).

2.7 State of the art

There are many parts in a suspension system that affect its behavior, which is further complicated with the addition of a controllable suspension. In recent years, the effect of many different characteristics on controllable suspension have been the subject of study, including the configuration of its elements (He *et al.*, 2024), its controllers robustness (Metzler *et al.*, 2021; Huang *et al.*, 2021), its energetic efficiency (L. Pires and McMahon, 2013; Abdelkareem *et al.*, 2018), the effect of components non-linearities (Laiq Khan and Khan, 2016; Jiang and Cheng, 2023; Kilicaslan, 2022; Min and Wei, 2024), the effect of modeling passengers (Nagarkar *et al.*, 2018), semi-active device choice (Li *et al.*, 2021) and control law choice and design (Valdivieso-Soto *et al.*, 2023; Sename, 2021; Jurisch, 2022). It should be noted that most modern research doesn't focus on just one of the mentioned aspects, but on the interplay between two or more.

It is of note that a significant amount of studies on controllable suspensions are performed on active suspensions. While of less interest for this work, because certain techniques and methods can be generalized to semi-active systems, information pertaining to active systems will be brought up when relevant.

2.7.1 Suspension modeling

For the suspension system, different systems, as well as suspension arrangements and geometries, are tested. Semi-active dampers are realized very frequently with MR dampers (Chen *et al.*, 2023; Min and Wei, 2024; Boreiry *et al.*, 2019; Jamadar *et al.*, 2021; Žáček *et al.*, 2022), but not exclusively. ER dampers (Huang *et al.*, 2021; Morato *et al.*, 2019) and solenoid valves dampers (van der Sande *et al.*, 2022; Qing *et al.*, 2023; Jiang *et al.*, 2024) are also used.

MR dampers are a field of study in and of themselves, with Abdul Aziz *et al.* (2022) reviews the many models of MR dampers existing, as well as the fields these models are most commonly applied. In the specific field of vehicular applications, there are different aspects which are delved deeply. Parametric modeling techniques like the Bouc wen, Bingham and Sigmoid still see use (Rossi *et al.*, 2018; Silva *et al.*, 2022; Sharma and Sharma, 2018; Zhu *et al.*, 2019), but modern approaches have begun to model dynamical uncertainties more and more with black box models such as with Neural Networks (Chen *et al.*, 2023; Xiong *et al.*, 2024; Pang *et al.*, 2018). Many research items in the literature are concerned with improving the MR damper design to improve certain characteristics, with the most relevant for this dissertation being the control response time (Yoon *et al.*, 2019, 2021; Žáček *et al.*, 2022). Boreiry *et al.* (2019) analyses the properties of a vehicular MR damper system and concluded the inclusion of the MR damper makes the system chaotic, demonstrating that the non-linear behavior of the damper can create unforeseen consequences when applied to vehicles.

While semi-active dampers' ride height control is considered subpar by the literature (Gillespie, 2021), as demonstrated in Table 2.1, ZhiHong *et al.* (2025) recently demonstrated that the MR damper asymmetry can actually be used to play in its favor for ride height control, albeit in a velocity dependent manner due to the device passivity conditions.

Some authors sought to obtain further performance improvements by combining semi-active dampers and inerters together (Chen *et al.*, 2014; Tan *et al.*, 2025; Li *et al.*, 2021). A negative stiffness device has also been proposed to be used with a MR damper (Hu *et al.*, 2025). Combining different semi-active devices can expand the

Work performed on active systems seek out the optimal arrangement of the controllable elements with regards to other passive elements (He *et al.*, 2023, 2024) show that while the classical parallel component distribution can powerful, exploring different configurations can prove beneficial for even further performance gains.

A side note is that while not directly applicable in road vehicle applications, much research exists on the vibration control of other types of land vehicles with MR damper SAS (e.g. Miao *et al.* (2024)). Some of the concepts in these areas can be useful for improving the performance of road vehicles such as cars, motorcycles and trucks.

2.7.2 Vehicle modeling

There are many different ways to evaluate a vehicle dynamical behavior. The dynamical models, which model the vehicle as a set of masses, springs and dampers, is a very common technique. The 1/4 vehicle model is still widely used in modern research, as exemplified many times so far (Min and Wei, 2024; Swethamarai and Lakshmi, 2022; Hu *et al.*, 2025). The half vehicle model, which besides vertical dynamics can either model roll/longitudinal (Khan *et al.*, 2020; Otkur *et al.*, 2022) or pitch/lateral dynamics (Xiao *et al.*, 2022; Hassan *et al.*, 2023), is the next up in complexity. Finally, the full vehicle model (Ricco *et al.*, 2024; Kim *et al.*, 2023) is able to fully represent all major vehicle dynamics vibrations. Minor vibration modes, such as from the vehicle structure, might still be absent.

To determine the relative popularity of the vehicle models for controllable suspensions in vehicular applications, a quantitative research was performed on the websites 'ScienceDirect' and 'Taylor & Francis'. The relative figures were based on the number of articles found for the keywords '((X) AND (vehicle) AND (suspension) AND (semi active)) NOT (underwater OR aircraft OR rail)', where X was '(1/4 OR quarter)' for the quarter vehicle model, '(half OR (1/2 NOT 1/4))' for the 1/2 vehicle model and '(full OR 7dof)' for the full vehicle model. Review articles were excluded, and only articles categorized as 'Research articles' in 'Engineering'/'Engineering & Technology' were considered. The figures were summed. The results are available in Figure 2.26.

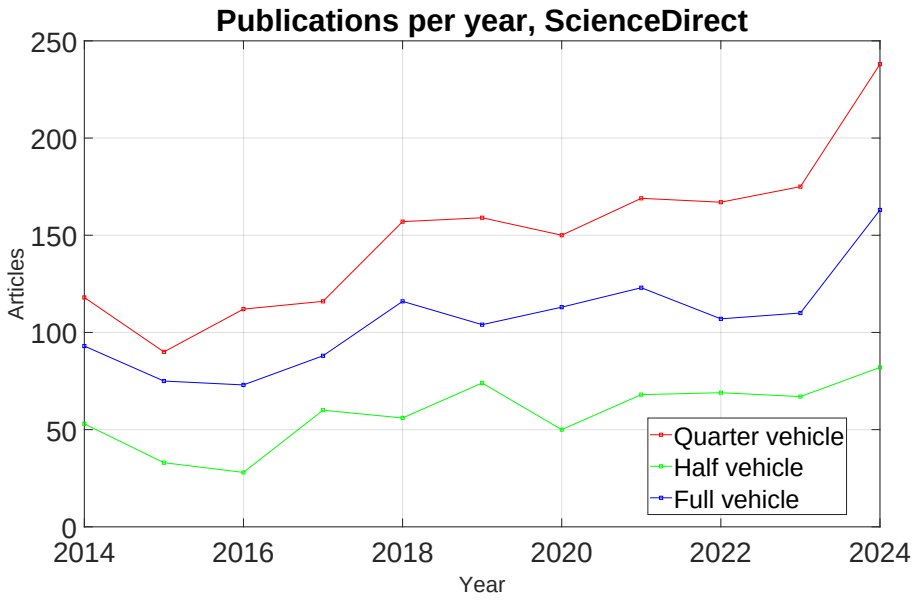

Figure 2.26. Publications per year for each vehicle model, sum total for websites 'ScienceDirect' and 'Taylor & Francis'.

Likely owing to its simplicity, the 1/4 vehicle model is the most commonly used. Full vehicle models, both active and semi-active, are also used in moderation. While being simpler than the full vehicle model, the 1/2 vehicle model is last. A possible explanation is because, while the full vehicle model is the most complex choice, researchers willing to use models more complex than the quarter vehicle might have fewer incentives to compromise fidelity over complexity. Overall, these "simpler" dynamical models are still very popular, as they can be augmented to better model certain phenomena without adding unnecessary complexity to the rest of the model.

These are not the only possible dynamical models. More complex models take into account details of the real vehicle which are not captured in these simplifications. The work by (Swethamarai and Lakshmi, 2022) has a single degree of freedom dynamical model of the passenger included in its 1/4 vehicle formulation, while Nagarkar *et al.* (2018) includes not only a dynamical passenger model with many degrees of freedom, but a full vehicle model as well. Nagarkar and Vikhe (2016) studies the active control of a Macpherson suspension, which has non-linear terms. Multibody dynamical models are also used in some advanced research, because they can take into account emergent non-linear interactions between many components (Wu *et al.*, 2024; He *et al.*, 2022; Pan *et al.*, 2021). Other advantages include its

capacity to take into the vibrational mode of components like the chassis (Lu *et al.*, 2023), which can improve comfort characteristics beyond what simpler models.

2.7.3 Controllers

As already stated in Section 2.5, many different controllers are employed in vehicular suspension. However, the control need not be performed by a single technique. A common trend in the last few years consists of combining different control schemes to provide better characteristics, such as performance or robustness (Swethamarai and Lakshmi, 2022; Taghavifar, 2021; Nguyen and Nguyen, 2023). This approach grants more freedom to the designer to use different controllers to deal with specific challenges that they are specially suited for, resulting in a well rounded controller.

The PID family is the most popular industrial controller (Ogata, 2010) and has been applied for vehicular suspension control purposes in a myriad of ways (Nagarkar *et al.*, 2018; Laiq Khan and Khan, 2016; Ergin and Yatak, 2023; Rao, 2014). By itself, the traditional form is not well suited for non-linear systems, which motivates the use of non-linear forms such as the fractional PID or in combination with other controllers. For instance, the Fuzzy controller is chosen (Yin *et al.*, 2023; Kasemi *et al.*, 2012; Mahmoodabadi and Nejadkourki, 2022) due to its capacity to deal with non-linearities by enabling an adaptable behavior while being fairly simple to design and combine with other systems. The fractional PID, on the other hand, uses fractional calculus principles to add fractional integral and derivative terms, adding degrees of freedom to the controller and increasing its suitability to deal with non-linear phenomena. It has also seen frequent use for non-linear control applications Yin *et al.* (2024); Gao and Li (2023). Given that both the Fuzzy and fractional PID approaches are proposed as means of compensating the traditional PID weakness in dealing with non-linear systems, the question of which is better naturally arises. Li *et al.* (2024) compares the non-linear performance gains between the fractional PID and the Fuzzy PID approach, with the fractional PID coming out on top, but not with a large margin. Swethamarai and Lakshmi (2022) combines both techniques and compares it to a simple PID and fractional PID. The results show that adding the Fuzzy controller to the fractional PID system further reduces vibrations to a similar degree that employing the fractional PID does over the PID approach, or that the PID does over the passive vehicle. As such, while the Fractional technique has a slight edge over the Fuzzy application on its own, it can still be further improved by being complemented by the Fuzzy system. While common, its combined use is not limited to PID controllers (Liu *et al.*, 2008; Chen *et al.*, 2017).

The Optimal control family of controllers is the runner up in industrial use (Ogata, 2010), and naturally has seen use in vehicular suspension control. While the traditional linear form is still used for non-linear problems (Nagarkar *et al.*, 2018; Akgül and Unluturk, 2023), there are approaches which seeks to make it more suitable for these systems. They follow the same pattern as the PID system: Combining it with different controllers to provide an adaptable behavior (Gao and Li, 2023) or use techniques better suited for non-linearities, such as the SDRE technique (Kilicaslan, 2022) or the MPC technique (Metzler *et al.*, 2021; Jurisch, 2022).

Hook controllers, such as the Groundhook or Skyhook controller, have been traditionally employed for suspension control. While considered not as effective as modern controllers, their simplicity and acceptable performance has motivated many works to either employ them (Žáček *et al.*, 2022; van der Sande *et al.*, 2022) or compare their results to them (Ricco *et al.*, 2024). Modern iterations include adaptive versions (Lu *et al.*, 2023) and more effective forms of the traditional schemes as well, such as fractional calculus based Skyhook schemes (Zolotas and Goodall, 2018).

Owing to their versatility, Neural networks see use both by themselves (Ghoniem *et al.*, 2020; Xiong *et al.*, 2024) and in combination, often with the PID due to the latter's mentioned popularity (Jiang and Cheng, 2023; Pedro *et al.*, 2014; Taghavifar, 2021). While they can offer great performance and adaptability, its design parameters are black-boxes (Kimball *et al.*, 2024), making them harder to interpret compared to Fuzzy systems. Another popular choice is that of Sliding Modes (Pusadkar *et al.*, 2019; Nguyen, 2023; Liu *et al.*, 2008), which present a more traditional Lyapunov based approach, but is harder to design. Lastly, the Linear Parameter Varying technique has also been used extensively (Do *et al.*, 2011; Morato *et al.*, 2019), and it provides good behavior with a simpler design, at the cost of needing a linearization for each region contemplated (Sename, 2021).

A synthesis of the control techniques has been made available in Table 2.4.

Table 2.4. Synthesis for the relevant controllers in semi-active suspension. Data is subjective based on material found, and is might not represent all the possible technique variations. Sample bibliography is non-extensive.

Controller family	Controller name	Implementation difficulty	Performance for linear system	Performance for non-linear system
Fuzzy[a]	Standard	Fair	Good	Average
Hook[b]	Groundhook	Easy	Average	Poor
	Skyhook	Easy	Average	Poor
	Hybrid	Easy	Average	Poor
	Hook+PID	Fair	Great	Average
LPV[c]	Standard	Fair	Good	Average
Neural[d]	Standard	Challenging	Excellent	Great
Optimal[e]	LQR	Fair	Great	Poor
	MPC	Challenging	Great	Good
	SDRE	Challenging	Great	Good
PID[f]	Standard	Easy	Average	Poor
	Fuzzy	Fair	Great	Good
	Fractional	Challenging	Great	Good
Sliding modes[g]	Standard	Challenging	Great	Good

[a] Qing *et al.* (2023).
[b] Žáček *et al.* (2022); Hong *et al.* (2000); Lu *et al.* (2023); Novák and Valášek (1996).
[c] Morato *et al.* (2019); Sename (2021).
[d] Ghoniem *et al.* (2020); Kimball *et al.* (2024).
[e] Akgül and Unluturk (2023); Metzler *et al.* (2021); Kilicaslan (2022).
[f] Nagarkar *et al.* (2018); Kasemi *et al.* (2012); Li *et al.* (2024).
[g] Isacchi and Ripamonti (2024).

For a brief summary of control applied on vehicular MR dampers specifically, Wang *et al.* (2024) performs a review of the ways the MR suspensions are applied in vehicular suspensions, showcasing how the MR damper is dealt with from the point of view of control.

2.7.4 Impressions

The possible complexity of each of these topics creates the need for a compromise between positive and negative aspects of more detailed models. On one hand, greater behavior fidelity and a more through exploration of possible configurations can provide more confidence in the optimality of the obtained solution. On the other hand, more complex models can be harder to model, be very computationally expensive and having too many different techniques interplaying can confound the effect of individual choices. Some authors in the literature have also expressed similar views (Kimball *et al.*, 2024). Lastly, as put by Yu *et al.* (2023), there's a gap between the academic output on active suspensions and its adoption by the industry, caused by practical limitations such as size, mass, power requirements, cost and reliability. While some of these issues are mitigated by a SAS, solutions combining too many advanced techniques may be unfeasible due to exceeding practical requirements, even if the techniques individually don't. This can be hard to predict and burdensome to check.

In order to implement any advanced combination of different systems, proper time must be allocated to through validation of the components by themselves and together.

3 METHODOLOGY

In this chapter, the procedures to be performed in order to achieve the objectives outlined in Chapter 1 and the tools needed to perform them are outlined, with the reasoning behind the choices made explained in depth. The details of the computational implementation of such procedures are left for Chapter 4.

A full description of the work methodology, including the research steps, can be observed in Figure 3.1.

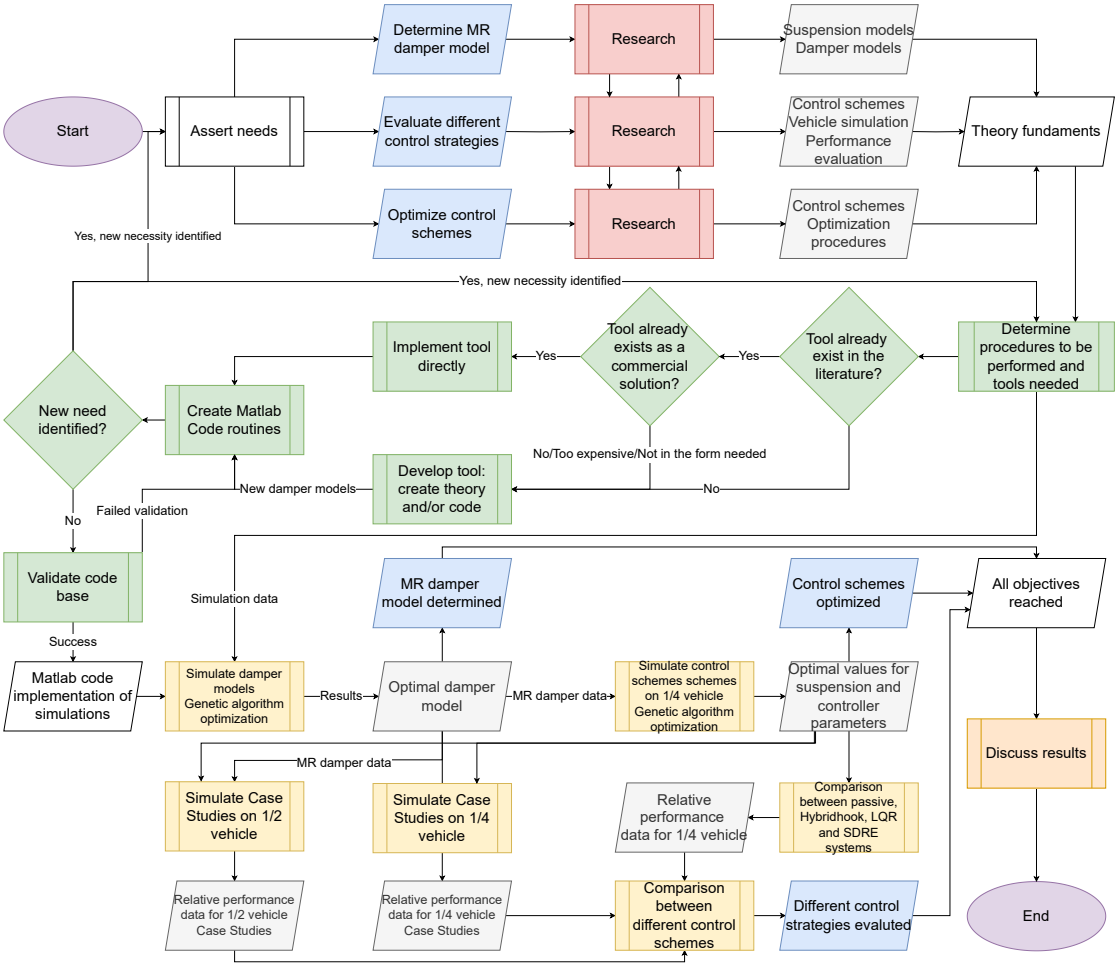

Figure 3.1. Full methodology employed in the development of the present work.

An analysis will be performed to compare the effectiveness of different control schemes at performing vibration attenuation tasks on vehicles. It was decided to perform a computation

analysis carried out through simulations, as the time and monetary constraints made an experimental analysis impossible.

The chapter is divided into sections. Section 3.1 concerns the choices made for representing the vehicle in the simulations, as well as the solution techniques utilized. Section 3.2 concerns the choices made for studying the diverse MR damper models used in the simulations. Section 3.3 discusses the road models used and the choices made for their representation. Section 3.4 discusses the metrics chosen for evaluating the system as well as the techniques employed and their parameters. Section 3.5 discusses the controllers used, their parameter choices and algorithmic implementation. Section 3.6 explains the optimization procedure undertaken and its parameters, specially the NSGA-II. Finally, Section 3.7 details the parameters used in all simulations performed using the techniques previously laid out in the Chapter.

3.1 VEHICLE MODEL

To represent the vehicles, the 1/4 vehicle model and the 1/2 vehicle model were chosen. The 1/2 vehicle model variant chosen was the one composed of the front and back wheels. The vehicle characteristics were chosen for each test case based on what literature works were available for use in validation.

In order to test the behavior of the model, certain free parameters had to be chosen. The collection of constant system parameters for the vehicle models was dubbed a ”vehicle”.

For the 1/4 vehicle model, a single vehicle was proposed for all tests. This was not always the case: Initially, there were two types of vehicle, and both were to be used in the evaluation of the performance of different controller schemes. The first would be aimed at replicating the conditions of a prior similar simulation from (Ferreira, 2022), while the second had rounded up coefficients for easier readability. However, it was deemed that the simulations in (Ferreira, 2022) would be too different from the ones to be performed in the present work, and a single vehicle was settled upon at the end. This vehicle is referred to as Type #1.

For the 1/2 vehicle model, only one combination of vehicle parameters was proposed too. Its parameters were based on the vehicle Type #1 proposed for the 1/4 vehicle model. This choice was made because the 1/2 vehicle model will be used to evaluate the same objectives as the 1/4 vehicle Type #1 under the same conditions. This combination of vehicle parameters was denominated Type #2.

The 1/4 vehicle mathematical model was defined in the manner of equation (2.29), while the 1/2 vehicle mathematical model was defined in the manner of equation (2.49). For both models, all springs and masses were considered as having constant values in time, and all variables were considered to have their exact values know.

3.1.1 Analytical solution

The passive suspension model frequency domain behavior may be obtained analytically. To this end, equations (2.35), (2.42), (2.43) and (2.44) were programmed and solved using the computer software Matlab. However, it was decided that further development of analytical solution methods were not of interest, as the systems they could solve were of limited scope and were also solvable by other methods to a satisfactory degree. The solutions obtained by the analytical methods were redundant with the numerical solutions, and as such were not included in the present work beyond its use as a validation tool.

3.1.2 Numerical solution

The passive suspension model has analytical and numerical solutions. On the other hand, the MR damper suspension model may not always be solved analytically in a practical manner, due to the complexity of the MR damper formulation as well as the complexity of the control scheme. It may, however, be solved numerically. As such, a code suite capable of obtaining the numerical solutions of both passive and semi-active suspensions was developed.

To obtain the time domain response, the system described in equation (2.29) will be numerically integrated with a Runge-Kutta algorithm in the Simulink software ambient. The Runge-Kutta algorithm chosen was the hybrid 4th and 5th order method, available as a built-in function in Matlab under the alias ”ODE45”.

As is the case for the 1/4 vehicle model, the 1/2 passive suspension may also be solved analytically and numerically, while the semi-active variations may not always be. It was decided to solve the 1/2 vehicle mathematical model only in a numerical manner. It was not necessary to develop a code suite from the ground-up for this task. Instead, it was enough to modify the suite developed for the 1/4 vehicle model to extend its capabilities to 1/2 vehicle models.

The procedure for obtaining the 1/2 vehicle model solution is the same as the one for the 1/4 vehicle model. To obtain the time domain response, the system described in equation (2.49) will be numerically integrated with a Runge-Kutta algorithm in the Simulink software ambient. The Runge-Kutta algorithm chosen was the hybrid 4th and 5th order method, available as a built-in function in Matlab under the alias ”ODE45”.

To obtain the frequency response of both systems, a Fourier transform will be applied to the time domain results of the displacement variables. In order to eliminate non-steady state effects, the first few seconds of the simulation were discarded from the Fourier transformation. These procedures are described in more depth in their dedicated section, namely Section 3.4.

3.2 MR DAMPER MODEL

With the purpose of evaluating what model would be used for the MR damper, it was elected to perform a comparison study between different models of relevance in the literature as well

as a new proposed model based on modifications from the literature. The best damper model and its parameters were chosen based on its ability to conform to experimental data. Additional consideration was given to the model's computational performance under simulation.

Three different models from the literature were considered as candidates for the MR damper behavior model to be used, based on their relevance in the literature and perceived strong points. These were the Bingham, Bouc-wen and double Sigmoid models. A fourth model was proposed based on modifications to the double Sigmoid Wang model due to issues regarding convergence as well as precision improvements. It was denominated the Wang-II model, and was also evaluated. Lastly, an alternative modified model, whose purpose was better behavior under transient excitations, was also tested.

A Bingham based model was chosen due to its high usage in the literature as well as its simplicity. The Bingham body model was picked out as a compromise between simplicity and features, as its the simplest Bingham model which contains two out of the four behaviors desired, the non-linear force rise and the non-zero force at zero speed. More complete models based on the Bingham model are available, but they require the solution of complex partial differential equations that make the implementation complex and the numerical solution very costly.

A Bouc-wen based model was chosen due to it being the most used model while possessing moderate complexity. Kwok *et al.* (2007)'s version was picked because it allows for asymmetries in the force-velocity. While a normalized formulation could have been chosen, it was opted not to because the gains in parameter identification celerity did not outweigh the gains in complexity. It possesses the four desired properties, making it a good candidate. It is main drawback is that its formulation is a differential equation, needing integration.

A double Sigmoid model was chosen due to its good performance in the literature while being of moderate complexity. Because the experimental data used in the present works was previously fit to the Wang model (Silva *et al.*, 2022), the Wang model is of special interest. Its behavior matching the four desired qualities for a MR damper, but it doesn't need a differential equation like the Bouc-Wen formulation, using a Sigmoid expression instead. It does, however, have the most parameters out of the three considered models. The same reasoning led to the choice of the Wang-II model, which may show improvements at the cost of more variables. Given the stability issues detected in some situations, modifications for the v_m parameter was also tested.

3.2.1 Simulation under test bench conditions

In order to imitate the conditions encountered in a test bench experiment, an idealized test bench simulation will be employed.

The test bench model refers to the simulation of the models as if they were loaded on an ideal test bench. This means that the excitation variables such as terminal displacement, relative velocity and acceleration are all imposed in an exact manner, with the damper resulting force being an open loop with regards to its excitation condition.

3.2.2 Numerical solution

The solution of the systems will be performed numerically. To this end, the systems were implemented in Matlab's Simulink environment. The respective model coefficients will be loaded into the code routine and the solution will be carried out taking into account the model and dynamical variables.

The systems may be under a test bench condition or a vehicle simulation condition. For test bench conditions, the dynamical load variables will be fed to the system from an external predetermined source. For vehicle simulation conditions, the damper system will be subject to whichever numerical solution schemes the vehicle simulation is. As an example, in the quarter vehicle simulations, the damper model will be numerically integrated by the 4th/5th order Runge-Kutta method ODE45 together with the rest of the system.

3.2.3 Model comparison and optimal coefficient determination

To compare the models put forth and determine the most adequate model, a fit comparison will be performed between them. The fit comparison is a process where the results of an experimental bench test on an MR damper are compared to the results of the numerical damper models under the same excitation conditions.

The comparison will be performed by simulating the damper model with the same loading conditions as the experimental damper according to the data provided, and measuring the difference in predicted and measured force. The model's parameters will be iterated until an optimal combination is obtained. The optimal combination is determined by having the lowest aggregate error in the steady state region.

The details of the optimization procedure are available in Section 3.6.

The data provided contains three parameters for each data point: time, displacement and measured force. To obtain the velocity and acceleration values, a simple backwards finite differences scheme was applied, with the formulas being

$$\dot{v}_i = \frac{v_{i+1} - v_i}{t_{i+1} - t_i} \qquad\qquad \ddot{v}_i = \frac{\dot{v}_{i+1} - \dot{v}_i}{t_{i+1} - t_i} \tag{3.1}$$

where i is the i-th data point sorted in time. The missing values for the last data points were substituted as 0. Because this is occurs beyond the steady-state region used in the evaluation, this makes no difference.

3.3 Road excitation

For representation of the road condition, an ISO grade B compliant profile of adequate power were chosen. In certain validation tests, a sine or linear rise excitation were chosen in order to recreate the conditions of the work in the literature being replicated. Lastly, in certain tests, a bump and linear rise were used for purposes of testing the vehicle under transient road

conditions.

There were four different excitations considered for the purposes of road excitations and test bench excitations:

1. A sinusoidal wave
2. A bump excitation
3. A linear rise excitation
4. A 1st order ISO profile

It was decided, when necessary to generate the profile, to do so in a Matlab or Matlab Simulink environment for all contemplated excitations.

The Sine wave and Linear rise excitations were used when validating the code suite used for solving the 1/4 vehicle model, as their deterministic nature made it simpler for results from the literature using them to be reproduced.

The Sine wave was also used for as the excitation in the test bench simulations. This excitation was obtained in the form of a data series containing the results of the experimentally applied Sine wave for the cases in which simulation data was being compared to the experimental data, while it was generated in Matlab otherwise.

The first order ISO road excitation was used as an input for the vehicles road profile, as they more closely model an actual road over other models. The 2nd order ISO road excitation was considered, but the β coefficient could not be reliably sourced form the literature. The simplicity and effectiveness of the 1st order profile made it be chosen in the end.

The GWN excitation was initially used as a source of random excitation, because it resembled a road profile while having a constant power output on all frequencies. This simplified the analysis of the system's gain curve because the excitation power was evenly spread across the frequency band. However, its use was eventually abandoned in favor of the ISO style road excitation. For non-linear systems, the gain results for excitations with different spectral characteristics are not necessarily the same, so testing on a model which more closely resembled a real road gave results which better approximated reality.

The Bump and Linear rise were both used on vehicle simulations performed on the results of the optimized vehicles, as a source of deterministic excitations that mimic real obstacles found on a regular urban drive.

3.3.1 Sine wave

For the sinusoidal wave, the implementation was performed with the function 'sin' when using the Matlab scripting environment or with the block function "Sine Wave" when using the Simulink environment.

The Equation used for the Sine wave is equation (2.57). The sine wave has 4 parameters: the amplitude, the frequency, the phase and the bias. The values of amplitude and frequency were test dependent. The phase and bias were 0 for all contemplated uses of the sine wave excitation in this work. When necessary, the frequency value was multiplied by a factor of $\frac{1}{2\pi}$ to make it a value of cycles/second instead of radians/second.

For Simulink simulations, the values of amplitude and frequency were set by directly inputting the block value in the Simulink environment.

3.3.2 Linear rise excitation

For the Linear rise excitation, the implementation was performed using the "Step" block function when using the Simulink environment. In the Matlab script environment, the Linear excitation was programmed by using an if-statement that returned the higher or lower value depending on whether the value inputted was before or after the bump position.

The equation used for the Linear rise is equation (3.2). The linear rise excitation magnitude and rise time were set by directly inputting the block value in the Simulink environment. For the Matlab, the value were directly written into the code. The expression is, then,

$$LR(T_1, I, t) = \begin{cases} 0 & t < T_1 \\ I & t \geq T_1 \end{cases} \tag{3.2}$$

where T_1 is the Linear Rise start time and I is the Linear Rise height.

3.3.3 Bump excitation

The Bump excitation was implemented according to equation (3.3). It is a cosine shaped bump function, and is defined in terms of the simulation time:

$$Bump(t, I) = \begin{cases} \frac{I}{2}(1 - cos\left(2\pi\frac{t-T_1}{T_2-T_1})\right) & T_1 \leq t \leq T_2 \\ 0 & Otherwise; \end{cases} \tag{3.3}$$

where I is the height, T_1 is the obstacle first contact time and T_2 is the last contact time. The 'A' class from the the Brazilian Traffic Signaling Manual (CONTRAN, 2022) was chosen to represent the excitation.

3.3.4 First order ISO road

The ISO road was executed as a 1st order model, which is defined by the formulation (2.67) in the frequency domain and Equation (2.75) in the time domain. The time domain equation was implemented in Simulink with a "Band-Limited White Noise" block, an 'integrator' block and a 'gain' block. The diagram is presented in Chapter 4 as Figure 4.7. The model constants are

either taken from the ISO grade or from the literature.

The ISO grade B was adopted. This results in a ϕ_0 of $6.4 \cdot 10^{-6}\ m^3/rad$. The value of α was adopted as 0,127, as recommended in the literature (Tyan *et al.*, 2009).

The random profile still needs a GWN variable for its time profile generation, as defined in equation (2.75). Equation (2.78) determines a factor of $\frac{v}{2\pi}$ for obtaining the GWN power, but an additional factor of $\frac{1}{\pi}$ was necessary for the values to match. This factor comes from the fact that the Simulink block dimension is Hz while its power is for a double sided spectrum. The dimension conversion creates an additional $\frac{1}{2\pi}$ term, while the conversion from double to single sided spectrum creates a scale factor of 2, resulting in a $\frac{1}{\pi}$ factor. The final value used in the spectrum recreation as the power value in the "Band-limited white noise" block was

$$P = \frac{8\phi_0 v}{\pi^2} \tag{3.4}$$

where v is the vehicle travel velocity in m/s, and ϕ_0 is given in m^3/rad. For validation purposes, the simplification for σ on equation (2.80) was adopted when calculating the analytical frequency profile.

3.4 VERTICAL DYNAMIC METRICS

Three metrics were chosen for all vehicle models to evaluate the performance of the control schemes. They were the Road-hold metric for the handling property and the UPBD RMS and Upper body acceleration (UPBA) RMS for comfort. For 1/2 vehicle model, the RMS of the vehicle pitch will also be used, and the Road-hold metric was split into one for each of the tires.

The performance parameters will be evaluated on a vehicle equipped with either a passive suspension, an idealized semi-active suspension or a semi-active suspension with a realistic behaving MR damper simulation.

The metrics were calculated from the frequency response. First, the frequency response for steady state conditions is obtained. If more the systems of equation was solved more than once for different conditions, the frequency response is calculated for each one of them, and the final frequency response is the averaged value from all frequency responses obtained. Then, equation (2.88) will be applied for calculating the RMS of the UPBD and UPBA as well as the angular displacement and acceleration when relevant, and equation (2.91) will be used for calculating the Road-hold of all lower bodies.

An additional metric was used for the time domain simulation results, the contact force. Its formulation is

$$C_F = (x_u - z)k_u. \tag{3.5}$$

The reason this quantity was used is that it measures a very similar quantity to the Roadhold, but has no division by the road displacement z. In the time domain results, the excitations are transient, meaning they often have zero road displacement even when the tire is still oscillating. This would lead to very high Roadhold values which are hard to read and not representative of

performance. As such, measuring the contact force allows the Handling property to be studied more effectively in the time domain for transient obstacles.

3.4.1 Calculation methodology

The metrics were calculated was by a numerical uniform discrete Fourier transform, performed on Matlab with the function "`fft`" on the variable data. The response is only calculated for the time span in which the system was under steady state. The system's simulation has a non-uniform time step, but still collects the results in an uniform time delta so as to standardize the results.

The parameters used are such that frequency response is returned for a fixed frequency interval ranging from 0 to 100 Hz with equally spaced intervals of 1/64 Hz. This is done so as to standardize the frequency response across many different non-uniform transforms, as well as remove very high frequency components that are known from the outset to have negligible response due to their distance from the resonant frequencies.

In some simulation conditions, more than one time response will be calculated for a given system, where all parameters but the GWN random seed are the same. In those cases, the individual gains will be calculated by diving the frequency domain results for the vehicle by the results for the road at each individual frequency. The final response will then be calculated from the average of all standardized frequency responses at each frequency. This frequency response averaging process was demonstrated in (Ferreira *et al.*, 2022) for a GWN type profile and in (Ferreira *et al.*, 2025) for an ISO B 1st order type profile.

The combined frequency domain data is calculated from them by taking the harmonic mean of the individual frequency domain results, for the UPBA RMS and UPBD RMS, and the arithmetic mean, for the Lower body displacement (LWBD) peak gain. The effect of using an arithmetic or geometric mean is demonstrated in Figures 3.2 for the UPBD RMS and 3.3 for the UPBD peak gain. The curves are for various combinations of parameters between 10^2 and 10^4 As it can be seen from the figures, the geometric mean tends to provide a faster convergence towards the true mean in all cases, and is more stable to outliers. However, due to a mistake in the functions set up, the arithmetic mean ended up still being used for the LWBD peak gain.

It should be brought to attention that the curves which present the most errors are the ones with odd combinations of damping and stiffness (10 000 Ns/m with 200 N/m for example), which end up being less relevant as they are very far from the optimal combinations studied in this dissertation.

The combined frequency domain data is also filtered, being subjected to a Savitsky-Sgolay filter with Matlab's '`smoothdata`' function. The parameters used are 6 for '`degree`' and either 0.04 or 0.02 for '`smoothing factor`', with 0.04 being used for the UPBA RMS and UPBD RMS, and 0.02 being used for the UPBD. These parameters were fine tuned so as to improves accuracy without deforming the function shape too much.

For the comfort metrics UPBD and UPBA RMS, the relevant time variable was the UPBD

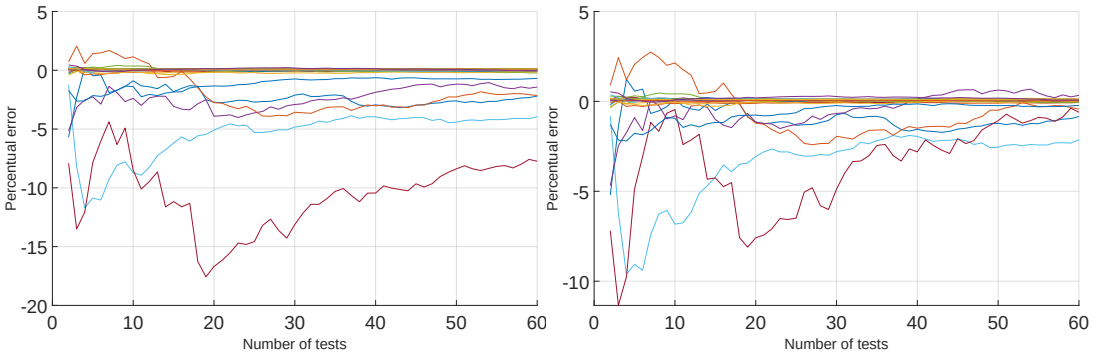

(a) Arithmetic mean **(b)** Geometric mean

Figure 3.2. UPBA RMS error as a function of test cases used, 25 sample curves.

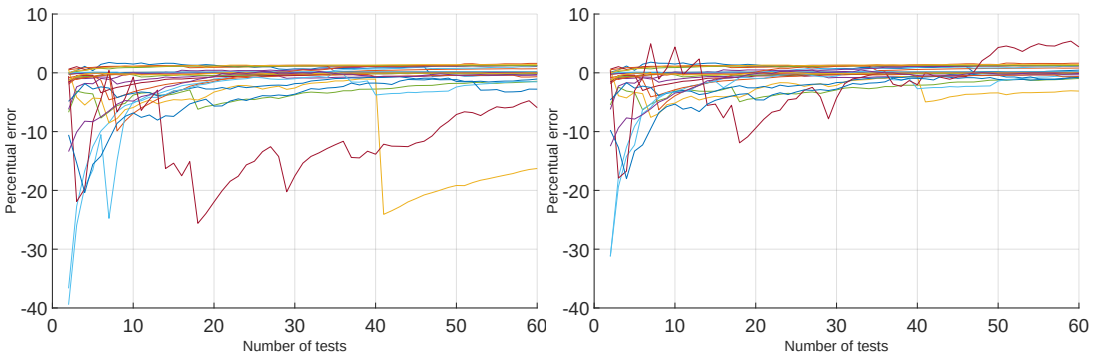

(a) Arithmetic mean **(b)** Geometric mean

Figure 3.3. LWBD peak gain error as a function of test cases used, 25 sample curves.

and UPBA respectively. For the Road-hold metric, the relevant variable was the LWBD. For 1/2 vehicle, in which there is more than one lower body, the frequency was individually calculated for both. The steady-state time domain data will be multiplied by a Blackman window function through Matlab's '`blackman`' function, which improves the accuracy of the results. Figures 3.4 and 3.5 demonstrates the impact this procedure has. Depending on the curve, the filter has more or less impact, but in general it provides an improvement. The impact on high frequencies is extreme (on the order of 1000% and beyond), but due to their low magnitude the bulk of the improvement comes from better performance at lower frequencies.

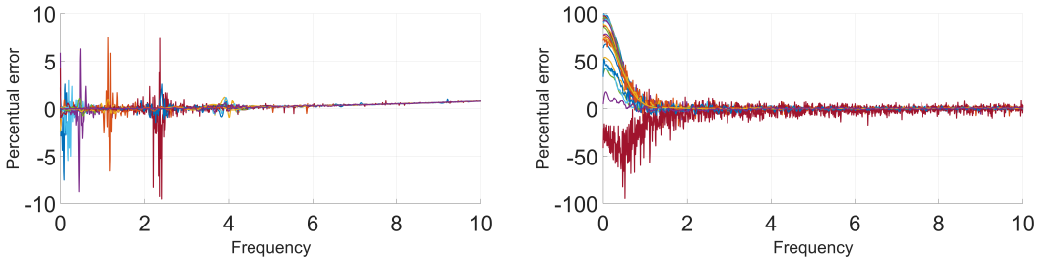

(a) Blackman filter **(b)** No filter

Figure 3.4. UPBA RMS error comparison between using the Blackman filter function and not using it, 25 sample curves.

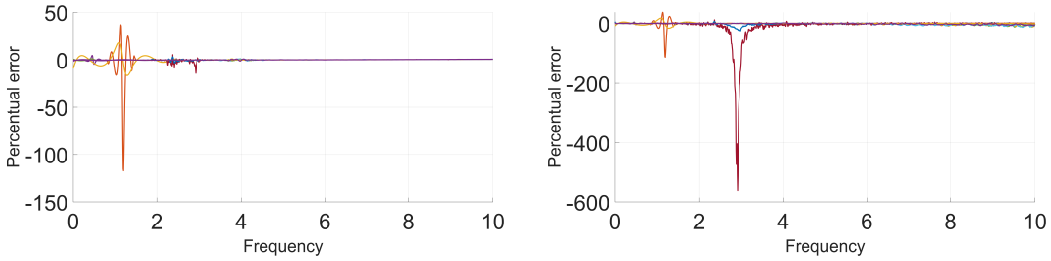

(a) Blackman filter **(b)** No filter

Figure 3.5. LWBD peak gain error comparison between using the Blackman filter function and not using it, 25 sample curves.

The UPBA RMS required acceleration data for both the vehicle and the road. This was obtained by calculating the 2nd derivative of the data with the '`diff`' function from Matlab. It was done in this manner over directly obtaining acceleration data from the simulation because the results were far more accurate this way.

For the RMS metric, the integral is performed numerically through Matlab's built-in function "`trapz`".

For the Road-hold metric, the maximum value of the frequency response is calculated by using the "`max`" function from Matlab, and subtracting 1 from the value.

The data treatment choices were obtained based on trial and error procedures, with the values which resulted in the most accurate results with regards to the analytical validation data being picked.

3.4.2 Aggregate performance analysis

In some cases, the results obtained will take the form of many different solutions, each one Pareto optimal. To analyze these results as a whole, two techniques were employed. First, a line fit of the log was used to characterize the performance of a solution. It takes the form of

$$log_{10}(H_\infty) = a \cdot log_{10}(H_2) + b \tag{3.6}$$

where a and b are the fit coefficients, H_∞ is the Roadholding metric and H_2 is the comfort metric. In this respect, a represents the trade-off between comfort and handling for a certain set of solutions, while b represents the baseline H_∞ performance in which this trade-off occurs. The ratio between the a coefficient of two solutions s_1 and s_2 indicate the relative trade-off T_D, while the ratio between the b coefficient of two solutions indicate the relative baseline performance B_S, as in

$$T_D(s_1, s_2) = \frac{a_{s_2}}{a_{s_1}} \tag{3.7}$$

and

$$B_S(s_1, s_2) = \frac{b_{s_2}}{b_{s_1}}. \tag{3.8}$$

A small B_S indicates the solution in the denominator has better performance on average, while the T_D indicates whether this performance difference increases or decreases as the handling is prioritized. This is done by feeding the log_{10} of the populations' metrics to Matlab's "`fit`" function with the "`poly1`" setting.

The second technique consists of a correlation analysis between the coefficients and the metrics. This indicates how much increasing or decreasing a variable directly impacts the vehicle performance. An absolute coefficient close to 1 indicates a nearly perfect correlation between the variable and the metric, while a coefficient near 0 indicates the variable's effect is not as straightforward. The coefficients are, then, a way to identify whether the impact of certain variables can be easily explained by a linear relationship. To this end, Matlab's "`corr`" function will be used.

Only results with a p confidence value of 1e-4 or lower will be considered as valid relationships. The correlation will be calculated between the log_{10} value of the metrics and the value of the variables, as well as for the log_{10} of the metrics and the log_{10} value of the variables. If no significant correlation is found the log-linear correlation but is for the log-log correlation, its value will be used instead. Otherwise, the log-linear correlation value will be exposed by default.

3.4.3 Half vehicle additional metrics

When considering the 1/2 vehicle model metrics, what constitutes as the gain becomes more complex due to the multiple excitations. This is a MIMO (multiple input, multiple output) system. Two approaches were evaluated: to consider the system gain as based on the front wheel excitation for all measured outputs but those from the rear wheel, or to create an equivalent input for different measures. It was decided that the main way the gains in the 1/2 vehicle model would be represent would be through the traditional front wheel excitation, in order to increase the comparability of the work performed with the literature. The approach of using the equivalent gain was nonetheless employed as an additional analysis. Its results are limited to the appendix, so as to not clutter the Results section.

For the front wheel and the rear wheel dynamics, the input was considered as the front and rear wheel excitations r_f and r_r, respectively. For the upper body, the inputs were divided between the vertical and rotational dynamics. For upper body the vertical dynamics, the equivalent road input r_v was modeled as

$$r_v = \frac{r_f + r_r}{2}. \tag{3.9}$$

This is the mean value between the front and back tire's excitations. This was determined based on the idea that the excitations on the front and rear wheels would have equal contribution to the upper body vertical dynamics. As for the upper body rotational or angular dynamics, the equivalent road input r_ω was modeled as

$$r_\omega = arctan\left(\frac{r_f - r_r}{d_f + d_r}\right) \tag{3.10}$$

where d_f and d_r are the distances of the front and rear wheel to the vehicle's center of gravity respectively. This equivalent input is based on the fact that the angular input to the upper body would be based on the relative displacement between the front and rear wheel and the distance between the wheels. This creates a right triangle of base $d_r + d_f$ and height $r_f - r_r$, whose ratio is the tangent of the angle r_ω.

3.4.4 Control metrics

In order to measure the effectiveness of the control, three different quantities were measured: two for control saturation and one for average current. The force saturation F_{sat} is defined as the percentage of time spent with the control force being clipped to the MR damper limits, and is described as

$$F_{sat} = 100 \sum_{t=0}^{t_f} \left(\frac{Sat(t)}{t_f} \right) \tag{3.11}$$

$$Sat(t) = \begin{cases} 1 & u_a(t) \; ! = u(t) \\ 0 & u_a(t) \quad = u(t) \end{cases} \tag{3.12}$$

where t_f is the total time, u is the MR damper control force and u_a is the controller command force. It is multiplied by 100 to return a percentage value. This quantity represent the percentage of the time the system spends unable to enact the control force desired by its controller. The semi-active saturation F_{sas} is very similar to the F_{sat}, also measuring a percentage of time spent with the control force being clipped to the MR damper limits, but considers only the cases in which it clips to the MR damper 0 current boundary. It is defined as

$$F_{sas} = 100 \sum_{t=0}^{t_f} \left(\frac{Sas(t)}{t_f} \right) \tag{3.13}$$

$$Sas(t) = \begin{cases} 1 & (u_a(t) \; ! = u(t)) || (u(t) = F(I = 0)) \\ 0 & else; \end{cases} \tag{3.14}$$

where F is the MR damper force at current I equals 0. This quantity measures the time in which the system is unable to met the controller desired force because it falls outside the SAS device minimal, 0 current value. Together, these two metrics evaluate how much the controller is being held back by limitations of its SAS suspension.

A final metric to be measured is the average current A_{avg}. It is simply the mean current employed in the evaluated time span of the test. It is obtained through brute force calculations, in which the MR damper force for a discrete set of possible currents is calculated and the nearest value is obtained. To this end, 111 equally spaced points between 0 and 2.5 A and 11 equally spaced points between 2.525 and 20 A were used. This spacing is due to the exponential relationship between force and current, where 99,9% of the MR damper force at 20 A is already reached at 2.5 A. Finer grading at high currents is thus not important. Using this method, it was possible to obtain the correct Force-Current pair value with a maximum of 5% relative Force

error and an average of 0,3%.

According to documentation on the MR dampers used in Santade (2017), the expected terminal voltage at a MR damper is 12 V, while the expected maximum intermittent current is 2 A. While this describes a damper slightly smaller than the ones used in this Thesis, these values are roughly in line with the expected value for the employed damper model. This means that, even if 20 A were actually drawn in a continuous fashion, the maximum power consumption by the SAS system would be 240 W. The real value falls closer to 24 W, given the specifications provided. Since SAS power consumption is not withing the scope of the present work, the total power consumption will not be used as a design parameter.

3.5 SEMI-ACTIVE CONTROL

Two control strategies families were contemplated: The Hook family and the Optimal family. For the Hook class of controllers, the Hybridhook was tested. For the Optimal class, the LQR and SDRE controllers were tested.

To obtain the controllers' parameters, a multi-objective genetic optimization for optimal comfort and safety metrics will be performed.

All controllers were programmed into Matlab's Simulink environment. They will be solved alongside the equation systems in the manner described in Section 3.1. Additionally, the Skyhook and Groundhook controllers which compose the Hybridhook controller were programmed into Matlab scripts for preliminary testing and validation.

All controllers follow a basic pattern: the immediate state variables are fed into the controller, as well as the system constants. The required steps for the controller feedback gain to be obtained are performed. Then, the product of said gain times the state vector is compared to the possible values the embedded actuator may actually assume. If the value desired is within the actuator possible range, it becomes the employed control action at that time-step. If the value is above or bellow, the closest value possible is instead applied.

The allowed values for the actuator are a range between the lowest and greatest force the contemplated semi-active suspension was calculated to be able to perform given the conditions. For an idealized semi-active damper, the range of allowed values is directly determined at the design period. For the realistic MR damper models, these values are obtained by calculating the force at 0 current and at a very high current, guaranteed to have reached a saturation behavior. Due to the discussed monotonic properties of the MR damper model used with regards to the force and current relationship, calculating the damper force at zero and max currents is enough to provide the interval of possible forces.

The saturation current value was adopted as 20 A, but it should be made explicit that this is not a suggestion that a current anywhere near this value should be employed in real life. Instead, a reasonable high value should be determined based on the specific damper characteristics and an individual optimization procedure should be performed given said parameters. The value of 20 A was adopted because it guarantees that any damper contemplated will be guaranteed

to return its saturation value, but the behavior at 5 A and 20 A was observed as practically equal for the contemplated dampers. The value of 20 A simply removes the need for fine tuning to be performed.

3.5.1 Hybridhook formulation

The Hybridhook formulation chosen was the one in equation (2.125). The Groundhook formulation used in the Hybridhook formulation was the one in equation (2.120), while the Skyhook formulation used was the one in equation (2.121). The reasoning used for picking these formulations for the Hybridhook system is the simplicity and ease of implementation in real vehicular systems.The Groundhook formulation selected was chosen because it is both the simplest one available and the least costly one to implement in a real system due to the lower number of sensors. The Skyhook formulation selected was chosen because it was the simplest one available in the literature.

3.5.2 LQR formulation

The formulation chosen for the LQR was the one described in equations (2.111), (2.100) and (2.103). The $\boldsymbol{Q}$ matrix is a 4 by 4 positive definite matrix, while $\boldsymbol{R}$ is a 1 by 1 matrix. In practice, $\boldsymbol{R}$ is a scalar value, but it is represented as a matrix because this is not always the case.

Instead of directly optimizing each of the matrix's coefficients, matrices which are positive definite or positive semidefinite were defined in terms of a lower triangular matrix $\boldsymbol{U}$, such that

$$\boldsymbol{U} = \begin{bmatrix} U_{1,1} & 0 & 0 & 0 \\ U_{2,1} & U_{2,2} & 0 & 0 \\ U_{3,1} & U_{3,2} & U_{3,3} & 0 \\ U_{4,1} & U_{4,2} & U_{4,3} & U_{4,4} \end{bmatrix} \tag{3.15}$$

$$\boldsymbol{Q} = \boldsymbol{U}\boldsymbol{U}'. \tag{3.16}$$

As long as $\boldsymbol{U}$ diagonal has no negative entries, this ensures that the final matrix is positive semidefinite as well. This is because $\boldsymbol{U}$ is a Cholesky decomposition of $\boldsymbol{Q}$, which guarantees the positive semidefinite properties of $\boldsymbol{Q}$ (Horn and Johnson, 2013).

3.5.3 SDRE formulation

The SDRE controller needed a choice regarding the parametrization of the non-linear system matrices. The chosen parametrization of the $\boldsymbol{A}(\boldsymbol{x})$ matrix for the 1/4 vehicle was as follows:

$$\boldsymbol{A}(\boldsymbol{x})\ \boldsymbol{x} = \left(\begin{bmatrix} 0 & 0 & 1 & 0 \\ 0 & 0 & 0 & 1 \\ -\frac{k_s}{m_s} & \frac{k_s}{m_s} & 0 & 0 \\ \frac{k_s}{m_u} & -\frac{k_s+k_u}{m_u} & 0 & 0 \end{bmatrix} + \begin{bmatrix} 0 & 0 & 0 & 0 \\ 0 & 0 & 0 & 0 \\ 0 & 0 & -\frac{f(\dot{v})}{m_s} & \frac{f(\dot{v})}{m_s} \\ 0 & 0 & \frac{f(\dot{v})}{m_u} & -\frac{f(\dot{v})}{m_u} \end{bmatrix} \right) \begin{bmatrix} x_s \\ x_u \\ \dot{x}_s \\ \dot{x}_u \end{bmatrix}. \tag{3.17}$$

In this equation, $f(\dot{v})$ is the gradient of the damper force with regards to its relative terminal velocity at 0 current. This is similar to the standard parametrization of the SDC[1] method, and represent the system's non-actuated instantaneous behavior.

The $\boldsymbol{Q}(\boldsymbol{x})$ and $\boldsymbol{R}(\boldsymbol{x})$ matrices are the weight matrices in equation (2.104). They were assumed to fulfill the same properties of positive definitiveness and semi-definitiveness the state independent weights $\boldsymbol{Q}$ and $\boldsymbol{R}$ had to.

The $\boldsymbol{R}(\boldsymbol{x})$ matrix has been parameterized as the sum of two coefficients R_1 and R_0, in the manner as follows:

$$\boldsymbol{R}(x) = \mathbf{R}_0 + \frac{1}{|f(\boldsymbol{x})|}\mathbf{R}_1. \tag{3.18}$$

Where $\boldsymbol{R_0}$ and $\boldsymbol{R_1}$ are two symmetric square matrix with 1 free parameters each. $\boldsymbol{R_1}$ is multiplied by $\frac{1}{|f(\boldsymbol{x})|}$ because this term was perceived as represented the predicted controller "stiffness" with regards to change, as in what would the perceived cost of controlling the j-th state variable given what the new i-th state variable value would be and the non-linearities of the controller.

The $Q(x)$ matrix, too, has been parametrized as the sum of two coefficients Q_0 and Q_1, defined as

$$\boldsymbol{Q}(x) = \boldsymbol{Q}_0 + |f(\boldsymbol{x})|\boldsymbol{Q}_1. \tag{3.19}$$

Where $\boldsymbol{Q_0}$ and $\boldsymbol{Q_1}$ are two symmetrical 4 by 4 matrix with 10 free parameters each. This equation is similar to the one used for $\boldsymbol{R}(\boldsymbol{x})$, but has the $f(\boldsymbol{x})$ term in the denominator instead. As with $\boldsymbol{Q}$, $\boldsymbol{Q_0}$ and $\boldsymbol{Q_1}$ were optimized through the matrix $\boldsymbol{U}$ as described in equations (3.15) and (3.16).

3.5.4 Controller tuning

The optimal choice of the parameters for the Optimal controller family was too complex to be performed analytically or manually. Because of this, it was left to a genetic algorithm optimization. In order to have like-for-like comparisons, the Hybridhook controller was also optimized through a genetic algorithm procedure.The details of the procedure are in Section 3.6.

[1] SDC (State Dependent Coefficients) or apparent linearization, is the name of the method used for creating the matrix with variable coefficients. For further information, see Çimen (2010).

3.5.5 Numerical solution

As previously state, all numerical solutions were carried out in the Simulink environment, with the Hook family also being solved in the Matlab environment.

For the Hook controllers, the state variables will be fed to equation (2.118) so the desired actuator force can be calculated given the controller parameters.

For the LQR controllers, once the state parameters are made available to the controller, it is necessary to solve the system's associated Riccati equation. For the standard LQR, this procedure is performed only once, before the system is even simulated. For the SDRE system, the terms of the Riccati equation are changed at every time step, and as such it needs to be recalculated every time step. This process is schematized in Figure 3.6.

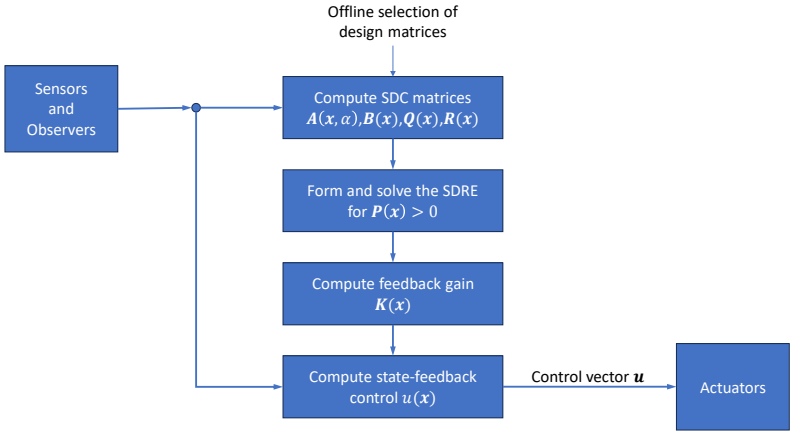

Figure 3.6. Algorithm procedures for calculation of the SDRE control. Adapted from Çimen (2010).

For the SDRE system, the first step is to calculate the terms which changed. In the contemplated procedures, those are the $A(x)$, $R(x)$ and $Q(x)$ matrices. These updated matrices are then fed to the solution loop. This loop calculates the solution to the Riccati equation. For the first iteration, this is done through the numerical residual minimizing algorithm embedded on Simulink with the default solution algorithm. For the second iteration, Matlab's '`icare`' function was used instead, due to its greater speed. If `icare` fails, the minimizing function `fminsearch` is called instead. The initial guess provided for the solution is the solution of the previous time step, and the first guess and initial value upon system initialization is the solution of the LQR case.

The choice of a residual minimizing algorithm instead of a root finding algorithm is because if the equation is not solvable given the specific system state, the gain value which minimizes the Riccati equation is instead chosen as an approximation. This option was chosen over matrix choices that guaranteed solvability or hing the system because, if said property mattered for performance enough, it should naturally appear in the solutions obtained through the optimization procedures. The importance of the associated Riccati equation solvability will also

be evaluated at the end of the optimization process.

3.5.6 Control scheme for 1/2 vehicle models

The control laws can take into account more state variables when applied to a 1/2 vehicle model. However, because the control schemes will be fine tuned for 1/4 vehicle models, the control schemes will instead be applied locally on each wheel. That is, each suspension will have an independent controller that takes into account the relative displacement and velocity between its wheel and the chassis portion directly above it. This requires that an equivalent local 1/4 vehicle model to be fed to the controller.

The local and global tire coordinates are the same. The local and global coordinates for the upper body are related by the expression

$$x_{s,local} = x_s + x_\theta d_r \tag{3.20}$$

where d_r is the distance from the wheel to the center of mass, having a positive signal for the front wheel and negative signal for the rear wheel to take into account their forces' opposite effects on the body's rotation.

The equivalent upper mass is related to the bodies' masses by the expression

$$m_{s,local} = m_s + \frac{J}{d_r} \tag{3.21}$$

which simply converts adds the inertial mass divided by the suspension's leverage to the total mass.

3.6 OPTIMIZATION

All processes which required optimization will be handled with the use of genetic algorithms. This choice was taken because genetic algorithms can be applied to a wide range of problems, being able to handle:

- Multi-objective optimizations
- High number of optimization variables
- Objective functions with no explicit gradient

For the MR damper optimization, the algorithm used was the standard embedded Matlab 2022a algorithm, whose source in the literature has not been discovered as of the time of writing. This choice was made given the optimization for the MR damper was less demanding. Because it was single objective, there was no need to guarantee the Matlab algorithm was specially tailored to be able to handle multi objective optimizations. Because the individuals were cheap

to evaluate, computational efficiency was less important. Furthermore, any weaknesses in convergence could be overcompensated by a high number of individuals and generations.

For the SDRE optimization, neither conditions of single objective or cheap individual evaluations were true. As such, the NSGA-II was chosen as a robust option of genetic algorithm that would guarantee reasonable performance, convergence speed and Pareto front generation.

The optimization procedures which will be performed for the vehicle simulations were improved over many iterations. A first round of optimizations was performed under limited conditions solely for the LQR and SDRE controlled vehicles, with fewer optimization variables, individuals and generations, as well as fewer and shorter simulations. These results were published in (Ferreira *et al.*, 2022). Compared to these earlier iterations, the optimizations to be performed will be applied on all contemplated vehicle types (passive, Hybridhook, LQR, SDRE), will allow the suspension passive parameters to be optimized as well and will more individuals and generations, more simulations per individual, longer simulation times and more robust data filtering methods.

3.6.1 Damper parameter selection

To determine the best damper model, it was decided to compare them against the experimental data to determine the best performing model. Because the models had degrees of freedom in the form of coefficients, the best performing coefficients needed to be found. It was decided to obtain them through a genetic optimization. The coefficients are to be iterated for each model until the best fitting combination is found given the search parameters.

The results will be based on the models match to experimental data. The data series for time, displacement and force from the experiment performed in (Silva *et al.*, 2022) were generously provided by the author for this purpose.

The genetic algorithm optimization was implemented in Matlab. The genetic algorithm chosen was the standard implementation present in the Matlab 2022a software. A different optimization was carried out for each individual proposed model. The fitness function chosen is the minimization of the quantity described in equation (3.22). The optimization parameters are in Table 3.1. The fitness function is, then,

$$C = \sum_{t=t_0}^{t_f} |F_{exp}(t) - F_{fcn}(E(t), h)|. \tag{3.22}$$

In this expression, C is the cost function, t_0 is the start time, t_f is the finish time, $F_{exp}(t)$ is the experimental force measured at time t and $F_{fcn}(x, t, h)$ is the force expressed by the model at time t with excitation parameters $E(t)$ and constant model parameters h.

To calculate the force at time t and $E(t)$ from an individual with parameters h, each model will be numerically solved at each point of the data series in sequential manner with respect to time, so as to guarantee proper initialization of the variables that depend on time history

and to ensure the proper time evolution of the ODE of the Bouc-wen model. The numerical integration of the ODE will be carried out with Matlab's built-in Runge-Kutta 4th/5th order numerical integrator.

The fitness function chosen was the sum of the absolute difference between the model predicted force and the experimental force over a period of time in which the damper was at steady state. The time span was selected so as to guarantee it began and ended during steady state while providing the maximum amount of data points possible.

Table 3.1. Genetic optimization parameters

Parameter	Timespan	Number of individuals	Generations
Value	100s	1080	300

The results from the best individual from the genetic optimization process for each model will be compared, with the model which achieves the lowest cost function being chosen for realistic damper simulations as the most precise. Convergence criteria were stall of the best solution for 10 consecutive generations or 300 generations simulated. If the second criteria was met, it was checked whether there were still significant improvements in the solution or changes in the solution space, or whether the improvements obtained were numerically insignificant.

An additional procedure will be performed to the best v_m formulation for the Wang model. For the v_m simulations, the simulation parameters are shown in Table 3.2. All simulations were performed using Matlab's Simulink routines.

Table 3.2. Parameters for the v_m stability simulation.

Parameter	Sine amplitude	White noise power	Simulation duration
Value	10^{-3} m	1 W	100 s
Parameter	Initial x, $\dot{x}$ and $\ddot{x}$	K	M_1
Value	0	1 N/m	1000 Kg

3.6.2 Vehicle parameter optimization

The optimization parameters are available in Table 3.3, and the optimization bounds are available in Tables 5.10, 5.9 and 5.8. The optimization methodology is available in Figure 3.7.

All variables but "κ" were optimized as the exponential coefficients. For example, a variable such as "k_s" is encoded in the optimization by the gene "G_{k_s}" as a value between 2 and 8. When simulating, "k_s" is then set to the value "$10^{G_{k_s}}$". This was done because many values have a logarithmic relationship with the optimized variables, and encoding the values this way gives a better parameter distribution more easily.

Some variable can be negative. For those, a special relationship between the gene and the variable was used. For a variable "V" with a gene value "G", "G" mapped to "V" by the expression

$$V = 10^{|G|-4} sgn(n). \tag{3.23}$$

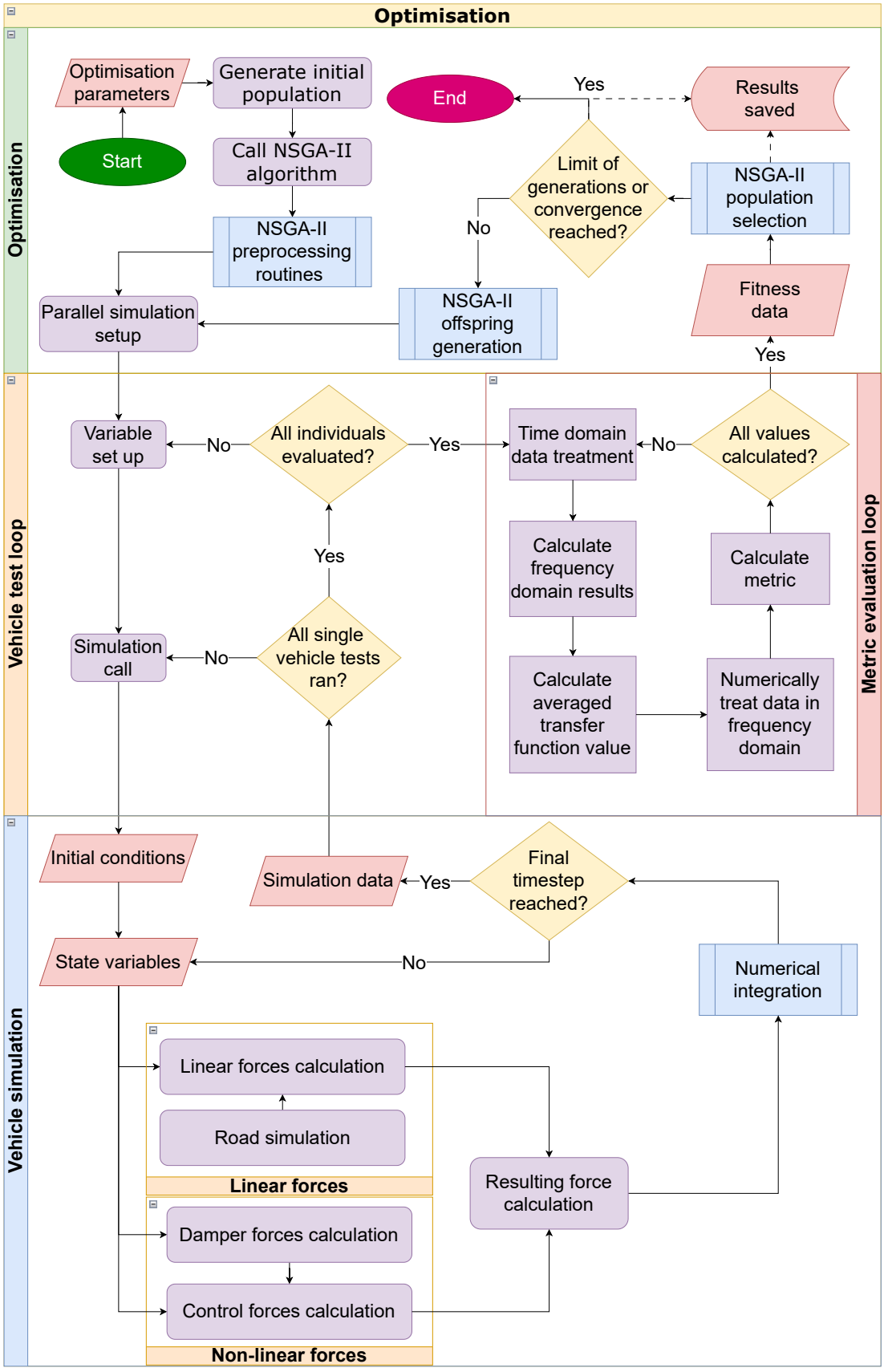

Figure 3.7. Diagram of the optimization procedure undertaken for the quarter vehicle optimizations.

Table 3.3. Properties of the second optimization algorithm and analysis. SBX[a] stands for Simulated Binary Crossover. LHS[b] stands for Latin Hypercube Sampling.

Property	Value	Property	Value
Fitness calculation and offspring creation parameters			
White noise band cut-off	200 Hz	Max spectrum frequency	100 Hz
Number of averages	30 per individual	Crossover probability	85%
Tournament pool size	2/3 of population	Tournament size	6
Parent selection function	Tournament	Mutation distribution index	20
Encoding	Real	Crossover distribution index	20
Mutation operator	Polynomial mutation	Crossover operator	SBX[a]
Population parameters			
Number of generations	100	Population size	500
Initial population selection	LHS[b]	Additional constraints	No

In this formulation, the gene's sign is variable's sign, while the variable's magnitude is proportional to the gene's absolute value. By offsetting the gene by minus four, magnitudes smaller than $|10^0|$ can appear, and "V" minimum value becomes $|10^{-4}|$. This does creates a "blind spot", as values between $\pm 10^{-4}$, except for 0 (due to the sign function), are impossible. However, the better distribution and the small region size make this a reasonable trade off.

As for the two MR damper variables which are optimized, "a_1" and "f_0", their gene codes for the exponent of a multiplier of their nominal value:

$$f_{0(opt)} = f_{0(nom)} 5^G \tag{3.24}$$

$$a_{1(opt)} = a_{1(nom)} 2^G. \tag{3.25}$$

In other words, "$a_{1(opt)}$" may be twice as big or small as its nominal value, while "$f_{0(opt)}$" may be 25 times as big or small as its nominal value. The reason for this specific representation was to make it possible for the MR damper to be optimized while guaranteeing the values don't stray too far from the damper which has been physically realized, as while no optimized value has any guarantee of corresponding to a possible MR damper, values which are significantly different have a higher risk of being impossible.

3.7 SIMULATION PARAMETERS

Different simulation demanded different parameters. This was due to differences in computational methods used, different information acquisition goals and different needs. All the parameters chosen and their reasoning's are the same for the 1/4 and 1/2 vehicle models.

The parameters used for the time domain simulation of the optimizations performed on the passive, MR Hybridhook, MR LQR and MR SDRE systems are available in Table 3.4. The same parameters were used for calculating the frequency domain results for the Case Studies. The parameters used for the time domain simulations of the deterministic obstacles for all controllers are in Table 3.5.

Table 3.4. Simulation parameters for the time domain simulation for optimization of vehicle type #1, as well as the simulations for the frequency domain data of the Case Studies.

Property	Value	Property	Value
Integrator	ODE45	Steady state interval	16 seconds
Minimum simulation frequency	200 Hz	Simulation time	144 seconds
White noise band cut-off	200 Hz	Frequency analysis range	100 Hz
Controller update frequency	50 Hz	Vehicle speed	10 m/s
Excitation type	1st order ISO B		

Table 3.5. Simulation parameters for the time domain simulation of deterministic obstacles, all cases.

Property	Value	Property	Value
Integrator	ODE45	Steady state interval	16 seconds
Minimum simulation frequency	200 Hz	Simulation time	20 seconds
White noise band cut-off	200 Hz	Frequency analysis range	100 Hz
Controller update frequency	50 Hz	Obstacle encounter time	16 s
Excitation type 1	Speed Bump	Vehicle speed	8,33 m/s
Peak height	8 cm	Length	3,6 m
Excitation type 2	Linear Rise	Vehicle speed	1,39 m/s
Peak height (cm)	5 cm		

The minimum simulation frequency is based on the white noise generation and data acquisition frequencies. The system has to be simulated at least every 5 ms in order to correctly update the white noise block in the road generation, as well as to capture the simulation data. The road update frequency was decided so as to have no. The data capture rate was decided based on the experimentally determined biggest value with which all frequency domain results for the analyzed systems reliably converged.

The integration time step bounds were determined so as to ensure three demands were met:

1. The equations converged;
2. Frequencies of up to 100 Hz could be obtained by the Fourier transform;
3. All sub components of the simulation, such as the MR damper or the controller simulation, had their behaviors constant with greater time granularity;

For the first demand, a lower limit of 10^{-8} seconds was chosen. It was observed that lowering this limit did little to increase the quality of results, as system configurations that did not converge with this time step were generally unable to converge with lower time steps, with steps as low as 10^{-32} s being tested with no success cases. They did, however, take longer to simulate, as they would decrease the time step and take longer to diverge. Meanwhile, systems that did not diverge showed little improvement in their precision or changes in their behavior. As per (Proakis and Manolakis, 2014), the second demand requires a minimum time step of 10^{-2} seconds.

The third demand value was found to be dependent on the road simulation frequency, as that dictated the bare minimum convergence requirements. Frequencies lower than the road's GWN have significant differences between each other for simulations with equal conditions. As such, the integration time step bounds were 10^{-8} s for the lower and unbounded for the upper, as the upper integration time step bound was already enforced by the minimum simulation frequency.

The 20 ms update intervals for the controller were based on the limits of electronics and dampers. For electronics, Çimen (2010) claims:

> *"SDRE control laws can be implemented at speeds greater than 600 Hz and up to 2 kHz sample rates, [...] using commercial, off-the-shelf processors."*

A maximum frequency of 50 Hz was already a reasonable bound in 2010, and modern electronics are certainly more capable. For damper reaction time, it varies between implementations. For commercial applications, 20 ms is a reasonable value (Jeyasenthil *et al.*, 2019; Yoon *et al.*, 2021). For MR dampers specially tailored for a fast response, Žáček *et al.* (2022) developed an MR damper capable of 8.5 ms reaction time, Yoon *et al.* (2021) developed an MR damper with a 7.8 ms reaction time, and the same author (Yoon *et al.*, 2019) also developed an MR damper with a 1.9 ms reaction time. Here, the reaction time is defined as the time it takes the damper to reach 95% of the desired control force.

It stands to reason that a 50 Hz frequency gives a reasonable time span for the controller command to take full physical effect. With these factors in consideration, it was decided that a 20 ms response time without considering the damper transient behavior was a fair compromise between what is physically possible to do and whats practical for simulation purposes. Faster controller speeds demand more resources to simulate, while modeling the damper transient response can also be a burden for the simulation computational load.

The vehicle speed was set to 10 m/s or 36 km/h because this corresponds to an intermediary speed. It is fast enough for its behavior to be representative of inner city cruise speeds (60 km/h), but not so fast as to be significantly different from the slower speeds a vehicle might be at when facing obstacles such as speed bumps. The cut off frequency of the white noise used to generate the road profile was set as 4 times the analyzed frequency range, so as to encompass the whole studied response range.

The simulation time and number of samples were based on the best cost benefit found for results precision and computational time. As demonstrated in published works by the author (Ferreira *et al.*, 2022, 2025), the inherent randomness of the white noise excitations coupled with the non-linearities of the control schemes create a significant variation in the gain response obtained from different simulations with the same parameters. To account for this effect, the simulations were ran multiple times with the same parameters. The final individual simulation time length and number of runs for each parameter combination was decided based on a balance of results precision, computational time and computation hardware leveraging.

The total simulation time parameter was chosen given four different necessities:

1. Guarantee that the Fourier transform of the system was able to discern apart frequencies of at least 0,25 Hz
2. Make sure the system frequency response was solely from the steady-state response
3. Be as short as possible so as to save computational time
4. Give consistent, reliable results

At least 8 seconds of simulation were needed for the first condition (Proakis and Manolakis, 2014), and 16 seconds were needed for the second. The second value was determined through direct observation of the transient state behavior over many dampers, with 16 seconds being considered a conservative margin. For the third and fourth conditions, the 8 seconds were observed to not be enough to make reasonable estimates of the frequency domain response, with much greater simulation times being necessary. This is likely because the non-linearities made 8 second spans unreliable, as they caused unpredictable variations that could not be drowned out by the average behavior due to the time spans. The actual reason notwithstanding, a simulation time of 128 s was determined as good enough, with shorter time windows yielding subpar results. A power of 2 was chosen because it slightly increases the performance of the FFT algorithm. Adding the 16 seconds for the transient response elimination results in 144 seconds of simulation.

It is unlikely all systems tested would require the same demanding parameters the worst cases simulations require. Still, to ensure all simulation results were comparable, all systems were solved using the same parameters. When running a code within Matlab, certain tasks may be split and solved in parallel. The parallel simulations were ran using Matlab's '`parsim`' function, which enables parallel Simulink simulations to be ran programmatically.

4 COMPUTATIONAL IMPLEMENTATION

This section contains the details of the computational implementation of the procedures described in the Methodology chapter. The algorithms are implemented in either the Matlab environment or Matlab's Simulink simulation environment. Additional diagrams of this Chapter can be found in Appendix F

All code used, including the Simulink files, can be found in the thesis repository, hosted in Github. The link to the repository is: `https://github.com/Leonardo-cr-ferreira/master_thesis_codes/tree/af7ae0cd0ed05db0c3286d010437de50435e6ddb`.

4.1 VEHICLE MODELS

The mathematical equations of the vehicle models were solved in Simulink. The vehicular system of equations is the most comprehensive set of equations solved in the work, as they involved not only the solution of the matrix system of equations of the vehicle model, but also the solution of the control schemes, damper model and road excitation.

The system was implemented in Simulink. The resulting Simulink diagram is in Figure 4.1a for the quarter vehicle model and in Figure 4.1b for the half vehicle model. In red are the linear components of the system, while in blue are the damper forces composed of the damper model and the controller. They are summed in the orange block, creating the resulting system equation. In green are the vehicle parameters. The road excitation is represented in purple, with the example used pertaining to a case with a GWN excitation. The yellow block represents the numerical integration, while the magenta blocks are the initial values of the state variables. The dark green blocks are outputs like observation blocks used for debugging as well as the data output block, while the white blocks are arithmetic blocks. An explanatory diagram of the system is in Figure 4.1c, with the same color scheme.

An advantage of this design procedure is that functionalities can be easily swapped without incurring in major diagram changes. Changes in controller or damper models can be done by simply substituting their respective blocks. Changing from a quarter car to a half car model can be done by changing the vehicle parameter variables and the internal code for the forces blocks, with the same logic being maintained.

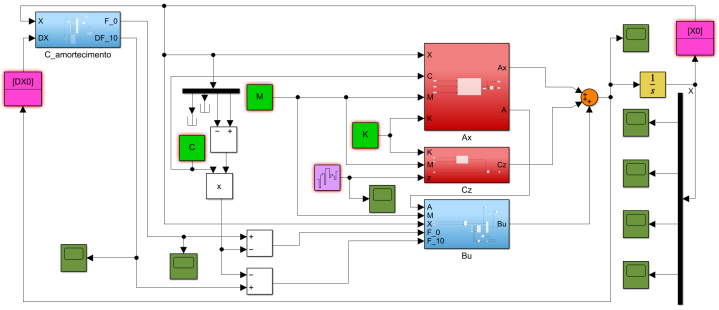

(a) Simulink diagram for quarter vehicle simulation.

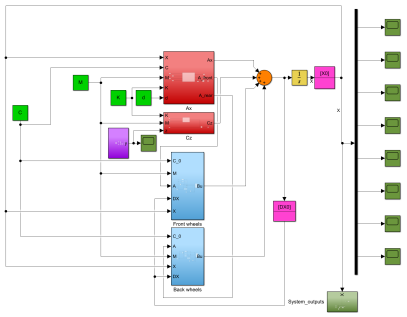

(b) Simulink diagram for half vehicle simulation.

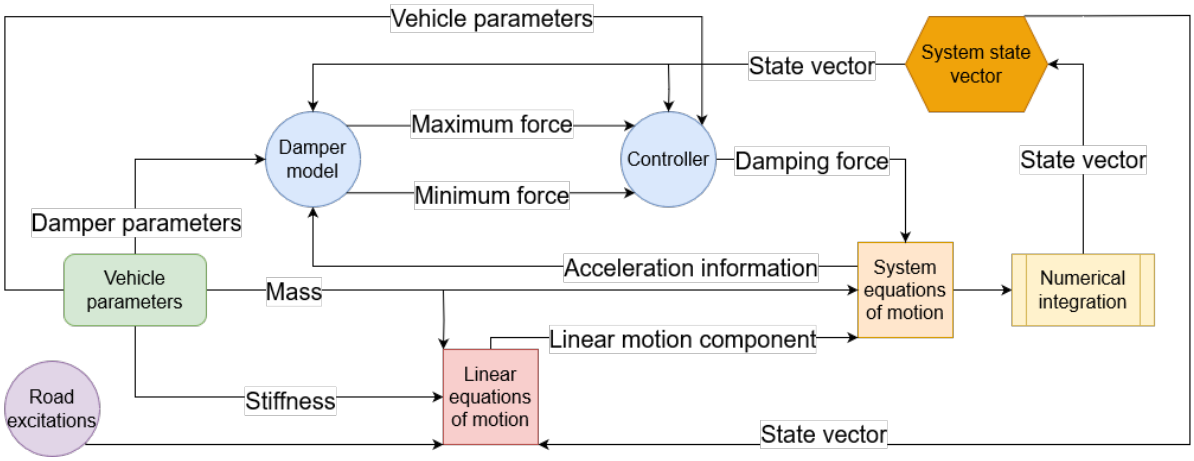

(c) Diagram of the vehicle simulation flowcharts

Figure 4.1. Vehicle simulation Simulink diagrams and flowchart.

4.1.1 Parameter blocks and variables

The blocks M, C and K contain the mass, linear damping and stiffness terms, respectively. Their dimensions are dependent on the vehicle model being used.

The quarter car model has 2 values for mass, 1 for linear damping and 2 for stiffness. They are ordered with the upper mass and stiffness first and the lower mass and stiffness second. These vectors are as such:

$$M = \begin{bmatrix} m_s \\ m_u \end{bmatrix} \quad K = \begin{bmatrix} k_s \\ k_u \end{bmatrix}. \tag{4.1}$$

The half-vehicle model has 4 values for its mass, 2 for its linear damping and 4 for its stiffness. They are ordered with the upper mass and front stiffness first, the front lower mass and stiffness second, the moment of inertia and rear upper stiffness third, and the rear lower mass and stiffness fourth. These vectors are as such:

$$M = \begin{bmatrix} m_{s,f} \\ m_{u,f} \\ J \\ m_{u,r} \end{bmatrix} \quad C = \begin{bmatrix} c_f \\ c_r \end{bmatrix} \quad K = \begin{bmatrix} k_{s,f} \\ k_{u,f} \\ k_{s,r} \\ k_{u,r} \end{bmatrix}. \tag{4.2}$$

The X variable refers to the vehicle state vector, while the z variable is the road excitation. The A variable is the state matrix, and the F_0 and F_10 are the damper minimum and maximum forces respectively. In the half-vehicle cases, the non-linear damper forces are ordered in the manner of the linear damper forces. The DX variable is the derivative of the vehicle state vector.

The linear equations of motion are described by blocks Ax and Cz. Ax contain the net derivatives of the state vector originating from the vehicle state variables multiplied by the system matrix A, and Cz contains the net derivatives of the state vector originating from the road excitation vector multiplied by the matrix C_z:

$$C_z = \begin{bmatrix} k_u \\ 0 \\ 0 \\ 0 \end{bmatrix}, \quad C_{z,4gdl} = \begin{bmatrix} k_{f,u} & 0 \\ 0 & k_{r,u} \\ 0 & 0 \\ 0 & 0 \end{bmatrix}. \tag{4.3}$$

The internals of block are displayed on Appendix F.

The non-linear damping and linear terms which dictate the derivatives of the state vector are added and integrated using the Simulink "Integrator" block. All block parameters are the standards. The '`ode45`' integrator was enforced through the command line function.

4.2 CONTROLLERS

4.2.1 Generic structure

The generic controller structure is demonstrated in Figure 4.2. This group composes the Bu block.

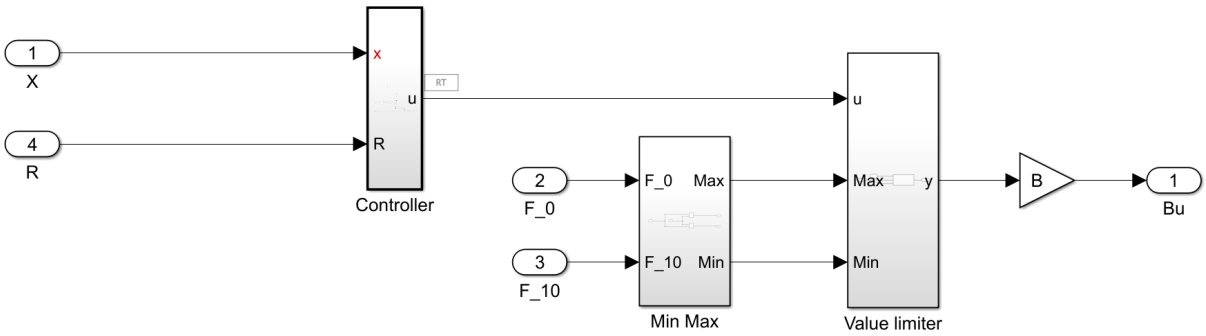

Figure 4.2. Simulink routine for a generic controller.

There are either three or four main structures in this format:

- A controller specific block;
- A minimum-maximum damper force ordering block;
- A value limiter unit;
- A local relative displacement calculation unit (half vehicle exclusive)

The controller unit receives the controller parameters, such as the state variables and the system parameters, X and A in this case respectively. It outputs a value u, which is the desired control force divided by the mass vector M.

The minimum-maximum damper force ordering block receives the damper 0 and maximum current forces, and decided which value is the lower and which value is the upper boundary. It then divides the boundaries by the mass vector M. This results in the Simulink block diagram in Figure F.3 for the quarter vehicle model.

The value limiter unit, which is actually the Simulink standard block ”Saturation (Dynamic)”, checks if the value is within the upper and lower boundaries of the semi-active damper actuation at that time step. If it is, the calculated value is outputted. If it is not, then the outputted value is the closest boundary’s.

For the Half vehicle case, an additional block which calculates the relative displacement and velocity at the front and rear suspensions coordinates is also added.

The controllers were implemented directly as Simulink block diagrams instead of codes in most cases, as it was found that Simulink was better able to handle successive zero-crossings when a routine is implemented in block form. The SDRE solver for its associated Riccati equation was the exception.

The controller specific block is substituted by whichever controller is desired for the simulation.

4.2.2 Implementations

The Hybridhook controller was calculated in Simulink, and its implementation can be observed in Figure F.4.

The linear LQR controller was also implemented into Simulink. As shown in Figure F.5, the LQR controller is an implementation of the LQR gain equation in Simulink block diagram form. The Riccati equation is solved once in the parameter setup script, and is fed directly into the system for faster solution.

The SDRE controller was implemented into Simulink in a manner very similar to the LQR linear controller, as it would be expected due to their similarities. The main differences are the addition of a block which calculates the variable matrices **A(x)**, **Q(x)** and **R(x)** and the solution of the associated Riccati equation on a Matlab script.

As shown in Figure F.6, the SDRE controller is also an implementation of the SDRE gain

equation in Simulink block diagram form. The Riccati equation is solved in the function block. It calculates the solution using primarily by calling up Matlab's function `icare`, which was determined to be the fastest alternative available. The routine makes use of initial values blocks to initialize the values, and a memory cell to use the last Riccati equation solution as the initial guess for the current one, speeding up the solution.

To make the system more robust, two fail safes were implemented. If the `icare` routine failed to solve the system, a slower but more reliable solution using Schur's factorization as described in Section 2.5.1 would be attempted. Still, some unsolvable problems could occur, such as the case when the determinant of **R(x)** was 0. This makes the **R(x)** matrix uninvertible, and the Riccati equation solution is undefined. In such cases, the last valid solution is instead passed on as the answer.

The **A(x)**, **Q(x)** and **R(x)** matrices were calculated in their own sub-routine shown in Figure F.7.

There are two Matlab function blocks in this sub-routine, whose code can be inspected in the repository. The leftmost one is responsible for calculating the MR damper force derivative $\frac{dF}{d\dot{v}(\dot{x})}$ at 0 current. In the figure shown, this is being done for the MR damper using Wang's model. The expression for this quantity is very extensive, and is fully displayed in the Appendix. Then, it is fed into the rightmost block, which calculates the state dependent matrices with the vehicle mass, the weight coefficients and damper force derivative data.

While not used in the present work, an additional state dependency on the MR damper second force derivative $\frac{d^2F}{d\dot{v}(\dot{x})^2}$ was also tested, and its formulation and parameters are retained in the block diagram provided.

4.3 MR DAMPER IMPLEMENTATION

The MR damper was implemented in either a test bench setup or a vehicle setup, which can be seen in Figure Figure F.8.

The vehicle setup is part of a bigger vehicle simulation structure as shown in Figure 4.1a. In Figure F.8, the shown diagram is an excerpt from a specific case in which Wang's model is being used.

4.3.1 Bingham simulation

The Bingham simulation is described by the diagram in Figure 4.3, with its internals being made explicit in Figure F.9.

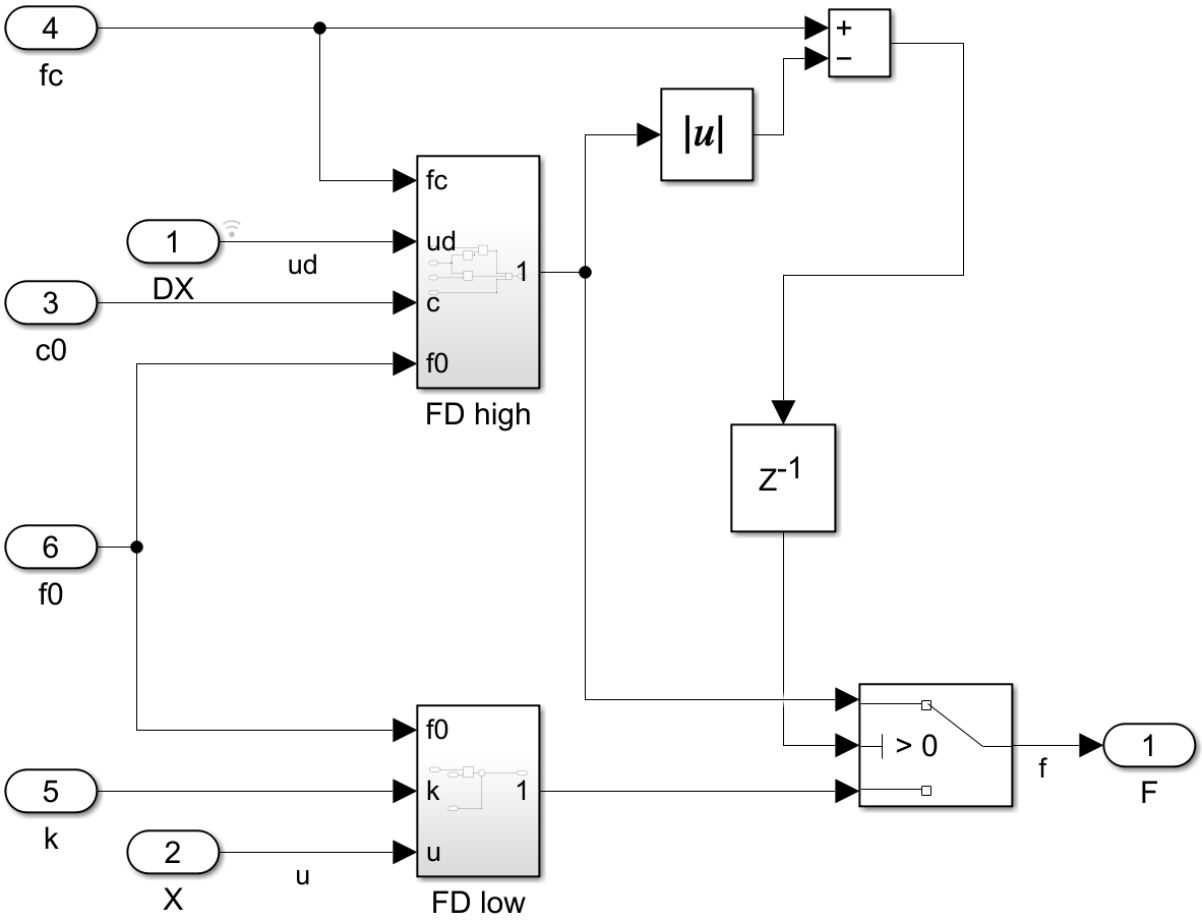

Figure 4.3. Simulink routine for the Bingham damper model.

A memory block is used so the force being compared is always the last step force, to avoid excessive zero crossing events.

4.3.2 Bouc-wen simulation

The Boucwen simulation is described by the diagram in Figure 4.4, with its internals being shown in Figure F.10.

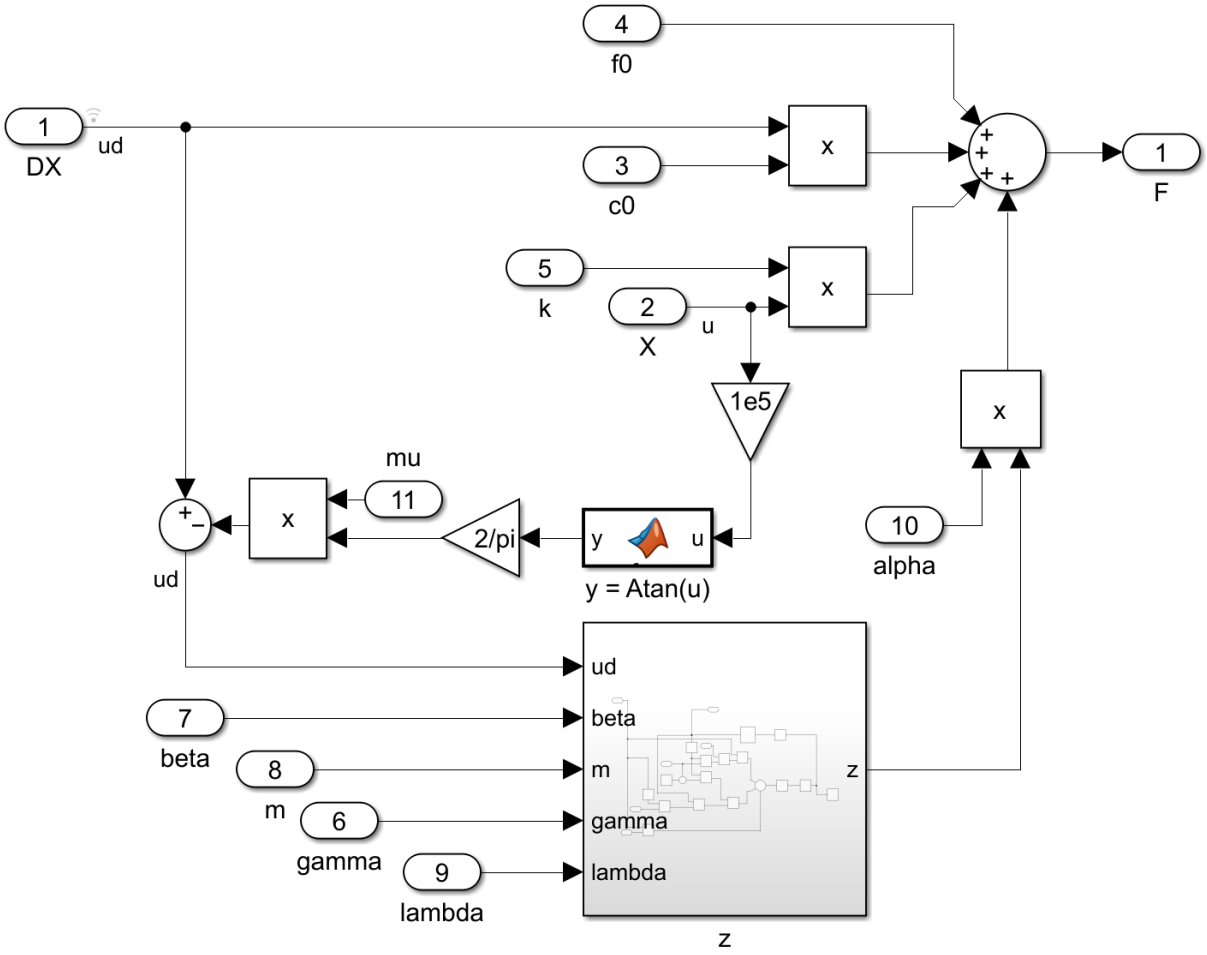

Figure 4.4. Simulink routine for the Bouc-wen damper model.

A saturation block set to a very high value is used to avoid numerical divergences occurring due to spurious oscillations associated with the evolution of the 'z' variable on start-up. Furthermore, the signal function was substituted by a inverse tangent (atan) function of the magnified velocity, due to to it being defined for 0 as well as providing a smoother transition when the signal changes value.

4.3.3 Wang and Wang-II simulation

The diagram for the Wang model is very extensive. The full diagram is shown in Figure F.11, but it has also been broken down into sections for ease of visualization. These views are constrained to Appendix F.

The Wang and Wang-II models are subject to one additional simulation, the test-bench with feedback condition. This was implemented in the manner of the Simulink diagram in Figure 4.5.

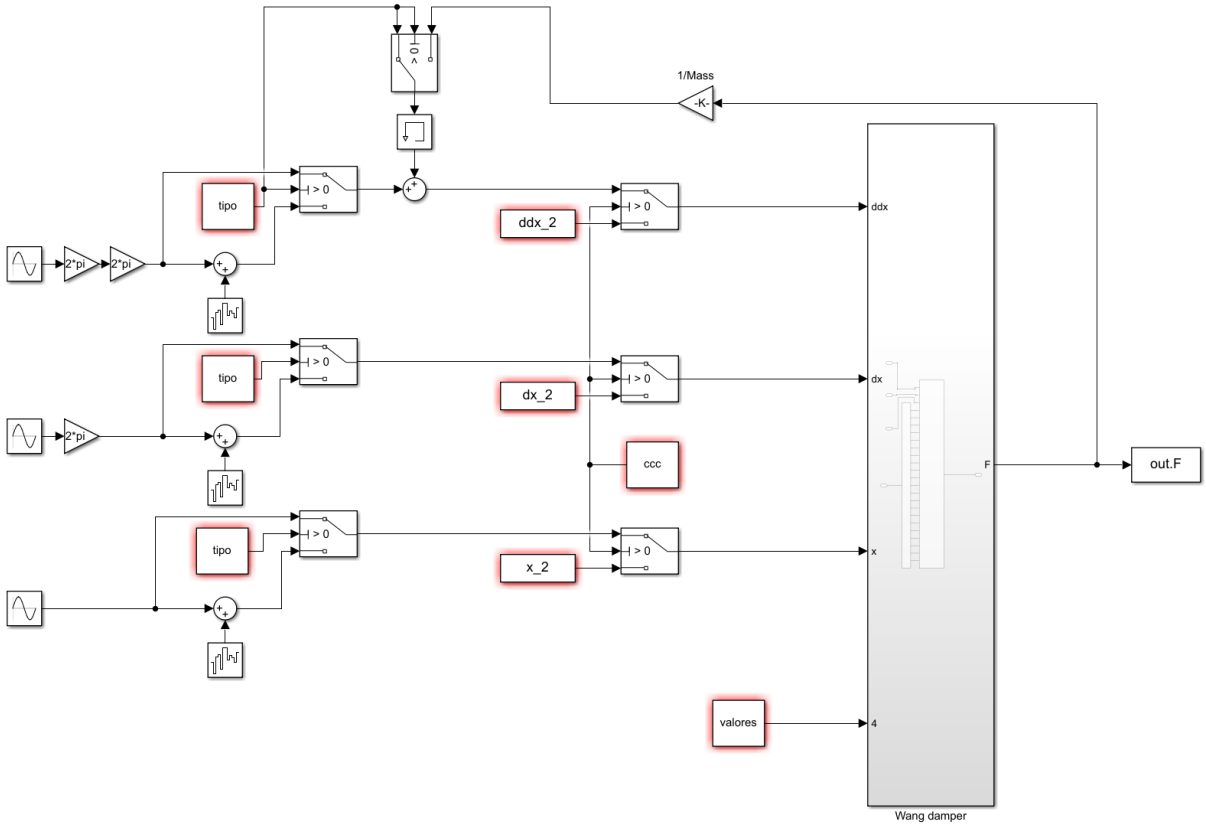

Figure 4.5. Simulink routine for the Wang damper model with added feedback.

This model allows for pure and noise added sinusoidal excitation of position, velocity and acceleration by changing the value of the variable ”tipo”, as well as a feedback effect as a function of mass as described by Figure 2.10. Because the forces acting on the mass are the Damper force and the coordinate difference between the variable x and the excitation times a spring constant, it is not necessary to explicitly model the spring. Instead, it can be implied by synchronizing the position and acceleration excitations. The effects of acceleration on the speed and position were omitted, due to the fact that this model was shown to be enough for the demonstration purposes it was built for and its results apply to the more general case.

4.4 EXCITATIONS

The Linear Rise is simply a Step function, and will not be shown here.

4.4.1 Bump excitation

The Bump was executed by outputting the cosine profile at the desired time, as shown in Figure 4.6.

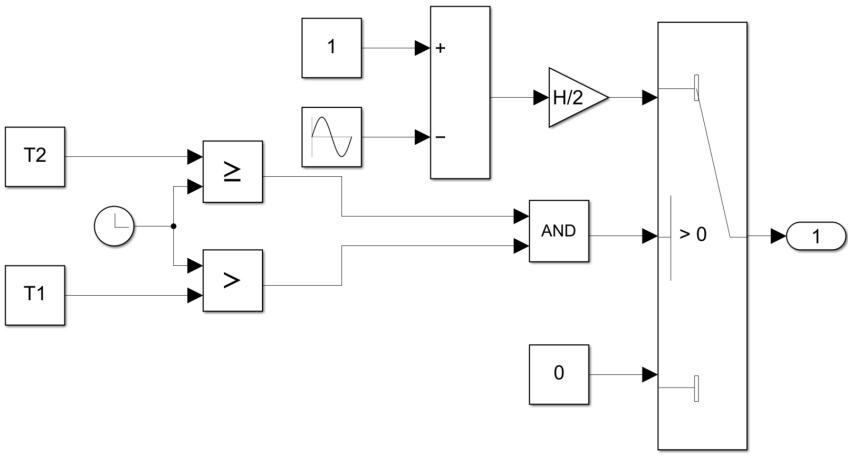

Figure 4.6. Simulink model of the Bump excitation.

4.4.2 ISO road

The ISO road was executed by filtering the GWN block as shown in Figure 4.7.

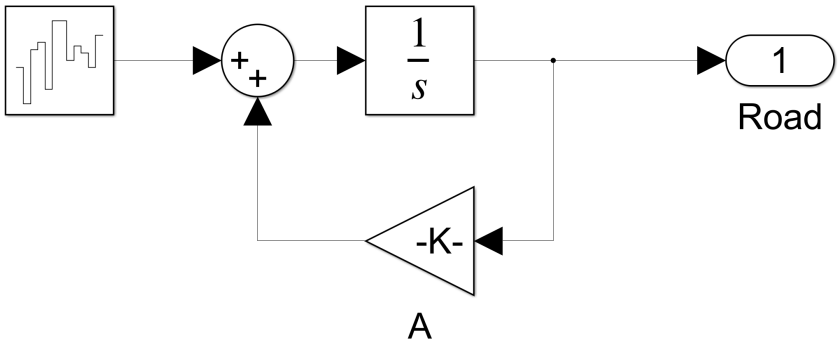

Figure 4.7. Simulink model of the 1st order ISO road. Reproduced from Ferreira *et al.* (2025).

4.4.3 Half vehicle road excitation

To create the road excitation for the half vehicle model, the road excitation was first created and fed to terms which excite the front wheel, while the terms that excite the rear wheel were subject to a delay using Matlab's `Transport Delay` block. This can be observed in Figure 4.8.

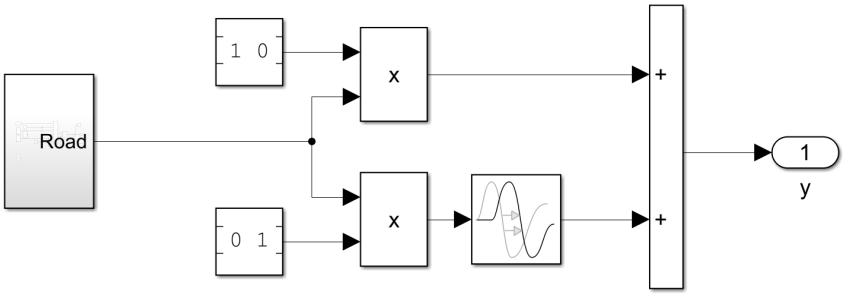

Figure 4.8. Simulink model of half vehicle road excitation creation procedure.

4.5 OPTIMIZATION

The genetic optimization was implemented using the codes in the repository, with further information being presented in Annex A. The general structure of the code sequence for the optimization procedure is as follows:

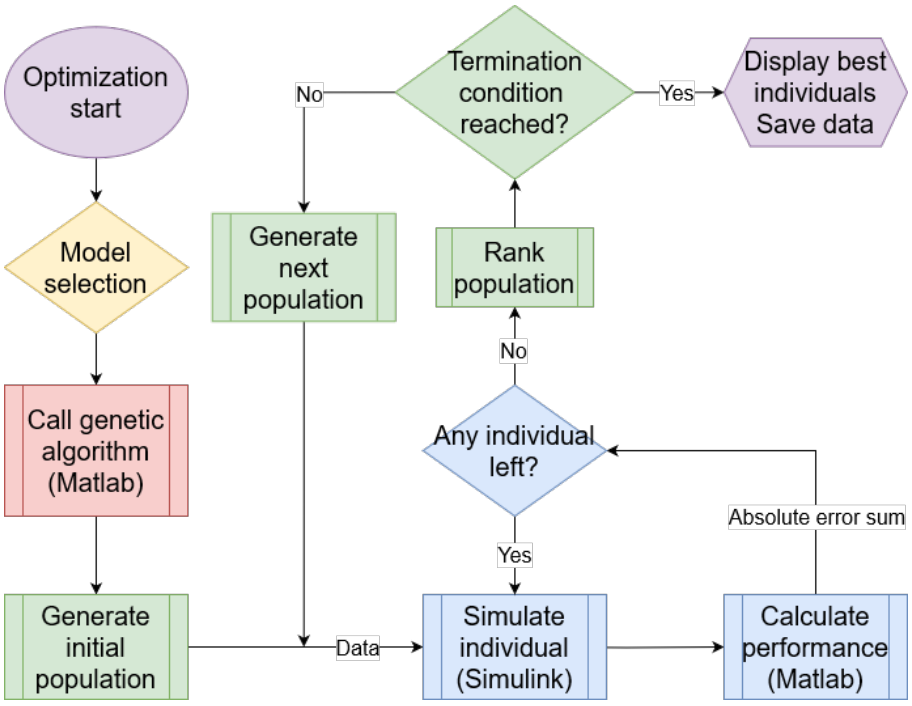

Figure 4.9. Generic code flow for the genetic optimization procedure.

4.5.1 Damper optimization

For the damper optimization, the code structure is given in Figure 4.10.

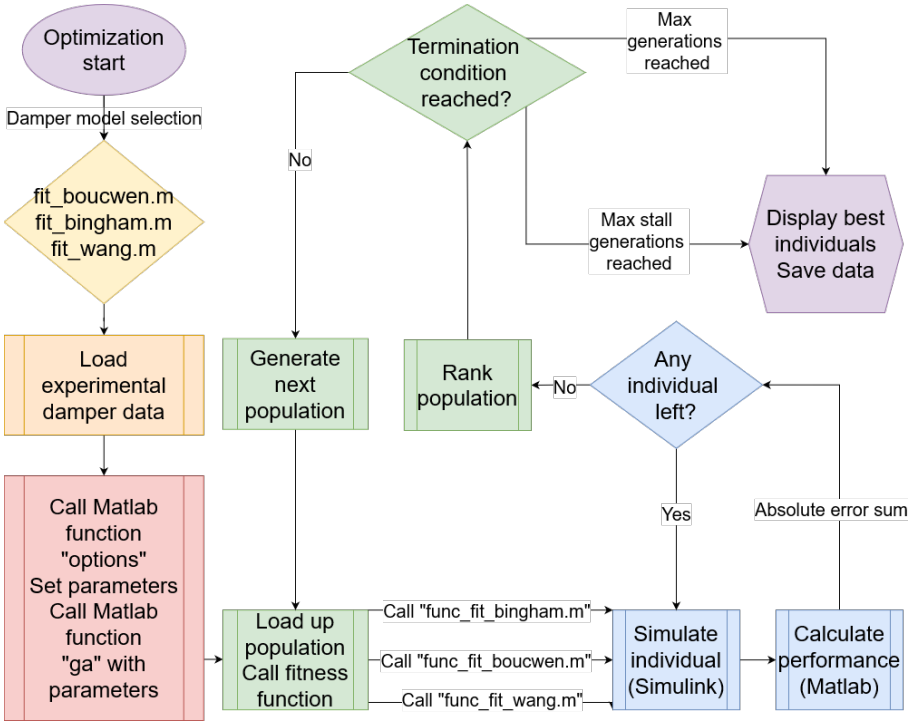

Figure 4.10. Code flow for the genetic optimization procedure of the damper model.

First, a decision is made regarding the damping model to be used. As the name implies, the functions ”`fit_boucwen.m`”, ”`fit_bingham.m`” and ”`fit_wang.m`” are used for the Bouc-wen, Bingham and Wang damper model, respectively. The Wang and Wang-II share the same optimization file, with modifications being to the number of variables and the Simulink function called on the individual simulation step being changed.

The experimental data for the damper is loaded, the optimization options are set using the ”options” function and the genetic optimization is called with the ”`ga`” command. The initial population is created and the specific simulation function is called for the damper model. Once again, the name shows clearly which function is for which model, with the functions ”`func_fit_boucwen.m`”,”`func_fit_bingham.m`” and ”`func_fit_wang.m`” being for the Bouc-wen, Bingham and Wang damper model, respectively.

The damper individuals are simulated in parallel, and their fitness is evaluated once all individuals are simulated. The `ga` function then ranks the individuals, and determines whether a stop condition has been reached. If it hasn’t, the ”`ga`” function creates the next population and repeats the process.

If either the maximum number of generations or stall generations has been reached, the simulation stop, the data is saved and the best individual is displayed.

All code data has further instructions on its use available on the Appendices.

4.5.2 Controller optimization

For the controller optimization, the code structure is given in Figure 4.11.

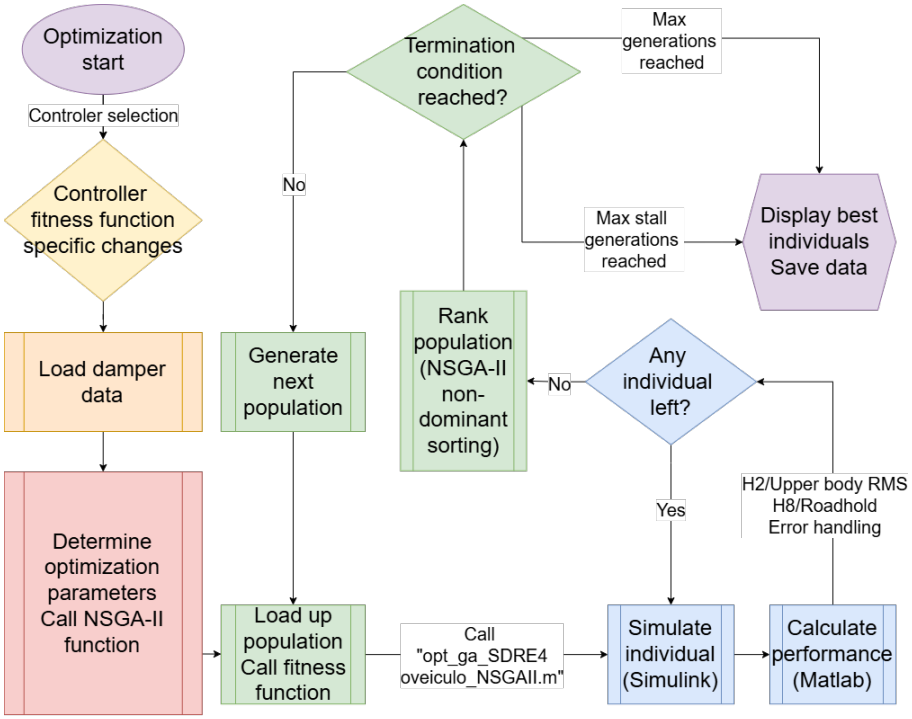

Figure 4.11. Code flow for the genetic optimization procedure of the LQR/SDRE controller.

First, the controller model needs to be chosen. Both the fitness function and the genetic algorithm optimization parameters must be changed to cater to either model. This involves changes to the number of genes in an individual. The Passive model has only 2 variables, and is the simplest of all models to optimize. If the Hybridhook model is used, this number increases to 6 variables, and if the LQR or SDRE with constant weights models are used, there are 15 variables which enter the simulation. Finally, if the SDRE model with variable weight matrices is used, there are 26 variables in the simulation.

Next, the damper model and NSGA-II algorithm parameters are set and the "NSGA-II" function is called. An external, already written implementation of the NSGA-II algorithm was used as the basis. It was made available by an user in the Matlab website (Seshadri, 2009), and is credited to Aravind Seshadri.

Because of the structure of the code, there's only one fitness function to be called, "`opt_ga_SDRE4oveiculo_NSGAII`". The simulation data is loaded onto Simulink and the individual is simulated many times in parallel, until all the request simulations have been performed. Then, the performance is calculated using the file "`H2.m`" for the UPBA RMS and "`H8.m`" for the Road-hold.

The population is then sorted and ranked via the NSGA-II algorithm. This is important because, given it is a multi objective optimization, the non-dominant sorting ensures a diverse solution. Then, the NSGA-II code implementation determines whether a stop condition has been reached. If it hasn't, the optimization function creates the next population and repeats the process. If either the maximum number of generations or stall generations has been reached, the simulation stop, the data is saved and the best individual is displayed.

All original code data is available on the code repository. The NSGA-II function is available in the reference link and in the Annex.

5 RESULTS AND DISCUSSION

The simulations and their results will be shown and discusses in this chapter. Table 5.1 contains a summary of all the simulations performed. Rows in cyan represent simulations in which only a single combination of parameters is analyzed. Rows in green represent simulations which are run with varying parameters for the purpose of optimization.

The term ”Standard” refers to the simultaneous evaluation of both the UPBA RMS and Road-hold metrics. The term ”Standard+” refers to the simultaneous evaluation of all relevant metrics, including the UPBA RMS, the UPBD RMS, the control metrics, and Road-hold metrics. ”L+B+I” refers to a system which is separately tested under a Linear rise, Bump and ISO B excitations.

In the context of the 1/2 vehicle model in Table 5.1, the term ”UPBD RMS” refers to both the upper body vertical and rotational displacement, while the acronyms Continuous (Cnt) and Hybridhook (HBH) are introduced for brevity reasons.

The procedures can be broadly divided into 2 major groups which are composed of 4 minor groups. The first major group, solely encompassing the group #1 of simulations, refers to the procedures performed for damper simulation, in which different rheological models were tested for fitness and convergence properties.

The second major group encompasses the minor groups #2, #3 and #4 of simulations. Group #2 refers to the optimization procedures which evaluated the effectiveness of the controllers when applied to a MR damper in a quarter vehicle simulation and compared it to a linear damper case. Group #3 of simulations refers to the simulations which evaluated the performance of selected optimized controllers against deterministic road obstacles. Group #4 analyses the same conditions of the #3 simulation group - an evaluation of the effectiveness of selected optimized controllers against deterministic road obstacles - but applied on a 1/2 vehicle model, evaluating the performance and observers whether or not the results differ significantly.

5.1 MR DAMPER SIMULATIONS

With the MR damper simulations, it was sought to ensure that the mathematical model chosen provided the most accurate behavior given the experimental data available and the simulation capabilities. Fluid simulations in the damper geometry were unfeasible due to both the lack of experimental data to use for comparison and the phenomenal computational power such simulations would require when performed to the extent necessary for an optimization.

Table 5.1. Simulation scheduling.

#	Model	Parameters	Damper model	Controller	Excitation	Metrics
1.1	Test bench	Best fit	Bingham MR	Passive	Time series	Abs error sum
1.2	Test bench	Best fit	Bouc-wen MR	Passive	Time series	Abs error sum
1.3	Test bench	Best fit	Wang MR	Passive	Time series	Abs error sum
1.4	Test bench	Best fit	Wang-II MR	Passive	Time series	Abs error sum
1.5	Test bench	Best fit	Wang MR	Passive	Sine+GWN	Convergence
1.6	Test bench	Best fit	Wang-II (1) MR	Passive	Sine+GWN	Convergence
1.7	Test bench	Best fit	Wang-II (2) MR	Passive	Sine+GWN	Convergence
1.8	Test bench	Type #1	Wang-II (1) MR	Passive	Sine+Bump	Convergence
1.9	Test bench	Type #1	Wang-II (2) MR	Passive	Sine+Bump	Convergence
2.1	1/4 vehicle	Type #1	Wang-II MR	Passive	ISO B	Standard
2.2	1/4 vehicle	Type #1	Wang-II MR	Cnt HBH	ISO B	Standard
2.3	1/4 vehicle	Type #1	Wang-II MR	LQR	ISO B	Standard
2.4	1/4 vehicle	Type #1	Wang-II MR	SDRE	ISO B	Standard
3.1	1/4 vehicle	Type #1	Ideal	Passive	L+B+I	Standard+
3.2	1/4 vehicle	Type #1	Wang-II MR	Cnt HBH	L+B+I	Standard+
3.3	1/4 vehicle	Type #1	Wang-II MR	LQR	L+B+I	Standard+
3.4	1/4 vehicle	Type #1	Wang-II MR	SDRE	L+B+I	Standard+
4.1	1/2 vehicle	Type #2	Ideal	Passive	L+B+I	Standard+
4.2	1/2 vehicle	Type #2	Wang-II MR	LQR	L+B+I	Standard+
4.3	1/2 vehicle	Type #2	Wang-II MR	SDRE	L+B+I	Standard+
4.4	1/2 vehicle	Type #2	Wang-II MR	Cnt HBH	L+B+I	Standard+

The available experimental data was limited to what had been ceded from the process in Silva *et al.* (2022), as performing further experiments would take too much time and require outside expertise to accomplish. As such, the damper model had to be both reasonably solvable in the time frame the future vehicle simulations would take place and to mimic the behavior of the experimental data as much as possible under the evaluated conditions.

To obtain the best possible combination of parameters a certain model could produce, a genetic optimization was performed until convergence was obtained. To obtain the best model, the results for the best case of each model were compared to one another. To determine if behavior in a vehicle simulation was consistent with the model in the case of the Wang and Wang-II model, a comparison test was ran in which two different formulations for the term v_m were used under force feedback condition.

5.1.1 Simulation procedures

For the simulations of the MR damper, two procedures were outlined: a general coefficient optimization defined by simulations #1.1-1.4 in Table 5.1 and a convergence test defined by simulations #1.5-1.6.

The constitutive models evaluated were the Bingham body, Kwok *et al.* (2007)'s Bouc-wen formulation, the original Wang model (Wang *et al.*, 2004) and the modified Wang-II model.

- The formula for the Bingham body model is equation (2.2);
- The Bouc-wen model is determined by equations (2.4), (2.6) and (2.7);
- The original Wang model equations are (2.11), (2.12), (2.13), (2.15) and (2.14);
- The formula for the Wang-II model are equations (2.21), (2.22) (2.12), (2.13), with (2.14) being in the optimization procedure and (2.16) being used in the convergence procedure;

The damper simulation under test bench settings was performed according to the procedures outlined in Section 3.2. The damper models in the optimization simulation battery were assumed to be under ideal test bench conditions, with their positions, velocity and acceleration being solely input variables. The output variable was the damper force. The damper models in the convergence simulation battery were under test bench conditions in which acceleration feedback was allowed, having their positions and velocity variables still being solely input variables, but its acceleration was allowed to take into account the effect of the damper's own force in it.

The coefficient optimization was performed according to the methods outlined in Section 3.6. Each evaluated damper model was subject to an optimization by genetic algorithm, with the final values for the model coefficients being determined at the end of the procedure.

5.1.2 Results

The results for the coefficients obtained with the genetic optimization are available in Table 5.2 for the Bingham model, Table 5.3 for the Bouc-wen model, Table 5.4 for the Wang model and Table 5.5 for the Wang-II model. The damper model optimization score results are in Table 5.6. The Table results can also be observed visually in Figures 5.2 and 5.1.

An important consideration is that the experimental data being used has no current variation. As such, any coefficient results for current dependent terms are possibly invalid. While not removed from the optimization, their value has been marked as such to avoid any confusion.

Table 5.2. Bingham body model optimized coefficients. Reproduced from Ferreira *et al.* (2023).

Constant	Value	Constant	Value
f_c (N)	1004.74	k (N/m)	$24.5 \cdot 10^3$
c (N s/m)	54.56	f_0 (N)	-0.91

Table 5.3. Bouc-wen model optimized coefficients. Reproduced from Ferreira *et al.* (2023).

Constant	Value	Constant	Value	Constant	Value	Constant	Value
n (adm)	$2.5 \cdot 10^7$	λ (adm)	577.50	μ (m/s)	-0.01	k (N/m)	577.50
α (N/m)	500.00	γ ($s^{n-1}m^{1-n}$)	-8.01	f_0 (N)	9.04	N/A	N/A
δ (1/m)	577.50	β ($s^{n-1}m^{1-n}$)	21.06	c (N s/m)	5052.84	N/A	N/A

Table 5.4. Wang model optimized coefficients. Red cells indicate the current dependent terms, which may be inaccurate. Adapted from Ferreira *et al.* (2023).

Constant	Value	Constant	Value	Constant	Value	Constant	Value
a_0 (adm)	$3.45{\cdot}10^4$	a_4 (s/m)	5.39	k_0 (adm)	3458.12	k_3 (adm)	1351.67
$a_1\ (m/s)^{-1}$	22.29	I_0 (amp)	-7.50	k_{1c} (adm)	67.38	k_4 (adm)	-0.1378
$a_2\ (amp)^{-1}$	0.038	I_1 (amp)	-1.10	k_{1e} (adm)	37.66	k_5 (adm)	0.3221
$a_3\ (amp)^{-1}$	-8.05	f_0 (N)	21.20	k_2 (adm)	1257.43	k_6 (adm)	$6.93{\cdot}10^{-3}$

Table 5.5. Wang-II model optimized coefficients. The coefficient γ was omitted due to it being rejected from the optimization. Red cells indicate the current dependent terms, which may be inaccurate. Adapted from Ferreira *et al.* (2023).

Constant	Value	Constant	Value	Constant	Value	Constant	Value
a_0 (adm)	$3.45{\cdot}10^4$	$a_4\ (m/s)^{-1}$	10.46	k_0 (adm)	3356.7	k_3 (adm)	1335.2
$a_1\ (m/s)^{-1}$	23.94	I_0 (amp)	-10,96	k_{1c} (adm)	67.41	k_4 (adm)	-0.1377
$a_2\ (amp)^{-1}$	-35.44	I_1 (amp)	14,80	k_{1e} (adm)	36.52	k_5 (adm)	0.3221
$a_3\ (amp)^{-1}$	-4.33	f_0 (N)	21.21	k_2 (adm)	1257.4	k_6 (adm)	$5.97{\cdot}10^{-3}$
$\eta_p\ (adm)$	1	$k_{cl}\ (N\ s/m)$	44,10	η_n (adm)	1.13	O (adm)	0.9718

Table 5.6. Genetic algorithm optimization final results lowest residuals. Adapted from Ferreira *et al.* (2023).

Model	Bingham	Bouc-wen	Original Wang	Modified Wang (Wang-II)
Residuals	29,8 $\cdot 10^4$ N	22,85 $\cdot 10^4$ N	7,07 $\cdot 10^4$ N	6,46 $\cdot 10^4$ N

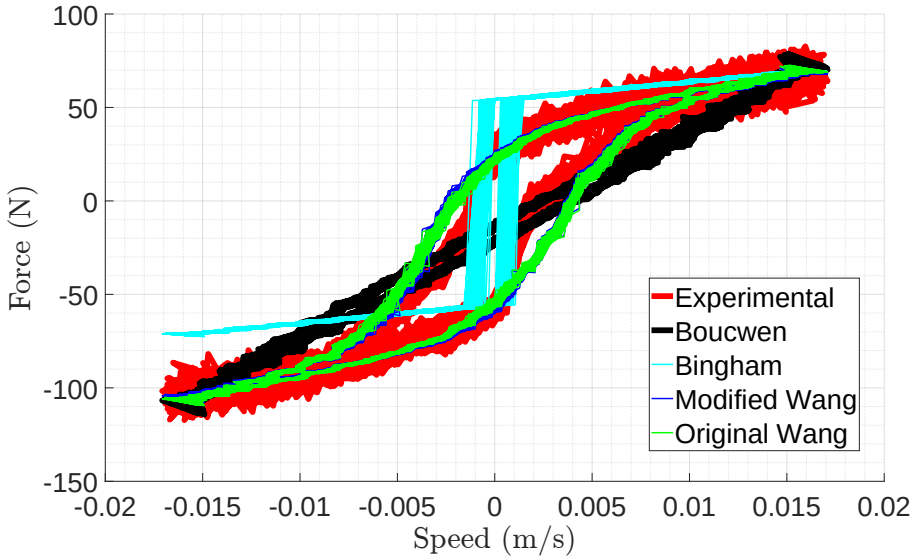

Figure 5.1. Results for the rheological functions, frequency domain. Adapted from Ferreira *et al.* (2023).

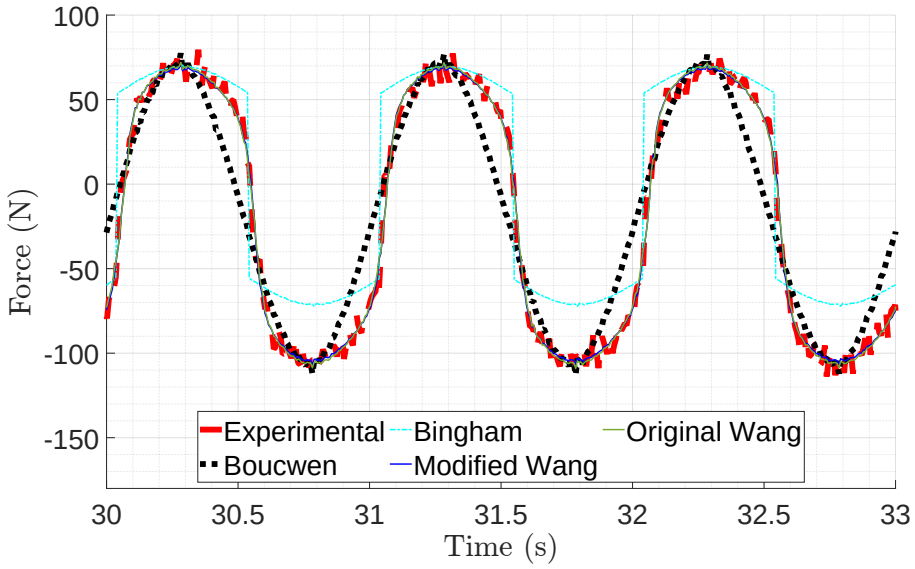

Figure 5.2. Results for the rheological functions, time domain. Adapted from Ferreira *et al.* (2023).

It can be observed the Wang-II formulation performed the best out of the contemplated models, followed by the original Wang formulation. The Bouc-wen formulation was unable to properly characterize the hysteresis loop seen in this MR damper characteristic curve, and the Bingham model lack of hysteresis contributed for a high total error. The Wang-II formulation showed an improvement of 8,6% error reduction, justifying its use.

Looking at the coefficients obtained for the Wang-II model, it can be seen that all parameters bar γ showed a different value from the assumed by the original Wang model. The γ parameter can be considered rejected, leaving the Wang-II model with 4 new degrees of freedom to a total of 20 total coefficients. An element noticed was the fact that most coefficients which remained unaltered were non dimensional, with the exception of the a_1 and f_0 coefficients. This might be because these two coefficients determine very tangible curve parameters. However, the lack of fit to curves with different current values might have led to spurious variation in some of the electric current based coefficients.

The results for the first v_m modification proposal experiment are in Figures 5.3 and 5.4.

As for the v_m formulation modification proposed, the for simulation results show that both damper models are equivalent under strictly steady-state sinusoidal excitations. However, when enough energy is added to the $\ddot{x}$ variable, such as in the form of white noise, the origination formulation quickly diverges. The new proposed formulation remains stable, as it is not mistakenly assuming the future velocity will be greater than it really is.

Another v_m formulation modification was also proposed. It trades off performance for better handling of short lived excitations. Its coefficients were obtained by performing an optimization solely on the coefficients of the v_m formulation. All other parameters were adopted as equal to those obtained for the Wang-II model optimization in Table 5.5. Because this v_m formulation seeks stability under transient conditions, this fit was performed on all the experimental data, not only the steady-state region. The results were as showcased in Table 5.7.

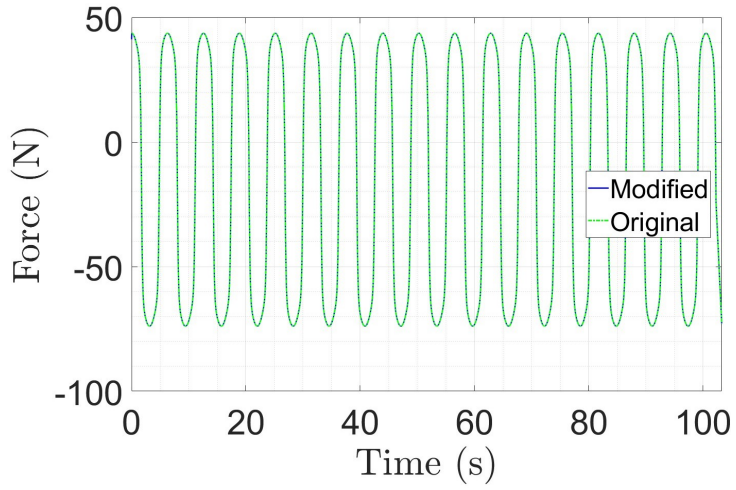

Figure 5.3. Comparison between original and modified formulations for Wang's damper model V_m parameter under a pure sine excitation. Reproduced from Ferreira *et al.* (2023).

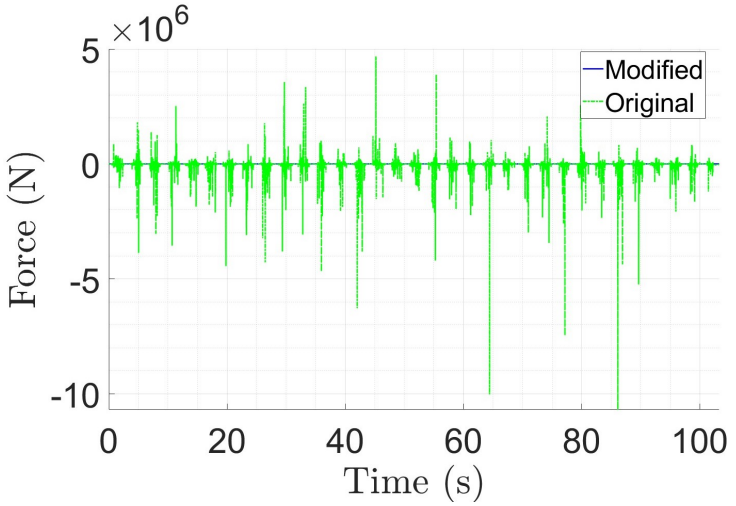

(a) Original and modified v_m.

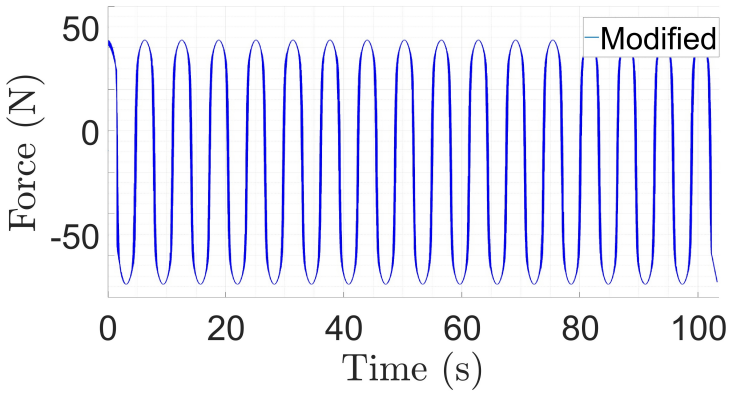

(b) Modified v_m only.

Figure 5.4. Comparison between original and modified formulations for Wang's damper model V_m parameter under a combined Sine and White noise excitation with feedback. Reproduced from Ferreira *et al.* (2023).

Quantity	C_1	C_2	C_3
Value	4.24	1.21	9.67

Table 5.7. Coefficients obtained for the second v_m formulation of the Wang-II model. Reproduced from Ferreira *et al.* (2025).

To first demonstrate that it is at least as stable as the first modified v_m proposed, the formulation was tested under the same conditions. The results for the Pure Sine excitation with no feedback are displayed in Figure 5.5, while the results for the Sine with added feedback excitations are displayed in Figure 5.6.

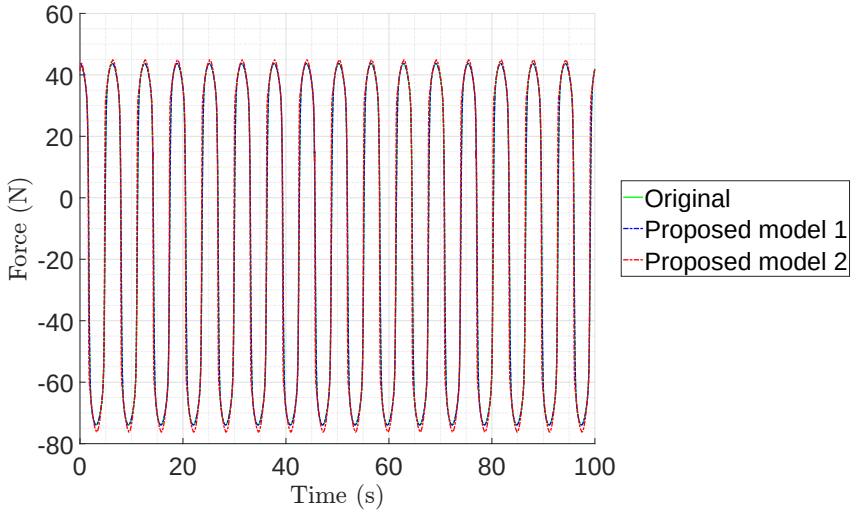

Figure 5.5. Comparison between original and modified formulations for Wang's damper model V_m parameter under a pure sine excitation.

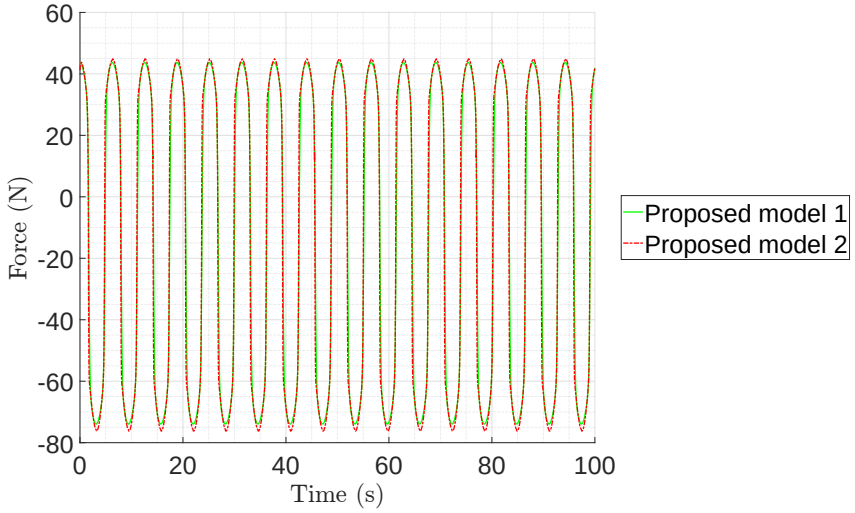

Figure 5.6. Comparison between the two modified formulations for Wang's damper model V_m parameter under a combined Sine and White noise excitation with feedback.

The second new formulation is able to remain stable under both scenarios, just as the first new formulation did. It does, however, show less of an agreement with Wang's original formulation under the pure Sine excitation. This performance difference is acceptable. Whether to use the first or the second modified formulation hinges on the capacity each formulation

has of handling all the modeling conditions that the studied vehicles will be exposed to. To demonstrate the difference between both models, they were exposed to a profile which is a superposition of a parabola and a sine wave, as seen in Figure 5.7. The results from this test are in Figure 5.8. The first v_m formulation under a pure sine wave has been added for comparison effects.

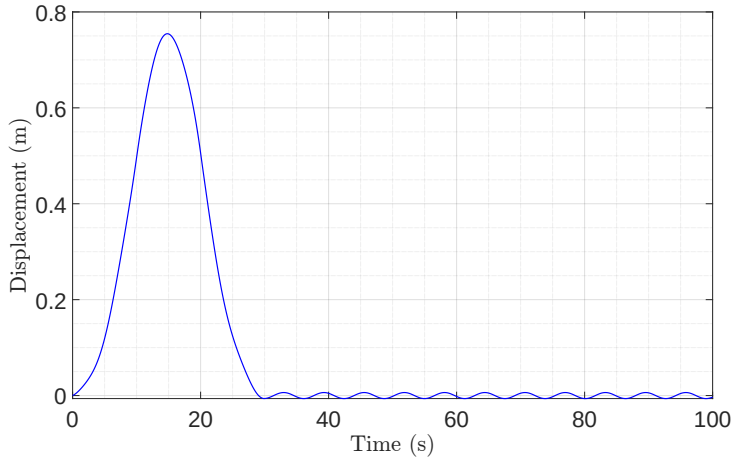

(a) Displacement profile.

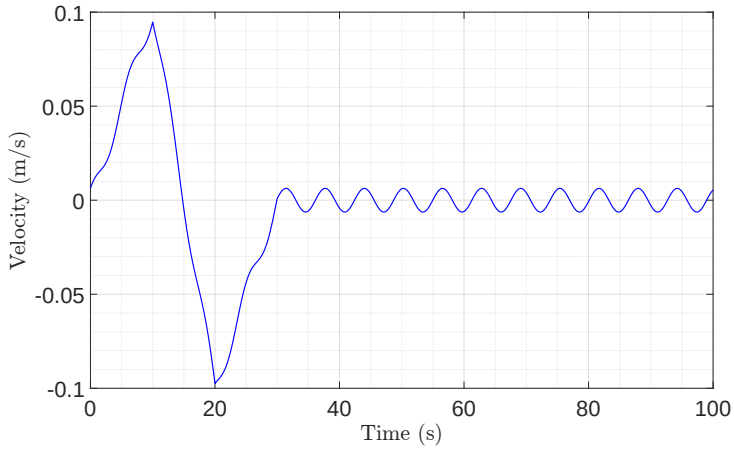

(b) Velocity profile.

Figure 5.7. Transient perturbation used for testing v_m formulations.

The results show that, after being exposed to the initial perturbation, the first v_m formulation force was permanently altered. The second v_m formulation, on the other hand, returned to normal after some time, matching the first simulation's result when not exposed to a transient perturbation. This case exemplifies the problem with the first formulation: transient events leave permanent marks on the damper model, as it has no mechanism for forgetting events. Model 1 is not fit for vehicle simulations which are not under steady state.

These results, while still being able to benefit from more studies, show that the new proposed Wang-II formulation, coupled with the v_m modification, is the best rheological model for the MR damper simulations out of all the contemplated models and should be used going forward. Although the first modified formulation is more accurate and delivers a better fit to the experimental data, the second modified formulation functions under more conditions while being

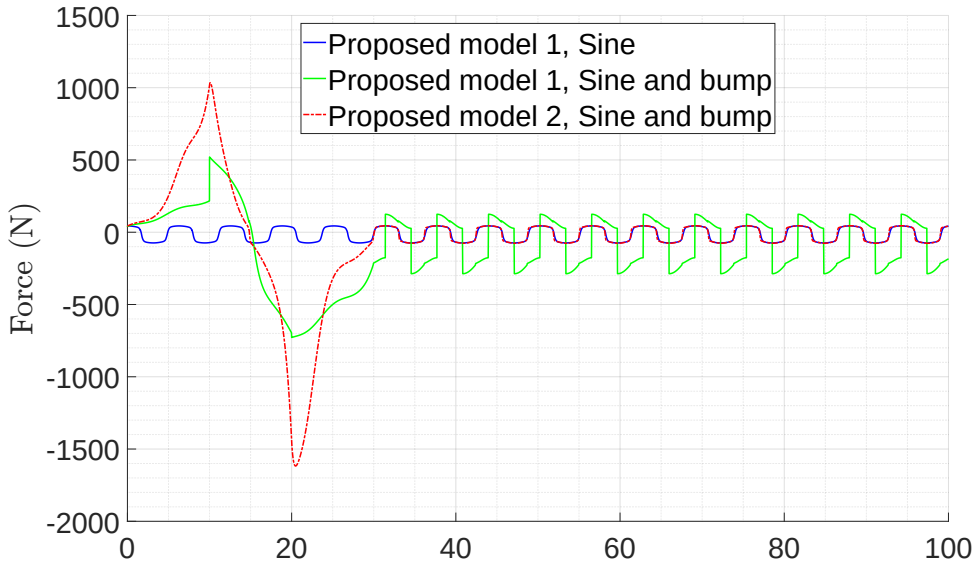

Figure 5.8. Difference between the behavior of the two v_m formulations on a feedback model going through a transient perturbation.

almost as accurate. Because of this, all vehicle simulations with the Wang-II model from here on will use the second v_m formulation. This model will be simply referred to as "Wang-II".

5.2 VEHICLE OPTIMIZATIONS

The vehicle optimization simulations sought to obtain the optimal combination of parameters for the proposed vehicles with respect to the Road-hold and UPBA RMS metrics. These vehicles were 1/4 vehicle models with either a passive damper or an MR damper under different controllers. This was accomplished by performing a genetic optimization on each vehicle case. The metrics were calculated by simulating the vehicle models and compiling the simulation results. The vehicles were subjected to a non-deterministic road profile following a 1st order approximation of an ISO grade B road.

The results for each case will be displayed and then commented upon. The presentation order will be for the passive case, the MR Hybridhook case, the MR LQR case, and finally the MR SDRE case.

The bounds for the optimization procedure are present in Table 5.8 for the passive model, in Table 5.9 for the MR Hybridhook model, in Table 5.10 for the MR LQR model and in Table 5.10 for the MR SDRE model. The SDRE coefficient ranges are valid for both the constant and x dependent version of the parameters.

Table 5.8. Bounds and variables for the second optimization procedure, vehicle with passive damper.

Variable	Upper bound	Lower bound	Variable	Upper bound	Lower bound
c_l	10^6	10^{-2}	k_s	10^8	10^2

Table 5.9. Bounds and variables for the optimization procedure, vehicle with MR damper and Hybridhook controller.

Variable	Upper bound	Lower bound	Variable	Upper bound	Lower bound
C_{hybrid}	10^7	10^0	κ	1	0
c_l	10^6	10^{-2}	f_0	$214.8{\cdot}5^2$	$214.8{\cdot}5^{-2}$
k_s	10^8	10^2	a_1	$1.75{\cdot}2^1$	$1.75{\cdot}2^{-1}$

Table 5.10. Bounds and variables for the second optimization procedure, vehicle with MR damper and LQR or SDRE controller.

Variable	Upper bound	Lower bound	Variable	Upper bound	Lower bound
$\boldsymbol{U}_{i,j}$ $(i \neq j)$	10^6	-10^6	$\boldsymbol{U}_{i,i}$	10^6	10^{-4}
R	10^{12}	10^{-4}	f_0	$71.6{\cdot}5^2$	$71.6{\cdot}5^{-2}$
c_l	10^6	10^{-2}	a_1	$1.75{\cdot}2^1$	$1.75{\cdot}2^{-1}$
k_s	10^8	10^2			

5.2.1 Simulation procedures

All 1/4 vehicle simulations shared certain parameters in common. These were the vehicle and damping parameters. Any parameter in the tables which is an optimization variable is superseded by its resultant value when analyzing an optimized vehicle.

The 1/4 vehicle model was dubbed vehicle type #1. The vehicle type #1 parameters were as showcased in Table 5.11. The vehicle type #1 parameters are used for all optimization procedures.

Table 5.11. Data for vehicle model type #1. Suspension variables are omitted due to being optimized in all scenarios.

Parameter	Value	Parameter	Value
M_s (kg)	300	M_u (kg)	30
K_u (N/m)	200 000		

The MR damper was modeled according to the results of Section 5.1. The model chosen was the Wang-II model, described by equations (2.21), (2.22) (2.12), (2.13) and (2.16). To enhance the comparability to the literature, the damper parameters used were the original Wang model parameters in (Wang *et al.*, 2004). The damper data is in Table 5.12. While a very similar set of simulations was performed in Ferreira (2022) and Ferreira *et al.* (2022), due to difference in simulation parameters, models and measurement techniques, it was not possible to directly compare the results between works.

The 1/4 vehicle simulation was performed in line with the information presented in Section 3.1. The vehicle was simulated in the time domain according to equation (2.32). The general numerical solution procedure was the one described in Section 4.1. The simulation parameters were the ones described in Section 3.7 and Table 3.4. The controller formulations were set up as described in Section 3.5.

Table 5.12. Coefficients used for the Wang-IIb model in the vehicle simulation. Variables in green are optimized in all scenarios, and their nominal values are for reference purposes. Adapted from Ferreira *et al.* (2025).

Constant	Value	Constant	Value	Constant	Value	Constant	Value
a_0 (adm)	1300	$a_4\ (m/s)^{-1}$	4.60	k_0 (adm)	112.5	k_3 (adm)	2.90
$a_1\ (m/s)^{-1}$	1.75	I_0 (amp)	0.05	k_{1c} (adm)	3.2	k_4 (adm)	0.095
$a_2\ (amp)^{-1}$	2.85	I_1 (amp)	0.08	k_{1e} (adm)	5.2	k_5 (adm)	0.65
$a_3\ (amp)^{-1}$	1.55	f_0 (N)	71.6	k_2 (adm)	19.4	k_6 (adm)	0.12
η_p (adm)	1	$k_{cl}(N\ s/m)$	0	η_n (adm)	1	O (adm)	1
C_1 (adm)	4.24	C_2 (adm)	1.21	C_3 (adm)	9.67		

5.2.2 Passive optimization results

The results of the passive optimization are available in Figure 5.9. They are compared to the results obtained for the validation data of the numerical system, which is a parametric exploration of the coefficients.

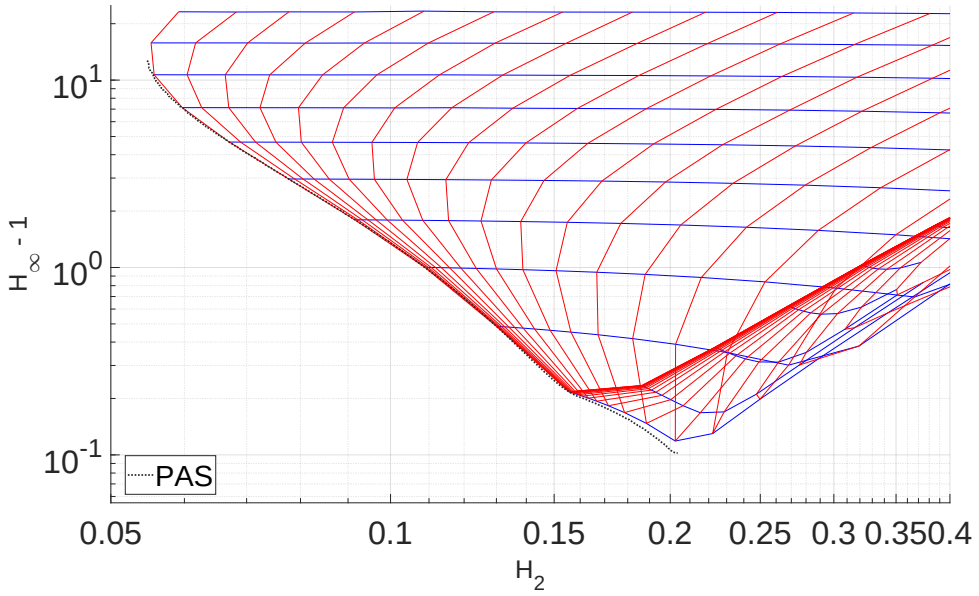

Figure 5.9. Results for the optimization of the passive system. Adapted from Ferreira *et al.* (2025).

The optimization results match the validation data. This demonstrates the optimization procedure is functioning correctly, and provides a performance baseline for all further optimizations. The results converged in just 25 generations. This is due to the low number of parameters. The line fit for the coefficients returned the expression $log_{10}(H_\infty) = log_{10}(H_2) \cdot (-3.52) - 3.44$.

Table 5.13. Table of the correlation coefficients between the variables and the metrics for the Passive controller.

	Passive optimization results	
Variable	H_2	$H_\infty - 1$
$log_{10}(k_s)$	0.81	-0.46
$log_{10}(c_l)$	0.95	-0.94

The correlation results demonstrate that the Handling and Comfort metrics are directly proportional to the damping and stiffness of the suspension in the Pareto front region. This direct relationship will prove important in other cases, but it is exceptionally strong in the Passive system, where no other variables can affect the system. An important nuance is that these results do not show minimizing the damping will always lead to better comfort, for example. It only shows that, amongst the combinations which are optimal, a lower damping leads to more comfort and less handling. Decreasing the damping beyond the optimal parameter region may yield worse results.

5.2.3 Hybridhook optimization results

The results of the Hybridhook optimization are available in Figure 5.10. They are compared to the results obtained for the Passive optimization. An analysis of the optimized coefficients are available in Table 5.14.

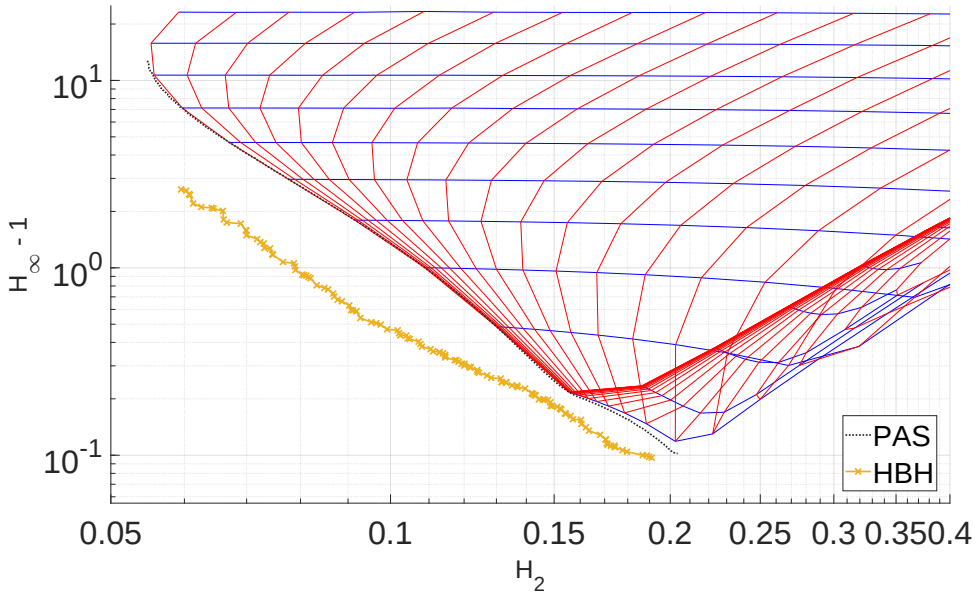

Figure 5.10. Results for the optimization of the Hybridhook system. Adapted from Ferreira *et al.* (2025).

As can be observed, the Hybridhook results dominate the Passive results. The line fit for the coefficients returned the expression $log_{10}(H_\infty) = log_{10}(H_2) \cdot (-2.79) - 3.07$. Using the procedure described in Section 3.4.2 with the Hybridhook and Passive results, these optimization results show an improvement around 79.2% less steep for the Hybridhook over the Passive results, and a baseline improvement to about 89.2%. This is reflected by the fact that the Hybridhook results have a small edge over the Passive results for the systems in the region with better Roadholding, but the gap widens as comfort is prioritized.

The correlation table demonstrates that, for the Hybridhook system, the c_l and k_s are still very directly important, even if not as correlated to performance as they were for the passive system. The MR damper variables were also very important, with the a_1 variable having a very noticeable impact on performance comparable to the passive suspension elements. The

Table 5.14. Table of the correlation coefficients between the variables and the metrics for the Hybridhook controller.

	Hybridhook optimization results				
Variable	H_2	$H_\infty - 1$	Variable	H_2	$H_\infty - 1$
C_{hybrid}	-0.975	0.775	$log_5(f_0)$	0.665	-0.470
κ	0.341	-0.652	$log_2(a_1)$	-0.845	0.848
$log_{10}(k_s)$	0.945	-0.705	$log_{10}(c_l)$	0.890	-0.970

controller variables were both important, with the C_{hybrid} variable having a nearly 1:1 correlation to H_2 performance. The variable κ, which determines whether the system is more akin to a Skyhook or Groundhook controller, surprisingly did not have an easily observed impact. Rather than simply transitioning from Skyhook to Groundhook to prioritize handling over comfort, it seems the relationship is more complex than that.

5.2.4 LQR optimization results

The results of the passive optimization are available in Figure 5.9. They are compared to the results obtained for the Passive and the Hybridhook optimizations. An analysis of the optimized coefficients are available in Table 5.15.

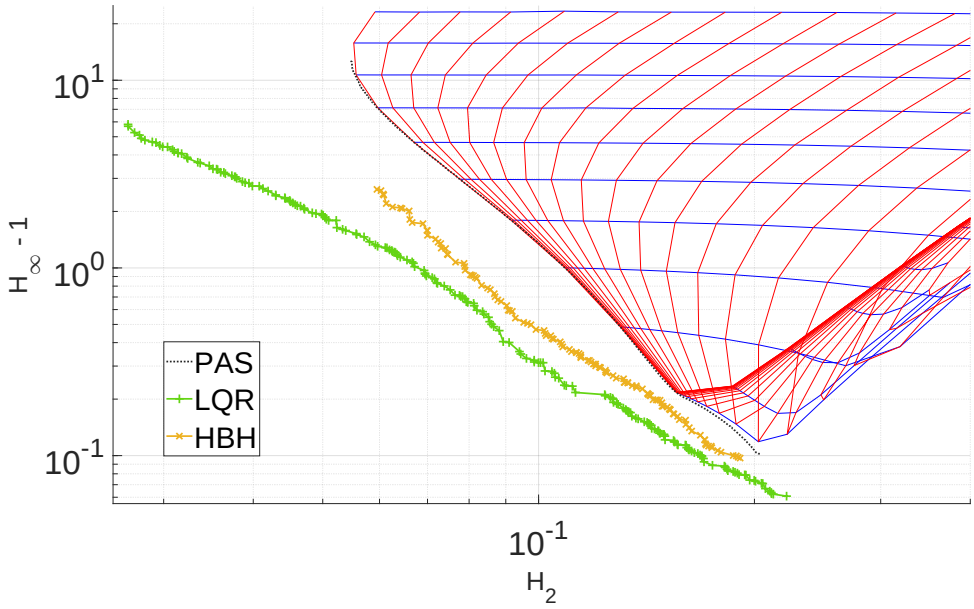

Figure 5.11. Results for the optimization of the LQR system. Adapted from Ferreira *et al.* (2025).

The optimization results show the LQR improved the system to an even greater extent than the Hybridhook controller, dominating it along with the Passive results. The line fit for the coefficients returned the expression $log_{10}(H_\infty) = log_{10}(H_2) \cdot (-2.227) - 2.739$. This is an improvement to around 79.6% of the baseline Passive performance, with a curve 64.6% less steep for the LQR system. This has the same consequences as it did for the Hybridhook system, where the performance gap widens as comfort is given more priority.

Table 5.15. Table of the correlation coefficients between the variables and the metrics for the LQR controller. Cells in green are those which showed no significant correlation in a linear scale, but did so in a log scale. Reproduced from Ferreira *et al.* (2025).

	LQR optimization results				
Variable	H_2	$H_\infty - 1$	Variable	H_2	$H_\infty - 1$
R	0.885	-0.618	$U_{3,3}$	-0.334	0.468
$U_{1,1}$	-0.454	.358	$U_{4,3}$	0.532	-0.263
$U_{2,1}$	-0.704	0.492	$U_{4,4}$	0.624	-0.718
$U_{3,1}$	0.802	-0.402	$log_{10}(k_s)$	0.949	-0.793
$U_{4,1}$	0.966	-0.843	$log_5(f_0)$	-0.547	-0.652
$U_{2,2}$	0.747	-0.588	$log_2(a_1)$	-0.547	0.411
$U_{3,2}$	-0.299	0.000	$log_{10}(c_l)$	0.944	-0.909
$U_{4,2}$	0.489	-0.626			

The correlation table reveals some variables have an impact more directly than others. The results obtained for the Hybridhook are still valid for the LQR controller: k_s and c_l are both very important for the system's performance, even if the MR damper is improving its behavior, and the MR damper parameters do have a noticeable impact on performance, even if not as directly. This time, a_0 was not as directly impactful on performance, possibly due the number of parameters or possibly because the LQR controller has more options for compensating it, making its value own its own less less impactful than its value relative to other variables.

The $U_{i,j}$ coefficients demonstrate a spread in direct contributions. $U_{4,1}$ had the most direct impact on the metrics, being strongly associated with the H_2 and negatively associated with the H_∞. Most values had a moderate direct relationship with the metrics, and a few, like $U_{3,2}$, had very little. However, whether this means that $U_{3,1}$ has no impact or that it simply is not linearly correlated with the metrics has not been answered.

For all variables, nearly all values were close to the mean, with only values in extreme percentiles showing more deviations. Using a k-means algorithm, the presence of clusters has also been detected. As such, its likely that such extreme values belong to certain parameter subgroups in which their unusual value compensates for some difference.

5.2.5 SDRE optimization results

There were two optimizations performed on the SDRE controller, one with variable weight matrices $\boldsymbol{Q}(\boldsymbol{x})$ and $\boldsymbol{R}(\boldsymbol{x})$, and one with constant weight matrices $\boldsymbol{Q}$ and $\boldsymbol{R}$. The results of the SDRE optimization with static weight matrices are available in Figure 5.12, while the results of the one with variable weight matrices are available in Figure 5.13. They are compared to the results obtained for the Passive, the Hybridhook and the LQR optimizations. An analysis of the optimized coefficients are available in Table 5.16.

The first optimization was considered converged in 100 generations, while the second optimization was determined as converged in 120. The first optimization succeeded in outperforming the Passive case for most of the domain, but not all. The second one failed. Its unclear

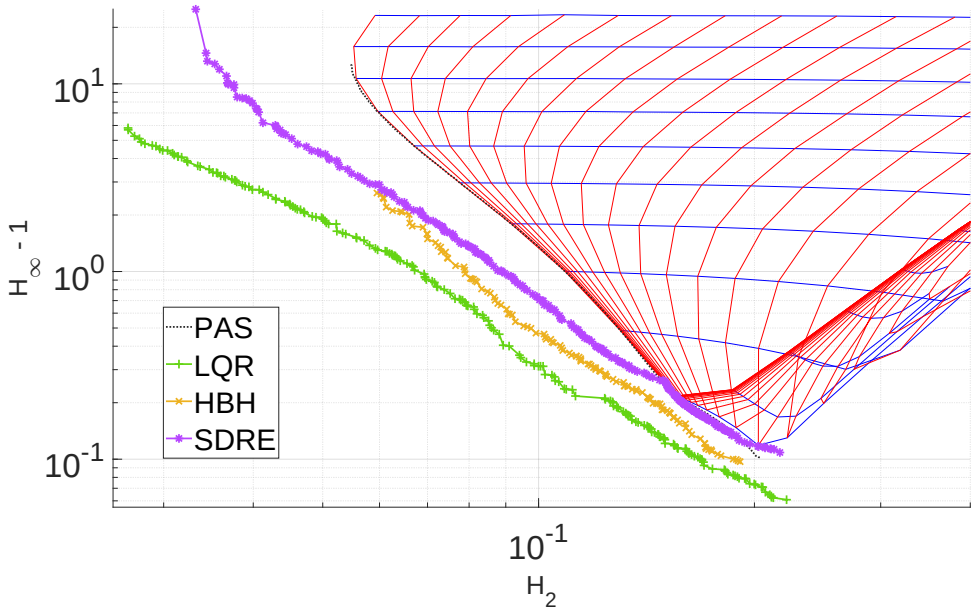

Figure 5.12. Results for the optimization of the SDRE system with constant weight matrices. Adapted from Ferreira *et al.* (2025).

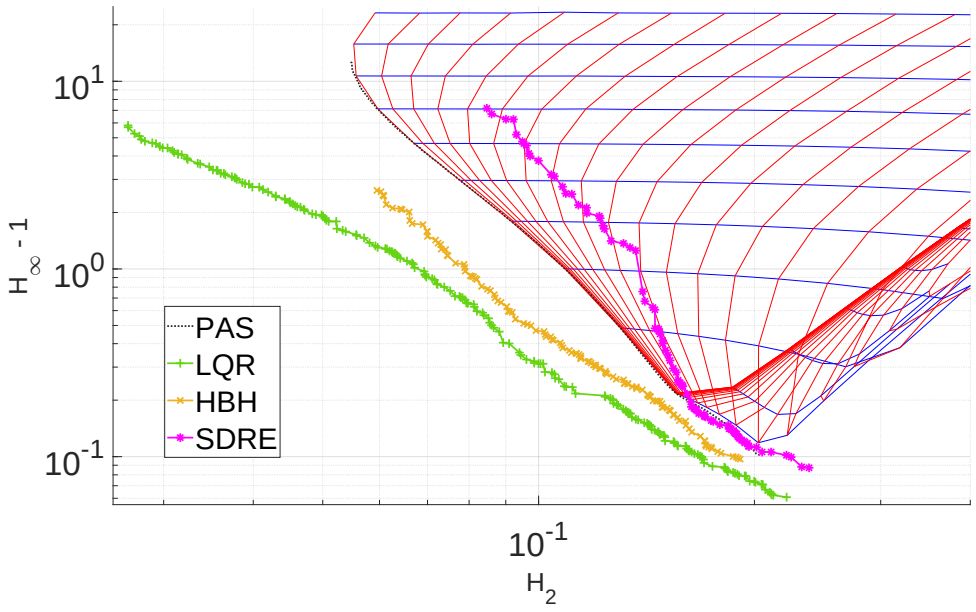

Figure 5.13. Results for the optimization of the SDRE system with variable weight matrices. Adapted from Ferreira *et al.* (2025).

as to why. Possible reasons are:

- Low number of individuals for number of decision variables caused premature convergence into local minima;
- The function $\dot{f}(x)$ is not a good candidate for controlling weight matrices;
- The $\boldsymbol{Q}(\boldsymbol{x})$ and $\boldsymbol{R}(\boldsymbol{x})$ forms chosen were not good;
- The SDRE parametrization chosen is not very effective for the problem at hand;

All but the last one do not apply to the first optimization, as it had constant weight matrices and the same number of coefficients as the LQR optimization, but both failed to perform better than their alternatives, the Hybridhook and LQR. Because the second optimization failed to a greater extent, it is possible more than one of these issues are true: the standard parametrization is not effective for this problem, which was compounded by poor weight function choices and premature convergence.

Because the second optimization was a complete failure, only the first optimization results will be analyzed further. This decision has also been made based on premature analysis of the case studies of Section 5.3, which also returned unremarkable results. From here on, the first optimization results for the SDRE controlled suspension will be simply referred to as the SDRE optimization results.

The line fit for the coefficients returned the expression $log_{10}(H_\infty) = log_{10}(H_2) \cdot (-2.66) - 2.81$. This is an improvement to around 82% of the baseline Passive performance, with a curve 76% less steep for the SDRE system. This has the same implications of the LQR and Hybridhook results, of a performance gap which widens as comfort is prioritized, but unlike those two, the performance of the SDRE actually meets and even gets dominated by the Passive Pareto front. The same is true for the Hybridhook system, which eventually gets dominated by the SDRE system, but because the Hybridhook front ends right before the region where the two would meet, this is not visible in the results.

Because the baseline improvement as well as the steepness of the curve are lower than the Hybridhook, the SDRE curve should, in theory, dominate it. However, this is a linear approximation of the curve, which does not fully capture its shape.

Table 5.16. Table of the correlation coefficients between the variables and the metrics for the SDRE controller.

	SDRE optimization results				
Variable	H_2	$H_\infty - 1$	Variable	H_2	$H_\infty - 1$
R	0.873	-0.453	$U_{3,3}$	-0.899	0.470
$U_{1,1}$	-0.852	0.413	$U_{4,3}$	-0.845	0.398
$U_{2,1}$	0.764	-0.321	$U_{4,4}$	0.813	-0.375
$U_{3,1}$	-0.704	0.292	$log_{10}(k_s)$	-0.178	-0.195
$U_{4,1}$	0.872	-0.449	$log_5(f_0)$	0.634	-0.366
$U_{2,2}$	0.852	-0.440	$log_2(a_1)$	0.909	-0.595
$U_{3,2}$	0.778	-0.318	$log_{10}(c_l)$	0.913	-0.886
$U_{4,2}$	0.825	-0.385			

Compared to the LQR, some variables had their impact changed. $U_{4,1}$ was no longer the most directly impactful control term, with $U_{3,3}$ taking its place. Most controller parameters remained at a relatively moderate level of linear association with performance. The signals of $U_{2,1}$, $U_{3,1}$, $U_{3,2}$, $U_{4,3}$ were flipped. The variable k_s had a negative association for both comfort and safety, which is atypical given it was positively associated with the H_2 and negatively associated with the H_∞ for all other controllers. Inspecting the variables, k_s was the minimal value of 0,01 N/m for all values. It seems the SDRE system performed better with little to no

spring stiffness.

The variables also clustered around their means with some outliers having extreme values, and clustering has been detected with k-means algorithms.

5.3 QUARTER VEHICLE CASE STUDIES

The optimization of the vehicles was a success. However, its results have some limitations: they were carried out under specific circumstances, that of a random road profile generated by a 1st order white noise filter for an ISO B grade PSD. Furthermore, they were analyzed as aggregate quantities, and individual results were not evaluated. This motivated additional tests to be carried out.

First, three solutions were picked from each optimization for an in-depth analysis. They were chosen to represent three different ways to design the vehicle's suspension: one focused on Handling, another with focus on Comfort focused and a design aimed at Balancing both qualities. Then, their UPBD, UPBA and LWBD frequency domain results for an ISO B random road excitation were individually analyzed according to the parameters in Table 3.4. Finally, the designs were then subjected to two transient road vibrations: a Linear Rise and a Bump, which sought to represent a road curb and a speed bump. The obstacle properties are available in Table 3.5. Their results were inspected in the time domain. Its control and command statistics were also analyzed according to the metrics laid out in Section 3.4, and are presented after all other analyses have been carried out.

The selection criteria for each design case was their Roadhold. The Comfort oriented vehicle is the solution whose Roadhold is closest to 1.8, the Balanced vehicle is the one whose Roadhold is closest to 0.5, and the Handling oriented vehicle is the one whose Roadhold is closest to 0.17. This was done so that similar solutions could be compared for each optimization, with the differences in the comfort metric being highlighted by the equivalent Roadhold performance. The values of 1.8, 0.5 and 0.17 were arbitrarily picked based on the perception of what entailed to a Comfort, Balanced and Handling oriented vehicle in the final optimization results.

The case studies names' will be shortened to Han, Com and Bal in the figures. The chosen designs points are displayed in Figure 5.14, and their parameters are displayed on Tables 5.17, 5.18, 5.19, and 5.20.

Table 5.17. System parameters' gene values for the Case studies, Passive. Adapted from Ferreira *et al.* (2025).

	Variable	k_s	c_l	H_2	$H_\infty - 1$
Passive	Handling	3.66	3.45	0.17	0.17
	Balanced	2.00	3.26	0.13	0.50
	Comfort	2.00	2.95	0.09	1.78

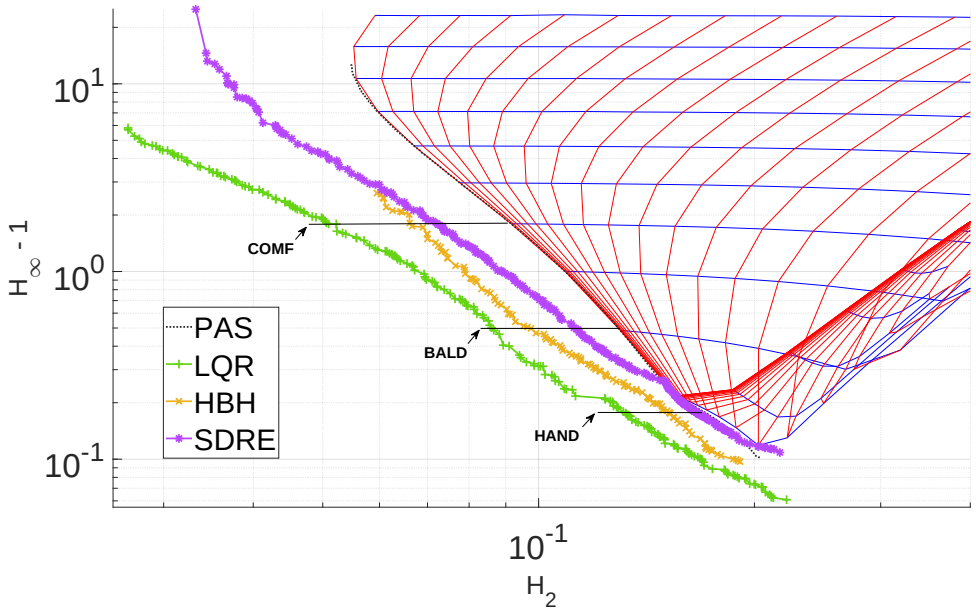

Figure 5.14. Case studies points for each suspension control scheme.

Table 5.18. System parameters' gene values for the Case studies, Hybridhook controller.

	Variable	C_{hybrid}	κ	k_s	$log_5(f_0)$	$log_2(a_1)$	c_l	H_2	$H_\infty - 1$
Hybridhook	Handling	3.81	1.00	4.28	-0.25	0.24	3.11	0.15	0.17
	Balanced	4.20	1.00	3.80	-0.27	0.46	2.80	0.10	0.50
	Comfort	4.29	0.97	3.63	-0.30	0.52	2.28	0.07	1.78

Table 5.19. System parameters' gene values for the Case studies, LQR controller. Adapted from Ferreira *et al.* (2025).

	Variable	R	$U_{1,1}$	$U_{2,1}$	$U_{3,1}$	$U_{4,1}$	$U_{2,2}$	$U_{3,2}$	$U_{4,2}$	$U_{3,3}$
LQR	Handling	3.47	8.35	3.36	-7.48	7.04	6.29	-1.68	0.75	5.52
	Balanced	3.54	8.58	4.28	-7.89	6.82	6.54	-1.41	1.10	5.39
	Comfort	2.93	8.45	4.01	-7.74	6.04	5.57	-1.72	0.66	6.09
	Variable	$U_{4,3}$	$U_{4,4}$	k_s	$log_5(f_0)$	$log_2(a_1)$	c_l	H_2	$H_\infty - 1$	N/A
	Handling	4.49	1.63	3.63	-1.38	0.04	3.13	0.13	0.17	N/A
	Balanced	3.06	1.44	3.44	-1.14	0.14	2.76	0.09	0.50	N/A
	Comfort	3.00	1.28	2.91	-1.31	0.32	2.41	0.05	1.79	N/A

Table 5.20. System parameters' gene values for the Case studies, SDRE controller.

	Variable	R	$U_{1,1}$	$U_{2,1}$	$U_{3,1}$	$U_{4,1}$	$U_{2,2}$	$U_{3,2}$	$U_{4,2}$	$U_{3,3}$
SDRE	Handling	9.43	3.16	4.23	-7.13	9.68	8.11	-7.70	3.58	0.50
	Balanced	1.64	9.75	-0.88	-6.42	-5.40	2.33	-9.53	-7.91	1.66
	Comfort	0.39	9.75	0.17	-5.55	-4.60	2.10	-9.34	-8.00	2.01
	Variable	$U_{4,3}$	$U_{4,4}$	k_s	$log_5(f_0)$	$log_2(a_1)$	c_l	H_2	$H_\infty - 1$	N/A
	Handling	-7.54	3.87	3.05	-1.91	0.80	3.40	0.17	1.17	N/A
	Balanced	-0.54	1.55	3.57	-2.00	-0.44	3.13	0.11	1.50	N/A
	Comfort	-1.03	1.70	3.35	-2.00	-0.20	2.78	0.07	2.80	N/A

5.3.1 Passive case studies

The passive optimization results are independently shown in this section to establish a baseline for the results of the optimized controllers.

5.3.1.1 ISO results

The frequency domain quarter vehicle results for the ISO excitation are in Figures 5.15a, 5.15b and 5.15c.

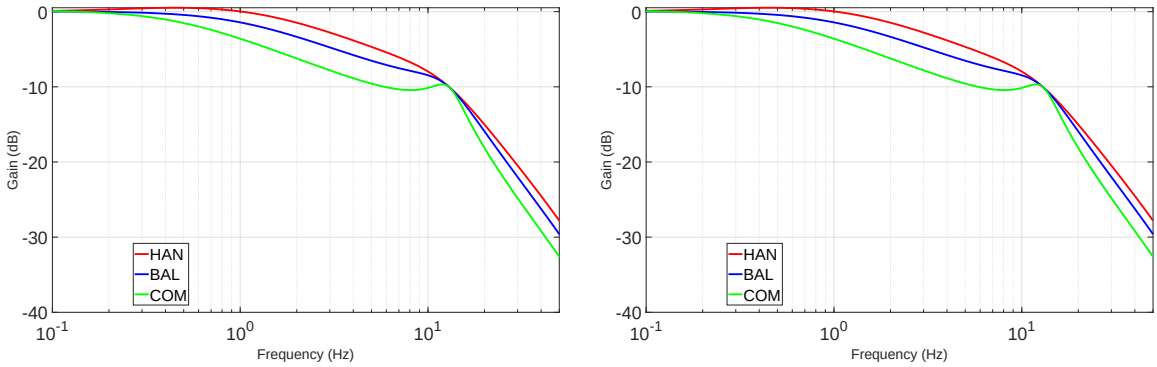

(a) UPBD

(b) UPBA

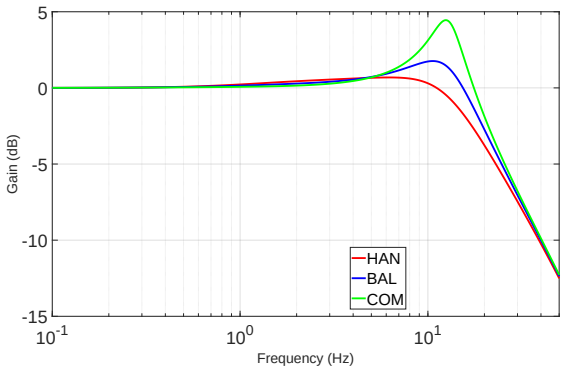

(c) LWBD

Figure 5.15. Frequency domain quarter vehicle response on a passive system under an ISO excitation. Adapted from Ferreira *et al.* (2025).

The results in Figure 5.15c show that, for the unsprung mass, the frequency with most resonance is around 10 Hz. The comfort oriented vehicle has a very pronounced peak gain, while the Handling system barely has a discernible peak. The results for the sprung mass displacement in Figure 5.15a are nearly identical to those of the acceleration. While the optimization focused on the UPBA, these results might indicate that the optimization might naturally transfer to the displacement. Lastly, the results in Figure 5.15b show that sprung mass main resonance is around 1 Hz for the Handling oriented vehicle to 0.1 Hz for the Comfort oriented vehicle. The sprung mass gain also sees a peak around the unsprung mass main frequency, but it has an overall magnitude far lower than the low frequency gain and as such has a minor impact on the RMS.

As such, the two resonance frequencies for the passive system are around 1 Hz and 10 Hz, with the higher frequency being associated with a greater gain on the tire and the lower with a greater gain on the chassis.

5.3.1.2 Bump results

The Bump excitation results are laid out in Figures 5.16a, 5.16b, 5.16c and 5.16d.

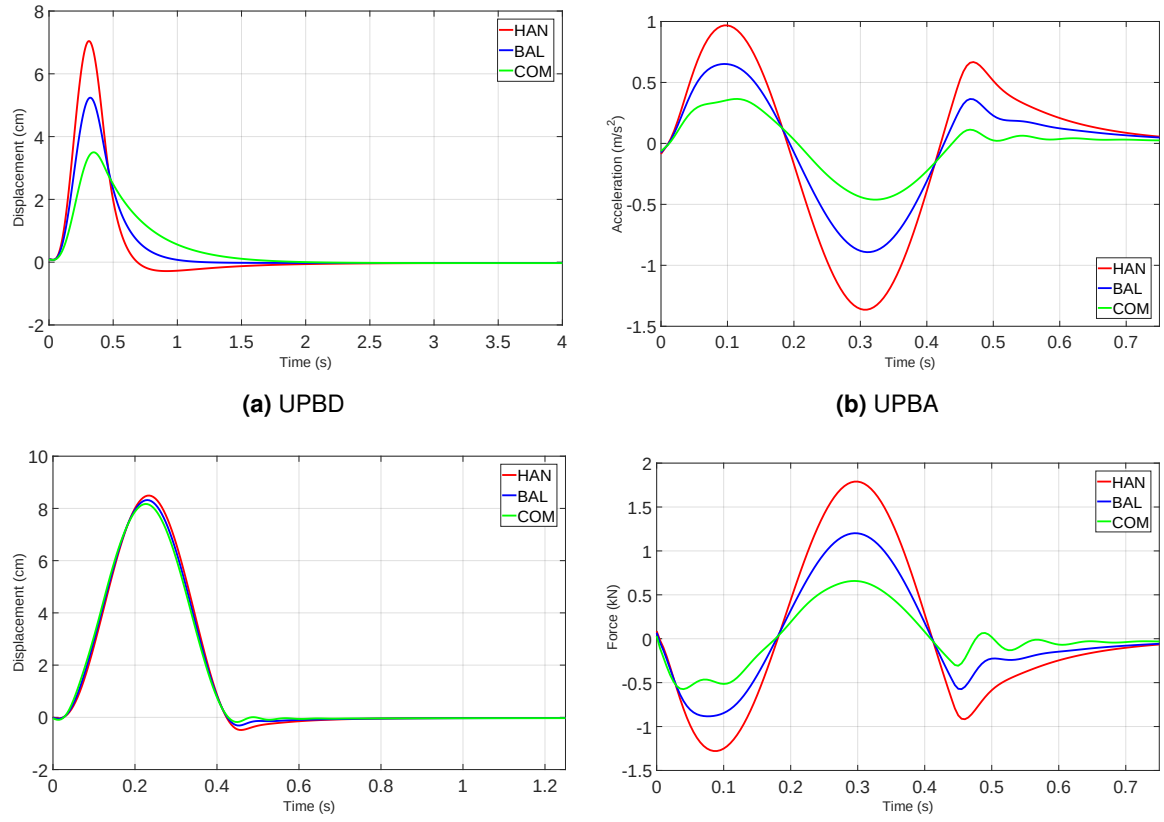

(a) UPBD **(b)** UPBA

(c) LWBD **(d)** Contact Force

Figure 5.16. Time domain quarter vehicle response on a passive system over a bump obstacle. Adapted from Ferreira *et al.* (2025).

The Contact force results in Figure 5.16d show the Comfort case outperforming the other cases, which is unexpected given this is a handling measure.

The LWBD results in Figure 5.16c are not very visually distinct from one another, but seem to confirm that the Comfort case had better performance in the handling characteristics. The UPBA results in Figure 5.16b show that the Comfort case had better results in the comfort metrics as well. The UPBD results in Figure 5.16a also confirm what the acceleration results showed, a better comfort performance for the Comfort controller in the comfort metrics.

In the Bump simulations, a counterintuitive result can be identified: The Comfort oriented vehicle performed better in all measures. It had lower Contact forces, lower accelerations and lower displacements. Given the higher Roadhold exhibited by the vehicle, this might seem odd. However, a closer analysis of the tire displacement gain in Figure 5.15c explains this

phenomena: while the Comfort has a higher peak gain at 10 Hz, it actually has a smaller gain up until around 5 Hz. Since this obstacle geometry is described by a cosine with a frequency of about 2,41 Hz, the Comfort controller is actually the best overall in the analyzed region. The frequency of 5 Hz is only attained for these Bump dimensions once the vehicle reaches 66,6 Km/h. Even then, the Comfort controller high gain at 10 Hz can be seen in the form of smaller, higher frequencies oscillations in the Contact Force.

These results show that, even if the vehicle is optimized for a certain scenario, changing the scenario can create different demands which do not agree with the optimization's definition of optimality.

5.3.1.3 Linear Rise results

The Linear Rise excitation results are laid out in Figures 5.17a, 5.17b, 5.17c and 5.17d.

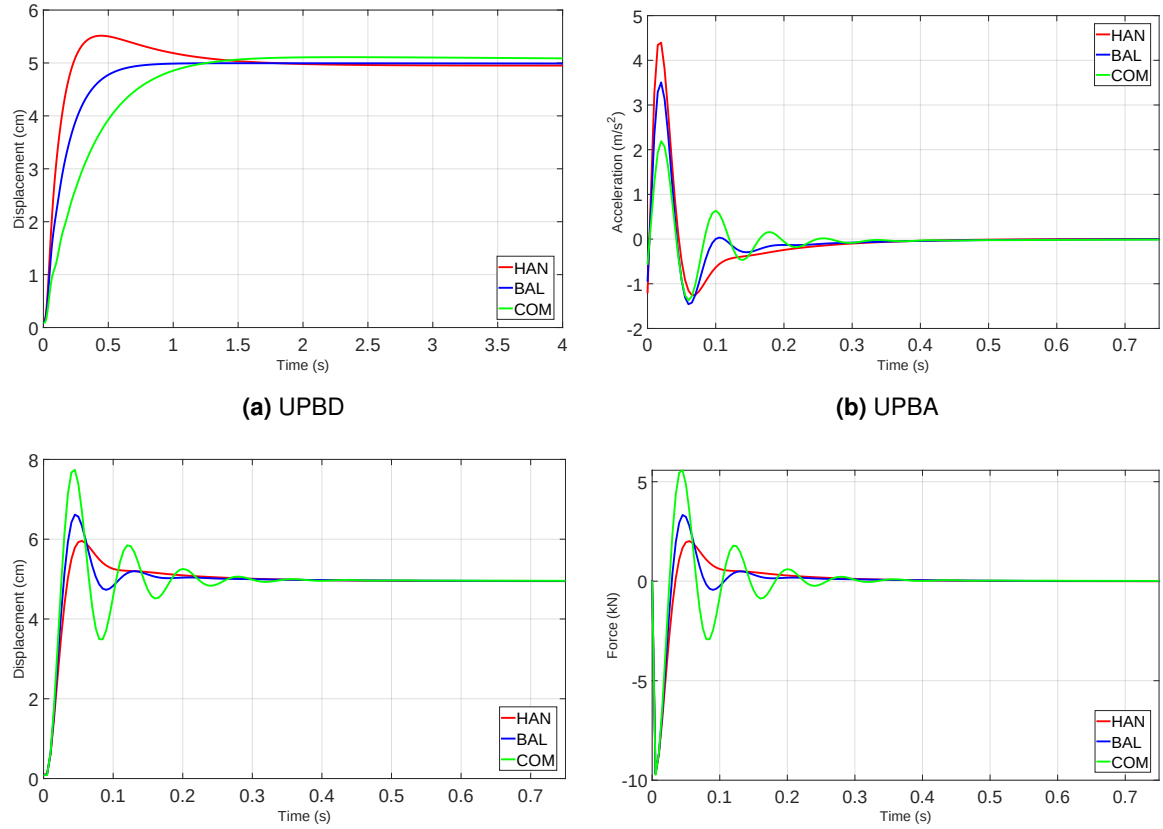

(a) UPBD

(b) UPBA

(c) LWBD

(d) Contact Force

Figure 5.17. Time domain quarter vehicle response on a passive system over a linear rise obstacle. Adapted from Ferreira *et al.* (2025).

The UPBD in Figure 5.17a shows that the Comfort cases have a gentler rise, but a longer settling time, with the Handling case having the greatest overshoot and the Balanced case having both the fastest convergence as well as the smallest overshoot. The UPBA results in Figure 5.17b show the Comfort controller having better comfort characteristics, followed by the Balanced and then the Handling cases, as would be expected. The Contact Force results in

Figure 5.17d show that the peak force is about -10 kN in all cases. This is because the Linear Rise profile is effectively instantaneous, which causes the peak force to simply be the profile displacement multiplied by the tire stiffness. This pattern repeats on every Linear Rise single test performed on the present work. The LWBD results in Figure 5.17c are unremarkable, being very similar to the Contact Force results. However, the tire results now no longer show the trend of the Comfort case outperforming the Handling and Balanced cases on handling oriented metrics.

Here, the results are as expected from the optimization. The Comfort vehicle showed the best performance with regards to the UPBD and UPBA, having the lowest peak and total acceleration and displacement. It had a somewhat slow convergence, with its displacement having a very small but long overshoot and its acceleration taking the longest to die down. The Handling vehicle had the smallest LWBD overshoot and contact force, and the worst comfort performance. The Balanced vehicle showed an intermediary performance between the Handling and Comfort vehicles. Because the Linear Rise excites far more frequency modes than the Bump, it showed results which better agreed with the optimization expectations, as they also were built on results that take into account the whole frequency domain.

5.3.2 Hybridhook case studies

The Hybridhook results are shown overlaid with the Passive results, which will act as a benchmark for performance.

5.3.2.1 ISO results

The frequency domain quarter vehicle results for the ISO excitation are in Figures 5.18a, 5.18b and 5.18c.

From the UPBD and UPBA response, it can be observed that most performance gains were had at low frequency bands. This is to be expected, as the upper body has most of its gain at lower frequencies. The improvement is most stark for the Comfort and Balanced vehicles. The UPBD results appear to contain more noise in their data, but the results remain very similar between the acceleration and displacement.

The LWBD response in Figure 5.18c appears to have an equal peak gain, but higher overall or RMS gain. The results are coherent with the optimization: it was determined that the peak gain was to be controlled, not the total gain. This is, however, an important characteristic: many articles in the literature measure handling as proportional to the RMS of the LWBD, and not the peak gain. As such, while the results have indeed been optimized for handling according to the stipulated metric, whether the Passive and Hybridhook vehicles with equal Roadhold have the same handling performance can be a point of contention.

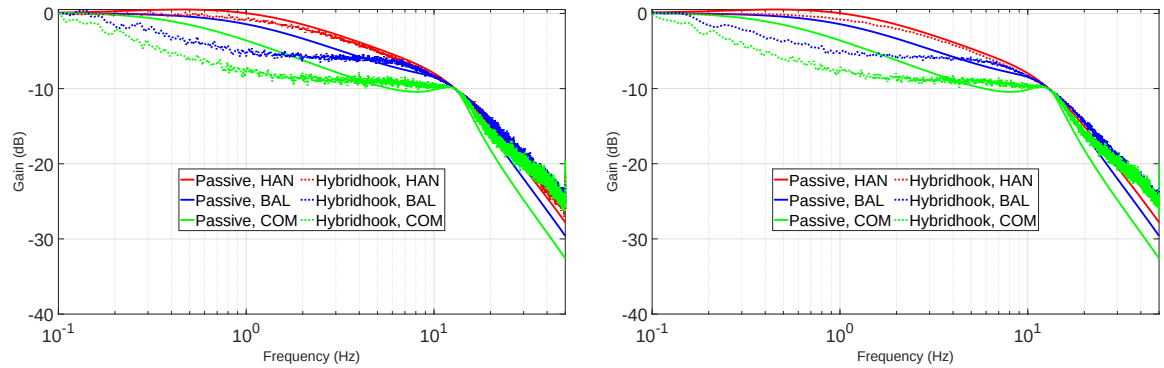

(a) UPBD **(b)** UPBA

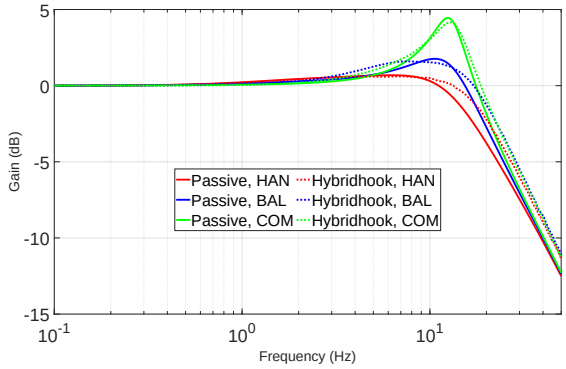

(c) LWBD

Figure 5.18. Frequency domain quarter vehicle response on a MR SAS system with the Hybridhook controller under an ISO excitation. Adapted from Ferreira *et al.* (2025).

5.3.2.2 Bump results

The Bump excitation results are laid out in Figures 5.19a, 5.19b, 5.19c and 5.19d. Table 5.21 contains the ratios between the results of the Hybridhook and passive cases. These results are also available in Table 5.30, which contains the ratio between all MR SAS cases and their passive counterparts side-by-side for an easier comparison.

The displacement data in Figure 5.19c for the LWBD is hard to visually inspect, but the results show that a smaller peak displacement was attained by all Hybridhook vehicles. The greatest improvement was seen by the Handling controller. The acceleration data in Figure 5.19b shows a weird pattern of sharp changes. This is because the controller is performing sudden strong changes in the force the MR damper exerts on the vehicle, also known as high jerk. Once again, the Handling vehicle failed to decrease the peak acceleration, this time having a greater negative peak acceleration in the same moment it had a greater peak positive Contact Force previously. The Balanced controller had similar behavior during the same time frame, but it decreased the peak and RMS acceleration. The Comfort controller did not show jumps at that same time mark, but soon after showed many jerk motions where the other controllers had already ceased. It still decreased peak and RMS accelerations, however.

The UPBD displacement data in Figure 5.19a, on the other hand, show bad results for all controllers. First, all Hybridhook systems showed a greater peak displacement for all cases.

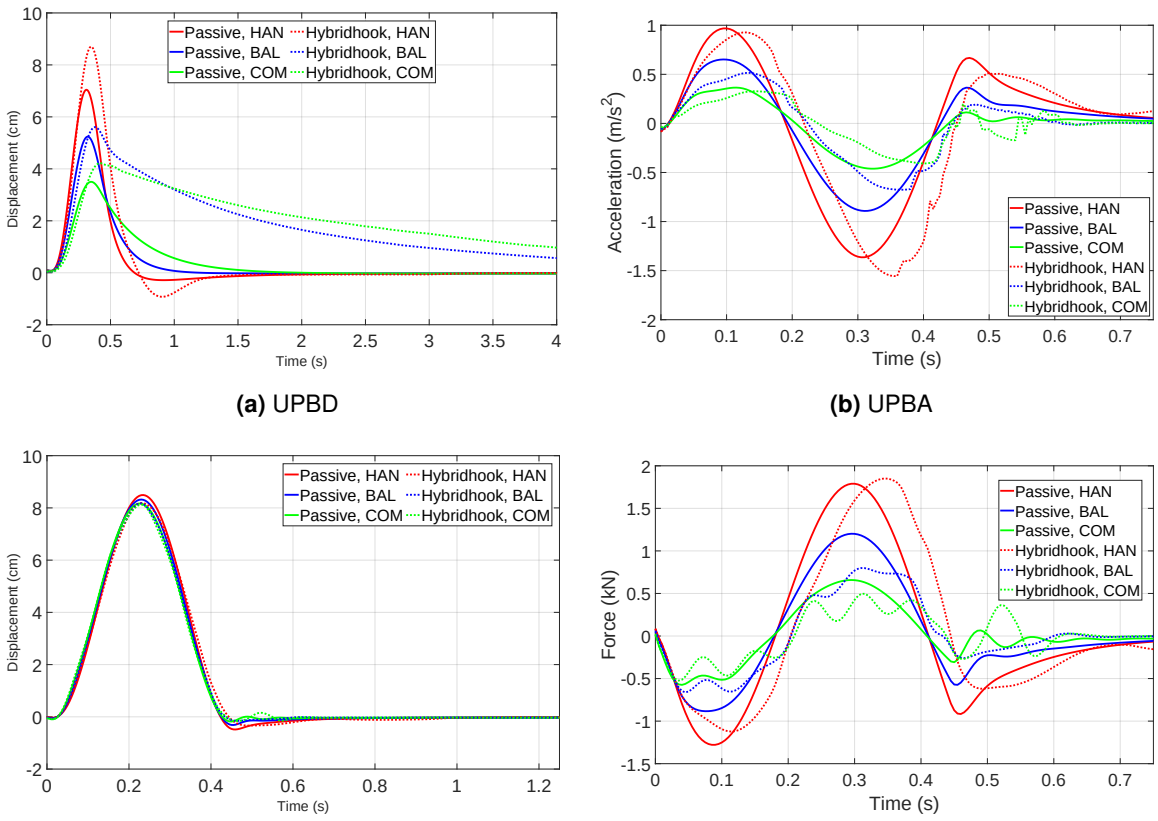

(a) UPBD **(b)** UPBA

(c) LWBD **(d)** Contact Force

Figure 5.19. Time domain quarter vehicle response on a MR SAS system with the Hybridhook controller over a bump obstacle. Adapted from Ferreira *et al.* (2025).

Second, the Comfort and Balanced controllers had enormously larger settling times, extending beyond the observed time frame. The peak Contact Force was decreased for the Comfort and Balanced controllers, but not for the Handling controller, which only managed to decrease its peak negative Contact force. The Handling controller response seems as thought it lags behind the passive controller, showing it likely has a phase delay effect. The high frequency oscillations associated with the tire resonant frequency are more evident in the Comfort and Balanced controllers here. This makes sense, as the gain in its frequency range has not been decreased for either the upper or lower body.

The Bump results show that the Hybridhook controller struggled with retaining its performance gains under its unusual conditions. It reproduced the trend seen in the Passive system, with the Comfort controller performing best overall for very much the same reasons. However, some differences were spotted.

From these results, it can be concluded that while the Hybridhook system improves the steady state performance, certain controllers are more robust than others to scenario changes. The Handling controller was unable to not only improve the performance, but actually decreased the vehicle performance in all metrics. The Balanced and Comfort controllers, while not perfect, showed an improvement in most criteria nonetheless.

Table 5.21. Relative performance values of the Hybridhook and passive quarter vehicle Case Studies under a Bump excitation.

Ratios	UPBA RMS	Peak UPBA	Peak Contact Force	Peak LWBD
Handling	109.1%	114.1%	103.4%	123.6%
Balanced	76.7 %	75.8 %	66.5 %	107.0%
Comfort	93.7 %	88.5 %	79.7 %	120.5%

5.3.2.3 Linear Rise results

The Linear Rise excitation results are laid out in Figures 5.20a, 5.20b, 5.20c and 5.20d. Table 5.22 contains the ratios between the results of the Hybridhook and passive cases. These results are also available in Table 5.31, which contains the ratio between all MR SAS cases and their passive counterparts side-by-side for an easier comparison.

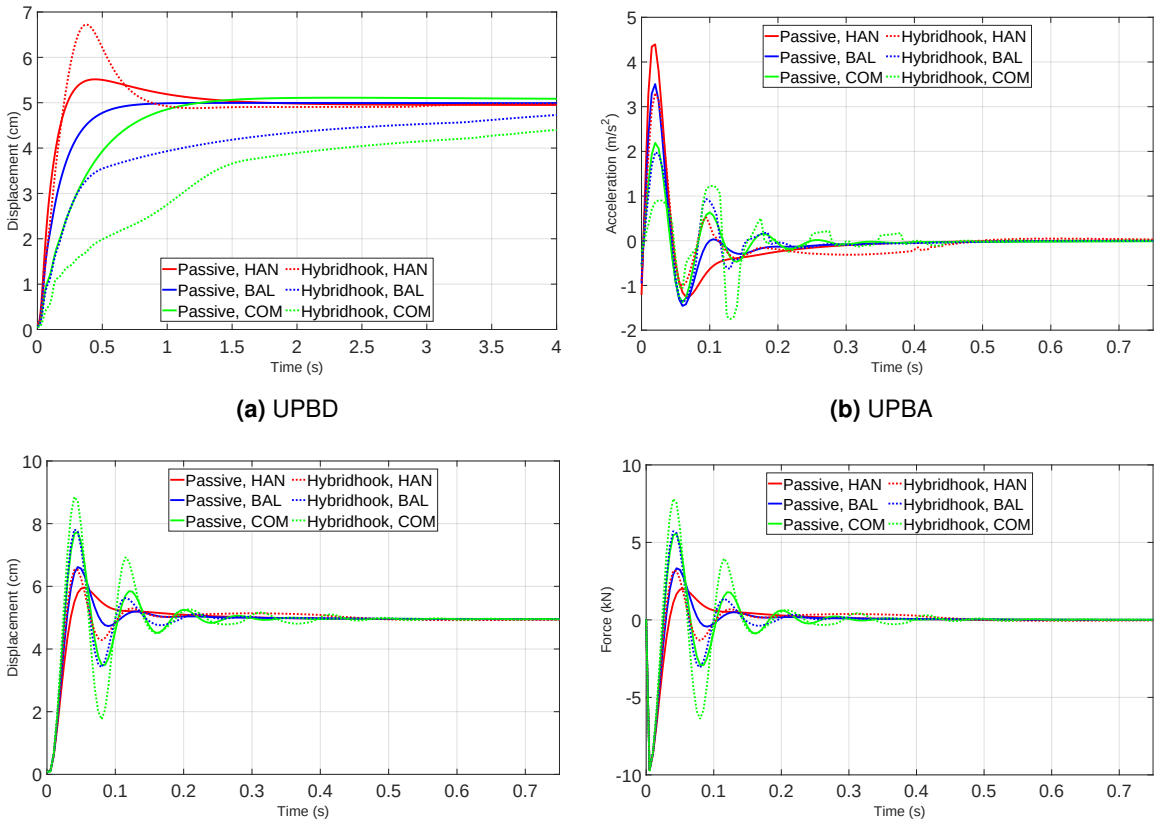

(a) UPBD

(b) UPBA

(c) LWBD

(d) Contact Force

Figure 5.20. Time domain quarter vehicle response on a MR SAS system with the Hybridhook controller over a linear rise obstacle. Adapted from Ferreira *et al.* (2025).

The UPBD in Figure 5.20a had a greater peak value for the Handling controller, but the Comfort and Balanced controllers had settling times so long that whether that qualifies as an improvement is up for debate. As seen in Figure 5.20b, all controllers managed to improve the peak UPBA and the UPBA RMS, while struggling with the handling. They still showed the jerking behavior seen with the Bump road, and the UPBA RMS did not improve as much as the peak value due to the controllers struggling to control the vibrations after the initial

motion. In Figure 5.20c, the peak LWBD was equal in the Balanced and Comfort cases, while it was far bigger in the Handling case, and had longer settling times on all cases as well. The peak Contact Force in Figure 5.20d was identical due to all vehicles reacting the same to the first encounter with the obstacle, but the controllers also amplified the following oscillations, increasing the settling time.

The Linear rise results have also returned to the expected relationship between the controllers, with the Handling controller having better handling characteristics and the Comfort controller better comfort characteristics.

These results, coupled with the Bump results, demonstrate that the Hybridhook controller does not generalize well for situations too different from the ones on which it was optimized. It has a hard time controlling the tire vibrations, and while it does better with the upper body vibrations, it still has some downsides tangled with its improvements such as longer settling times and jerky movement.

Table 5.22. Relative performance values of the Hybridhook and passive quarter vehicle Case Studies under a Linear Rise excitation.

Ratios	UPBA RMS	Peak UPBA	Peak Contact Force	Peak LWBD
Handling	77.4%	75.3%	99.9%	121.9%
Balanced	72.4%	56.4%	99.9%	100.0%
Comfort	98.4%	80.0%	99.7%	97.7 %

5.3.3 LQR case studies

5.3.3.1 ISO results

Just as with the Hybridhook controller, LQR results are shown overlaid with the Passive results, so as to make comparisons easier with other controllers.

The frequency domain quarter vehicle results for the ISO excitation are in Figures 5.21a, 5.21b and 5.21c.

The UPBD is once again very similar to the UPBA chart, but with more added noise. The UPBA results in Figure 5.21b are very similar to the ones found on the Hybridhook. Most of the RMS performance gain comes from the low frequencies, with the differential that the LQR controllers have low gain values for the entire low frequency band. The LWBD result in Figure 5.21c, compared to the Hybridhook controller, showed the same pattern of keeping the peak gain equal while having a greater total RMS, but to a lesser extent.

These results show that the overall strategy employed for vibration control in the quarter car vehicle is similar: decrease the gain at the lower frequency bands, which affect the upper mass the most, while keeping the lower mass under control. The LQR controller is, however, better able to execute this strategy.

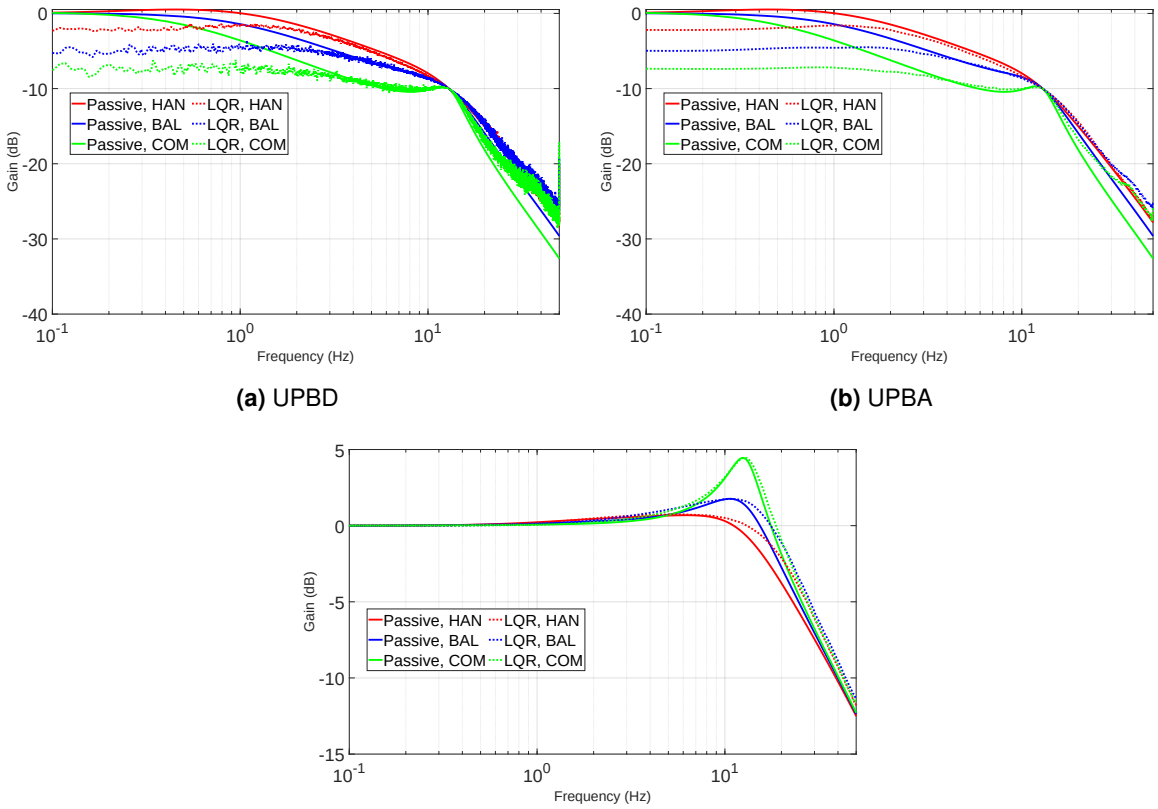

(a) UPBD

(b) UPBA

(c) LWBD

Figure 5.21. Frequency domain quarter vehicle response on a MR SAS system with the LQR controller under an ISO excitation. Adapted from Ferreira *et al.* (2025).

5.3.3.2 Bump results

The Bump excitation results are laid out in Figures 5.22a, 5.22b, 5.22c and 5.22d. The numerical values for the data is available in Table 5.23. Table 5.23 contains the ratios between the results of the LQR and passive cases. These results are also available in Table 5.30, which contains the ratio between all MR SAS cases and their passive counterparts side-by-side for an easier comparison.

In Figure 5.22a, the UPBD improved for all controllers, showing comparable settling times and lower peaks than their Passive counterpart. The Comfort controller performed specially well in this case. In Figure 5.22b, smaller peaks and RMS values were attained. The Handling controller still showed the least improvement, but performed much better than in the Hybridhook case. Furthermore, the jerking behavior was nearly absent, with a smooth ride in most of the domain. Some small force jumps can be observed in some moments, like at 0.5 s for the Comfort controller, but these are far milder than the ones experienced by the Hybridhook controller. The LWBD in Figure 5.22c is still hard to visually observe for the Bump case, but smaller peaks displacements were attained. The Contact Force in Figure 5.22d still showed smaller, high frequency oscillations for the Comfort and Balanced controllers, but it had no sudden jumps as the ones experienced by the Comfort controller in the Hybridhook case. And unlike the Hybridhook, the peak Contact Force was also improved for all Case studies.

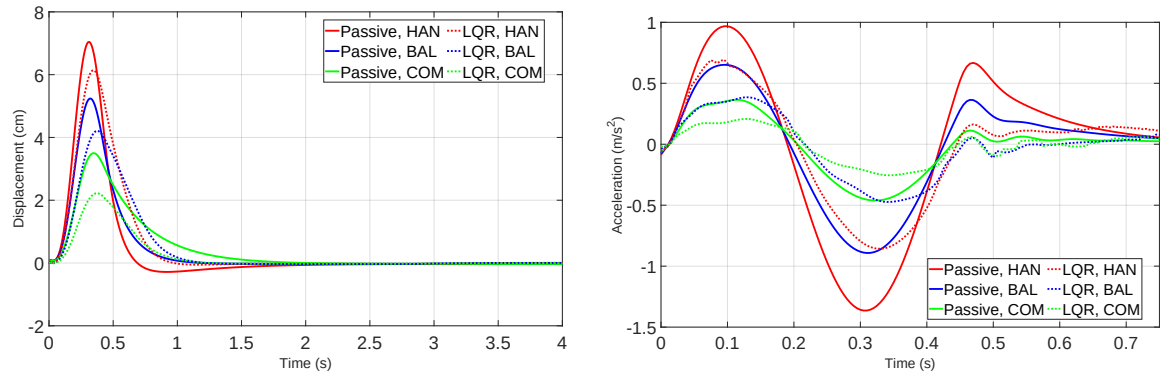

(a) UPBD

(b) UPBA

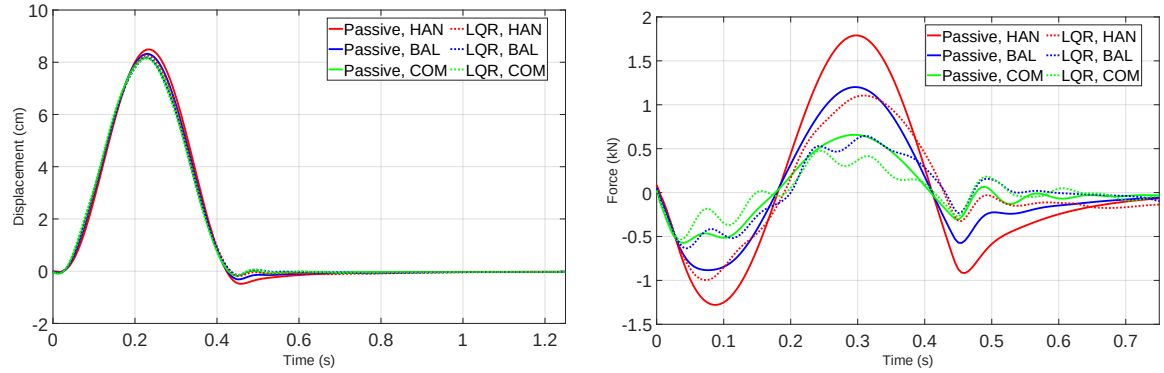

(c) LWBD

(d) Contact Force

Figure 5.22. Time domain quarter vehicle response on a MR SAS system with the LQR controller over a bump obstacle. Adapted from Ferreira *et al.* (2025).

The results show an improvement in performance, both relative to the Passive system and to the Hybridhook results. The observed trend of the Comfort controller having better performance for the Bump excitation continued, but this time all evaluated controllers improved in all metrics.

These results demonstrate that the LQR controller is able to control vibrations under conditions different from its training far more effectively than the Hybridhook controller. It showed improvements in all contemplated characteristics for all controller varieties. Some characteristics observed in previous tests, such as the Comfort controller dominance in the Bump test or the presence of high frequency oscillations associated with the system's second resonant mode, were still present.

Table 5.23. Relative performance values of the LQR and passive quarter vehicle Case Studies under a Linear Rise excitation. Reproduced from Ferreira *et al.* (2025).

Ratios	UPBA RMS	Peak UPBA	Peak Contact Force	Peak LWBD
Handling	65.2%	62.8%	61.8%	87.2%
Balanced	59.3%	53.1%	53.7%	80.3%
Comfort	59.6%	55.3%	81.6%	63.5%

5.3.3.3 Linear Rise results

The Linear Rise excitation results are laid out in Figures 5.23d, 5.23c, 5.23b and 5.23a. The numerical values for the data is available in Table 5.24. Table 5.24 contains the ratios between the results of the LQR and passive cases. These results are also available in Table 5.31, which contains the ratio between all MR SAS cases and their passive counterparts side-by-side for an easier comparison.

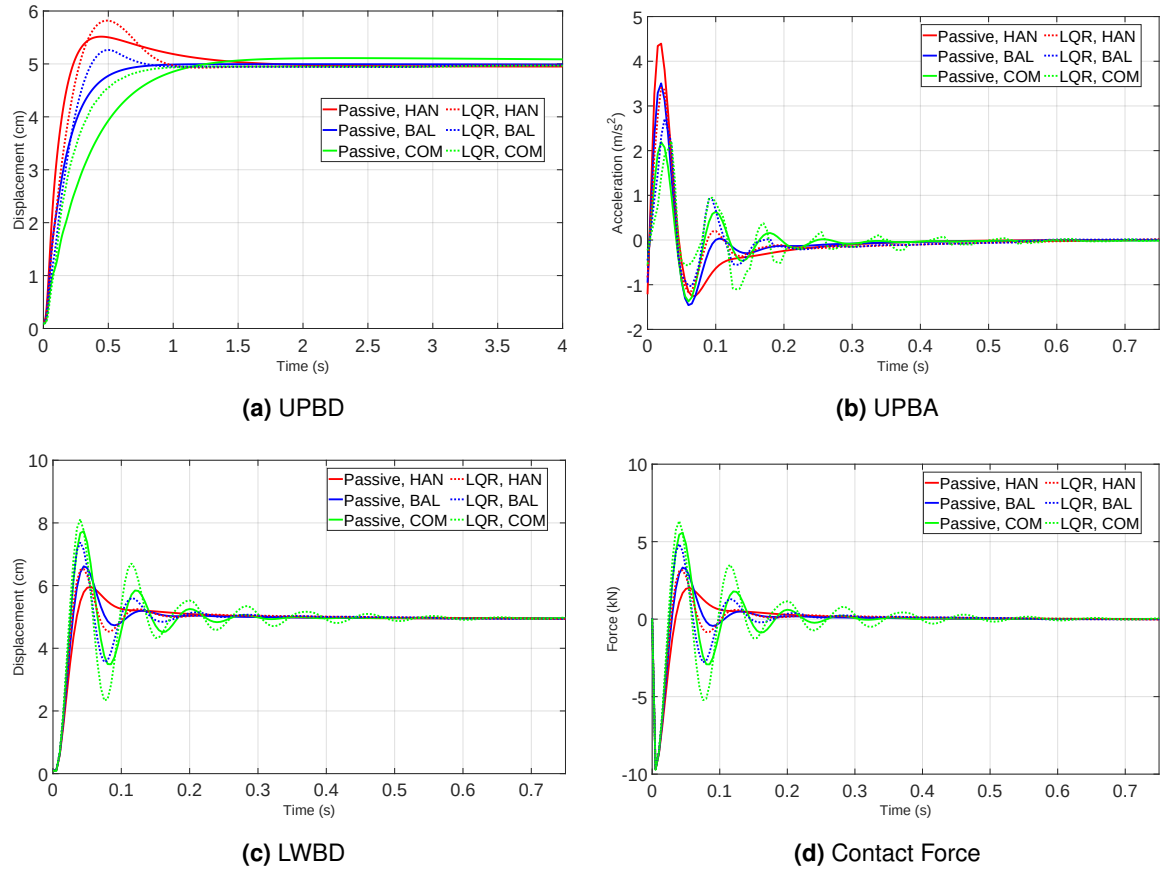

(a) UPBD **(b)** UPBA

(c) LWBD **(d)** Contact Force

Figure 5.23. Time domain quarter vehicle response on a MR SAS system with the LQR controller over a linear rise obstacle. Adapted from Ferreira *et al.* (2025).

The peak UPBD in Figure 5.23a had the opposite results, in which the Comfort controller was the only one which improved the peak value. Both the Comfort and Handling case had shorter settling times, while the Balanced case had a slightly longer settling time due to exhibiting some overshoot. Nonetheless, the differences in the UPBD were minor. Breaking the trend observed, in Figure 5.23b the LQR Comfort controller actually performed worse than not only the Passive system, but the Hybridhook Comfort controller as well for the peak UPBA. It also had worse UPBA RMS than the passive system, and did not manage to offer great improvements. The Balanced and Handling controllers, on the other hand, decrease the peak and RMS values, reneging the failure solely to the Comfort controller. The results in Figure 5.23c for the LWBD have the same results as the ones for the Contact Force, in which the LQR performed worse than the Passive but better than the Hybridhook systems. The peak Contact Force in Figure 5.23d was identical to the Passive case for all vehicles, which once again occurred because the

first force peak is nigh immitigable due to how sudden it is. The controllers also showed greater secondary peaks, just as the Hybridhook controlled vehicles did. However, their performance was still better than the Hybridhook, overshooting by smaller margins.

The LQR controller also behaved as expected for the Linear rise, in the sense that the controllers performed better in the aspects they are focused on. One unexpected results was that the Comfort focused controller showed bad results all around.

Overall, the results for the LQR controller show that it is not only better at controlling vibrations under random road conditions, but its performance gains translate well to deterministic obstacles. Despite being optimized for the UPBA, it showed good improvement to the UPBD as well. This contrasts heavily with the Hybridhook system, which struggled with both the Bump and Linear Rise obstacles, doubly so with regards to the UPBD. The LQR controllers were far more consistent, with only the Comfort oriented suspension showing issues for the UPBA in the Linear Rise. They also showed less jerky motions and shorter settling times. While not perfect, the LQR controller showed itself to be a far more effective and reliable controller than the Hybridhook.

Table 5.24. Relative performance values of the LQR and passive quarter vehicle Case Studies under a Linear Rise excitation. Reproduced from Ferreira *et al.* (2025).

Ratios	UPBA RMS	Peak UPBA	Peak contact force	Peak LWBD
Handling	76.3 %	77.6%	99.9%	105.5%
Balanced	80.5 %	77.4%	99.7%	105.4%
Comfort	101.2%	100.9%	99.6%	97.2%

5.3.4 SDRE case studies

5.3.4.1 ISO results

The frequency domain quarter vehicle results for the ISO excitation are in Figures 5.24c, 5.24b and 5.24a.

The same result seen for the UPBA is seen in Figure 5.24a for the UPBD, including its lackluster performance compared to its LQR counterpart. The results for the UPBA in Figure 5.24b show a similar behavior to the LQR case. Unlike it however, the Handling case's UPBA was unable to properly reduce its gain at lower frequencies, instead increasing it. The other cases managed to do, but to a lesser degree than the one achieved by the LQR. In Figure 5.24c, the LWBD was properly constrained into the same peak value as the Passive case. It is otherwise very similar to the LQR results.

These Gain plots are very similar to those of the LQR case. These results are unremarkable: they are similar to the LQR's, but offer a worse trade-off.

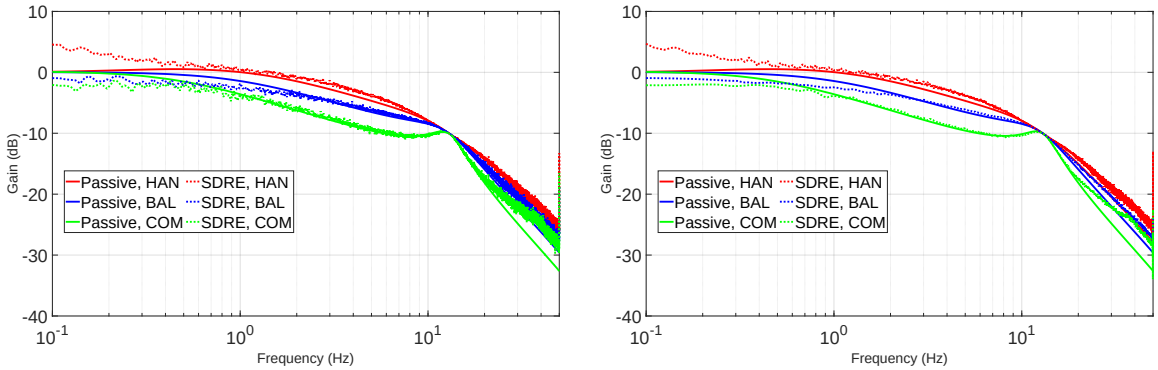

(a) UPBD **(b)** UPBA

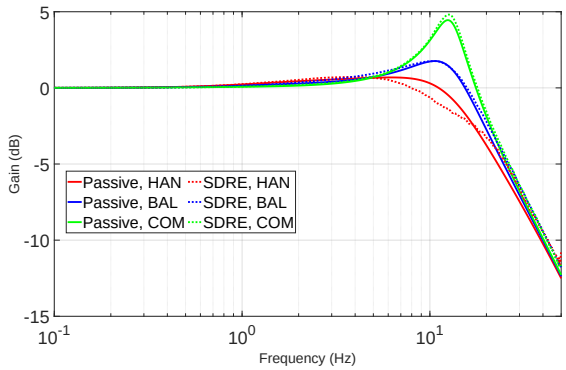

(c) LWBD

Figure 5.24. Frequency domain quarter vehicle response on a MR SAS system with the SDRE controller under an ISO excitation. Adapted from Ferreira *et al.* (2025).

5.3.4.2 Bump results

The Bump excitation results are laid out in Figures 5.25d, 5.25c, 5.25b and 5.25a. The numerical values for the data is available in Table 5.25. Table 5.25 contains the ratios between the results of the SDRE and passive cases. These results are also available in Table 5.30, which contains the ratio between all MR SAS cases and their passive counterparts side-by-side for an easier comparison.

In Figure 5.25a, a weird behavior was noticed in the Handling case's UPBD results: after reaching its peak and coming back to zero displacement, it instead keeps going down. An analysis into the curve beyond what is shown here reveals it reaches a steady state value lower than its initial value. This is likely due to the MR damper formulation incorrectly allowing the damper to keep its v_m value high despite no excitation. While better than its alternatives, the MR damper formulation chosen is not perfect, and sometimes it can interact with the controller to produce wrong values for the steady state displacement. The results in Figure 5.25b, besides being similar to the LQR but worse, also show some jumps in the acceleration, as seen in the Hybridhook but not in the LQR system. Figure 5.25c echoes the UPBA results, with its results also being essentially a worse version of the LQR. Figure 5.25d's results show the same trend observed before, where the Comfort case performs better in the Bump obstacle for comfort and handling metrics. Its results are, as seen in the ISO Case Studies, similar to the LQR but with

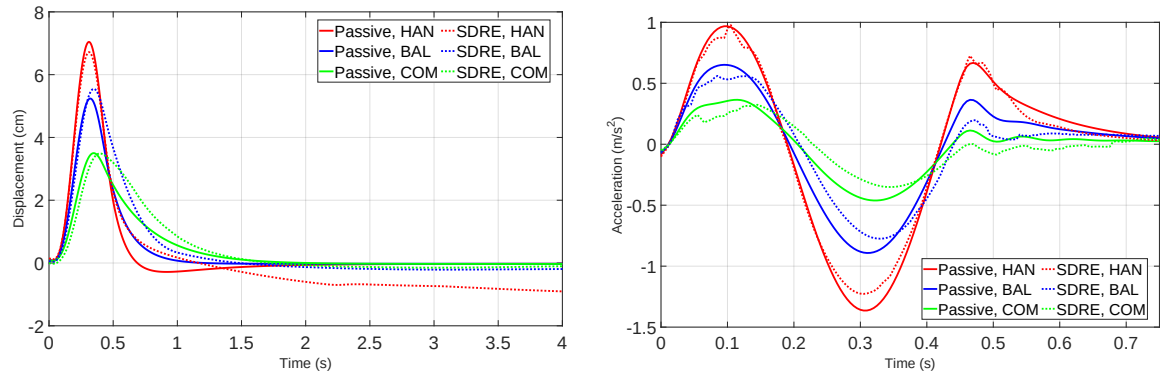

(a) UPBD

(b) UPBA

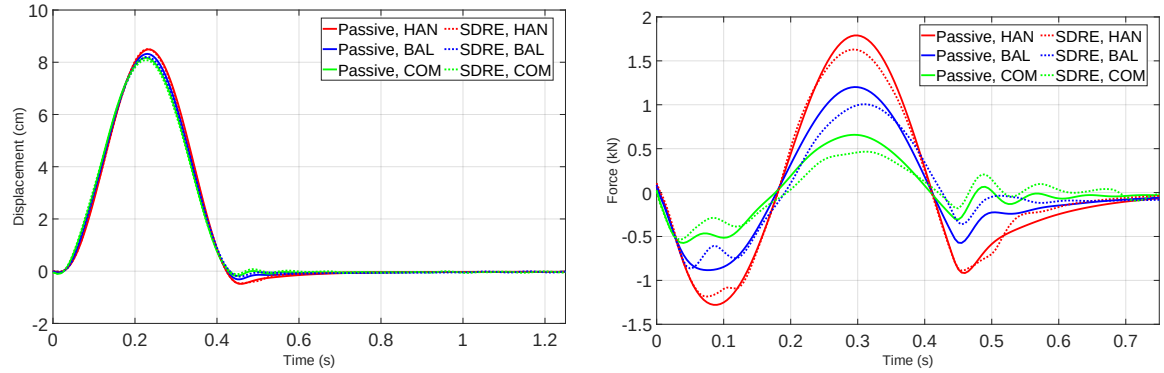

(c) LWBD

(d) Contact Force

Figure 5.25. Time domain quarter vehicle response on a MR SAS system with the SDRE controller over a bump obstacle. Adapted from Ferreira *et al.* (2025).

fewer improvements.

The results show an improvement in performance relative to the passive system, including for the Handling case. This is positive, given the Handling vehicle actually had a worse performance compared to its passive counterpart. This difference might be because this effect was most pronounced in frequency ranges which are lower than the Bump's, or because the SDRE formulation built-in adaptability protects its performance from degradation under such conditions.

Compared to the LQR, all results were worse. Compared to the Hybridhook, however, the Handling case was better in all metrics, while the Handling case was better in all metrics but the peak Contact Force, in which it was equal. The Balanced case was worse in the comfort metrics, but better in the safety metrics. It did, however, exhibit some of the jerky movement the Hybridhook controller exhibit as well. Overall, while it is a straight downgrade from the LQR controller, it still is able to offer some degree of performance improvement over the Hybridhook controller, as well as over the Passive case.

Table 5.25. Relative performance values of the SDRE and passive quarter vehicle Case Studies under a Bump excitation.

Ratios	UPBA RMS	Peak UPBA	Peak Contact Force	Peak LWBD
Handling	93.4%	90.0%	91.1%	95.4%
Balanced	87.8%	86.9%	83.7%	105.9%
Comfort	81.2%	76.0%	81.5%	99.7%

5.3.4.3 Linear Rise results

The Linear Rise excitation results are laid out in Figures 5.26d, 5.26c, 5.26b and 5.26a. The numerical values for the data is available in Table 5.26. Table 5.26 contains the ratios between the results of the SDRE and passive cases. These results are also available in Table 5.31, which contains the ratio between all MR SAS cases and their passive counterparts side-by-side for an easier comparison.

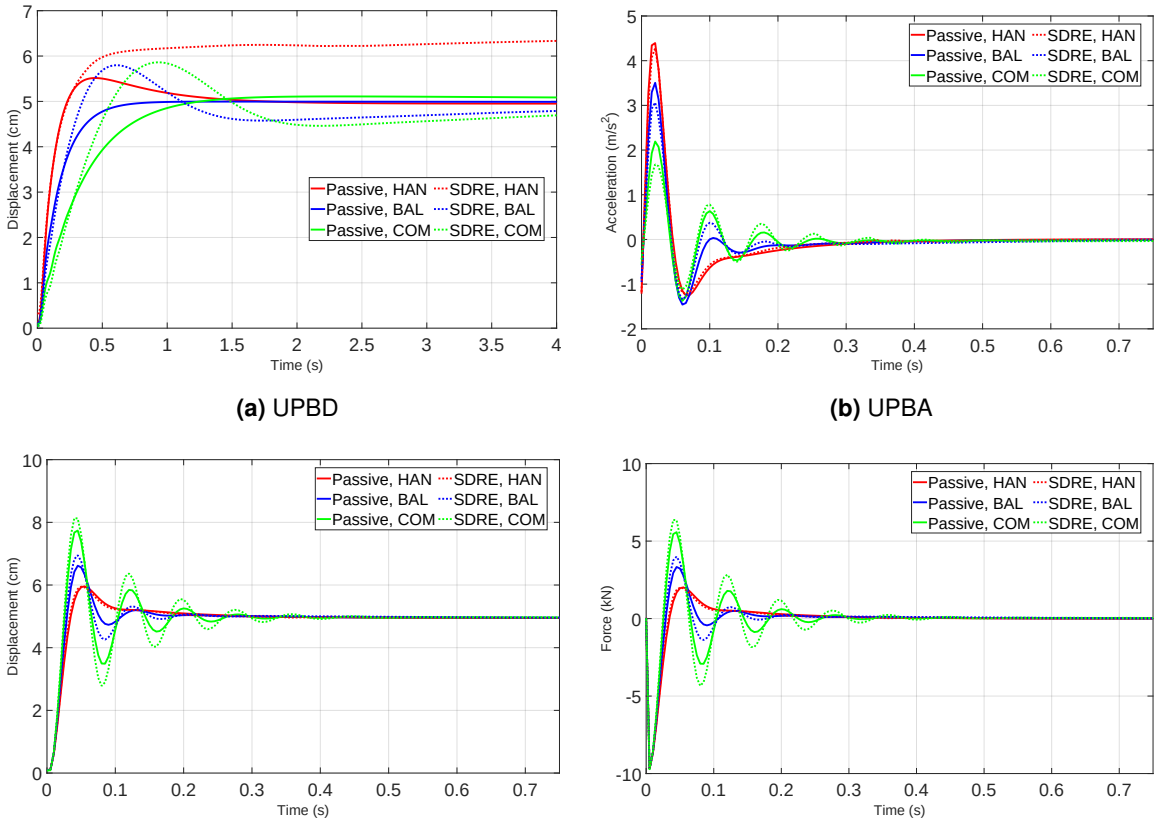

(a) UPBD **(b)** UPBA

(c) LWBD **(d)** Contact Force

Figure 5.26. Time domain quarter vehicle response on a MR SAS system with the SDRE controller over a linear rise obstacle. Adapted from Ferreira *et al.* (2025).

Most cases of the SDRE controller once again performed worse than their LQR counterpart, and this time they performed worse than the Hybridhook too. The sole exception is the Comfort controller, which actually managed to outperform all other options in the comfort metrics while retaining a similar peak Contact force. This is a positive result, but as previously mentioned, the peak Contact Force in the Linear Rise case is bounded by the force generated during the

initial contact, which is always roughly the same quantity regardless of controller. However, comparing its secondary peaks in Figure 5.25d to the LQR case in Figure 5.22d show that it does, indeed, keep up a similar level of performance in the contact force.

The Handling and Balanced case performed worse than the other controllers in all metrics, as well as worse than the Passive case in the handling metrics. Furthermore, the displacement in the Handling vehicle once again converged to a value different from its initial mean as seen in Figure 5.25a, demonstrating that its issues are not limited to the Bump obstacle.

The SDRE case study results paint a more positive picture than its optimization results did: the controller is able to maintain its performance under different circumstances, in certain cases actually outperforming cases from controllers which performed much better in the optimization. However, its performance is not consistent, with the Handling exposing some weaknesses in the damper model used. Furthermore, its performance was, overall, worse than the LQR and comparable to the Hybridhook by virtue being better sometimes. These results demonstrate the potential of the SDRE controller, but also that extensive work is required to extract its full potential, as the two optimization attempts performed in this thesis were unable to bring it to the level of the LQR.

Table 5.26. Relative performance values of the SDRE and passive quarter vehicle Case Studies under a Linear Rise excitation.

Ratios	UPBA RMS	Peak UPBA	Peak Contact Force	Peak LWBD
Handling	96.7%	97.4%	99.9%	117.3%
Balanced	88.5%	87.4%	99.9%	116.0%
Comfort	84.6%	76.7%	99.8%	114.7%

5.3.5 Control statistics and results

5.3.5.1 ISO results

The command and current results for the ISO excitation are displayed in Table 5.27.

Table 5.27. Control values of the quarter vehicle Case Studies under an ISO excitation. The variables F_{sat}, F_{sas} and A_{avg} stand for percentage of time under saturation due to force constraints, percentage of time under saturation due to semi-active constraints, and average current.

Controller	Handling	Balanced	Comfort	Metric
Hybridhook	89.6%	92.8%	93.9%	F_{sat}
	89.6%	91.7%	93.2%	F_{sas}
	0.04 A	0.27 A	0.22 A	A_{avg}
LQR	60.3%	65.6%	67.5%	F_{sat}
	40.4%	46.7%	47.5%	F_{sas}
	3.92 A	3.78 A	3.97 A	A_{avg}
SDRE	100%	100%	100%	F_{sat}
	51.2%	50.8%	57.3%	F_{sas}
	1.27 A	1.82 A	1.55 A	A_{avg}

The results for the ISO excitation show that the controller spends a very high percentage of the time not reaching the desired force values in all cases, with the LQR having the least saturation and the SDRE having the most. The SDRE was unable to reach its desired force output at all, which is likely related to the reason it had the worst performance of all three controllers. In fact, the performance of the controllers seems to be directly related to the proportion of time they spent unable to reach their desired force.

Overall, Comfort focused controllers spent more time saturated, a fact that can be explained by the semi-active saturation row: the increase in the time spent saturated is almost equal to the increase in time spent limited by the semi-active nature of the device.

The average current tends to be greater for Balanced controllers, followed by Comfort and then Handling ones. The reason for this is unknown. The Hybridhook had the lowest average currents, likely due to it spending most of its time at the lowest available force. The high currents drawn by the LQR are explained by the long times it spent unsaturated as well as saturated at the highest current level.

From these results, it can be concluded that under an ISO excitation, performance on a SAS depends on how well the controller utilizes its upper and lower force limits to spend as little time as possible saturated.

5.3.5.2 Bump results

The Bump excitation results are laid out in Figures 5.27a, 5.27b, 5.27c and 5.27d. The command and current results are displayed in Table 5.28.

Compared to the ISO excitation, the Hybridhook controller spent less time saturated under the Bump excitation, while the LQR spent more. Unlike with the ISO excitation, this did not translate into relative improvements, as there's no longer a relationship between saturation times and performance.

Despite the more similar saturation values, the Hybridhook tended to have greater current values. Looking at Figures 5.27a and 5.27b, it's perceived that while both controllers initially responded similarly to the excitation, the Hybridhook followed up with greater negative force values. This might be one of the reasons the Hybridhook had slightly higher saturation percentages, as it outputted great forces for longer periods of time.

The SDRE controller results show that its high saturation values are caused by very high command values, effectively turning the controller into a ”bang-bang” or ”on-off” type. This also partially explains why its performance has been subpar: it cannot control the system with the same precision the other controllers can. This also points to the SDRE matrix parametrization as being the likely culprit for its poor performance, with $\dot{f}(x)$ high values negatively affecting controller performance.

From these results, it can be concluded that under a Bump road excitation, the saturation time is not as important as it is in the ISO case: the SDRE controller consistently outperforms the Hybridhook, despite its high saturation, and the LQR higher saturation does not close the

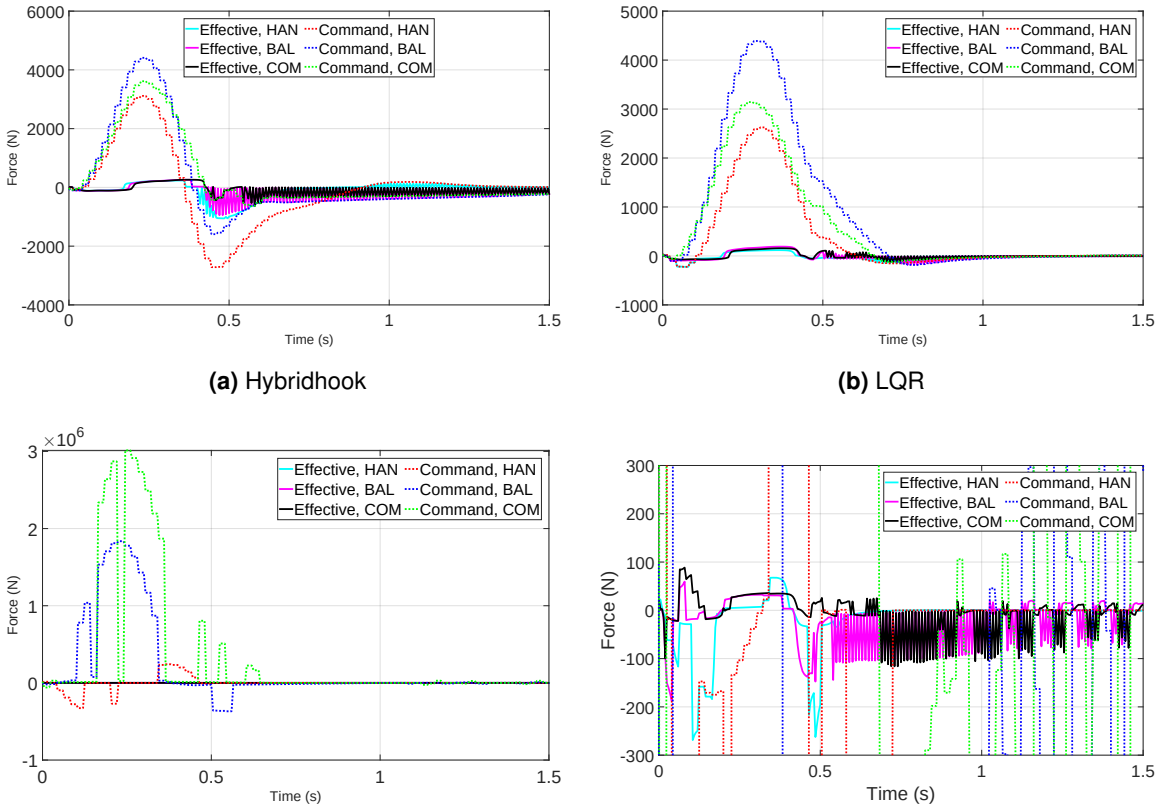

(a) Hybridhook

(b) LQR

(c) SDRE

(d) SDRE (zoom)

Figure 5.27. Time domain quarter vehicle control commands and effective forces over a Bump obstacle.

performance gap between it and the Hybridhook either.

Table 5.28. Control values of the quarter vehicle Case Studies over a Bump obstacle. The variables F_{sat}, F_{sas} and A_{avg} stand for percentage of time under saturation due to force constraints, percentage of time under saturation due to semi-active constraints, and average current.

Controller	Handling	Balanced	Comfort	Metric
Hybridhook	73.3%	82.3%	76.0%	F_{sat}
	60.0%	52.3%	52.6%	F_{sas}
	2.64 A	6.04 A	4.78 A	A_{avg}
LQR	70.7%	77.0%	75.0%	F_{sat}
	52.0%	53.3%	54.3%	F_{sas}
	3.33 A	4.37 A	3.85 A	A_{avg}
SDRE	100%	100%	100%	F_{sat}
	80.7%	44.0%	51.7%	F_{sas}
	0.11 A	2.20 A	1.85 A	A_{avg}

5.3.5.3 Linear Rise results

The Linear Rise excitation results are laid out in Figures 5.28a, 5.28b, 5.28c and 5.28d. The command and current results are displayed in Table 5.27.

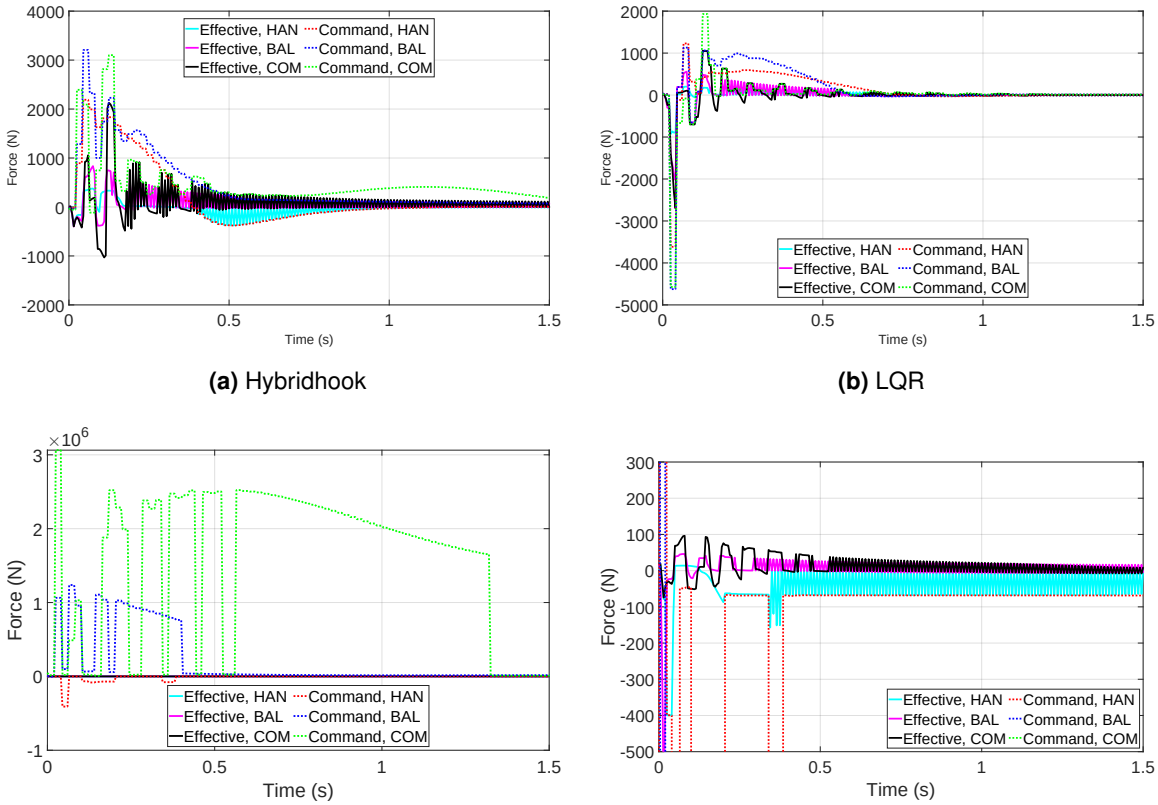

(a) Hybridhook

(b) LQR

(c) SDRE

(d) SDRE (zoom)

Figure 5.28. Time domain quarter vehicle control commands and effective forces over a Linear rise obstacle.

The Linear Rise results follow the Bump results trend of having higher saturation values for the LQR and lower values for the Hybridhook. Likewise, despite higher force saturation percentages, the Handling case for the LQR performed similar to the Hybridhook, while the SDRE Comfort case had the best comfort performance despite having similar percentages for saturation time as before.

Analyzing Figures 5.28a, 5.28b and 5.28c, it's noticeable that the LQR Comfort controller had an easier time matching its control force to the controller command, but that did not results in improved performance. The main pattern seems to be that controllers which attempted to have high positive forces performed best. Positive magnitude forces in the SAS attempt to bring the upper and lower bodies closer together, which implies that the best strategy for the Linear Rise Case is related to decreasing the relative motion between the bodies.

It can be concluded that, unlike for the ISO case, force saturation is not the best metric for predicting performance under the deterministic obstacles tested.

5.3.6 Case Studies performance overview

The results of the previous sections have been compiled here for ease of view and comparison. Table 5.30 has the relative performance between each controller on a MR SAS system

Table 5.29. Control values of the quarter vehicle Case Studies over a Linear rise obstacle. The variables F_{sat}, F_{sas} and A_{avg} stand for percentage of time under saturation due to force constraints, percentage of time under saturation due to semi-active constraints, and average current.

Controller	Handling	Balanced	Comfort	Metric
Hybridhook	73.0%	67.0%	90.3%	F_{sat}
	65.7%	51.3%	55.0%	F_{sas}
	1.46 A	3.36 A	7.08 A	A_{avg}
LQR	79.0%	71.3%	57.0%	F_{sat}
	57.7%	55.0%	54.0%	F_{sas}
	4.21 A	3.21 A	0.67 A	A_{avg}
SDRE	100%	100%	100%	F_{sat}
	45.3%	50.7%	52.0%	F_{sas}
	1.57 A	5.02 A	0.90 A	A_{avg}

and their passive counterparts for the Bump excitation case, while Table 5.31 has the data for the Linear Rise excitation.

Table 5.30. Relative performance values of the quarter vehicle MR SAS systems and passive Case Studies under a Bump excitation. Cells colored according to value. Green square indicates the best results for that metric in the test. White text added for better contrast.

Ratios	UPBA RMS	Peak UPBA	Peak Contact Force	Peak LWBD
Hybridhook				
Handling	109.1%	114.1%	103.4%	123.6%
Balanced	76.7%	75.8%	66.5%	107.0%
Comfort	93.7%	88.5%	79.7%	120.5%
LQR				
Handling	65.2%	62.8%	61.8%	87.2%
Balanced	59.3%	53.1%	53.7%	80.3%
Comfort	59.6%	55.3%	81.6%	63.5%
SDRE				
Handling	93.4%	90.0%	91.1%	95.4%
Balanced	87.8%	86.9%	83.7%	105.9%
Comfort	81.2%	76.0%	81.5%	99.7%

As previously commented, the LQR system provided the best performance uplift overall. The SDRE system performed better than expected, having better results than the Hybridhook system in the both the Handling and Comfort cases despite its Pareto front being dominated. It is specially surprising it outperformed the passive and Hybridhook systems in the Handling case, as its relative performance was even worse in that region. This showcases the SDRE capacity at handling non-linear systems outside the region it was trained on.

The Linear Rise results have the LQR system as the best, but the Hybridhook controller managed to compete in many instances. While tied for the number of performance metrics in which they're the best, the Hybridhook victories show greater performance gaps. The LQR system, nonetheless, showed much better qualitative properties. This time, the Hybridhook outperformed the SDRE in the Handling case, as was expected. Surprisingly, the best Comfort

Table 5.31. Relative performance values of the quarter vehicle MR SAS systems and passive Case Studies under a Linear Rise excitation. Cells colored according to value. Green square indicates the best results for that metric in the test. White text added for better contrast.

Ratios	UPBA RMS	Peak UPBA	Peak Contact Force	Peak LWBD
Hybridhook				
Handling	77.4%	75.3%	99.9%	121.9%
Balanced	72.4%	56.4%	99.9%	100.0%
Comfort	98.4%	80.0%	99.7%	97.7%
LQR				
Handling	76.3 %	77.6%	99.9%	105.5%
Balanced	80.5 %	77.4%	99.7%	105.4%
Comfort	101.2%	100.9%	99.6%	97.2%
SDRE				
Handling	96.7%	97.4%	99.9%	117.3%
Balanced	88.5%	87.4%	99.9%	116.0%
Comfort	84.6%	76.7%	99.8%	114.7%

case was the SDRE, once again demonstrating that despite its poor performance in the optimization, it is inherently more robust at dealing with highly non-linear systems. Overall, the handling metrics were harder to improve than the comfort metrics.

Qualitative issues were observed with the Hybridhook and SDRE, such as jerky movements, long settling times and unusual steady-state displacements. While some of these can be partially attributed to the MR damper model used, they nonetheless remain as challenges to be overcame if these controllers are to be implemented.

5.4 HALF VEHICLE CASE STUDIES

The 1/4 vehicle model is known for its good accuracy compared to higher order models despite its simplicity. However, this is largely based on results for passive systems. To determine the extent to which this was also true for the case of a system with a realistic MR damper with a controller, the case studies performed for the 1/4 vehicle were repeated for an equivalent 1/2 vehicle, and the results were compared. This also allowed for the 1/2 vehicle model performance with the controllers to be evaluated.

As discussed in the theoretical revision performed in Chapter 2, it is claimed that the quarter vehicle model is a good approximation of the full vehicle dynamics. However, this does not mean that controllers optimized for the quarter vehicle motion will translate well into higher order vehicles. In order to test the extent to which this occurs, the 1/2 vehicle models will be modeled with an equal pair of rear and front suspensions, each one a point from the Case Study performed in the quarter vehicle. This includes both the suspension physical properties as well as the control parameters. The 1/2 vehicle will have each suspension independently controlled based solely on their local coordinate measurements, as explained in Subsection 3.5.6.

As explained in Subsection 3.4.3, the upper body metrics will have their gain calculated

based on the equivalent road inputs r_v and r_ω for the vertical and rotational dynamics respectively. The alternative gain definitions, based on the front road profile r_f, will be available on Appendix C. Another decision made was to include only the results for the front wheel, as the results for the rear wheel are very similar. The results for the rear wheel will also be available on Appendix C.

The Case studies are available in Figure 5.14, with the suspension and controller parameters being available in Table 5.17 for the Passive vehicle, Table 5.18 for the vehicle with a MR damper and a Hybridhook controller, Table 5.19 for the vehicle with a MR damper and a LQR controller, and Table 5.19 for the vehicle with a MR damper and a SDRE controller.

5.4.1 Simulation procedures

The simulations of the 1/2 vehicle were largely the same as the ones for the Case studies performed on the 1/4 vehicle in Section 5.3, guaranteeing the comparability between the results of the two. The procedures will be restated here in brief.

The MR damper was modeled according to the results of Section 5.1, using the Wang-II model with the second modified v_m in eq. (2.23). The damper parameters used were the original Wang model parameters (Wang *et al.*, 2004), with the exception of the new v_m coefficients.

The vehicle was simulated in the time domain according to equation (2.49). The general numerical solution procedure was the one described in Section 4.1. The vehicle parameters were the same as vehicle type #2, available in Table 5.32. The simulation parameters were the ones described in Section 3.7 and Table 3.4. The obstacles were the Linear Rise and Bump, whose parameters are described in Table 3.5.

Table 5.32. Dynamics and geometrical parameters of mass, inertia, stiffness and CG distance used in the 1/2 vehicle simulation. The suspension parameters are case dependent.

Property	Value	Property	Value
Sprung mass m_s	600 kg	Chassis moment of inertia J	289 $kg.m^2$
Unsprung masses $m_{r,u}/m_{f,u}$	30 kg	Distance from rear axle to CG d_r	1.1 m
Tire stiffness $k_{f,u}/k_{r,u}$	200 000 N/m	Distance from front axle to CG d_f	0.9 m

The vehicle data was chosen to best approximate a 1/2 vehicle version of the vehicle type #1. For the data not available due to vehicle model differences, such as the upper body moment of inertia or the wheel's axle distance from the body's center of gravity, the values from de Lima *et al.* (2012) were used as a basis for their estimation. The axle distance was directly reproduced, and the moment of inertia was obtained by making its ratio with the upper mass the same in both works.

5.4.2 Passive case studies

The passive optimization results are independently shown in this section to establish a baseline for the results of the optimized controllers.

5.4.2.1 ISO results

The frequency domain half vehicle results for the ISO excitation are in Figures 5.29a, 5.29b, 5.29c, 5.29d and 5.29e. Given the vehicle 10 m/s velocity and its tire distance of 2 m, its expected that wavelengths of 0,2 s or 5 Hz will cause resonance in the rotational mode, while wavelengths of 0,4 s or 2,5 Hz will cause resonance in the vertical mode.

The UPBD results in Figure 5.29a show roughly the same as those of the UPBA, with very little to comment. The UPBR results in Figure 5.29c also show roughly the same as those of the UPBRA, with very little to comment. The UPBA results in Figure 5.29b demonstrate a constant gain at lower frequencies, which decreases as the frequency increases and shows temporary increases at resonances. The results for the UPBRA in Figure 5.29d are similar to the ones for the UPBA, but show a decrease in the gain as the frequency tends to zero. Instead, it has its peak at around 2.5 Hz, decreasing when moving away from it. Lastly, the results in Figure 5.29e show a similar behavior to the 1/4 vehicle, but with more oscillations in frequencies near the peak.

The UPBA, UPBD, UPBR and UPBRA confirmed the prediction made with regards to the resonance frequencies and the vehicle speed. The angular quantities had their resonance occur at frequencies which are even whole multiples of 2.5 Hz (starting at 5 Hz), while the vertical quantities resonance occurred at odd whole multiplies of 2.5 Hz. This is even more visible in the results constrained to Appendix C. Besides these resonances, the rotational modes saw the two peaks which were present in the 1/4 vehicle model. The first one is the low frequency peak associated with the sprung mass, which happens at around 0.5 Hz and is most visible in Figure 5.29c for the Comfort case. The second one is the one associated with the tire resonance, at around 12 Hz. The vertical modes also have a very subtle low frequency mode which is most visible in Figure 5.29a for the Handling case, and appear to have an additional resonant frequency at 15 Hz which would be associated with the tires. Because this coincides with the resonance due to the vehicle axle distances, it is not possible to confirm it decisively. However, the Comfort case has a much greater jump at such frequency than the other cases do, indicating the more a vehicle is handling oriented, the less it is affected by the resonance at this frequency, supporting this idea.

The unsprung mass main resonance still is around 10 Hz, as it was for the 1/4 vehicle, but it has many secondary peaks associated with it this time. From the upper body results, it seems that these oscillations are also related to the vehicle speed to axle distance ratio, with the peaks being associated to the vertical resonant frequencies and the troughs being associated with the rotational resonant frequencies.

These peaks seem to cause an interesting twist to the phenomena observed for the

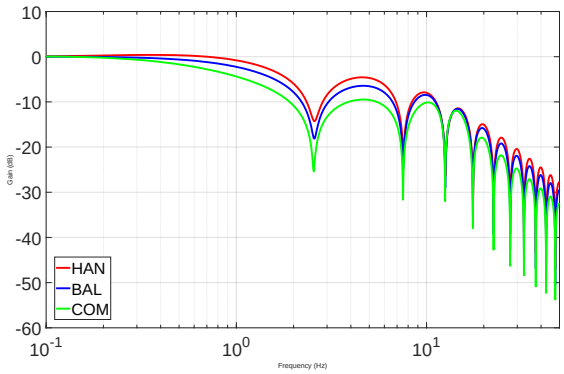

(a) UPBD

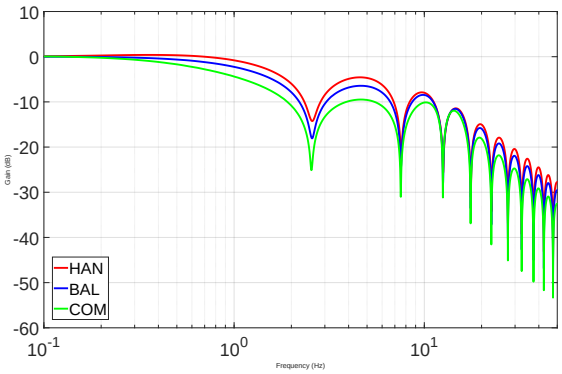

(b) UPBA

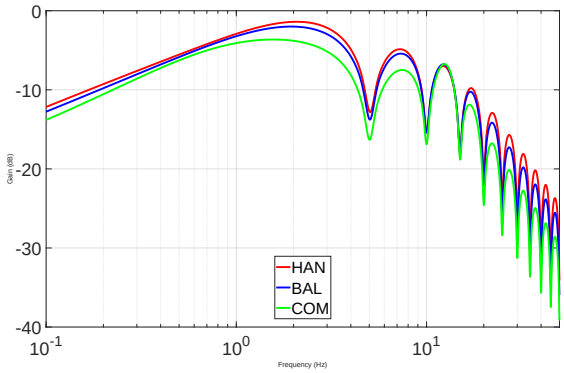

(c) Upper body angular displacement (UPBR)

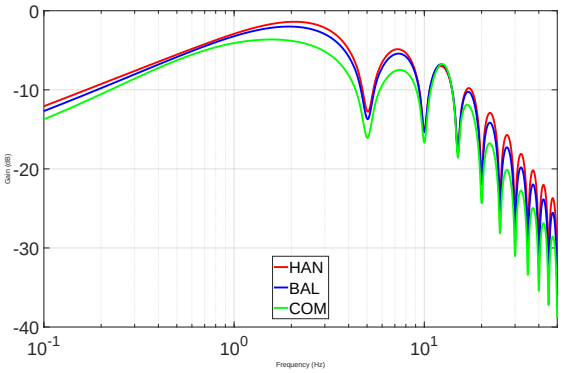

(d) Upper body angular acceleration (UPBRA)

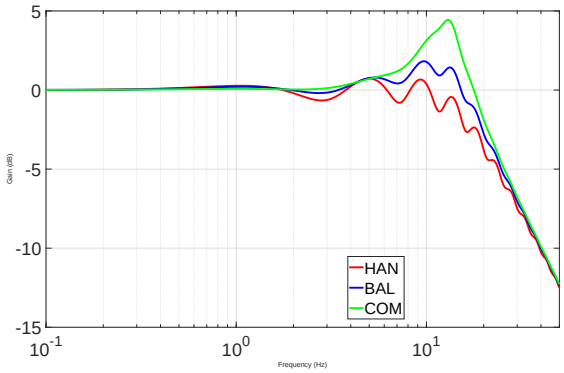

(e) LWBD

Figure 5.29. Frequency domain half vehicle responses on a passive system under an ISO excitation.

1/4 vehicle. Previously, the LWBD gain for the Comfort oriented vehicle was the lowest for frequencies below around 5 Hz. This time, it actually became band specific. At 5 Hz, it still has the lowest gain, but between 4 and 1.3 Hz the Handling and Balanced vehicle overtakes it, and the situation reverts again between 1.3 and 0.23 Hz. This means that the observed counterintuitive results for the Bump obstacle with the 1/4 vehicle, where the Comfort vehicle showed the best results for both handling and comfort, might not happen this time.

5.4.2.2 Bump results

The Bump excitation results are laid out in Figures 5.30a, 5.30b, 5.30c, 5.30d, 5.30e and 5.30f. Given the vehicle velocity of 8.33 m/s and the 2 m distance between the front and rear tire, the dynamics associated with the rear tire are expected to occur 0,24 s after those of the front tire.

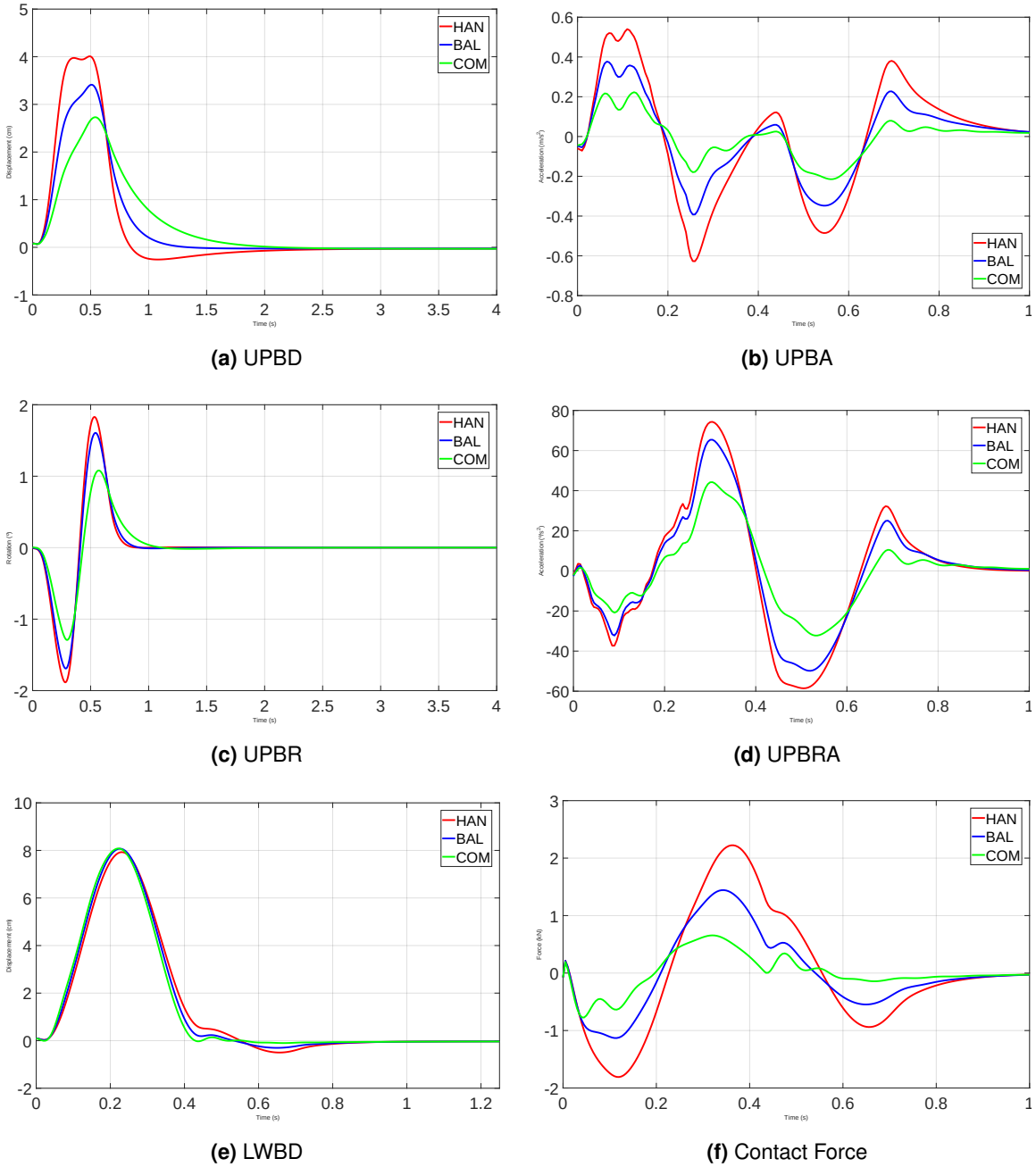

(a) UPBD **(b)** UPBA

(c) UPBR **(d)** UPBRA

(e) LWBD **(f)** Contact Force

Figure 5.30. Time domain half vehicle responses on a passive system over a bump obstacle.

In Figure 5.30a, the UPBD, like the UPBA, had an ”M” shaped crest, being the most evident in the Handling focused vehicle. It was far less pronounced in the other cases however, with the peak associated with the rear tire being the most pronounced. The UPBR displayed in Figure

5.30d was unremarkable, having an oscillation as one would expect: it tilts clockwise when the front tire goes up, anticlockwise when the rear tire goes up and then settles. Compared to the 1/4 vehicle, the displacement magnitudes were smaller.

In Figure 5.30b, the UPBA also exhibited similar results to the 1/4 vehicle at first. However, the first difference is that the two contacts with the bump created two peaks at the start, resulting in an ”M” shaped peak. The increase in degrees of freedom also cause the oscillations to take a different shape, with five major peaks and valleys occurring as opposed to three. Looking at the UPBRA results in Figure 5.30c, it is clear that this occurs because some of the energy is stored in the rotational moment of inertia. When dissipated, this causes some additional forces to be imposed in the vertical coordinate as well. The tires also cause some additional movement by themselves. Compared to the 1/4 vehicle, the acceleration magnitudes were smaller.

The front LWBD in Figure 5.30e is still not very visually descriptive, but the in this case, the Comfort vehicle actually had the highest wheel displacement. There was a bit of a secondary oscillation by the Handling and Balanced vehicles after settling, but nothing very noteworthy occurred in it. Compared to the 1/4 vehicle, the force and displacement magnitudes were greater. The Contact Force results in Figure 5.30f are similar to the ones for the quarter vehicle (Figure 5.16d), but the effects of the contact between the bump and the rear tire can be seen in the first tire Contact Force. As an example, there’s a small secondary bump at around the 0.5 s mark in all cases which is due to the vibrations of the second vehicle encounter with the bump being transmitted from the rear tire into the chassis into the front tire.

Despite the vehicle model change, the Comfort vehicle still exhibits the best performance for the Bump obstacle, with simultaneously better handling and comfort metrics. This extends to the rotational metrics added by changing the vehicle model from 1/4 to 1/2. The one major difference is that, in this case, the peak LWBD displacement was slightly lower for the Handling vehicle. However, the Comfort case was still superior in other handling metrics, only partially confirming what was expected from the Gain charts.

Overall, the results for the 1/2 vehicle show fewer vibrations in the sprung mass and more vibrations in the unsprung mass. The chassis’ peak vertical displacements and accelerations were lower, while the LWBD and Contact force of the front tire were higher. There are different possible reasons for this. The first is that the rotational degree of freedom absorbed some of the energy that was going into the vertical movement, decreasing its peak. The second is that, while the parameters proposed for the 1/2 vehicle were supposed to be equivalent to those of the 1/4 vehicle, they might be equivalent to more comfort oriented vehicles than anticipated. A third one is related to the peak and RMS values of the upper mass. While the peak values were lower for the upper mass, the RMS might not be, as the vibrations lasted longer. This might mean that, because the upper mass was twice as heavy as its 1/4 vehicle counterpart, it did not feel each individual contact with the bump as much, having lower peak values because the same total impulse per mass was spread over a longer time period.

5.4.2.3 Linear Rise results

The Linear Rise excitation results are laid out in Figures 5.31a, 5.31b, 5.31c, 5.31d, 5.31e and 5.31f. Given the vehicle velocity of 1.39 m/s and the 2 m distance between the tires, the dynamics of the rear tire are expected to happen 1,44 s after those of the front tire.

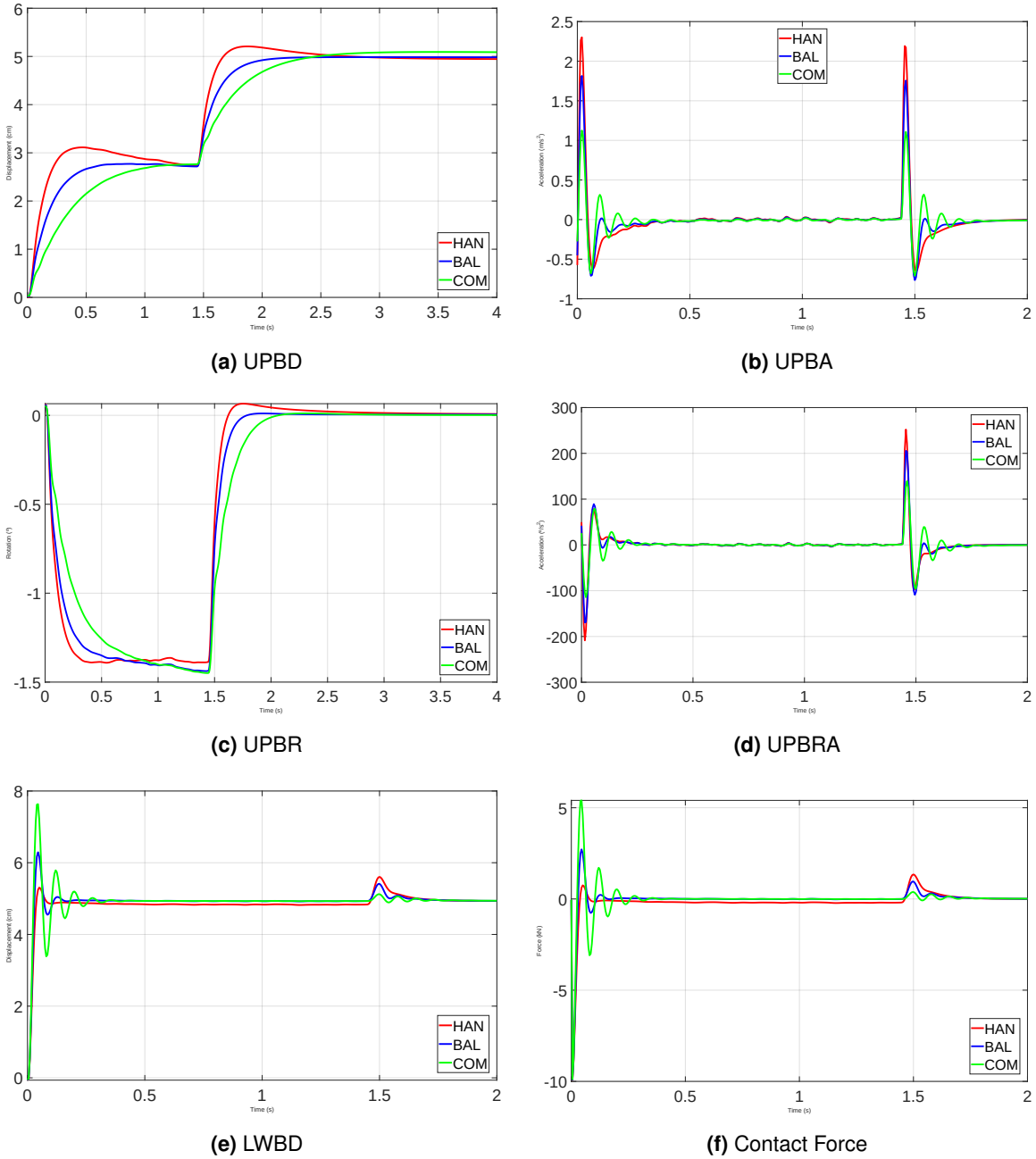

(a) UPBD

(b) UPBA

(c) UPBR

(d) UPBRA

(e) LWBD

(f) Contact Force

Figure 5.31. Time domain half vehicle responses on a passive system over a linear rise obstacle.

The UPBD results in Figure 5.31a support the conclusion observed for the tire results. All contemplated cases had already reached steady state by the time the rear tire makes contact with the linear rise obstacle. The phenomena observed in the UPBD results can also be seen in the UPBA results in Figure 5.31b, in which the vibrations are ”uncoupled”. The UPBR results in

Figure 5.31c follow the same trend, were the rotation nearly reaches steady state before being excited again. The UPBRA in Figure 5.31d, likewise, is nearly static by the time the system is excited again. The LWBD results in Figure 5.31e are also the same as their quarter vehicle counterparts, with very minute differences such as in which ms the peak displacement occurs. This is likely because, due to the lower vehicle velocity, the vibrations on one side of the vehicle have complete time to die down before the other side is excited. The front tire Contact force results in Figure 5.31f are very similar to those of the 1/4 vehicle, from the waveform shapes to the peak forces, which are nearly identical.

Here, the results also bear some resemblance to the 1/4 vehicle results. As before, the Handling vehicle and Comfort vehicle performances are optimized for their niches, with the Balanced case offering a middle ground. The 1/2 vehicle model has no effect on the peak -10 kN tire force, which is a consequence of the step function used for the Linear Rise model.

These results show that, under certain conditions, the 1/2 vehicle can be reliably approximated by the 1/4 vehicle model. They are the conditions in which each wheels is excited by itself, and all vibrations from the other wheel have been allowed to die down.

5.4.3 Hybridhook case studies

The Hybridhook results are shown overlaid with the Passive results, which will act as a benchmark for performance.

5.4.3.1 ISO results

The frequency domain half vehicle results for the ISO excitation are in Figures 5.32a, 5.32b, 5.32c, 5.32d and 5.32e.

Compared to the quarter vehicle results, the LWBD response in Figure 5.32e still maintains a roughly equal peak gain, but with a higher total gain. The consequences of the vibration control in the vertical degree of freedom can be observed in the rotational degree of freedom by looking at the UPBRA in Figure 5.32d and the UPBR in Figure 5.32c. They show a great increase in low frequency values compared to their passive counterparts, with the Handling case seeing the lowest increase by virtue of having the lowest decrease in the vertical results. However, the region between 0.4 and 2 Hz saw a decrease in both the rotational and vertical components.

The UPBA response in Figure 5.32b and UPBD response in Figure 5.32a are still decreased by attenuating the vibrations in low frequencies, and this time they show an additional behavior unique to the 1/2 vehicle model: in the gain peaks associated with the vehicle velocity to axis distance ratio, they show no discontinuity, instead coming down smoothly. These peaks are also bigger.

Overall, the results are fairly consistent with what was found for the 1/4 vehicle. They show that the quarter vehicle results generalize to the half vehicle model fairly well, but the addition of

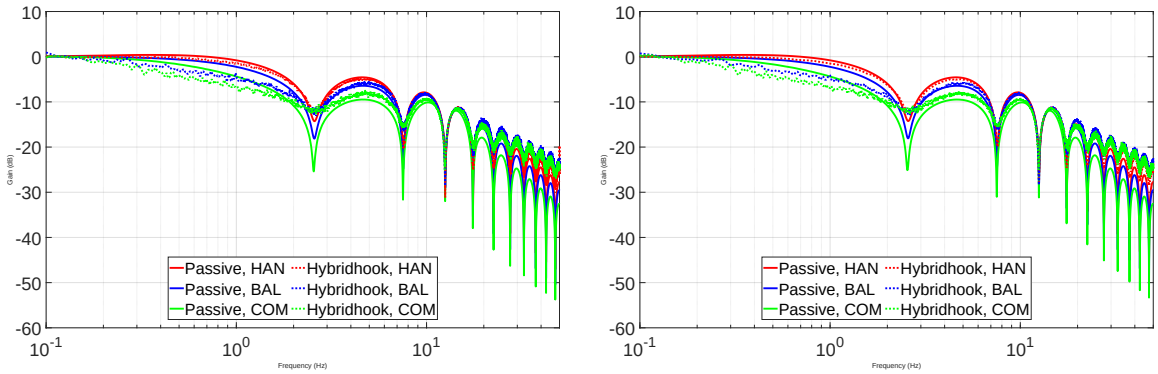

(a) UPBD

(b) UPBA

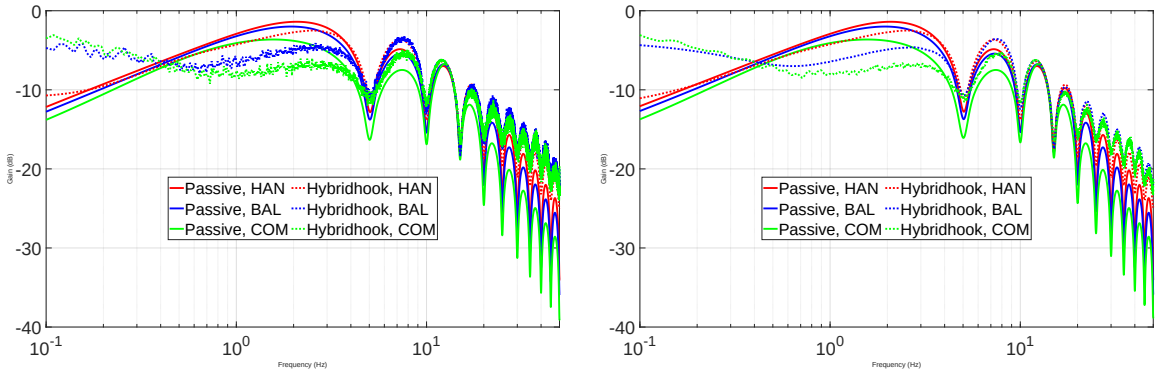

(c) UPBR

(d) UPBRA

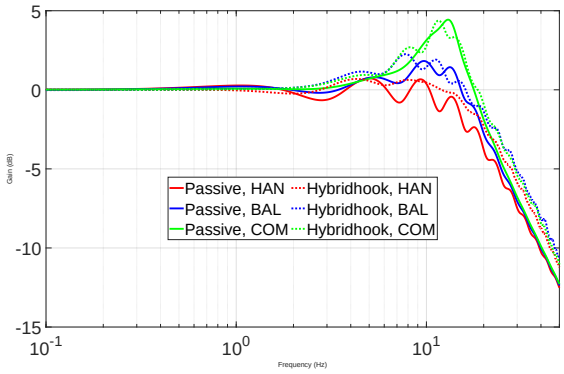

(e) LWBD

Figure 5.32. Frequency domain half vehicle responses on a MR SAS system with the Hybridhook controller under an ISO excitation.

the rotational degree of freedom which cannot be accounted for in any way for the 1/4 vehicle model meant it did not perform whenever the interaction between the modes became relevant.

5.4.3.2 Bump results

The Bump excitation results are laid out in Figures 5.33f, 5.33e, 5.33b, 5.33c, 5.33d and 5.33a.

The UPBR performance in Figure 5.33c and UPBRA performance in Figure 5.33d were

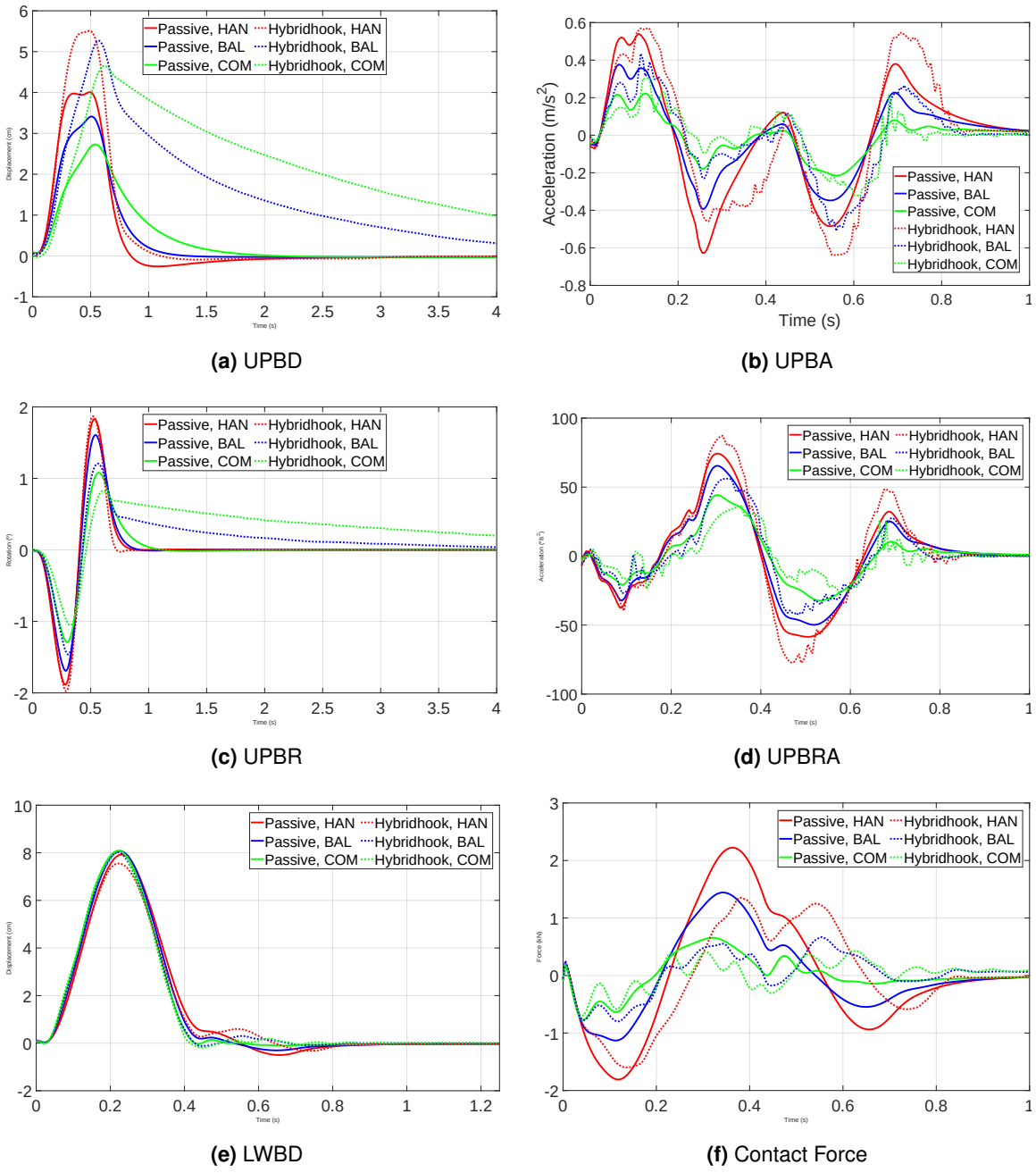

(a) UPBD **(b)** UPBA

(c) UPBR **(d)** UPBRA

(e) LWBD **(f)** Contact Force

Figure 5.33. Time domain half vehicle responses on a MR SAS system with the Hybridhook controller over a bump obstacle.

similar to the UPBD performance in Figure 5.33a and UPBA performance in Figure 5.33b respectively, which in turn resembled their 1/4 vehicle counterparts. One exception was the UPBD reaching a higher peak value in all cases, something that did not happen for either the rotational or quarter vehicle cases. The Comfort controller managed the best performance by reducing peak and RMS values, but took a very long time to reach steady state, dropping extremely slowly. The Handling case showed no improvement, reaching higher peak and RMS acceleration values. It also had nearly identical peak displacement values. Its one advantage was that, unlike the other two cases, it converged to conditions faster than the passive case. The Balanced case was a middle ground between the two, but behaved more closely to the

Comfort case in how it improved peak and RMS values at the cost of a slower return to steady state.

The Contact Force results in Figure 5.33f and of the front LWBD in Figure 5.33e show a moderate improvement over the passive case, while maintaining the better handling performance by the Comfort controller.

The Bump results show the Hybridhook controller performed, relative to its passive counterpart, arguably better on the 1/2 half vehicle compared to the 1/4 vehicle. By comparing the results in Table 5.33 with the quarter vehicle results in Table 5.21, many improvements are noticeable. The Handling controller improved in nearly all comforts metrics for the 1/2 with the exception of a small peak UPBR increase, while it made them all worse in the 1/4 vehicle case. It also showed an equal peak contact force, marginally better than its 1/4 vehicle counterpart. The Balanced controller showed a greater relative improvement compared to the 1/4 vehicle case, and the Comfort case was slightly worse in the UPBA RMS while improving the peak UPBA. On the down side, the Comfort and Balanced controllers no longer managed to improve the peak Contact force, which they did for the 1/4 vehicle model.

Some quirks seen in the 1/4 vehicle case remain, such as the presence of higher frequency oscillations associated with the tires in the contact force or the abrupt force jumps that make the vehicle jerky. Overall, the findings demonstrate that, while some of the performance measurements associated with comfort on the 1/2 vehicle model cannot be predicted by the 1/4 vehicle optimized suspension, the overall behavior on the 1/4 vehicle translates well to the 1/2 vehicle for the Hybridhook controller with some small performance degradation.

Table 5.33. Relative performance values of the Hybridhook and passive half vehicle Case Studies under a Bump excitation.

Ratios	UPBA RMS	UPBRA RMS	Peak UPBA	Peak UPBRA
Handling	118.1%	101.8%	118.1%	117.4%
Balanced	104.4%	129.9%	86.9%	85.8%
Comfort	134.5%	145.1%	94.4%	83.3%
Ratios	Peak UPBD	Peak UPBR	Peak LWBD	Peak contact force
Handling	137.4%	104.9%	95.2%	71.9%
Balanced	154.4%	86.4%	99.4%	55.3%
Comfort	170.4%	81.6%	100.4%	90.6%

5.4.3.3 Linear Rise results

The Linear Rise excitation results are laid out in Figures 5.34a, 5.34b, 5.34c, 5.34d, 5.34e and 5.34f.

The UPBD in Figure 5.34a and UPBR in Figure 5.34c saw lower peak values in the contemplated time frame for the Balanced and Comfort controllers due to their very slow response, while the Handling saw slightly higher values. The Comfort controller improved the acceleration measures at first, but just like the Comfort controller in 1/4 vehicle LQR case, it also experienced an unexpected force rebound at the second force peak (at around 0,15

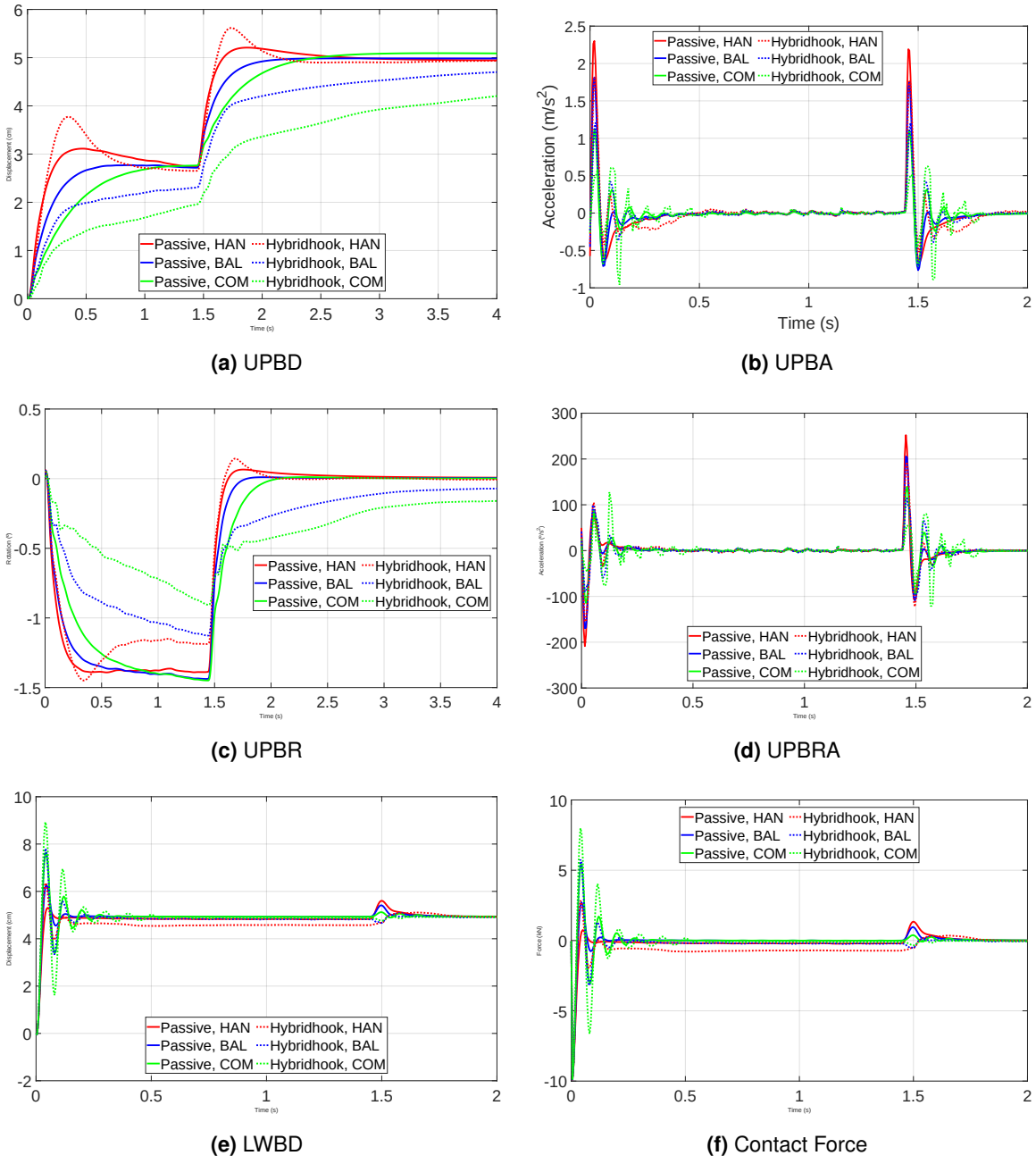

(a) UPBD **(b)** UPBA

(c) UPBR **(d)** UPBRA

(e) LWBD **(f)** Contact Force

Figure 5.34. Time domain half vehicle responses on a MR SAS system with the Hybridhook controller over a linear rise obstacle.

seconds), which made it lose most of its improvement in the UPBA in Figure 5.34b and actually perform worse in the UPBRA as shown in Figure 5.34d. The Balanced and Handling controllers performed better than their Passive counterparts with no real drawbacks.

The Contact Force results in Figure 5.34f and the front LWBD results in Figure 5.34e show similar results, in which most of the oscillations are the result of the direct contact of the tire, and a small ”rebound” movement is seen at the moment the rear tire makes contact. A permanent displacement is obtained by the front tire, which is dispersed once the rear tire makes contact. The Hybridhook systems show less response than its passive counterpart in the second encounter.

The Linear Rise results also closely resemble their 1/4 vehicle counterparts, with most of the main differences being the same as the ones found in the Bump results. Unlike the bump results, it did not show a higher peak UPBD for all controllers.

The main differential between the Hybridhook and Passive results lies in the long transient displacement period seen by the Balanced and Comfort controllers. Because of it, the effects of the front tire encounter with the obstacle had not yet been completely dispersed before the rear tire made contact, preventing the dynamics of the two wheels from being perfectly isolated from one another. Still, because the acceleration had mostly subsided at such point, the impact was minimal.

These and the Bump results show that the 1/4 vehicle performance of the Hybridhook controller is a reasonable predictor of performance on a 1/2 vehicle model. While a proper optimization performed on the 1/2 vehicle might yield more performance gains, specially by taking into account the angular displacement and acceleration into account, a suspension obtained from an optimization on a 1/4 vehicle model can be employed on a 1/2 vehicle model with good confidence for the Hybridhook case.

Table 5.34. Relative performance values of the Hybridhook and passive half vehicle Case Studies under a Linear Rise excitation.

Ratios	UPBA RMS	Peak UPBA	UPBRA RMS	Peak UPBRA
Handling	82.8%	80.2%	93.0%	82.6%
Balanced	70.9%	69.1%	81.8%	55.2%
Comfort	96.4%	80.7%	103.8%	91.5%
Ratios	Peak UPBD	Peak UPBR	Peak LWBD	Peak contact force
Handling	107.8%	104.2%	113.4%	99.0%
Balanced	99.7%	78.4%	124.2%	100.1%
Comfort	96.7%	62.6%	116.9%	100.2%

5.4.4 LQR case studies

Just as with the Hybridhook controller, LQR results are shown overlaid with the Passive results, so as to make comparisons easier with other controllers.

5.4.4.1 ISO results

The frequency domain half vehicle results for the ISO excitation are in Figures 5.35a, 5.35b, 5.35c, 5.35d and 5.35e.

The LQR results are similar to their 1/4 vehicle results, both in relation to the Passive and Hybridhook results. The LQR was able to successfully maintain the peak LWBD in Figure 5.35e at the same level, but compared to the Hybridhook, it was also able to subdue the oscillations related to the vehicle speed to axle distance much better, specially on the rear tires (which can be observed in Appendix C in Figure C.3e).

While it was not able to remove the same speed to axle peaks on the upper body oscillations,

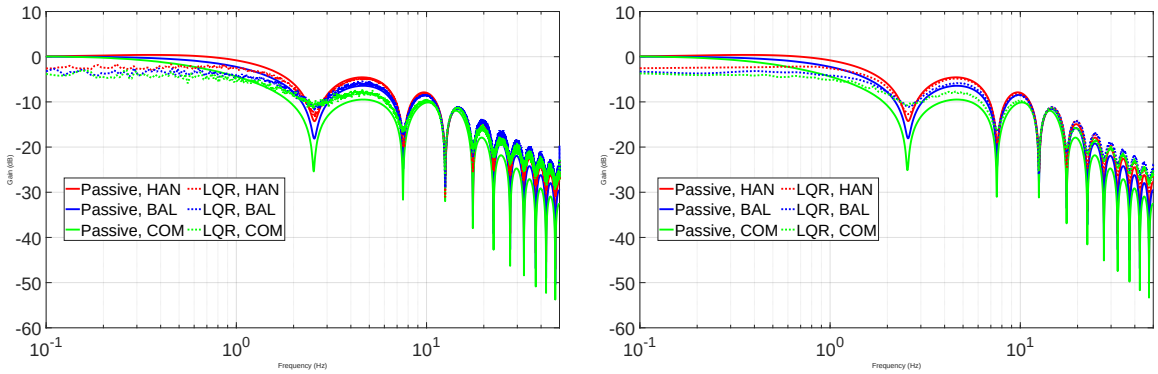

(a) UPBD

(b) UPBA

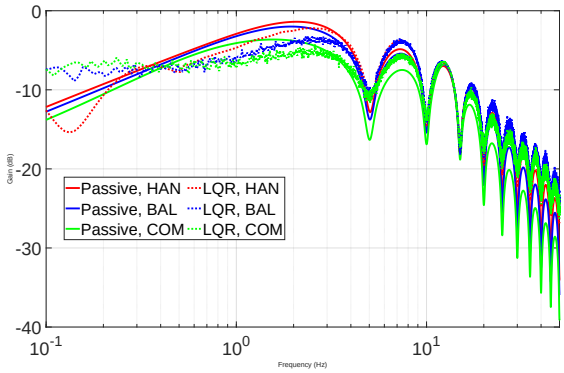

(c) UPBR

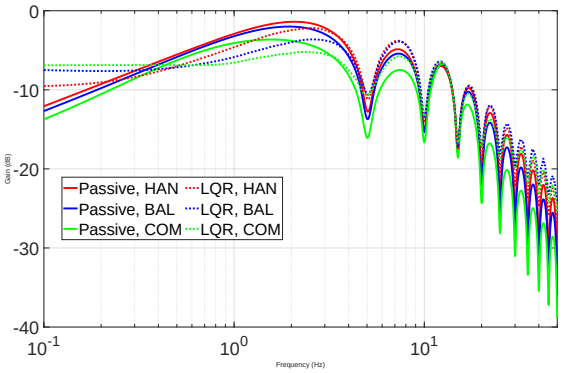

(d) UPBRA

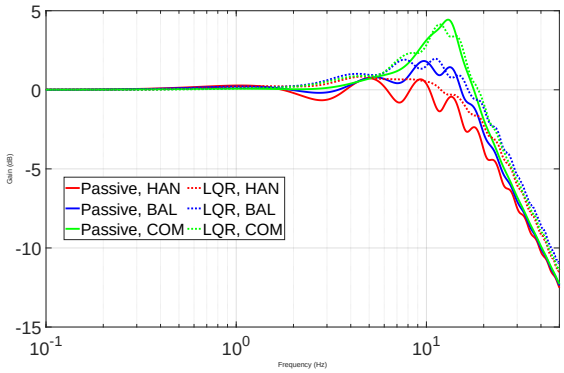

(e) LWBD

Figure 5.35. Frequency domain half vehicle responses on a MR SAS system with the LQR controller under an ISO excitation.

it did reduce the total vibration better, decreasing the gain at lower frequencies more consistently. While it did also see a rise in low frequency vibrations for the rotational degrees of freedom, they did not rise as much as they did in the Hybridhook.

From this, its possible to see that the superiority shown by the LQR controller in the 1/4 vehicle is also present in the 1/2 vehicle model, and many of the features observed in it are also carried, such as the consistent attenuation of low frequency vibrations in the upper body.

5.4.4.2 Bump results

The Bump excitation results are laid out in Figures 5.36a, 5.36b, 5.36c, 5.36d, 5.36e and 5.36f. The numerical values for the data is available in Table 5.23.

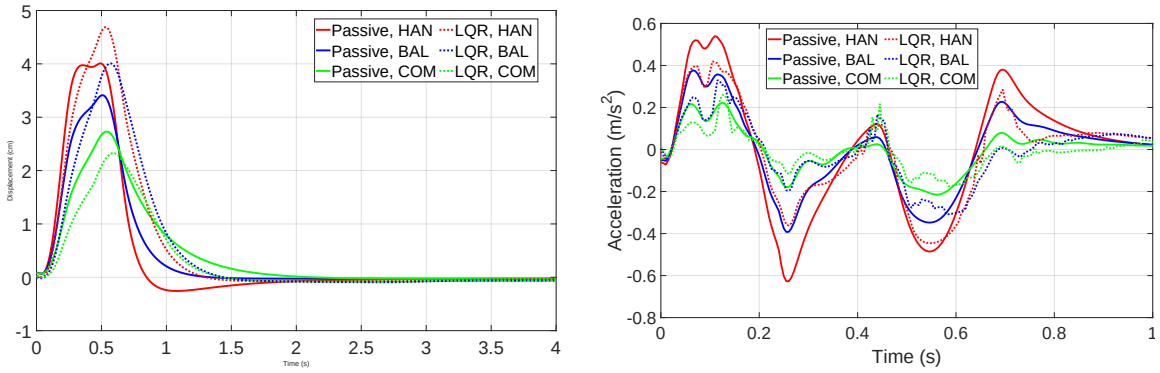

(a) UPBD

(b) UPBA

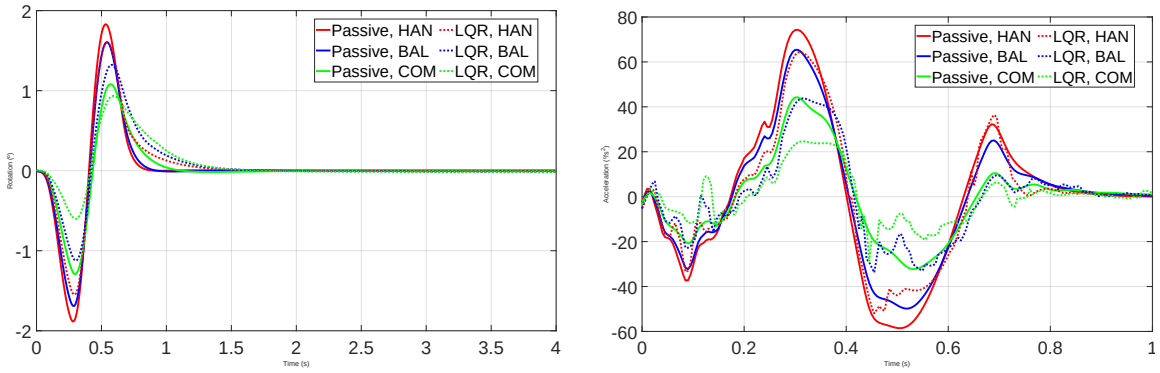

(c) UPBR

(d) UPBRA

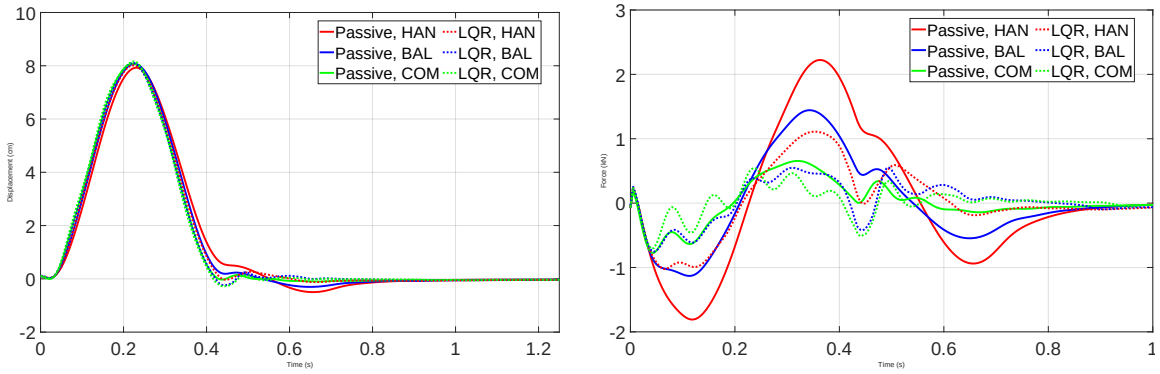

(e) LWBD

(f) Contact Force

Figure 5.36. Time domain half vehicle responses on a MR SAS system with the LQR controller over a bump obstacle.

The peak LWBD is one point where it got outperformed by the Hybridhook system, even though it was by very little. It also had roughly the same results as the passive system, and the Hybridhook still offers a worse trade-off.

The LQR failed in the peak UPBD in Figure 5.36a for the Handling and Balanced controllers and the peak UPBA in Figure 5.36b for the Comfort controller. However, the former converged

very quickly into the steady state, which was a prominent weak spot of the Hybridhook in both 1/4 and 1/2 systems, while the latter only occurred during a very short period of time, as evidenced by the UPBA RMS decreasing. Another thing of note is that, compared to the 1/4 vehicle, there was a lot more jerk in the UPBA, which is also evident in the UPBRA in Figure 5.36d. The UPBR in Figure 5.36c was, by contrast, a strict upgrade from its passive case, having far lower peaks and total RMS with comparable settling times.

The LQR controller once again performed much better than the Passive and Hybridhook cases. It had lower acceleration values across the board, and while it did not improve the LWBD, it did improve the peak Contact Force. Despite not being trained for diminishing rotational vibrations, it performed about as well on it as it did for vertical quantities.

Overall, the suspension optimized for the 1/4 vehicle with the LQR controller managed to improve the performance of the 1/2 vehicle, even it did not do it as well as it did for the 1/4 vehicle. It also struggled on the peak UPBD, which it did not in the 1/4 vehicle, showing that while most results can be generalized into the 1/2 vehicle from the 1/4 vehicle, that should be done with some caution as there are no guarantees.

Table 5.35. Relative performance values of the LQR and passive half vehicle Case Studies under a Bump excitation.

Ratios	UPBA RMS	Peak UPBA	UPBRA RMS	Peak UPBRA
Handling	76.7%	71.1%	86.1%	86.7%
Balanced	77.1%	84.1%	71.8%	66.9%
Comfort	85.2%	116.1%	65.8%	64.8%
Ratios	Peak UPBD	Peak UPBR	Peak LWBD	Peak Contact Force
Handling	117.0%	85.1%	101.1%	49.9%
Balanced	117.5%	78.1%	100.4%	52.3%
Comfort	85.3%	72.3%	101.0%	91.8%

5.4.4.3 Linear Rise results

The Linear Rise excitation results are laid out in Figures 5.37a, 5.37b, 5.37c, 5.37d, 5.37e and 5.37f. The numerical values for the data is available in Table 5.24.

The LQR results are similar to its 1/4 vehicle results. The Balanced, Handling and Comfort controller all had similar but worse results in the half vehicle, with the Comfort controller consistently performing worse than the passive case as well. Figures 5.37a to 5.37f all show unremarkable results, with stable behaviors and uncoupled excitations. It did, however, show good qualitative parameters, such as convergence times and low jitter.

Overall, the results confirm that the LQR controller is able to provide performance improvements for the 1/2 vehicle when optimized for a 1/4 vehicle model, but the performance improvements will not be as big.

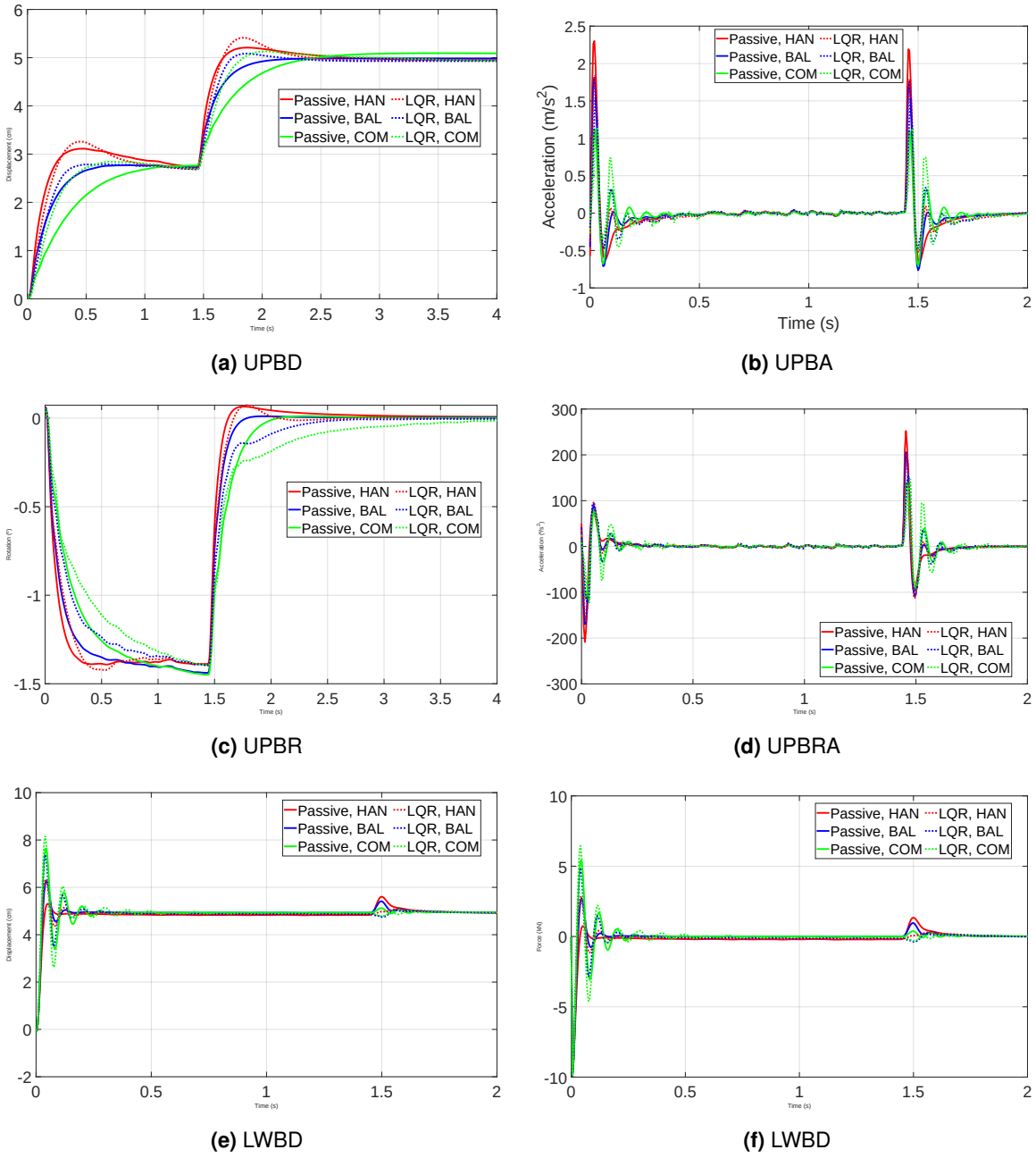

(a) UPBD **(b)** UPBA

(c) UPBR **(d)** UPBRA

(e) LWBD **(f)** LWBD

Figure 5.37. Time domain half vehicle responses on a MR SAS system with the LQR controller over a linear rise obstacle.

5.4.5 SDRE case studies

As has been established, the SDRE results will be shown overlaid with the Passive results, so as to make comparisons easier with other controllers.

5.4.5.1 ISO results

The frequency domain half vehicle results for the ISO excitation are in Figures 5.38a, 5.38b, 5.38c, 5.38d and 5.38e.

Table 5.36. Relative performance values of the LQR and passive half vehicle Case Studies under a Linear Rise excitation.

Ratios	UPBA RMS	Peak UPBA	UPBRA RMS	Peak UPBRA
Handling	79.1%	80.2%	91.5%	80.7%
Balanced	83.4%	85.0%	90.0%	76.0%
Comfort	110.9%	102.1%	111.8%	106.0%
Ratios	Peak UPBD	Peak UPBR	Peak LWBD	Peak contact force
Handling	103.9%	102.2%	113.2%	100.0%
Balanced	102.0%	97.1%	117.3%	100.1%
Comfort	100.7%	96.3%	107.0%	100.2%

The SDRE results are very similar to their Passive counterparts. Slight differences are seen in some select regions, such the tire oscillations due to the vehicle velocity-axis ratio in Fig. 5.38e being slightly attenuated in the Balanced case, the low frequency gain being slightly lower in the UPBA in Figure 5.38b and UPBD in Figure 5.38a, and the low frequency gain being higher in the UPBR in Figure 5.38c and UPBRA in Figure 5.38d. These results are, like in the 1/4 vehicle case, similar to the LQR results but with fewer improvements.

5.4.5.2 Bump results

The Bump excitation results are laid out in Figures 5.39a, 5.39b, 5.39c, 5.39d, 5.39e and 5.39f. The numerical values for the data is available in Table 5.25.

The SDRE controller had mixed results. Some values improved over the Passive system, while other increased by a lot. The best performing controller amongst the three cases was the Handling case.

The Handling controller improved the peak Contact Force and peak LWBD in Figures 5.39f and 5.39e respectively, as well as the peak and RMS UPBA in Figure 5.39b, but showed greater peaks for the UPBD and UPBR in Figures 5.39a and 5.39c respectively. The latter actually increased by more than twofold, an increase not seen in any other instance. This demonstrates that the SDRE displacement issues in the 1/4 vehicle, while not directly present here, still were a symptom of a poor displacement control. The UPBRA in Figure 5.39d also saw a peak and RMS increase, putting the Handling controller under both its Hybridhook and LQR counterpart.

The Balanced controller performance was either equal or worse than its Passive counterpart for the comfort metrics, showing a worse peak and RMS UPBRA, worse peak UPBD, and UPBR, and longer convergence times for the displacements. The handling metrics, the peak Contact Force and the LWBD, were improved.

The Comfort controller showed a performance level similar to the passive system as well, but failed to improve in most areas. Its peak Contact Force, as well as its UPBA RMS, were nearly the same as the Passive, while its peak UPBR,UPBD and UPBRA were worse. It performed worse in the displacement category, as did all SDRE controllers tested. It managed, at the very least, to improve the UPBRA peak and RMS values, as well as the LWBD, improving both

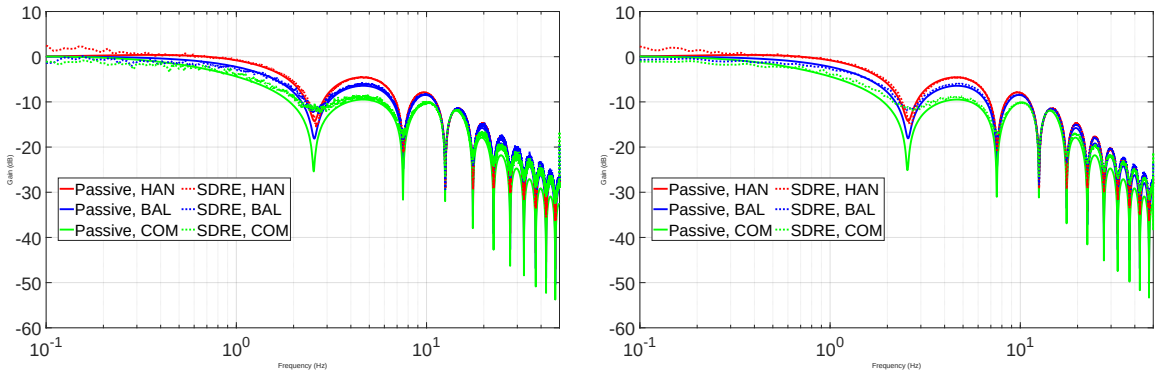

(a) UPBD

(b) UPBA

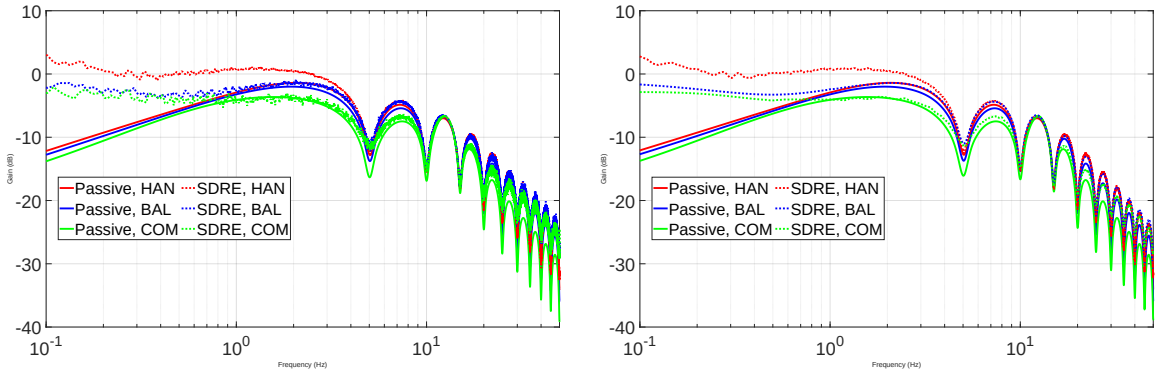

(c) UPBR

(d) UPBRA

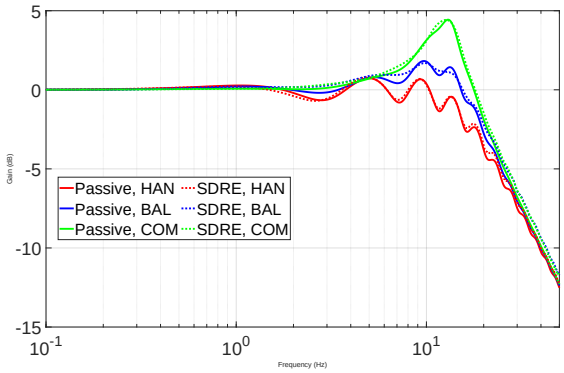

(e) LWBD

Figure 5.38. Frequency domain half vehicle responses on a MR SAS system with the SDRE controller under an ISO excitation.

comfort and handling metrics.

Overall, the 1/2 vehicle results for the Bump excitation demonstrate the SDRE controller struggling even more to bring performance improvements to its vehicle. This might be because the SDRE controller requires fine tuning, or just because the cases used were not very good to begin with.

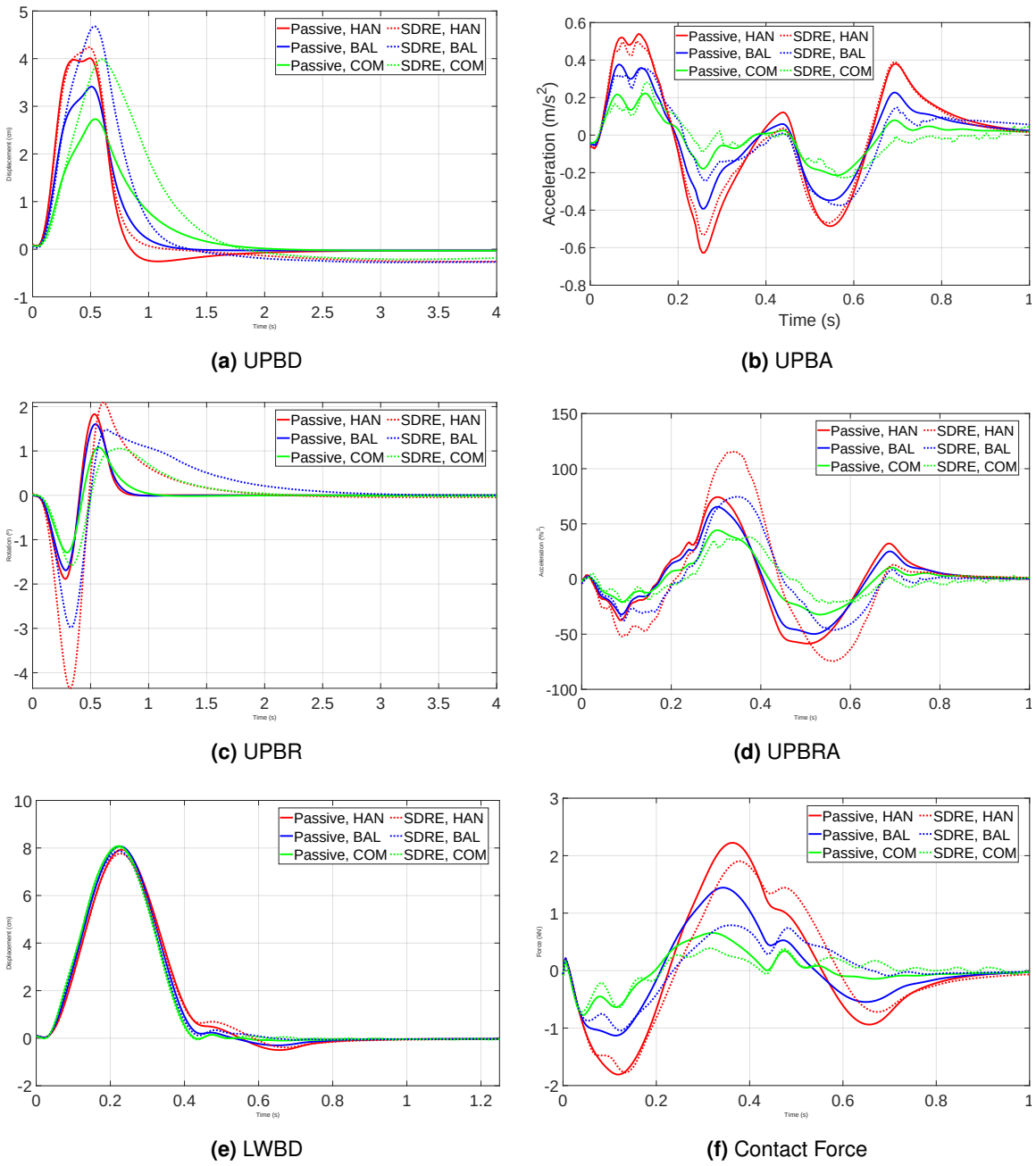

(a) UPBD **(b)** UPBA

(c) UPBR **(d)** UPBRA

(e) LWBD **(f)** Contact Force

Figure 5.39. Time domain half vehicle responses on a MR SAS system with the SDRE controller over a bump obstacle.

5.4.5.3 Linear Rise results

The Linear Rise excitation results are laid out in Figures 5.40a, 5.40b, 5.40c, 5.40d, 5.40e and 5.40f. The numerical values for the data is available in Table 5.26.

The Linear Rise results demonstrated some flaws of the solutions obtained for the SDRE controller at extreme degrees. The peak UPBR in Figure 5.40c shot to very high values, and all cases overshot their UPBD in Figure 5.40a.

Despite the issues with the displacements, the Comfort oriented vehicle managed to improve all acceleration metrics over its passive counterpart, having RMS values even better

Table 5.37. Relative performance values of the SDRE and passive half vehicle Case Studies under a Bump excitation.

Ratios	UPBA RMS	Peak UPBA	UPBRA RMS	Peak UPBRA
Handling	93.0%	84.7%	145.4%	155.3%
Balanced	97.5%	95.4%	110.0%	114.0%
Comfort	100.2%	125.8%	87.0%	85.8%
Ratios	Peak UPBD	Peak UPBR	Peak LWBD	Peak contact force
Handling	105.7%	230.9%	85.6%	97.9%
Balanced	137.1%	176.3%	72.2%	97.6%
Comfort	146.1%	122.4%	92.8%	99.2%

than the LQR Comfort case. Its peak LWBD in Figure 5.40e was also lower than the LQR, even if greater than the passive case. It failed to improve the peak Contact Force in Figure 5.40f, both for the first and second peak, but was at least about as good as the LQR. The Balanced case followed a similar path, but with more modest improvement in the acceleration metrics which saw it outperformed by the LQR and Hybridhook Balanced cases. The Handling case performed the worst, having a nearly equal RMS and peak UPBA in Figure 5.40b, worse UPBRA values in Figure 5.40d and the worst displacement results amongst all cases and controllers. It did maintain the peak LWBD and Contact Force equal to the Passive case at the very least. Compared to the Hybridhook, the same commentaries made for the LQR are valid, as they had exactly the same relative performance.

These results allow the conclusion that, while the SDRE did succeed in some isolated cases, it could not reliably improve the performance of the 1/2 vehicle model. The Comfort case performed the best in most cases, and it was indeed the case which performed best relative to its passive counterpart in the optimization. The few success cases of the SDRE controller do show, however, that the controller has great potential. If properly designed and tuned, its capacity to deal with non-linear changes may allow its parameters to be optimized under limited conditions but still perform optimally far outside their training range.

Table 5.38. Relative performance values of the SDRE and passive half vehicle Case Studies under a Linear Rise excitation.

Ratios	UPBA RMS	Peak UPBA	UPBRA RMS	Peak UPBRA
Handling	96.4%	97.3%	110.3%	106.9%
Balanced	88.3%	87.4%	95.9%	98.2%
Comfort	85.9%	79.2%	88.0%	83.7%
Ratios	Peak UPBD	Peak UPBR	Peak LWBD	Peak Contact Force
Handling	121.2%	551.8%	101.6%	100.0%
Balanced	116.9%	386.1%	107.4%	99.9%
Comfort	114.8%	276.2%	106.6%	100.0%

5.4.6 Control statistics and results

The control results for the half vehicle are very similar to the quarter vehicle results, and as such will only be superficially commented on. The Figures for the control action are presented

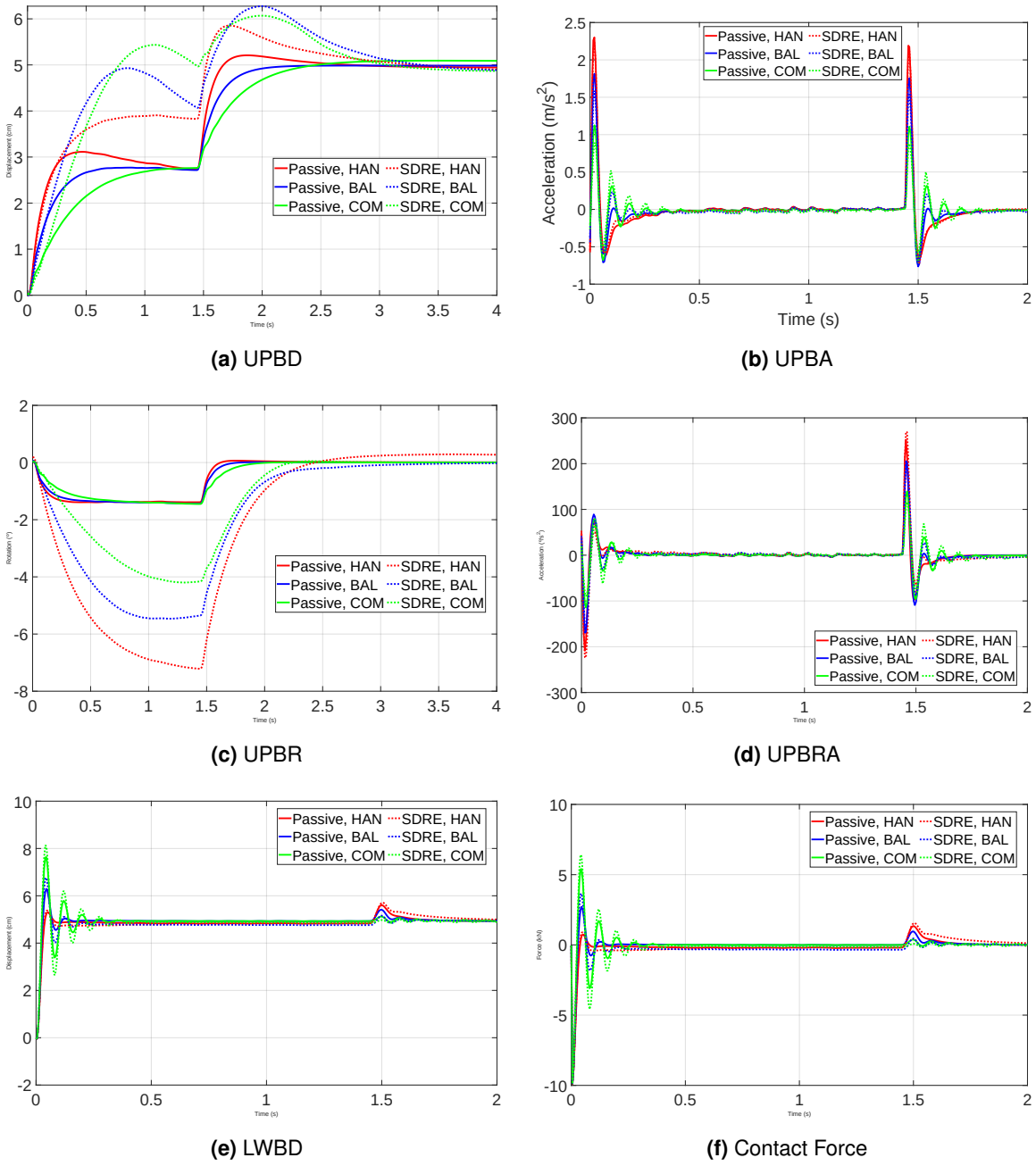

(a) UPBD **(b)** UPBA

(c) UPBR **(d)** UPBRA

(e) LWBD **(f)** Contact Force

Figure 5.40. Time domain half vehicle responses on a MR SAS system with the SDRE controller over a linear rise obstacle.

in Appendix C. All data refers to the front wheel suspension.

The command and current results for the ISO excitation as well as the Bump and Linear Rise obstacles are displayed in Table 5.39.

The results for the ISO excitation are more similar to those of quarter vehicle deterministic obstacles than of the random ones. The LQR showed higher saturation values than the Hybridhook, but had similar or better performance in most metrics. The SDRE force saturation percentage still was 100%. The force saturation still had a tendency of increasing as controllers focused more on comfort, but the change is no longer mostly explained by greater semi-active

Table 5.39. Control values of the half vehicle Case Studies under different excitations. The variables F_{sat}, F_{sas} and A_{avg} stand for percentage of time under saturation due to force constraints, percentage of time under saturation due to semi-active constraints, and average current.

ISO				
Controller	Handling	Balanced	Comfort	Metric
Hybridhook	64.4%	70.1%	71.2%	F_{sat}
	57.8%	55.0%	57.9%	F_{sas}
	1.44 A	3.07 A	2.72 A	A_{avg}
LQR	69.3%	75.2%	89.4%	F_{sat}
	42.0%	47.7%	47.6%	F_{sas}
	5.36 A	5.42 A	6.21 A	A_{avg}
SDRE	100%	100%	100%	F_{sat}
	65.2%	48.1%	54.2%	F_{sas}
	0.38	1.91 A	1.62 A	A_{avg}
Bump				
Controller	Handling	Balanced	Comfort	Metric
Hybridhook	80.0%	81.5%	76.0%	F_{sat}
	39.5%	47.0%	52.5%	F_{sas}
	7.59 A	6.47 A	4.37 A	A_{avg}
LQR	85.5%	83.5%	96.0%	F_{sat}
	38.5%	40.5%	47.5%	F_{sas}
	8.93 A	8.17 A	9.29 A	A_{avg}
SDRE	100%	100%	100%	F_{sat}
	79.5%	32.0%	54.5%	F_{sas}
	0.88 A	1.09 A	1.10 A	A_{avg}
Linear Rise				
Controller	Handling	Balanced	Comfort	Metric
Hybridhook	73.5%	68.8%	89.3%	F_{sat}
	56.3%	47.3%	52.8%	F_{sas}
	3.43 A	4.53 A	7.33 A	A_{avg}
LQR	99.3%	99.3%	84.8%	F_{sat}
	41.8%	45.0%	48.8%	F_{sas}
	11.40 A	10.77 A	7.24 A	A_{avg}
SDRE	100%	100%	100%	F_{sat}
	46.0%	73.8%	64.8%	F_{sas}
	5.29 A	0.40 A	1.17 A	A_{avg}

saturation percentages. The time extents in which there was saturation due to the semi-active nature of the controller, instead, changed without a pattern.

The Bump and Linear Rise results also show higher saturation values. There was not homogeneous trend: some cases had greater saturation in the Linear Rise obstacle, and some in the Bump. The LQR controller reached almost 100% saturation in the Linear Rise case, similar to the SDRE, but this showed no discernible trend either: while the latter had better results in the Comfort case, the former had better results in the Handling case. The LQR had very high average current values as well, but once again, what impact that had is not easily noticeable.

These results communicate that when compared to the quarter vehicle, the half vehicle control commands are similar in shape and magnitude, but show greater force and semi-active saturation. This follows the trend of other results for the half vehicle, which are similar but inferior to the quarter vehicle. The lack of clear trends the same way the quarter vehicle under ISO excitation had is possibly a reflection of no optimization being performed in the system, as the same absence of pattern emerged in the non-optimized scenarios for the quarter vehicle.

5.4.7 Case Studies performance overview

As with the 1/4 vehicle system, the 1/2 vehicle results of the previous sections have been compiled here for ease of view and comparison. Table 5.40 has the relative performance between each controller on a MR SAS system and their passive counterparts for the Bump excitation case, while Table 5.41 has the data for the Linear Rise excitation.

Table 5.40. Relative performance values of the half vehicle MR SAS systems and passive case studies under a Bump excitation. Cells colored according to value. Green square indicates the best results for that metric in the test. White text added for better contrast.

Hybridhook				
Ratios	UPBA RMS	Peak UPBA	UPBRA RMS	Peak UPBRA
Handling	118.1%	101.8%	118.1%	117.4%
Balanced	104.4%	129.9%	86.9%	85.8%
Comfort	134.5%	145.1%	94.4%	83.3%
Ratios	Peak UPBD	Peak UPBR	Peak LWBD	Peak contact force
Handling	137.4%	104.9%	95.2%	71.9%
Balanced	154.4%	86.4%	99.4%	55.3%
Comfort	170.4%	81.6%	100.4%	90.6%
LQR				
Ratios	UPBA RMS	Peak UPBA	UPBRA RMS	Peak UPBRA
Handling	76.7%	71.1%	86.1%	86.7%
Balanced	77.1%	84.1%	71.8%	66.9%
Comfort	85.2%	116.1%	65.8%	64.8%
Ratios	Peak UPBD	Peak UPBR	Peak LWBD	Peak Contact Force
Handling	117.0%	85.1%	101.1%	49.9%
Balanced	117.5%	78.1%	100.4%	52.3%
Comfort	85.3%	72.3%	101.0%	91.8%
SDRE				
Ratios	UPBA RMS	Peak UPBA	UPBRA RMS	Peak UPBRA
Handling	93.0%	84.7%	145.4%	155.3%
Balanced	97.5%	95.4%	110.0%	114.0%
Comfort	100.2%	125.8%	87.0%	85.8%
Ratios	Peak UPBD	Peak UPBR	Peak LWBD	Peak contact force
Handling	105.7%	230.9%	85.6%	97.9%
Balanced	137.1%	176.3%	72.2%	97.6%
Comfort	146.1%	122.4%	92.8%	99.2%

As with the 1/4 vehicle system, the LQR system provided the best performance uplift overall in the Bump case. The SDRE system performance remained better than expected,

outperforming the Hybridhook system in many cases in which it did not for the quarter vehicle system. Still, not shown in the tables are the qualitative issues observed with steady state values and convergence times.

Table 5.41. Relative performance values of the half vehicle MR SAS systems and passive case studies under a Linear Rise excitation. Cells colored according to value. Green square indicates the best results for that metric in the test. White text added for better contrast.

Hybridhook				
Ratios	UPBA RMS	Peak UPBA	UPBRA RMS	Peak UPBRA
Handling	82.8%	80.2%	93%	82.6%
Balanced	70.9%	69.1%	81.8%	55.2%
Comfort	96.4%	80.7%	103.8%	91.5%
Ratios	Peak UPBD	Peak UPBR	Peak LWBD	Peak contact force
Handling	107.8%	104.2%	113.4%	99.9%
Balanced	99.7%	78.4%	124.1%	100.1%
Comfort	96.7%	62.6%	116.9%	100.2%
LQR				
Ratios	UPBA RMS	Peak UPBA	UPBRA RMS	Peak UPBRA
Handling	79.1%	80.2%	91.5%	80.7%
Balanced	83.4%	85%	90%	76%
Comfort	110.9%	102.1%	111.8%	106%
Ratios	Peak UPBD	Peak UPBR	Peak LWBD	Peak contact force
Handling	103.9%	102.2%	113.2%	100%
Balanced	102%	97.1%	117.3%	100.1%
Comfort	100.7%	96.3%	107%	100.2%
SDRE				
Ratios	UPBA RMS	Peak UPBA	UPBRA RMS	Peak UPBRA
Handling	96.2%	97%	110.2%	106.8%
Balanced	88.1%	87.4%	96.2%	98.2%
Comfort	86.9%	78.9%	89.5%	83.6%
Ratios	Peak UPBD	Peak UPBR	Peak LWBD	Peak Contact Force
Handling	112.4%	551.8%	101.9%	100%
Balanced	125.9%	386.1%	107.5%	99.9%
Comfort	119.2%	276.2%	106.6%	99.9%

The Linear Rise results resemble the quarter vehicle results, with once again the LQR system being the best. The Hybridhook controller showed bad qualitative results, with lots of jitter and extremely long settling times. The SDRE, in turn, showed very high displacement values. This might be due to the damper model used, but nonetheless the LQR controller comes out on top in those metrics as well.

It is possible to observe that the SDRE managed to perform well in many metrics, specially with the Comfort case, being almost comparable to the LQR. Likewise, the Hybridhook controller was the best performer for the Balanced case. However, only the LQR did not suffer with the qualitative issues mentioned.

Overall, these results reinforce the findings of the quarter vehicle model, with the LQR controller being the best. While the controllers mostly succeeded in subduing the vibrations,

including the new angular metrics, the performance uplift was less than in the quarter vehicle case, likely due to the aforementioned new degrees of freedom. The potential of the SDRE controller was demonstrated, but issues with the current iteration were also identified.

6 CONCLUSIONS AND FUTURE PERSPECTIVES

The present work set out to evaluate the effectiveness of a semi-active suspension in controlling a vehicle comfort and safety metrics when equipped with a realistically modeled MR damper. To this end, a toolbox of vehicle simulation routines was developed on the Simulink environment, and an array of simulations were performed. A new phenomenological model based on the Sigmoid model (Wang *et al.*, 2004) model was proposed. Its effectiveness was compared to three other notorious models: the Bingham, Bouc-wen and the original model (Wang *et al.*, 2004). Dynamical behavior simulations were carried out on the 1/2 and 1/4 vehicle models, and the effect of both the Hook family (Skyhook and Groundhook) and the Optimal control strategy family (LQR and SDRE) was observed in the time and frequency domain.

The present work proposed a modification of the Sigmoid MR damper model put forth by Wang *et al.* (2004). The new model modified key parameters, proposing 5 additional degrees of freedom to the system. Furthermore, a modification for the instantaneous/peak velocity parameter was proposed for both Sigmoid based models. The new proposed formulation showed an 8,6% better experimental data fit over the next best performing model. Of the 5 new degrees of freedom proposed, 4 were used and 1 was rejected as irrelevant by the optimization. The genetic algorithm was effective at performing the optimal parametric identification of all models.

The new expression for the peak velocity parameter was observed to improve the results of simulations under random excitations with mass elements, a setup more representative of the conditions found by an MR damper inserted in a vehicle. Both the Wang and Wang-II model showed improvements, with the changes preventing divergence under high acceleration conditions and grounding the hysteresis behavior on past excitation conditions as opposed to future ones. These results have been published into two articles, with most results being contained in the congress publication (Ferreira *et al.*, 2023) and some small amounts in the journal publication (Ferreira *et al.*, 2025). This modification was successfully applied on the subsequent vehicle simulations.

The results for the 1/4 vehicle simulations showed that all controllers improved MR damper behavior. The suspension parameters were successfully obtained from a multi-objective optimization process performed by the NSGA-II. Solution diversity was shown by the presence of a wide Pareto optimal frontier. The LQR controller showed the best performance in both the optimization and the case studies. The Hybridhook and SDRE controller traded blows, with the Hybridhook outperforming it in most of the optimization and some case studies, while the SDRE overcame the Hybridhook in a few cases. The 1/4 vehicle results for the Passive and

LQR vehicle were obtained as the result of writing an article, with it being currently under peer review (Ferreira *et al.*, 2025). Some preliminary results, which were not included in the thesis, were also published as a congress article into (Ferreira and Morais, 2023).

With regards to the 1/2 car model, the results observed in the 1/4 car model were only partially replicated. The improvement was inconsistent, and some metrics were better in certain contexts but worse in others. However, the overarching picture was similar to the 1/4 vehicle. The LQR performed best by reducing the low frequency vertical vibrations while keeping the tire vibrations under control. The Hybridhook came in second with fewer improvements and more instances of performance degradation over the Passive case. The SDRE performed overall worse for the 1/2 vehicle, being in most instances the worst controller amongst the ones tested by making the performance worse and having many qualitative issues. Despite this, it did have an unusually good result in one specific instance.

These findings show that the results obtained in the simpler model can be extrapolated, to some extent, to more complete models of similar parameters. However, the results of the 1/4 vehicle model cannot describe more complex vehicles with very high precision. For example, the 1/4 model could not predict the interaction effects between the vehicle velocity and the wheel axis distance, nor could it take into account how its attenuation of the low frequencies bands in the vertical metrics would negatively impact the angular displacement and acceleration in the same region. This means that while behavior may be satisfactorily estimated by a lower complexity model, fine performance comparisons and the optimization of controller parameters need to be performed on higher dimensional models.

6.1 FUTURE WORKS

Many different venues may be pursued in future works. The MR damper model developed here is more accurate than the options it was put up against, but it still showed issues under certain loads which where too different from the conditions in which it was fit. Improving the MR damper model by modifying the presented model to address these issues or fitting the presented model to data that is more diverse is a clear path towards improving what has been presented thus far. Given current trends in the literature, improving the model capacity to model unknown dynamics by employing Neural Networks is a suggested path for a modification of the model.

Semi-active dampers are not the only device considered as cost effective alternatives to active suspensions for dynamical control of vehicles. Devices such as inerters, aerodynamic surfaces and even semi-active springs have been employed in the literature for the same goal, often in tandem. The analysis of such devices to the same depth as the one performed in this work might prove advantageous, as they might be able to compensate for the weak points of each other. The inclusion of additional devices also brings the possibility of a conjoint control strategy being evaluated, which opens up an additional venues for research into control schemes.

With regards to vehicle simulations, the controllers shown here are, as demonstrated in the

Theoretical Fundamentals (Chapter 2), not the only options for vehicular SAS control. Future works may expand the results obtained here by performing it with different controllers. Another option is to perform the optimization procedure employed on the 1/4 vehicle model on higher order models, such as the 1/2 or full vehicle model, allowing comparisons to be drawn between the performance of a controller optimized on a higher and lower order system.

A slightly different direction would be to expand the models into a vehicle simulator in which a human can interact with it. The vehicle models used have used estimated vehicle behavior and human comfort by employing road models and performance metrics, but by having a simulator in which a human could input commands and receive visual and vibrational feedback in real time, a more realistic comfort and safety profile of the simulated system could be assessed.

The SDRE controller tested in this thesis was not as successful as the LQR, despite the system non-linearities. More studies may be conducted on how to improve the SDRE performance for the problem at hand, in order to determine whether it is a reasonable alternative to non-linear control of MR dampers or whether these systems are beyond the controller capacity.

Lastly, while a great deal of effort has been dedicated into modeling the studied systems so their behavior closely matches that of reality, the need for experimental validations is not eliminated. Experimental testing of the vehicle models, as well as of actual fully fledged vehicles, can provide data that is more precise and which can be used for validation of the computational simulations performed. Future works may focus on the experimental reproduction of the present work's results, in order to gauge the extent with which the performed computational simulations can be utilized as a way of predicting the real world behavior of a vehicle with a MR damper.

6.2 CONCLUSION

The MR damper is a device able to provide a reasonable performance uplift at the cost of a low-moderate energy consumption. The effectiveness of the device is heavily reliant on the controller utilized as well as its tuning, with none of the evaluated control strategies being the best in all parameters. The LQR strategy performed best and was the most reliable, but it was clear that the MR damper SAS can still provide more gains than the LQR was able to realize.

The choice of whether to use the MR damper is reliant on the extent to which the controller parameters and the suspension components can be matched to it. This can process can be performed more thoroughly by employing computer simulations and optimization routines, but this requires precise descriptions of the MR damper behavior.

More studies are necessary to determine the full capacities of these highly non-linear devices, but the methods and techniques evaluated in this Thesis, coupled with the available literature, strongly suggest that MR dampers are currently a viable alternative to improving a vehicle's ride and handling qualities beyond what is possible with passive systems.

REFERENCE LIST

Abdelkareem, M. A., Xu, L., Guo, X., Ali, M. K. A., Elagouz, A., Hassan, M. A., Essa, F., and Zou, J. (2018). Energy harvesting sensitivity analysis and assessment of the potential power and full car dynamics for different road modes. *Mechanical Systems and Signal Processing*, 110:307–332. https://doi.org/10.1016/j.ymssp.2018.03.009. (Cited on pages 22, 38, 44, and 55.)

Abdul Aziz, M., Mohtasim, S. M., and Ahammed, R. (2022). State-of-the-art recent developments of large magnetorheological (MR) dampers: a review. *Korea-Australia Rheology Journal*, 34(2):105–136. https://doi.org/10.1007/s13367-022-00021-2. (Cited on pages 13, 14, 17, and 56.)

Abebaw, B., You, W.-H., Lee, J., and Lee, K. (2020). Parameter identification of bouc-wen model for magnetorheological (mr) fluid damper by a novel genetic algorithm. *Advances in Mechanical Engineering*, 12:168781402095054. https://doi.org/10.1177/1687814020950546. (Cited on pages 17 and 53.)

Aghababaei, R., Brodsky, E. E., Molinari, J.-F., and Chandrasekar, S. (2022). How roughness emerges on natural and engineered surfaces. *MRS Bulletin*, 47(12):1229–1236. https://doi.org/10.1557/s43577-022-00469-1. (Cited on page 35.)

Ahmadian, M. (2017). Magneto-rheological suspensions for improving ground vehicle's ride comfort, stability, and handling. *Vehicle System Dynamics*, 55(10):1618–1642. https://doi.org/10.1080/00423114.2017.1323106. (Cited on pages 10, 11, 12, 23, and 49.)

Ahmed, A. (2001). Ground transportation systems. In Braun, S., (ed.), *Encyclopedia of Vibration*. Elsevier, 3rd edition. (Cited on page 38.)

Akgül, T. and Unluturk, A. (2023). Comparison of pso-lqr and pso-pid controller performances on a real quarter vehicle suspension. In *2023 Innovations in Intelligent Systems and Applications Conference (ASYU)*, pages 1–6. https://doi.org/10.1109/ASYU58738.2023.10296830. (Cited on pages 58 and 59.)

Aljarbouh, A. and Fayaz, M. (2020). Hybrid modelling and sliding mode control of semi-active suspension systems for both ride comfort and road-holding. *Symmetry*, 12. (Cited on page 50.)

American National Standards Institution (2011). *Telecom Glossary 2000* (American National Standard: T1.523-2001). Technical report. (Cited on page 38.)

Bakker, E., Nyborg, L., and Pacejka, H. B. (1987). Tyre modelling for use in vehicle dynamics studies. *SAE Transactions*, 96:190–204. http://www.jstor.org/stable/44470677 (Accessed: 2024-03-05). (Cited on page 29.)

Boreiry, M., Ebrahimi-Nejad, S., and Marzbanrad, J. (2019). Sensitivity analysis of chaotic vibrations of a full vehicle model with magnetorheological damper. *Chaos, Solitons & Fractals*, 127:428–442. https://www.sciencedirect.com/science/article/pii/S0960077919302577. (Cited on pages 22, 55, and 56.)

Brasil (2018). Presidência da República, Secretaria-Geral, Subchefia para Assuntos Jurídicos, Lei nº 13.755, de 10 de dezembro de 2018. Estabelece requisitos obrigatórios para a comercialização de veículos no Brasil; institui o Programa Rota 2030 - Mobilidade e Logística; dispõe sobre o regime tributário de autopeças não produzidas; e altera as Leis n º 9.440, de 14 de março de 1997, 12.546, de 14 de dezembro de 2011, 10.865, de 30 de abril de 2004, 9.826, de 23 de agosto de 1999, 10.637, de 30 de dezembro de 2002, 8.383, de 30 de dezembro de 1991, e 8.989, de 24 de fevereiro de 1995, e o Decreto-Lei nº 288, de 28 de fevereiro de 1967. (Cited on page 1.)

Buhari, R. and Seblan, A. A. (2022). Road profile generation based on real road profile for the whole life pavement performance input data. *IOP Conference Series: Earth and Environmental Science*, 1022(1):012037. https://dx.doi.org/10.1088/1755-1315/1022/1/012037. (Cited on page 36.)

Chen, C., Ma, R., and Ma, W. (2023). Ga-lqr for vehicle semi-active suspension with bilstm inverse model of magnetic rheological damper. *Transactions of The Canadian Society for Mechanical Engineering*, 47(3):423–435. https://www.sciencedirect.com/science/article/pii/S0315897723000083. (Cited on pages 55 and 56.)

Chen, M. Z., Hu, Y., Li, C., and Chen, G. (2014). Semi-active suspension with semi-active inerter and semi-active damper. *IFAC Proceedings Volumes*, 47(3):11225–11230. 19th IFAC World Congress. https://doi.org/10.3182/20140824-6-ZA-1003.00138. (Cited on pages 23 and 56.)

Chen, S.-A., Wang, J.-C., Yao, M., and Kim, Y.-B. (2017). Improved optimal sliding mode control for a non-linear vehicle active suspension system. *Journal of Sound and Vibration*, 395:1–25. https://www.sciencedirect.com/science/article/pii/S0022460X1730113X. (Cited on page 58.)

CONTRAN (2022). Manual brasileiro de sinalização de trânsito. In *Dispositivos auxiliares*, volume VI, chapter 5.1, pages 64–67. CONTRAN. https://www.gov.br/transportes/pt-br/assuntos/transito/arquivos-senatran/docs/copy_of___06___MBST_Vol._VI___Dispositivos_Auxiliares.pdf. (Cited on pages 33, 34, and 67.)

Dagnall, H. (1986). *Exploring surface texture*. Rank Taylor Hobson. (Cited on page 35.)

Davis, B. R. and Thompson, A. G. (2001). Power spectral density of road profiles. *Vehicle System Dynamics*, 35(6):409–415. https://doi.org/10.1076/vesd.35.6.409.2039. (Cited on page 39.)

de Lima, J. G. M., de Morais, M. V. G., and de Araújo, M. L. (2012). Avaliação qualitativa do comportamento não linear de modelo de meio veículo. *VII Congresso Nacional de Engenharia Mecânica*. (Cited on pages 27 and 138.)

Deb, K., Agrawal, R. B., *et al.* (1995). Simulated binary crossover for continuous search space. *Complex systems*, 9(2):115–148. (Cited on page 54.)

Deb, K. and Deb, D. (2014). Analysing mutation schemes for real-parameter genetic algorithms. *International Journal of Artificial Intelligence and Soft Computing*, 4(1):1–28. (Cited on page 55.)

Deb, K., Pratap, A., Agarwal, S., and Meyarivan, T. (2002). A fast and elitist multiobjective genetic algorithm: Nsga-ii. *IEEE Transactions on Evolutionary Computation*, 6(2):182–197. https://doi.org/10.1109/4235.996017. (Cited on pages 53, 54, and 55.)

Dharankar, C., Hada, M., and Chandel, S. (2016). Numerical generation of road profile through spectral description for simulation of vehicle suspension. *Journal of the Brazilian Society of Mechanical Sciences and Engineering*, 39. https://doi.org/10.1007/s40430-016-0615-6. (Cited on pages 35, 36, 38, 39, and 40.)

Do, A., Sename, O., Dugard, L., and Soualmi, B. (2011). Multi-objective optimization by genetic algorithms in h∞/lpv control of semi-active suspension. *IFAC Proceedings Volumes*, 44(1):7162–7167. 18th IFAC World Congress. https://doi.org/10.3182/20110828-6-IT-1002.01950. (Cited on pages 53 and 59.)

Dominguez, A., Sedaghati, R., and Stiharu, I. (2008). Modeling and application of mr dampers in semi-adaptive structures. *Computers & Structures*, 86:407–415. https://doi.org/10.1016/j.compstruc.2007.02.010. (Cited on page 17.)

Els, P., Theron, N., Uys, P., and Thoresson, M. (2007). The ride comfort vs. handling compromise for off-road vehicles. *Journal of Terramechanics*, 44(4):303–317. https://doi.org/10.1016/j.jterra.2007.05.001. (Cited on page 2.)

Ergin, T. and Yatak, M. Ö. (2023). Optimal control method of semi-active suspension system and processor-in-the-loop verification. *Applied Sciences*, 13(20). https://www.mdpi.com/2076-3417/13/20/11253. (Cited on pages 38 and 58.)

Erlicher, S. and Point, N. (2004). Thermodynamic admissibility of bouc–wen type hysteresis models. *Comptes Rendus Mécanique*, 332(1):51–57. https://doi.org/10.1016/j.crme.2003.10.009. (Cited on page 17.)

Ferreira, L. D. C. R. (2022). Modelagem dinâmica do comportamento de amortecedores magnetoreologico para aplicação em suspensão veicular semi-ativa. [Bachelor's thesis, Universidade de Brasília. (Cited on pages 27, 62, 108, and 182.)

Ferreira, L. D. C. R., Avila, S., and Morais, M. (2022). Parametric optimization of quarter vehicle suspension model by response map technique. In *Proc. of the XLIII Ibero-Latin American Congress on Computational Methods in Engineering*. (Cited on pages 23, 69, 79, 84, and 108.)

Ferreira, L. D. C. R. and Morais, M. (2023). Optimization of the lqr and sdre control scheme for a non-linear semi-active mr damper on a quarter vehicle model. In *Proc. of the 27th International Congress of Mechanical Engineering*. https://publicacoes.softaliza.com.br/cilamce2023/article/view/5137. (Cited on pages 7, 23, 48, and 164.)

Ferreira, L. D. C. R., Morais, M., and Avila, S. (2025). Lqr semi-active control and optimization of quarter vehicle model with a sigmoid model of magnetorheological damper. *Manuscript submitted for publication*. (Cited on pages 7, 69, 84, 94, 105, 109, 110, 111, 112, 113, 115, 116, 117, 118, 119, 121, 122, 123, 125, 126, 127, 128, 129, 130, 131, 163, and 164.)

Ferreira, L. D. C. R., Morais, M., and Silva, D. M. (2023). Modelling mr dampers under non-harmonic excitations through logistic curve models. In *Proc. of the XLIV Ibero-Latin American Congress on Computational Methods in Engineering*. (Cited on pages 7, 14, 15, 16, 19, 53, 101, 102, 103, 104, and 163.)

Fleps-Dezasse, M. and Brembeck, J. (2016). Lpv control of full-vehicle vertical dynamics using semi-active dampers. *IFAC-PapersOnLine*, 49(11):432–439. 8th IFAC Symposium on Advances in Automotive Control AAC 2016. https://doi.org/10.1016/j.ifacol.2016.08.064. (Cited on pages 22, 32, 39, and 53.)

Fuller, A. T. (1963). Bibliography of pontryagm's maximum principle. *Journal of Electronics and Control*, 15(5):513–517. https://doi.org/10.1080/00207216308937602. (Cited on page 45.)

Gao, J. and Li, H. (2023). Tuning parameters of the fractional order pid-lqr controller for semi-active suspension. *Electronics*, 12:4115. https://doi.org/10.3390/electronics12194115. (Cited on page 58.)

García-Pozuelo, D., Gauchia, A., Olmeda, E., and Diaz, V. (2015). Bump modeling and vehicle vertical dynamics prediction. *Advances in Mechanical Engineering*, 6:736576–736576. https://doi.org/10.1155/2014/736576. (Cited on pages 32 and 33.)

Gawronski, W. (2004). *Advanced Structural Dynamics and Active Control of Structures*. Springer, 1st edition. (Cited on pages 41, 46, and 48.)

Ghoniem, M., Awad, T., and Mokhiamar, O. (2020). Control of a new low-cost semi-active vehicle suspension system using artificial neural networks. *Alexandria Engineering Journal*, 59(5):4013–4025. https://doi.org/10.1016/j.aej.2020.07.007. (Cited on page 59.)

Gillespie, T. D. (2021). *Fundamentals of Vehicle Dynamics*. SAE International, 2nd edition. (Cited on pages 2, 3, 8, 9, 10, 11, 22, 23, 29, 30, 38, 40, 42, 43, and 56.)

Gomes, P., Morais, M., and Teixeira, E. (2023). Otimização paramétrica de modelo linear de ¼ veículo excitada pelo perfil de pista aleatório da iso 8608:2016. *Revista Interdisciplinar de Pesquisa em Engenharia*, 9:11–26. (Cited on page 43.)

Gong, S. (1993). *Study of in-plane dynamics of tires*. [PhD thesis, Technical University of Delft. https://ui.adsabs.harvard.edu/abs/1993PhDT.....25G. (Cited on page 29.)

Han, K., Hu, Y., Zeng, D., Yu, Y., Xiao, L., Yang, J., Liu, W., and Gao, L. (2024). Vehicle attitude control of magnetorheological semi-active suspension based on multi-objective intelligent optimization algorithm. *Actuators*, 13(12). https://www.mdpi.com/2076-0825/13/12/466. (Cited on page 53.)

Hassan, M., Elsayed, A., El-Souhily, B., Elgamal, H., and Elshabasy, M. M. (2023). Investigating the effect of augmenting the anti-roll-bar with a torsional-dynamic-absorber on the handling-stability and the ride-comfort of the off-road-vehicles. *Alexandria Engineering Journal*, 81:29–45. https://www.sciencedirect.com/science/article/pii/S1110016823007974. (Cited on page 56.)

He, H., Li, Y., Clare, L., Jiang, J. Z., Al Sakka, M., Dhaens, M., Burrow, S., Neild, S., and Conn, A. (2023). A configuration-optimisation method for passive-active-combined suspension design. *International Journal of Mechanical Sciences*, 258:108560. https://www.sciencedirect.com/science/article/pii/S0020740323004629. (Cited on page 56.)

He, H., Li, Y., Jiang, J. Z., Burrow, S., Neild, S., and Conn, A. (2024). Enhancing the trade-off between ride comfort and active actuation requirements via an inerter-based passive-active-combined automotive suspension. *Vehicle System Dynamics*, 62(3):556–579. https://doi.org/10.1080/00423114.2023.2184703. (Cited on pages 55 and 56.)

He, L., Pan, Y., He, Y., Li, Z., Królczyk, G., and Du, H. (2022). Control strategy for vibration suppression of a vehicle multibody system on a bumpy road. *Mechanism and Machine Theory*, 174:104891. https://www.sciencedirect.com/science/article/pii/S0094114X22001537. (Cited on page 57.)

Hong, K.-S., Sohn, H.-C., and Hedrick, J. K. (2000). Modified Skyhook Control of Semi-Active Suspensions: A New Model, Gain Scheduling, and Hardware-in-the-Loop Tuning . *Journal of Dynamic Systems, Measurement, and Control*, 124(1):158–167. https://doi.org/10.1115/1.1434265. (Cited on pages 22 and 59.)

Horn, R. A. and Johnson, C. R. (2013). *Matrix analysis*. Cambridge Press, 2 edition. (Cited on page 75.)

Hrovat, D., Barak, P., and Rabins, M. (1983). Semi-active versus passive or active tuned mass dampers for structural control. *Journal of Engineering Mechanics*, 109. (Cited on page 52.)

Hu, T., Jiang, L., Pan, L., Chen, B., Gong, N., Yang, J., Gong, X., and Sun, S. (2025). Development of a semi-active suspension using a compact magnetorheological damper with negative-stiffness components. *Mechanical Systems and Signal Processing*, 223:111842.

https://www.sciencedirect.com/science/article/pii/S0888327024007404. (Cited on page 56.)

Huang, W., Zhao, J., Yu, G., and Wong, P. K. (2021). Intelligent vibration control for semiactive suspension systems without prior knowledge of dynamical nonlinear damper behaviors based on improved extreme learning machine. *IEEE/ASME Transactions on Mechatronics*, 26(4):2071–2079. (Cited on page 55.)

Ighravwe, D. and Oke, S. (2015). Maintenance workforce performance enhancement in a fuzzy environment with multiplicity of criteria in manufacturing system. *Suranaree Journal of Science and Technology*, 23. (Cited on page 54.)

Inman, D. J. (2013). *Engineering Vibration*. Prentice Hall, 4th edition. (Cited on page 36.)

Isacchi, G. and Ripamonti, F. (2024). A robust and fail-safe semi-active vertical damper to improve ride comfort. *Vehicle System Dynamics*, 0(0):1–23. https://doi.org/10.1080/00423114.2024.2398033. (Cited on page 59.)

Ismail, M., Ikhouane, F., and Rodellar, J. (2009). The hysteresis bouc-wen model, a survey. *Archives of Computational Methods in Engineering*, 16:161–188. https://doi.org/10.1007/s11831-009-9031-8. (Cited on pages 13, 14, and 16.)

International Organization for Standardization (1997). *Mechanical vibration and shock — Evaluation of human exposure to whole-body vibration* (ISO 2631-1:1997). Standard, Geneva, CH. (Cited on pages 1, 2, and 41.)

International Organization for Standardization (2016). *Mechanical vibration — Road surface profiles — Reporting of measured data* (ISO 8608:2016). Standard, Geneva, CH. (Cited on pages 35, 36, and 38.)

Jamadar, M.-e.-H., Desai, R. M., Kumar, H., and Joladarashi, S. (2021). Analyzing quarter car model with magneto-rheological (mr) damper using equivalent damping and magic formula models. *Materials Today: Proceedings*, 46:9944–9949. International Mechanical Engineering Congress 2019. https://doi.org/10.1016/j.matpr.2021.02.706. (Cited on pages 23, 32, and 55.)

Jeyasenthil, R., Yoon, D. S., and Choi, S.-B. (2019). Response time effect of magnetorheological dampers in a semi-active vehicle suspension system: performance assessment with quantitative feedback theory. *Smart Materials and Structures*, 28(5):054001. https://dx.doi.org/10.1088/1361-665X/ab0cb4. (Cited on page 84.)

Jiang, X., Chen, T., Xiong, X., Zeng, J., Zhao, Y., Chen, R., Hao, W., and Cheng, T. (2024). The self-tuning fuzzy sliding mode control method for the suspension system with the lstm network road identification. *Journal of Sound and Vibration*, 581:118401. https://www.sciencedirect.com/science/article/pii/S0022460X24001640. (Cited on page 55.)

Jiang, X. and Cheng, T. (2023). Design of a bp neural network pid controller for an air suspension system by considering the stiffness of rubber bellows. *Alexandria Engineering Journal*, 74:65–78. https://doi.org/10.1016/j.aej.2023.05.012. (Cited on pages 55 and 59.)

Jurisch, M. (2022). Vertical trajectory planning: an optimal control approach for active suspension systems in autonomous vehicles. *Vehicle System Dynamics*, 60(11):3788–3809. https://doi.org/10.1080/00423114.2021.1979238. (Cited on pages 55 and 58.)

Karnopp, D. (1995). Active and Semi-Active Vibration Isolation. *Journal of Vibration and Acoustics*, 117(B):177–185. https://doi.org/10.1115/1.2838660. (Cited on pages 3 and 23.)

Karnopp, D., Crosby, M. J., and Harwood, R. A. (1974). Vibration Control Using Semi-Active Force Generators. *Journal of Engineering for Industry*, 96(2):619–626. https://doi.org/10.1115/1.3438373. (Cited on pages 23, 49, 50, and 51.)

Kasemi, B., Muthalif, A. G., Rashid, M. M., and Fathima, S. (2012). Fuzzy-pid controller for semi-active vibration control using magnetorheological fluid damper. *Procedia Engineering*, 41:1221–1227. International Symposium on Robotics and Intelligent Sensors 2012 (IRIS 2012). https://www.sciencedirect.com/science/article/pii/S187770581202704X. (Cited on pages 58 and 59.)

Katoch, S., Chauhan, S. S., and Kumar, V. (2021). A review on genetic algorithm: past, present, and future. *Multimedia Tools and Applications*, 80(5):8091–8126. https://doi.org/10.1007/s11042-020-10139-6. (Cited on pages 53, 54, and 55.)

Khamis, A., Naidu, D. S., and Kamel, A. M. (2014). Nonlinear finite-horizon regulation and tracking for systems with incomplete state information using differential state dependent riccati equation. *International Journal of Aerospace Engineering*, 2014:178628. https://doi.org/10.1155/2014/178628. (Cited on page 45.)

Khan, M. A., Abid, M., Ahmed, N., Wadood, A., and Park, H. (2020). Nonlinear control design of a half-car model using feedback linearization and an lqr controller. *Applied Sciences*, 10(9). https://doi.org/10.3390/app10093075. (Cited on pages 27, 32, 44, and 56.)

Kilicaslan, S. (2022). Control of active suspension system in the presence of nonlinear spring and damper. *Scientia Iranica*, 29(3):1221–1235. https://doi.org/10.24200/sci.2021.58189.5607. (Cited on pages 32, 39, 55, 58, and 59.)

Kim, J., Lee, T., Kim, C.-J., and Yi, K. (2023). Model predictive control of a semi-active suspension with a shift delay compensation using preview road information. *Control Engineering Practice*, 137:105584. https://doi.org/10.1016/j.conengprac.2023.105584. (Cited on pages 22, 32, and 56.)

Kimball, J. B., DeBoer, B., and Bubbar, K. (2024). Adaptive control and reinforcement learning for vehicle suspension control: A review. *Annual Reviews in Control*, 58:100974. https://www.sciencedirect.com/science/article/pii/S1367578824000427. (Cited on pages 59 and 60.)

Koch, G., Fritsch, O., and Lohmann, B. (2010). Potential of low bandwidth active suspension control with continuously variable damper. *Control Engineering Practice*, 18(11):1251–

1262. Special Issue on Automotive Control Applications, 2008 IFAC World Congress. https://doi.org/10.1016/j.conengprac.2010.03.007. (Cited on page 39.)

Koch, G. P. A. (2011). Adaptive control of mechatronic vehicle suspension systems. [Master's thesis, TECHNISCHE UNIVERSITÄT MÜNCHEN]. (Cited on pages 10, 11, 23, 31, and 38.)

Kučera, V. (2011). Riccati equations and their solution. In Levine, W. S., (ed.), *The Control Systems Handbook: Control System Advanced Methods*, volume 3 of *Electrical Engineering Handbooks*, chapter 14, pages 19–20. CRC Press, 2 edition. (Cited on page 47.)

Kwok, N., Ha, Q., Nguyen, M., Li, J., and Samali, B. (2007). Bouc–wen model parameter identification for a mr fluid damper using computationally efficient ga. *ISA Transactions*, 46(2):167–179. https://doi.org/10.1016/j.isatra.2006.08.005. (Cited on pages 3, 13, 16, 53, 64, and 100.)

L. Pires, M. C. Smith, N. E. H. and McMahon, R. A. (2013). Design trade-offs for energy regeneration and control in vehicle suspensions. *International Journal of Control*, 86(11):2022–2034. https://doi.org/10.1080/00207179.2013.830197. (Cited on page 55.)

Laiq Khan, S. Q. and Khan, U. (2016). Adaptive pid control scheme for full car suspension control. *Journal of the Chinese Institute of Engineers*, 39(2):169–185. https://doi.org/10.1080/02533839.2015.1091427. (Cited on pages 55 and 58.)

Lenkutis, T., Čerškus, A., Šešok, N., Dzedzickis, A., and Bučinskas, V. (2020). Road surface profile synthesis: Assessment of suitability for simulation. *Symmetry*, 13:68. https://doi.org/10.3390/sym13010068. (Cited on page 36.)

Li, G., Xu, H., Ruan, Z., Liu, Q., Gan, Y., Lifan, Y., Zhu, W., and Hu, G. (2024). Design and performance evaluation of a novel fractional order pid control strategy for vehicle semi-active suspension. *Advances in Mechanical Engineering*, 16. https://doi.org/10.1177/16878132241241435. (Cited on pages 58 and 59.)

Li, W., Dong, X., Yu, J., Xi, J., and Pan, C. (2021). Vibration control of vehicle suspension with magneto-rheological variable damping and inertia. *Journal of Intelligent Material Systems and Structures*, 32(13):1484–1503. https://doi.org/10.1177/1045389X20983885. (Cited on pages 23, 55, and 56.)

Liu, H., Nonami, K., and Hagiwara, T. (2008). Active following fuzzy output feedback sliding mode control of real-vehicle semi-active suspensions. *Journal of Sound and Vibration*, 314(1):39–52. https://www.sciencedirect.com/science/article/pii/S0022460X08000242. (Cited on pages 58 and 59.)

Lu, Y., Khajepour, A., Soltani, A., Li, R., Zhen, R., Liu, Y., and Wang, M. (2023). Gain-adaptive skyhook-lqr: a coordinated controller for improving truck cabin dynamics. *Control Engineering Practice*, 130:105365. https://www.sciencedirect.com/science/article/pii/S0967066122001964. (Cited on pages 58 and 59.)

M. Valášek and M. Novák (1996). Ground hook for semi-active damping of truck's suspension. In *Proc. of CTU Workshop 96*, pages 467–468, CTU Prague, Brno. Engineering Mechanics. (Cited on pages 3, 49, and 51.)

Ma, X. Q., Wang, E. R., Rakheja, S., and Su, C.-Y. (2002). Modeling hysteretic characteristics of mr-fluid damper and model validation. In *Proceedings of the 41st IEEE Conference on Decision and Control, 2002.*, volume 2, pages 1675–1680 vol.2. https://doi.org/10.1109/CDC.2002.1184761. (Cited on page 17.)

Mahmoodabadi, M. J. and Nejadkourki, N. (2022). Optimal fuzzy adaptive robust pid control for an active suspension system. *Australian Journal of Mechanical Engineering*, 20(3):681–691. https://doi.org/10.1080/14484846.2020.1734154. (Cited on page 58.)

Majdoub, K. E., Giri, F., and Chaoui, F. (2013). Backstepping adaptive control of quarter-vehicle semi-active suspension with dahl mr damper model. *IFAC Proceedings Volumes*, 46(11):558–563. 11th IFAC Workshop on Adaptation and Learning in Control and Signal Processing. https://doi.org/10.3182/20130703-3-FR-4038.00001. (Cited on pages 23, 32, 33, and 34.)

Mazzilli, V., De Pinto, S., Pascali, L., Contrino, M., Bottiglione, F., Mantriota, G., Gruber, P., and Sorniotti, A. (2021). Integrated chassis control: Classification, analysis and future trends. *Annual Reviews in Control*, 51:172–205. https://www.sciencedirect.com/science/article/pii/S1367578821000055. (Cited on pages 2 and 44.)

Melo, M. A. (2017). Análise comparativa de estratégias para suspensão semiativa em um modelo de 1/4 de veículo. [Bachelor's thesis, Universidade de Brasília]. (Cited on pages 23, 34, and 182.)

Metzler, M., Tavernini, D., Gruber, P., and Sorniotti, A. (2021). On prediction model fidelity in explicit nonlinear model predictive vehicle stability control. *IEEE Transactions on Control Systems Technology*, 29(5):1964–1980. (Cited on pages 55, 58, and 59.)

Miao, Y., Rui, X., Wang, P., Zhu, H., Zhang, J., and Wang, J. (2024). Nonlinear dynamic modeling and analysis of magnetorheological semi-active suspension for tracked vehicles. *Applied Mathematical Modelling*, 125:311–333. https://doi.org/10.1016/j.apm.2023.09.027. (Cited on page 56.)

Min, D. and Wei, Y. (2024). An adaptive control strategy for a semi-active suspension integrated with intelligent tires. *Mechanical Systems and Signal Processing*, 212:111281. https://www.sciencedirect.com/science/article/pii/S0888327024001791. (Cited on pages 29, 30, 55, and 56.)

Mitra, A. C., Desai, G. J., Patwardhan, S. R., Shirke, P. H., Kurne, W. M., and Banerjee, N. (2016). Optimization of passive vehicle suspension system by genetic algorithm. *Procedia Engineering*, 144:1158–1166. International Conference on Vibration Problems 2015. https://doi.org/10.1016/j.proeng.2016.05.087. (Cited on pages 22 and 53.)

Morato, M. M., Nguyen, M. Q., Sename, O., and Dugard, L. (2019). Design of a fast real-time lpv model predictive control system for semi-active suspension control of a full vehicle. *Journal of the Franklin Institute*, 356(3):1196–1224. https://www.sciencedirect.com/science/article/pii/S0016003218307002. (Cited on pages 55 and 59.)

Nagarkar, M., Bhalerao, Y., Patil, G. V., and Patil, R. Z. (2018). Multi-objective optimization of nonlinear quarter car suspension system – pid and lqr control. *Procedia Manufacturing*, 20:420–427. 2nd International Conference on Materials, Manufacturing and Design Engineering (iCMMD2017), 11-12 December 2017, MIT Aurangabad, Maharashtra, INDIA. https://doi.org/10.1016/j.promfg.2018.02.061. (Cited on pages 55, 57, 58, and 59.)

Nagarkar, M. P. and Vikhe, G. J. (2016). Optimization of the linear quadratic regulator (LQR) control quarter car suspension system using genetic algorithm. *Ingeniería e Investigación*, 36:23 – 30. http://www.scielo.org.co/scielo.php?script=sci_arttext&pid=S0120-56092016000100004&nrm=iso. (Cited on pages 22, 30, 38, 53, and 57.)

Nassar, A. and Al-Ghanim, A. (2018). Modeling, simulation, and control of half car suspension system using matlab/simulink. *International Journal of Science and Research (IJSR)*, 7. https://doi.org/10.21275/ART20179298. (Cited on page 34.)

Nguyen, D. N. and Nguyen, T. A. (2023). Proposing an original control algorithm for the active suspension system to improve vehicle vibration: Adaptive fuzzy sliding mode proportional-integral-derivative tuned by the fuzzy (afspidf). *Heliyon*, 9(3):e14210. https://www.sciencedirect.com/science/article/pii/S2405844023014172. (Cited on page 58.)

Nguyen, T. A. (2023). Research on the sliding mode – pid control algorithm tuned by fuzzy method for vehicle active suspension. *Forces in Mechanics*, 11:100206. https://doi.org/10.1016/j.finmec.2023.100206. (Cited on pages 32, 39, and 59.)

Norton, R. (2006). *Machine Design: An Integrated Approach*. Pearson Prentice Hall. https://books.google.com.br/books?id=tmviAAAACAAJ. (Cited on page 30.)

Novák, M. and Valášek, M. (1996). A new concept of semi-active control of truck's suspension. In *Proc. of AVEC 96*, pages 141–151, Aachen. (Cited on pages 49 and 59.)

Ogata, K. (2010). *Modern Control Engineering*. Instrumentation and controls series. Prentice Hall. (Cited on pages 23 and 58.)

Oke, S., Akanbi, O., Oyawale, F., *et al.* (2007). Mathematical modelling of the road bumps using laplace transform. *International Journal of Science and Technology*. (Cited on page 32.)

Otkur, M., Alshammari, N., Abdullah, N., Alkandari, D., Thyab, H., and Alduwaisan, L. (2022). Optimization of suspension system parameters for a suv. In *Proceedings of the 8th World Congress on Mechanical, Chemical, and Material Engineering (MCM'22)*. https://doi.org/10.11159/icmie22.137. (Cited on pages 27, 32, 42, 44, and 56.)

Pacejka, H. B. and Bakker, E. (1992). The magic formula tire model. *Vehicle System Dynamics*, 21(sup001):1–18. https://doi.org/10.1080/00423119208969994. (Cited on page 29.)

Pan, Y., Nie, X., Li, Z., and Gu, S. (2021). Data-driven vehicle modeling of longitudinal dynamics based on a multibody model and deep neural networks. *Measurement*, 180:109541. https://www.sciencedirect.com/science/article/pii/S0263224121005182. (Cited on page 57.)

Pang, H., Liu, F., and Xu, Z. (2018). Variable universe fuzzy control for vehicle semi-active suspension system with mr damper combining fuzzy neural network and particle swarm optimization. *Neurocomputing*, 306:130–140. https://doi.org/10.1016/j.neucom.2018.04.055. (Cited on pages 27, 32, 39, 44, and 56.)

Pedro, J. O., Dangor, M., Dahunsi, O. A., and Ali, M. M. (2014). Particle swarm optimized intelligent control of nonlinear full-car electrohydraulic suspensions. *IFAC Proceedings Volumes*, 47(3):1772–1777. 19th IFAC World Congress. https://doi.org/10.3182/20140824-6-ZA-1003.02469. (Cited on page 59.)

Prabakar, R., Sujatha, C., and Narayanan, S. (2009). Optimal semi-active preview control response of a half car vehicle model with magnetorheological damper. *Journal of Sound and Vibration*, 326(3):400–420. https://doi.org/10.1016/j.jsv.2009.05.032. (Cited on pages 27, 39, 42, and 44.)

Prabakar, R. S., Sujatha, C., and Narayanan, S. (2016). Response of a half-car model with optimal magnetorheological damper parameters. *Journal of Vibration and Control*, 22(3):784–798. https://doi.org/10.1177/1077546314532300. (Cited on page 27.)

Proakis, J. G. and Manolakis, D. G. (2014). *Digital Signal Processing: Pearson New International Edition*. Pearson Education Limited, USA, 4th edition. (Cited on pages 25, 41, 42, 83, and 85.)

Pusadkar, U. S., Chaudhari, S. D., Shendge, P., and Phadke, S. (2019). Linear disturbance observer based sliding mode control for active suspension systems with non-ideal actuator. *Journal of Sound and Vibration*, 442:428–444. https://www.sciencedirect.com/science/article/pii/S0022460X18307491. (Cited on page 59.)

Qing, Y., Hongliang, Z., Songlin, C., Weiwei, M., and Yongfeng, J. (2023). Designing a switched takagi-sugeno fuzzy controller for cdc semi-active suspensions with current input constraint. *Mechanical Systems and Signal Processing*, 199:110450. https://www.sciencedirect.com/science/article/pii/S0888327023003588. (Cited on pages 55 and 59.)

Rao, K. D. (2014). Modeling, simulation and control of semi active suspension system for automobiles under matlab simulink using pid controller. *IFAC Proceedings Volumes*, 47(1):827–831. 3rd International Conference on Advances in Control and Optimization of Dynamical Systems (2014). https://doi.org/10.3182/20140313-3-IN-3024.00094. (Cited on page 58.)

Ricco, M., Alshawi, A., Gruber, P., Dhaens, M., and Sorniotti, A. (2024). Nonlinear model predictive control for yaw rate and body motion control through semi-active and active

suspensions. *Vehicle System Dynamics*, 62(6):1587–1620. https://doi.org/10.1080/00423114.2023.2251615. (Cited on pages 56 and 59.)

RICHARDS, F. J. (1959). A Flexible Growth Function for Empirical Use. *Journal of Experimental Botany*, 10(2):290–301. https://doi.org/10.1093/jxb/10.2.290. (Cited on page 17.)

Rill, G. and Castro, A. (2020). *Road Vehicle Dynamics: Fundamentals and Modeling with MATLAB®*. CRC Press, 2nd edition. https://doi.org/10.1201/9780429244476. (Cited on page 23.)

Rossi, A., Orsini, F., Scorza, A., Botta, F., Belfiore, N., and Sciuto, S. (2018). A review on parametric dynamic models of magnetorheological dampers and their characterization methods. *Actuators*, 7:16. https://doi.org/10.3390/act7020016. (Cited on page 56.)

Ružinskas, A. and Sivilevičius, H. (2017). Magic formula tyre model application for a tyre-ice interaction. *Procedia Engineering*, 187:335–341. https://doi.org/10.1016/j.proeng.2017.04.383. (Cited on pages 29 and 35.)

Santade, F. (2017). *Análise dinâmica de amortecedores não lineares assimétricos, com histerese e sujeitos a folga e avaliação do efeito temperatura*. [PhD thesis, Universidade Estadual Paulista]. (Cited on pages 13, 14, and 74.)

Sapiński, B. and Filuś, J. (2003). Analysis of parametric models of mr linear damper. *Journal of Theoretical and Applied Mechanics*, 41. (Cited on page 15.)

Savaresi, S., Poussot-Vassal, C., Spelta, C., Sename, O., and Dugard, L. (2010). *Semi-Active Suspension Control Design for Vehicles*. Elsevier Science. https://books.google.com.br/books?id=Wor8ye8tVbAC. (Cited on pages 8, 10, 23, 32, and 38.)

Schiehlen, W. (2006a). White noise excitation of road vehicle structures. *Sadhana*, 31(4):487–503. https://doi.org/10.1007/BF02716788. (Cited on pages 36, 37, and 40.)

Schiehlen, W. (2006b). White noise excitation of road vehicle structures. *Sadhana*, 31:487–503. https://doi.org/10.1007/BF02716788. (Cited on page 38.)

Sename, O. (2021). Review on lpv approaches for suspension systems. *Electronics*, 10(17). https://doi.org/10.3390/electronics10172120. (Cited on pages 55 and 59.)

Seshadri, A. (2009). *NSGA - II: A multi-objective optimization algorithm*. MATLAB Central File Exchange. https://www.mathworks.com/matlabcentral/fileexchange/10429-nsga-ii-a-multi-objective-optimization-algorithm (Accessed: 2024-23-02). (Cited on pages 97 and 205.)

Sevin, E. and Pilkey, W. D. (1971). *Optimum shock and vibration isolation*. Shock and Vibration Information Center, US Department of Defense. (Cited on page 38.)

Sharma, S. K. and Sharma, R. C. (2018). Simulation of quarter-car model with magnetorheological dampers for ride quality improvement. *International Journal of Vehicle Structures & Systems*. https://doi.org/10.4273/ijvss.10.3.03. (Cited on page 56.)

Shinozuka, M. (1972). Monte carlo solution of structural dynamics. *Computers & Structures*, 2(5):855–874. https://doi.org/10.1016/0045-7949(72)90043-0. (Cited on page 39.)

Shirahatti, A., Prasad, P., Panzade, P., and Kulkarni, M. (2008). Optimal design of passenger car suspension for ride and road holding. *Journal of The Brazilian Society of Mechanical Sciences and Engineering - J BRAZ SOC MECH SCI ENG*, 30. https://doi.org/10.1590/S1678-58782008000100010. (Cited on page 22.)

Silva, D. M. D. d., Ávila, S. M., and Morais, M. V. G. d. (2022). Sistema de suspensão semi-ativa automotiva utilizando amortecedor magneto-reológico. In de Educación a Distancia (España), U. N., (ed.), *XV Congreso Iberoamericano de Ingeniería Mecánica*. (Cited on pages 13, 56, 64, 79, and 100.)

Soliman, A. and Kaldas, M. (2021). Semi-active suspension systems from research to mass-market – a review. *Journal of Low Frequency Noise, Vibration and Active Control*, 40(2):1005–1023. https://doi.org/10.1177/1461348419876392. (Cited on pages 3, 10, 11, 12, 51, and 52.)

Soltane, S., Montassar, S., Mekki, O. B., and Fatmi, R. E. (2015). A hysteretic bingham model for mr dampers to control cable vibrations. *Journal of mechanics of materials and structures*. https://doi.org/10.2140/jomms.2015.10.195. (Cited on page 3.)

Swethamarai, P. and Lakshmi, P. (2022). Adaptive-fuzzy fractional order pid controller-based active suspension for vibration control. *IETE Journal of Research*, 68(5):3487–3502. https://doi.org/10.1080/03772063.2020.1768906. (Cited on pages 56, 57, and 58.)

Taghavifar, H. (2021). Ekf estimation based pid type-2 fuzzy control of electric cars. *Measurement*, 173:108557. https://www.sciencedirect.com/science/article/pii/S0263224120310800. (Cited on pages 58 and 59.)

Tan, B., Tan, X., Liu, J., Ning, D., Liu, P., and Xie, Y. (2025). Cooperative compensation control for a novel semi-active electromagnetic suspension integrating with variable damper and variable inertance. *Mechanical Systems and Signal Processing*, 226:112344. https://www.sciencedirect.com/science/article/pii/S0888327025000457. (Cited on page 56.)

Tener, D. R. (2004). Overcoming the ride/handling compromise - a cockpit adjustable suspension system. In *SAE 2004 World Congress & Exhibition*. (Cited on page 2.)

Theunissen, J., Tota, A., Gruber, P., Dhaens, M., and Sorniotti, A. (2021). Preview-based techniques for vehicle suspension control: a state-of-the-art review. *Annual Reviews in Control*, 51:206–235. https://www.sciencedirect.com/science/article/pii/S1367578821000183. (Cited on page 44.)

Tyan, F., Hong, Y.-F., Tu, S.-H., and Jeng, W. (2009). Generation of random road profiles. *Journal of Advanced Engineering*, 4. (Cited on pages 37, 40, and 68.)

Valdivieso-Soto, A., Galluzzi, R., and Bustamante-Bello, R. (2023). Analysis of comfort oriented control strategies for automotive suspension system. In *2023 International Symposium on Electromobility (ISEM)*, pages 1–8. (Cited on pages 44 and 55.)

Valášek, M., Novák, M., Šika, Z., and Vaculín, O. (1997). Extended ground-hook - new concept of semi-active control of truck's suspension. *Vehicle System Dynamics*, 27(5-6):289–303. https://doi.org/10.1080/00423119708969333. (Cited on pages 49 and 51.)

van der Sande, T. P. J., Merks, M. H. M., Lindeman, E., and Nijmeijer, H. (2022). Rule-based control of a semi-active suspension system for road holding using limited sensor information: design and experiments. *Vehicle System Dynamics*, 60(12):4226–4244. https://doi.org/10.1080/00423114.2021.2007270. (Cited on pages 55 and 59.)

Wang, E. R., Ma, X. Q., Rakheja, S., and Su, C. Y. (2004). Modeling asymmetric hysteretic properties of an mr fluids damper. *43rd IEEE Conference on Decision and Control*. (Cited on pages 3, 13, 17, 22, 100, 108, 138, and 163.)

Wang, Z., Liu, C., Zheng, X., Zhao, L., and Qiu, Y. (2024). Advancements in semi-active automotive suspension systems with magnetorheological dampers: A review. *Applied Sciences*, 14:7866. https://doi.org/10.3390/app14177866. (Cited on pages 3 and 60.)

Widner, A., Tettamanti, T., and Tihanyi, V. (2022). Framework for vehicle dynamics model validation. *IEEE Access*, 10:35422 – 35436. https://doi.org/10.1109/ACCESS.2022.3157904. (Cited on page 22.)

Wu, X., Pan, Y., Wang, G., and Hou, L. (2024). Pitch motion suppression of electric vehicle active suspensions based on multibody dynamics. *Mechanism and Machine Theory*, 198:105667. https://www.sciencedirect.com/science/article/pii/S0094114X24000946. (Cited on page 57.)

Xiao, F., Hu, J., Jia, M., Zhu, P., and Deng, C. (2022). A novel integrated control framework of afs, ass, and dyc based on ideal roll angle to improve vehicle stability. *Advanced Engineering Informatics*, 54:101764. https://www.sciencedirect.com/science/article/pii/S1474034622002221. (Cited on page 56.)

Xiaoliang, C., Wei, W., Xu, L., Zhang, S., and Zhao, S. (2022). Parameter identification of bouc-wen model for mr damper by parameter sensitivity analysis and modified pso algorithm. *International Journal of Applied Electromagnetics and Mechanics*, 69:1–19. https://doi.org/10.3233/JAE-210214. (Cited on page 17.)

Xiong, X., Chen, C., Liu, Y., Li, Z., and Xu, F. (2024). Research on performance magnetorheological semi-active suspension based on improved gray wolf algorithm-optimized linear quadratic regulator control. *International Journal of Dynamics and Control*, 12(11):4157–4170. https://doi.org/10.1007/s40435-024-01482-9. (Cited on pages 3, 56, and 59.)

Xu, Y. and Ahmadian, M. (2013). Improving the capacity of tire normal force via variable stiffness and damping suspension system. *Journal of Terramechanics*, 50(2):121–132. https://doi.org/10.1016/j.jterra.2013.03.003. (Cited on page 22.)

Xue, X., Zhang, L., and Sun, Q. (2010). Parameter identification and simulation of the noise-involved hysteretic model using improved genetic algorithm. In *2010 International Confer-*

ence on Measuring Technology and Mechatronics Automation, volume 2, pages 868–871. https://doi.org/10.1109/ICMTMA.2010.482. (Cited on page 53.)

Yin, Z., Su, R., and Ma, X. (2023). Dynamic responses of 8-dof vehicle with active suspension: Fuzzy-pid control. *World Electric Vehicle Journal*, 14:249. https://doi.org/10.3390/wevj14090249. (Cited on page 58.)

Yin, Z., Wang, R., Ma, X., and Su, R. (2024). Fractional-order piλdμ control to enhance the driving smoothness of active vehicle suspension in electric vehicles. *World Electric Vehicle Journal*, 15:184. https://doi.org/10.3390/wevj15050184. (Cited on page 58.)

Yoon, D.-S., Kim, G.-W., and Choi, S.-B. (2021). Response time of magnetorheological dampers to current inputs in a semi-active suspension system: Modeling, control and sensitivity analysis. *Mechanical Systems and Signal Processing*, 146:106999. https://www.sciencedirect.com/science/article/pii/S088832702030385X. (Cited on pages 3, 56, and 84.)

Yoon, D.-S., Park, Y.-J., and Choi, S.-B. (2019). An eddy current effect on the response time of a magnetorheological damper: Analysis and experimental validation. *Mechanical Systems and Signal Processing*, 127:136–158. https://www.sciencedirect.com/science/article/pii/S0888327019301499. (Cited on pages 56 and 84.)

Yu, J., Dong, X., and Zhang, Z. (2017). A novel model of magnetorheological damper with hysteresis division. *Smart Materials and Structures*, 26(10):105042. https://doi.org/10.1088/1361-665X/aa87d6. (Cited on page 53.)

Yu, M., Evangelou, S., and Dini, D. (2023). Advances in active suspension systems for road vehicles. *Engineering*. https://doi.org/10.1016/j.eng.2023.06.014. (Cited on pages 2, 3, 8, 10, and 60.)

ZhiHong, L., JiaLing, Y., WenKu, S., and MingXia, F. (2025). A novel method of vehicle height control utilizing semi-active actuator. *Mechanical Systems and Signal Processing*, 223:111818. https://www.sciencedirect.com/science/article/pii/S0888327024007167. (Cited on page 56.)

Zhu, H., Rui, X., Yang, F., Zhu, W., and Wei, M. (2019). An efficient parameters identification method of normalized bouc-wen model for mr damper. *Journal of Sound and Vibration*, 448:146–158. https://doi.org/10.1016/j.jsv.2019.02.019. (Cited on pages 17 and 56.)

Zolotas, A. C. and Goodall, R. M. (2018). New insights from fractional order skyhook damping control for railway vehicles. *Vehicle System Dynamics*, 56(11):1658–1681. https://doi.org/10.1080/00423114.2018.1435889. (Cited on page 59.)

Çimen, T. (2010). Systematic and effective design of nonlinear feedback controllers via the state-dependent riccati equation (sdre) method. *Annual Reviews in Control*, 34(1):32–51. https://doi.org/10.1016/j.arcontrol.2010.03.001. (Cited on pages 3, 47, 48, 76, 77, and 84.)

Žáček, J., Šebesta, K., Mohammad, H., Jeniš, F., Strecker, Z., and Kubík, M. (2022). Experimental evaluation of modified groundhook car suspension with fast magnetorheological damper. *Actuators*, 11(12). https://doi.org/10.3390/act11120354. (Cited on pages 41, 51, 52, 55, 56, 59, and 84.)

APPENDIX A

APPENDIX: 1/4 VEHICLE SIMULATION VALIDATIONS

The 1/4 vehicle simulation Matlab code was validated in Ferreira (2022). The results for the simulations are displayed in Figure A.1, and the comparison of the numerical results with Melo (2017) are in Table A.1.

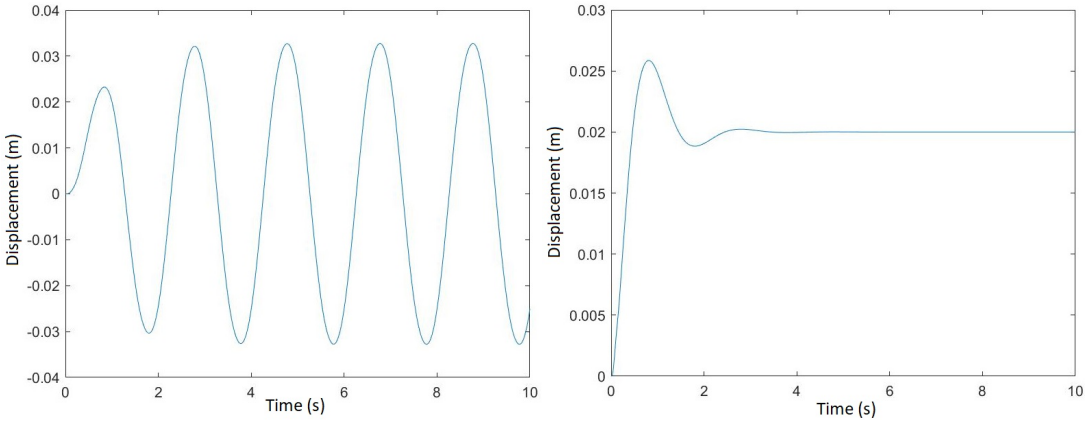

(a) Results for the 0,5 Hz Sine simulation.

(b) Results for the Linear rise simulation.

Figure A.1. Results for the validation according to the tests performed in Melo (2017).

Table A.1. Comparison between original values obtained by Melo (2017) and validation.

Maximum UPBD	Original	Validation
Linear rise	0,026 m	0,026 m
Sine	0,032 m	0,032 m

The data matched perfectly, with both the graphs and the values resulting in the same values. As such, the 1/4 vehicle simulation is considered validated, as well as the continuous Skyhook controller.

These results justify the continued analysis of the dynamic systems with the hitherto developed tools.

APPENDIX B

APPENDIX: OPTIMAL CONTROL EQUATIONS

DERIVATION OF THE RICCATI DIFFERENTIAL EQUATION

As stated in Section 2.5.1, the optimal control is the one that satisfies the condition

$$\frac{\partial H_a(x,u,t)}{\partial u} = 0. \tag{6.1}$$

By applying equations (2.110) and (2.112) in (2.97), the expression for equation (6.1) becomes

$$R(t)u(t) + B(t)^T\lambda(t) = 0. \tag{6.2}$$

Describing λ in terms of a symmetric matrix **P** and the vector **x** as

$$\lambda(t) = P(t)x(t), \tag{6.3}$$

the optimal control action is found as

$$u(t) = R(t)^{-1}B(t)^T P(t)x(t). \tag{6.4}$$

From this, the theory posits that the value of **L** is given by

$$L(t) = R(t)^{-1}B(t)^T P(t). \tag{6.5}$$

To find the value of **P**, the co-state equation given by

$$\frac{\partial H_a(x,u,t)}{\partial x} = -\dot{\lambda}(t) \tag{6.6}$$

is used. Applying equations (2.97) and (6.3) on (6.6), it is found that

$$\begin{aligned} &\frac{\partial x(t)^t A(t)^T}{\partial x}P(t)x(t) + \frac{\partial u(t)^T B(t)^T}{\partial x}P(t)x(t) + \\ &\frac{\partial x(t)^t Q(t)x(t)}{\partial x} + \frac{\partial u(t)^t R(t)u(t)}{\partial x}x(t) = -(\dot{P}(t)x(t) + P(t)\dot{x}(t)). \end{aligned} \tag{6.7}$$

By the derivation chain rule, $\frac{\partial A(x)x}{\partial x}$, $\frac{\partial B(x)u}{\partial x}$, $\frac{\partial x(t)^t Q(t)x(t)}{\partial x}$ and $\frac{\partial u(t)^t R(t)u(t)}{\partial x}$ are

$$\frac{\partial x^t A(x)^T}{\partial x} = A(t)^T + x(t)^T \nabla_x A(t)^T = A(t)^T + \sum_{i=0}^{n} x_i(t)^T \frac{\partial A(t)^t}{\partial x_i} \tag{6.8}$$

$$\frac{\partial u^T B(t)^T}{\partial x} = u(t)^T \nabla_x B(t) = \sum_{i=0}^{n} u_i^T \frac{\partial B(t)^t}{\partial x_i} \tag{6.9}$$

$$\frac{\partial x(t)^t Q(t)x(t)}{\partial x} = Q(t)x(t) + x(t)^T \nabla_x Q(t)x(t) = Q(t)x(t) + \left(\sum_{i=0}^{n} x_i(t)^T \frac{\partial Q(t)^t}{\partial x_i} \right) x(t) \tag{6.10}$$

$$\frac{\partial u(t)^t R(t)u(t)}{\partial x} = u(t)^T \nabla_x R(t)u(t) = \left(\sum_{i=0}^{n} u_i(t)^T \frac{\partial R(t)^t}{\partial x_i} \right) u(t), \tag{6.11}$$

which combined with equation (2.27) and the fact **P** is symmetric gives, gives

$$\begin{aligned} -(Q(t)x(t) + \frac{\partial x^t A(t)^T}{\partial x} P(t)x(t) + x(t)^T L(t)^T \nabla_x B(t) P(t)x(t) + x(t)^T \nabla_x Q(t)x(t) \\ + x(t)^T L(t)^T \nabla_x R(t) L(t)x(t)) = \dot{P}(t)x(t) + P(t)A(t)x(t) + L(t)^T B(t) P(t)x(t) \end{aligned} \tag{6.12}$$

This expression can be rearranged into two distinct groupings, based on their behavior as the system's time progresses to infinity. This results in the general solution to the Optimal control problem with quadratic costs and finite horizon, whose differential equation is known as the Riccati differential equation:

$$\begin{aligned} -\dot{P}(t) - x(t)^t \nabla A(t)^T P(t) - \frac{\partial (u(x(t))^T B(t)^T)}{\partial x} P(t) - \frac{\partial (u(x(t))^T R(t)^T u(x(t)))}{\partial x} P(t) \\ - \frac{\partial (x(t)^T Q(t)^T x(t))}{\partial x} P(t) = P(t)A(x) + A(x)^T P(t) + L(t)^T R(t) L(t) + Q. \end{aligned} \tag{6.13}$$

P CALCULATION

First, the system's Hamiltonian matrix as such is created:

$$H_a = \begin{bmatrix} A & -BR^{-1}B^T \\ -Q & -A^T \end{bmatrix} \tag{6.14}$$

Then, in order to increase the solution's precision in the cases some eigenvalues are too close, the matrix's Schur form $S = UH_aU^T$ is calculated. This decomposition results in the matrix S, that is upper quasi-triangular when real. The eigenvalues and eigenvectors of the S matrix are calculated, and the matrix is reordered according to its eigenvalues in descending order (also known as left half-plane reordering), becoming the reordered matrices $S_r = U_r H_{a_r} U_r^T$.

$$H_a \Rightarrow Schur\ Factorization \Rightarrow LHP\ Eigenvalue\ reordering \Rightarrow U_r \tag{6.15}$$

Then, P is obtained by separating the U matrix into 4 n by n corner regions where n is the

system dimension

$$U_r = \begin{bmatrix} U_{[1:n,1:n]} & U_{[n:2n,1:n]} \\ U_{[1:n,n:2n]} & U_{[n:2n,n:2n]} \end{bmatrix} \tag{6.16}$$

and performing the following operation:

$$P = \frac{U_{[1:n,n:2n]}}{U_{[1:n,1:n]}} \tag{6.17}$$

APPENDIX C

APPENDIX: 1/2 VEHICLE ADDITIONAL FIGURES

The additional results generated for the 1/2 vehicle system are contained in this appendix. They are the frequency domain rear wheel results, as well as the equivalent road input results.

PASSIVE

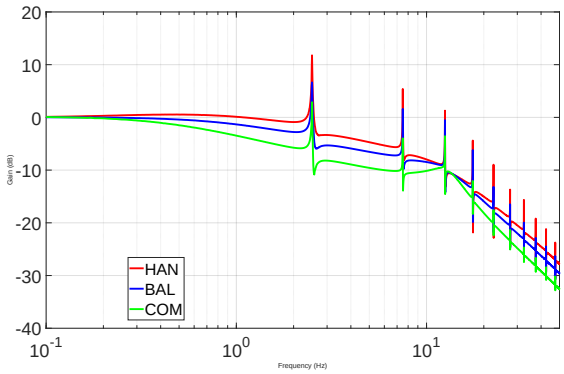

(a) UPBD

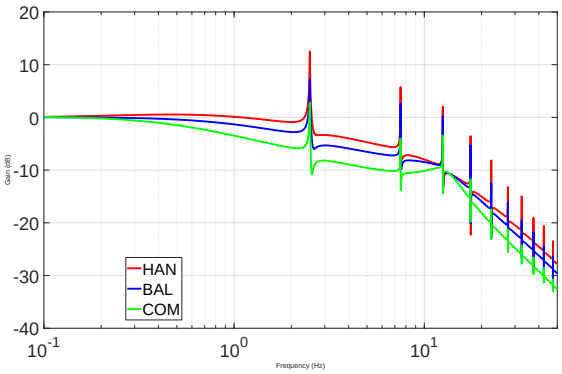

(b) UPBA

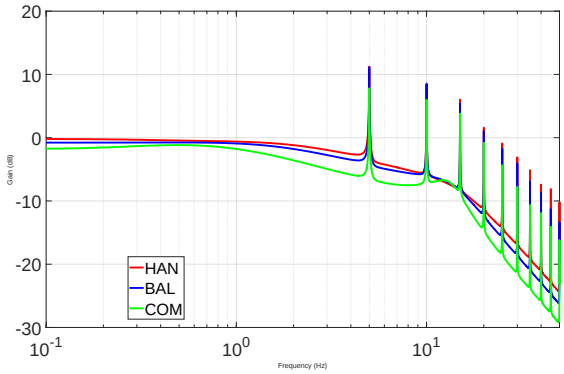

(c) UPBR

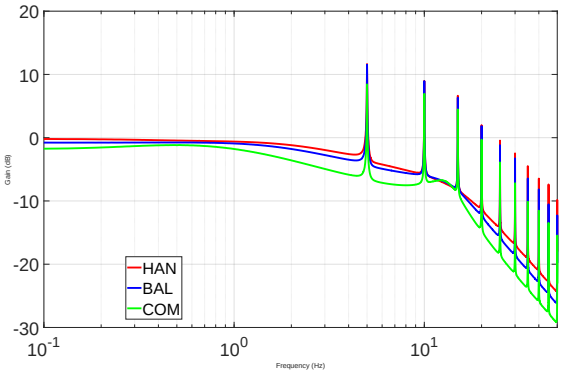

(d) UPBRA

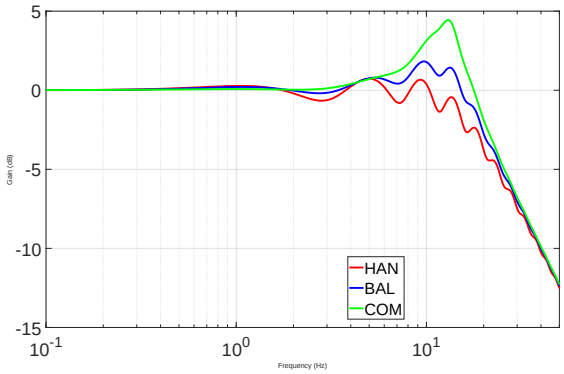

(e) Rear LWBD

Figure C.1. Alternative figures for the frequency domain half vehicle responses on a passive system under an ISO excitation.

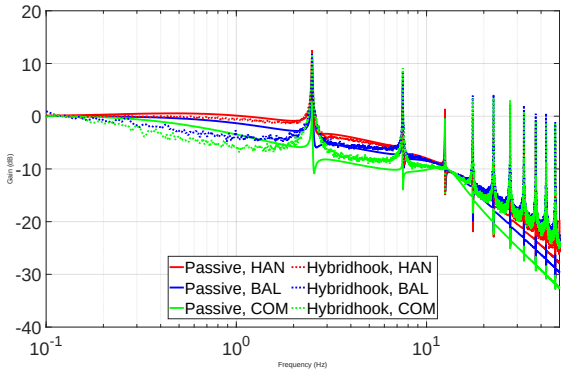

(a) UPBD

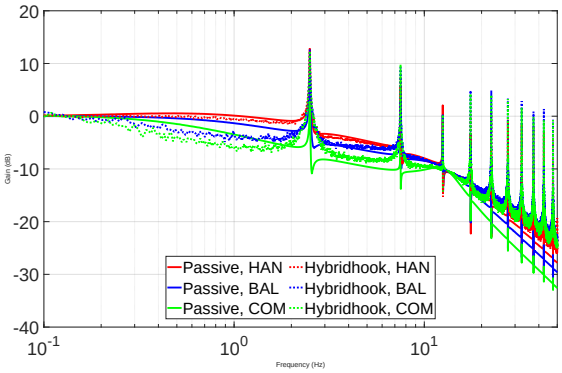

(b) UPBA

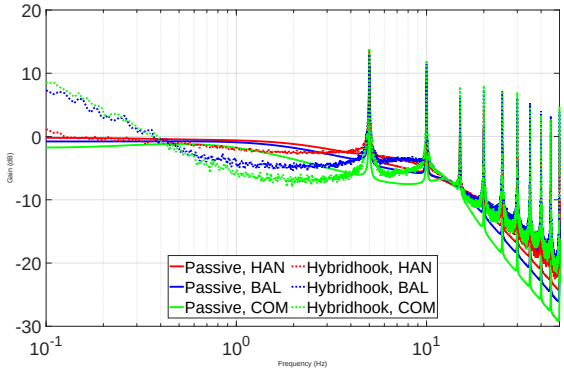

(c) UPBR

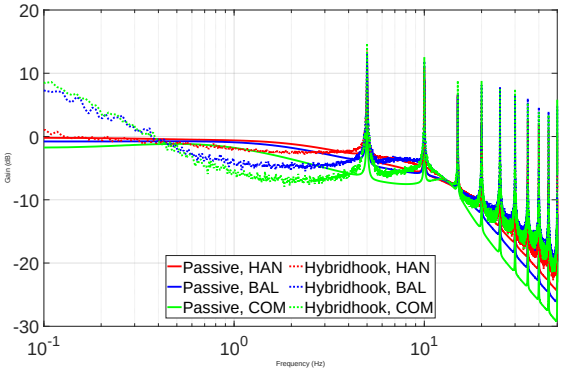

(d) UPBRA

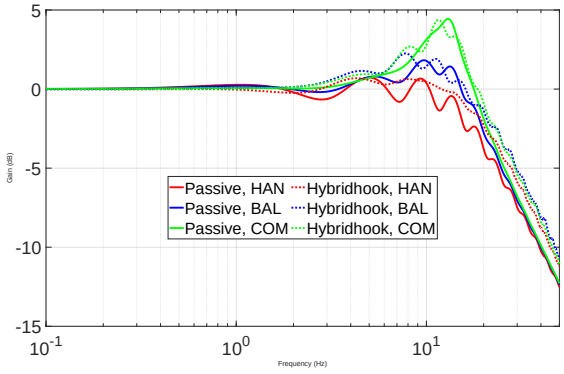

(e) Rear LWBD

Figure C.2. Alternative figures for the frequency domain half vehicle responses on a MR SAS system with the Hybridhook controller under an ISO excitation.

LQR

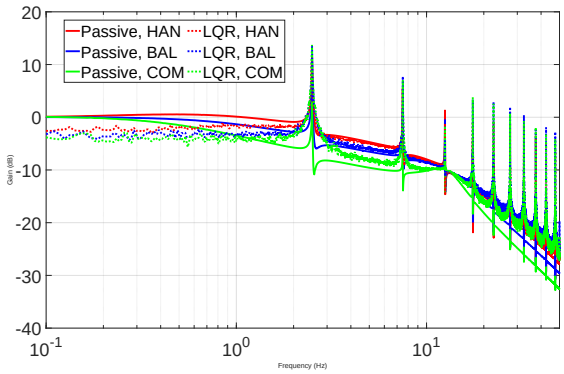

(a) UPBD

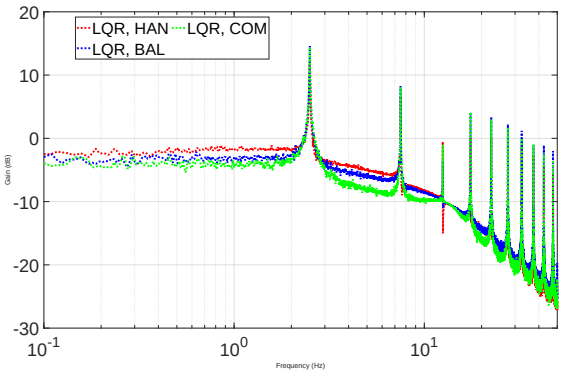

(b) UPBA

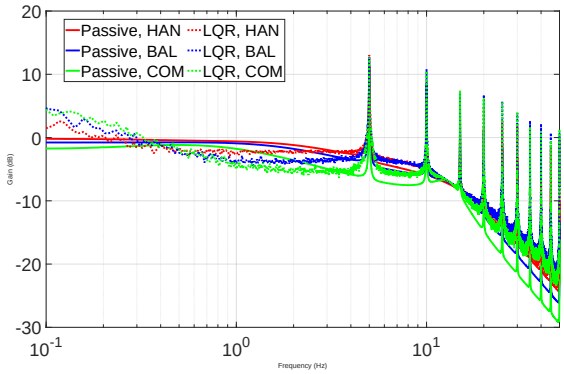

(c) UPBR

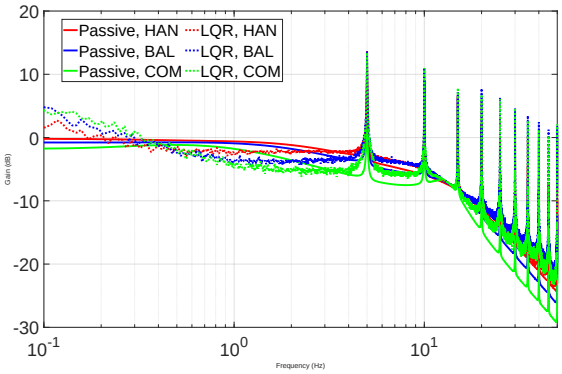

(d) UPBRA

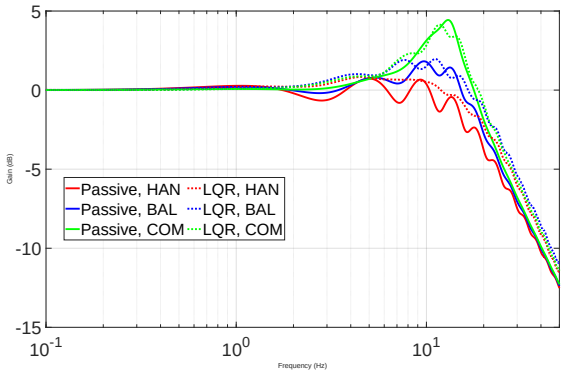

(e) Rear LWBD

Figure C.3. Alternative figures for the frequency domain half vehicle responses on a MR SAS system with the LQR controller under an ISO excitation.

SDRE

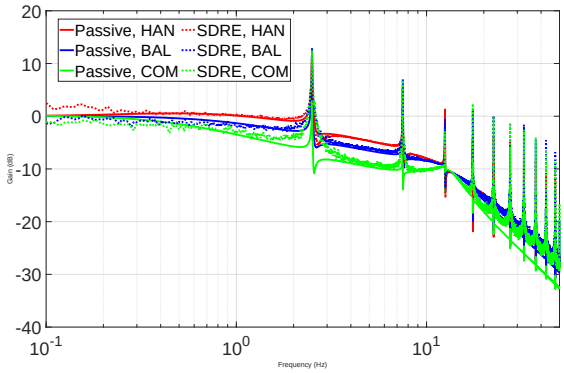

(a) UPBD

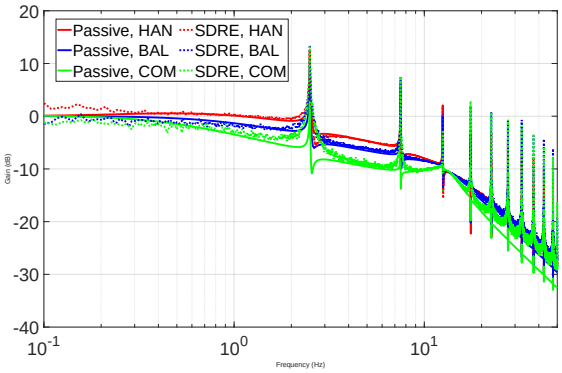

(b) UPBA

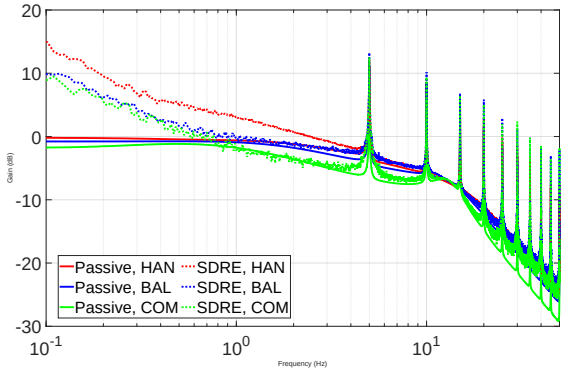

(c) UPBR

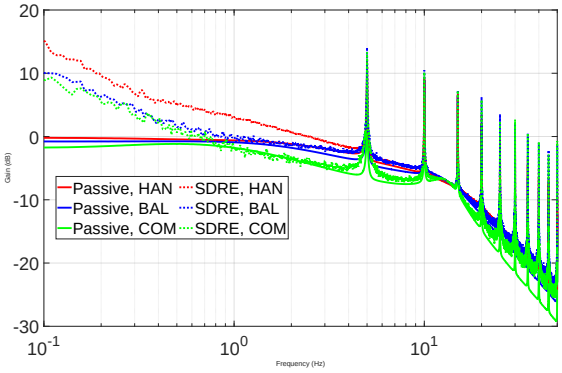

(d) UPBRA

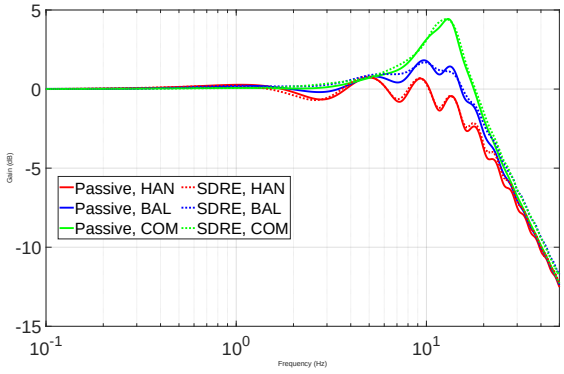

(e) Rear LWBD

Figure C.4. Alternative figures for the frequency domain half vehicle responses on a MR SAS system with the SDRE controller under an ISO excitation.

BUMP CONTROL FIGURES

The Bump excitation results are laid out in Figures C.5a, C.5b, C.5c and C.5d.

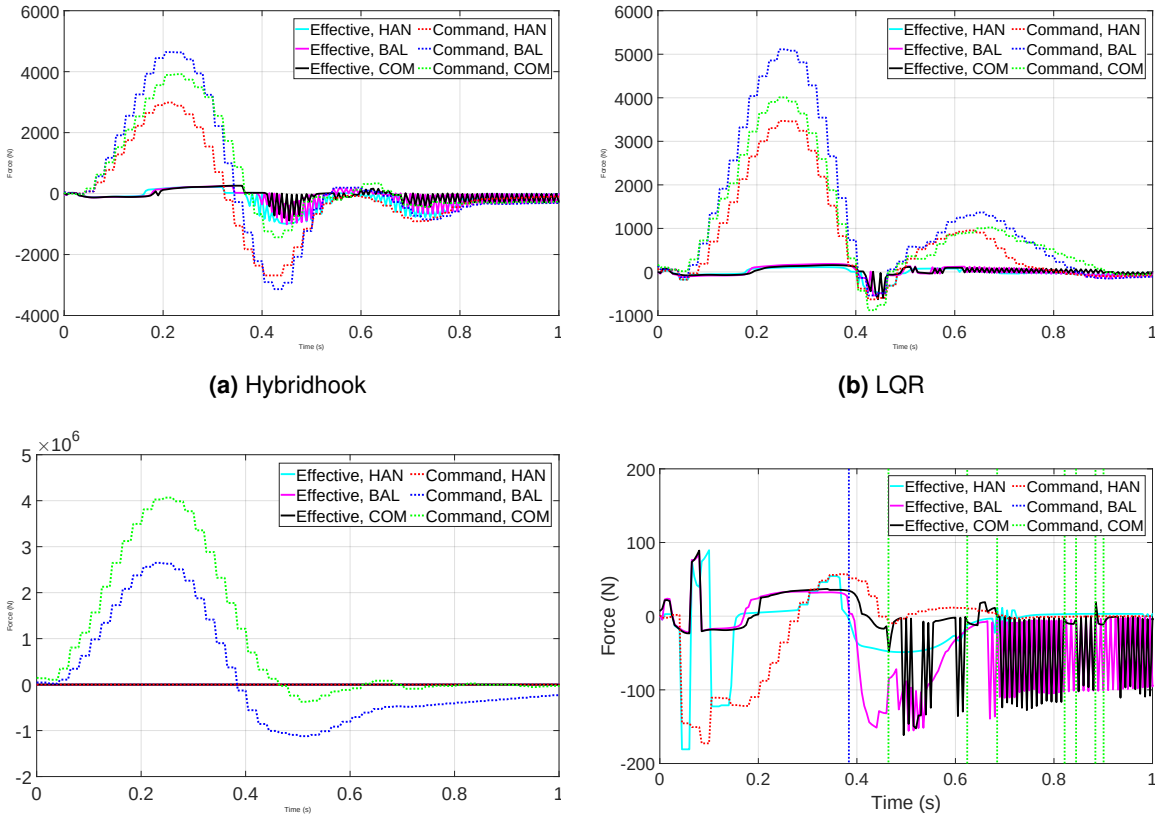

(a) Hybridhook

(b) LQR

(c) SDRE

(d) SDRE (zoom)

Figure C.5. Time domain half vehicle control commands and effective forces over a Bump obstacle.

LINEAR RISE CONTROL FIGURES

The Linear Rise excitation results are laid out in Figures C.6a, C.6b, C.6c and C.6d.

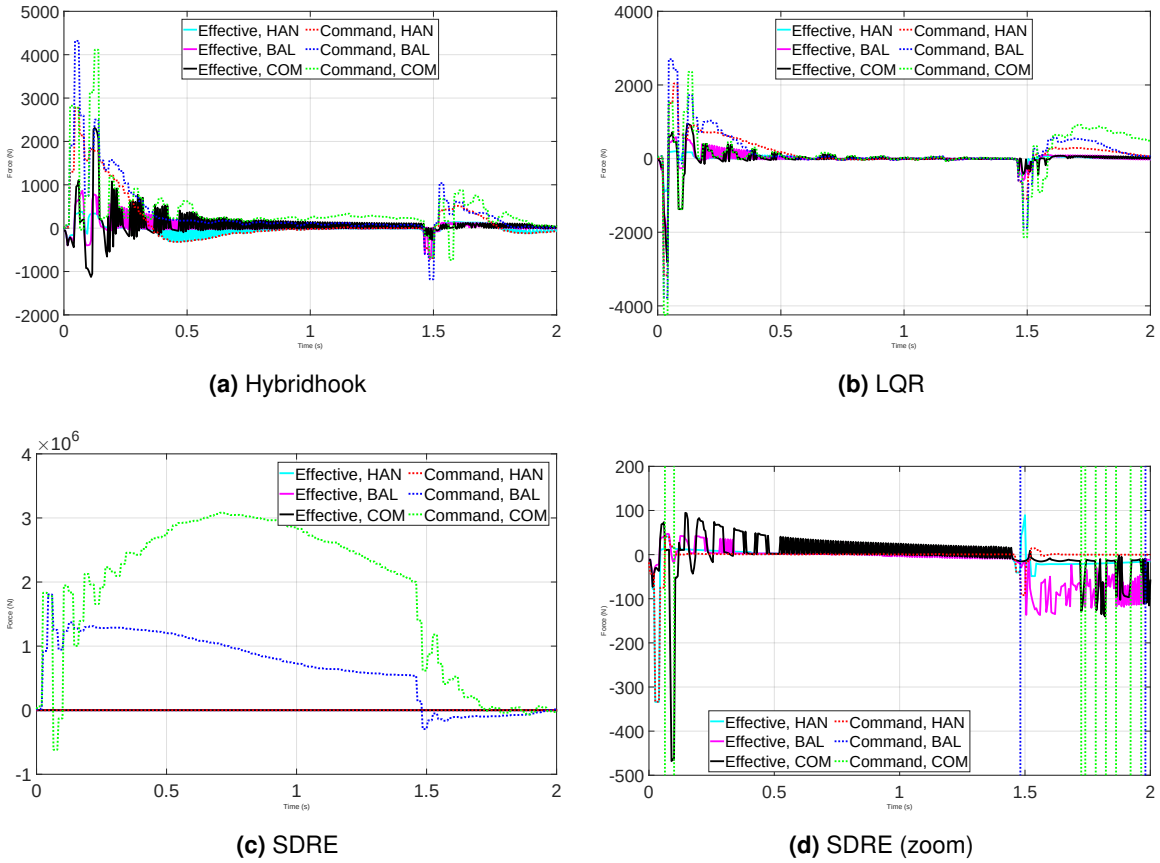

(a) Hybridhook

(b) LQR

(c) SDRE

(d) SDRE (zoom)

Figure C.6. Time domain half vehicle control commands and effective forces over a Linear rise obstacle.

APPENDIX D

APPENDIX: 1/4 VEHICLE SIMULINK SCRIPTS

The following codes are used in the Simulink simulations for the 1/4 vehicle simulations:

- AXRX.m
- dfdx.m
- funcao_forcas_aux_simulink.m
- funcao_forcas_aux2_simulink.m
- LQR_simulink.m

It should be noted that these codes do not exist outside the Simulink "Matlab code" blocks. They are written here as .m files for reproduction purposes only.

AXRX.m:

Used in the SDRE block which calculates the A(x) and R(x) matrices.

dfdx.m:

Used in the SDRE block which calculates the A(x) and R(x) matrices, in the subroutine which calculates the force derivative $\frac{dF}{d\dot{v}(\dot{x})}$.

funcao_forcas_aux_simulink.m:

Used in the Simulink block which calculates the linear system matrix A.

funcao_forcas_aux2_simulink.m:

Used in the Simulink block which calculates the linear excitation matrix C.

LQR_simulink.m:

Used in the SDRE block which calculates the solution or closest value to a solution for the associated Riccatti equation.

APPENDIX E

APPENDIX: DAMPER SIMULATION MATLAB SCRIPTS

The damper routines are all very similar in structure. They have a genetic algorithm main entrance function, and a function which evaluates the performance on the genetic algorithm.

For the Bingham damper simulation and optimization, the following codes are used:

- fit_bingham.m
- func_fit_bingham.m

For the Bouc-wen damper simulation and optimization, the following codes are used:

- fit_boucwen.m
- func_fit_boucwen.m

For the original Wang damper simulation and optimization, the following codes are used:

- fit_wang_og.m
- func_fit_wang_og.m

For the Wang-II damper simulation and optimization, the following codes are used:

- fit_wang_og.m
- func_fit_wang.m

It should be noted that the Wang and Wang-II models use the same entrance function. To switch between the modes, the number of variables in the genetic algorithm's options and in the initial population must be changed to the correct number (16 for the original model and 21 or 20 for the Wang-II depending on whether its wished to consider the discarded variable γ).

APPENDIX F

APPENDIX: ADDITIONAL SIMULINK DIAGRAMS

LINEAR EQUATIONS OF MOTION

The linear equations of motion are described by blocks Ax and Cz. Ax contain the net derivatives of the state vector originating from the vehicle state variables multiplied by the system matrix A, and Cz contains the net derivatives of the state vector originating from the road excitation vector multiplied by the matrix C. The internals of block Ax are displayed in Figure F.1, and of Cz in Figure F.2. The blocks contain two Matlab routines, funcao_forcas_aux and funcao_forcas_aux2_4gdl. They calculate the matrix for each system, and their code is available in the Appendix.

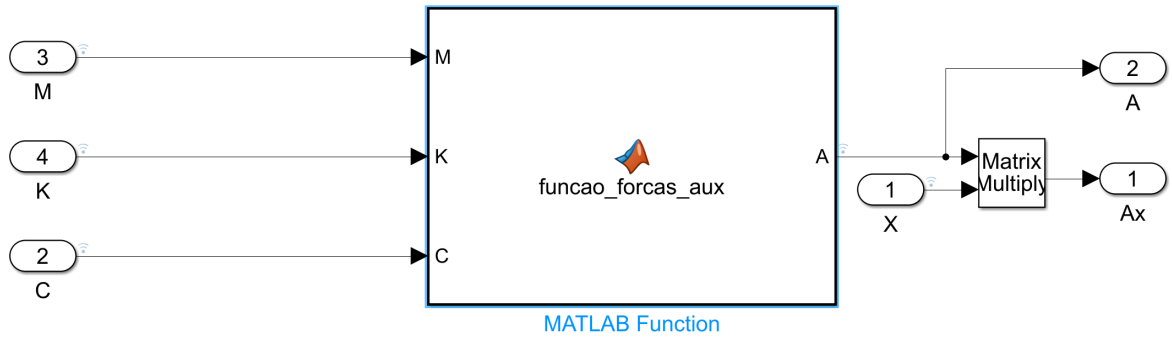

Figure F.1. Simulink routine for block Ax.

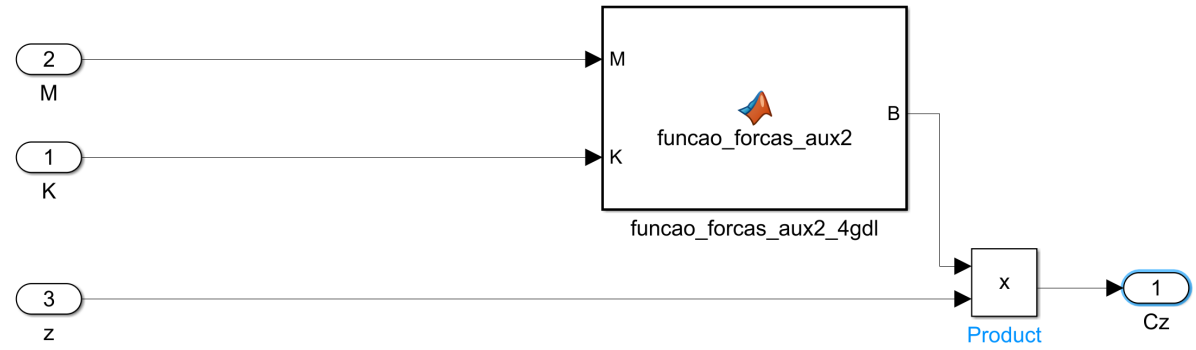

Figure F.2. Simulink routine for block Cz.

FORCE ORDERING BLOCK

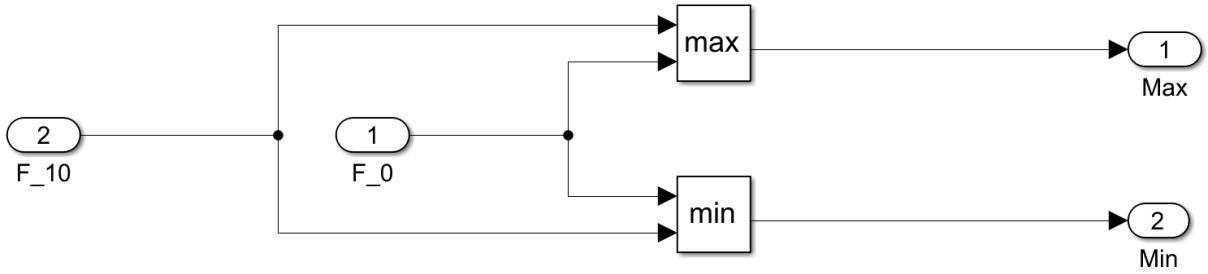

Figure F.3. Simulink routine for the minimum-maximum damper force ordering block.

CONTROLLERS

The Hybridhook controllers was implemented into Simulink. The diagrams is in Figure F.4.

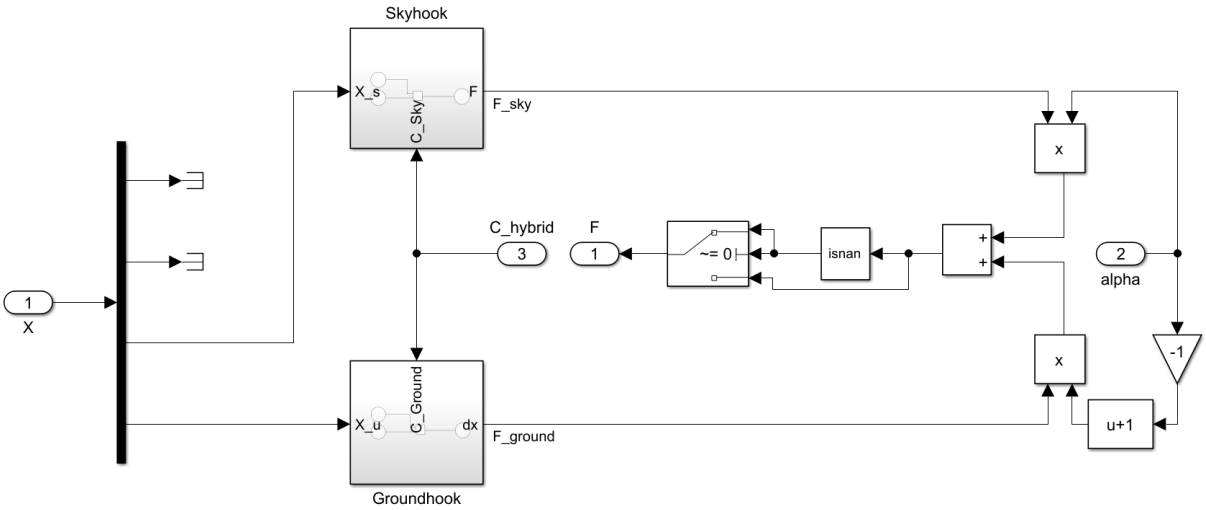

Figure F.4. Simulink routine for the Hybridhook controller.

These diagram calculates the desired force for each controller and combines them according to the hybridization constant `alpha`.

The LQR controller implementation was as shown in the diagram in Figure F.5.

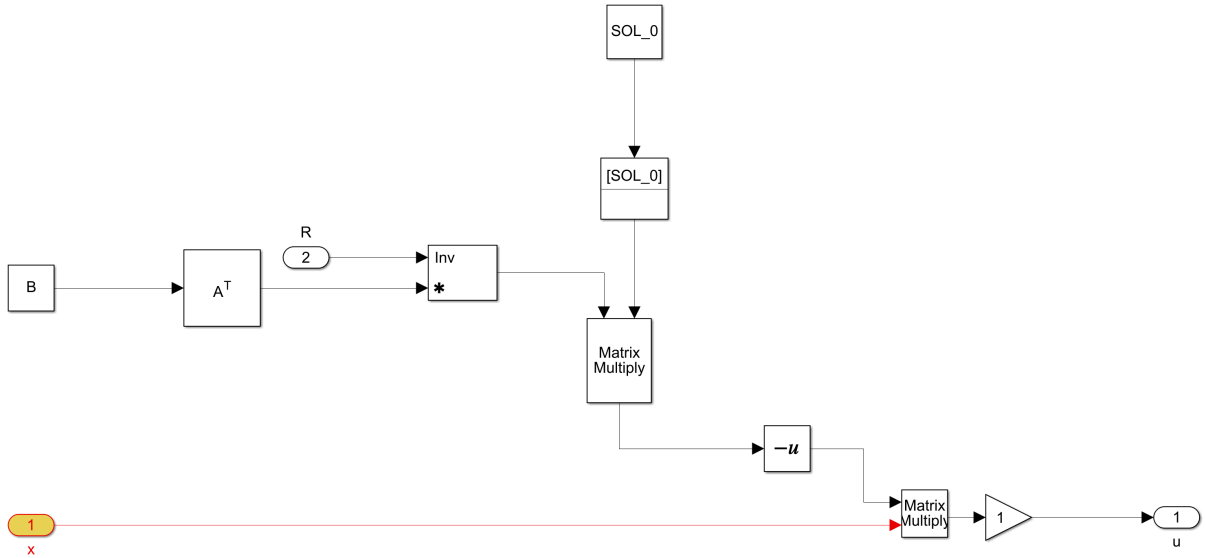

Figure F.5. Simulink routine for the LQR controller.

The SDRE controller implementation was as the diagrams in Figures F.6 and F.7.

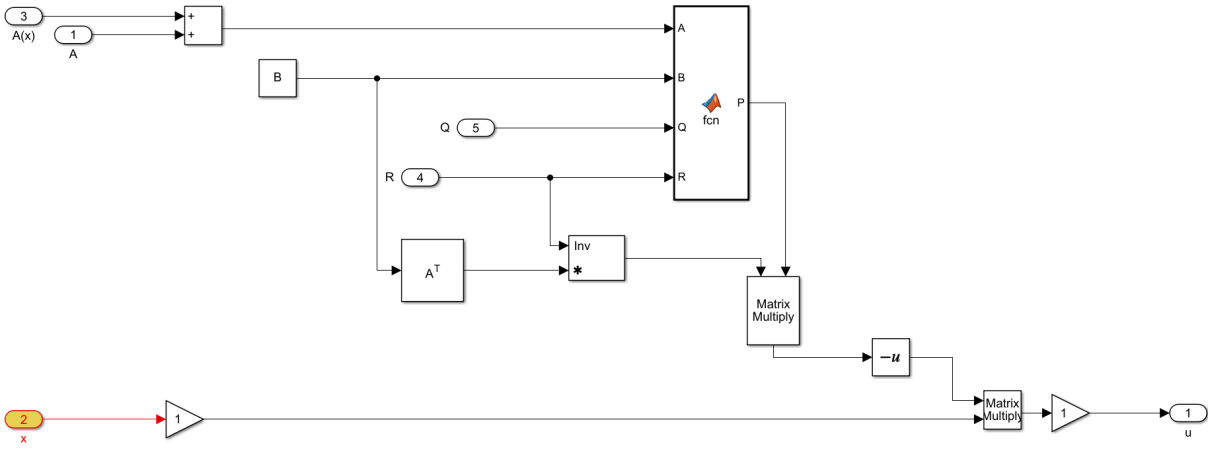

Figure F.6. Simulink routine for the SDRE controller.

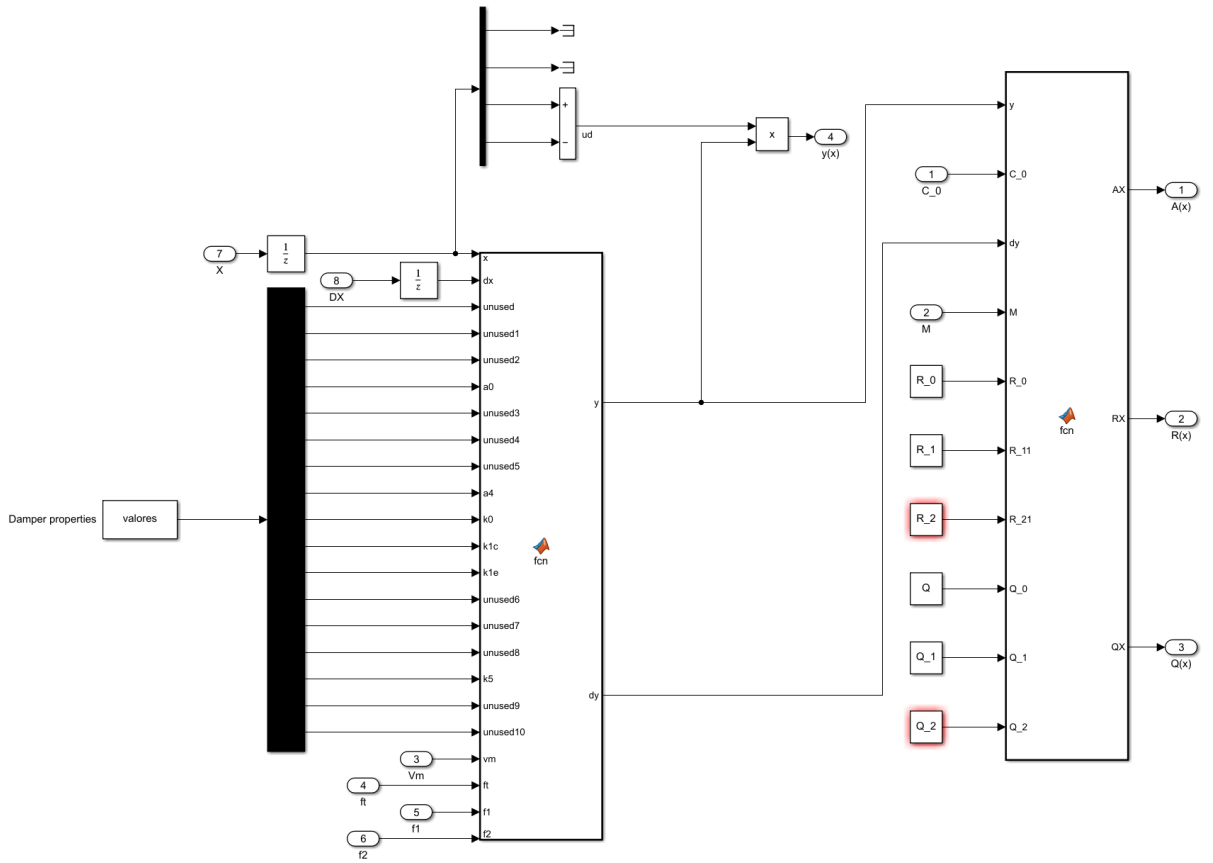

Figure F.7. Simulink routine for the block which calculates the **A(x)**, **Q(x)** and **R(x)** matrices.

DAMPER MODELS The test bench setup and the vehicle setup were as Figure F.8.

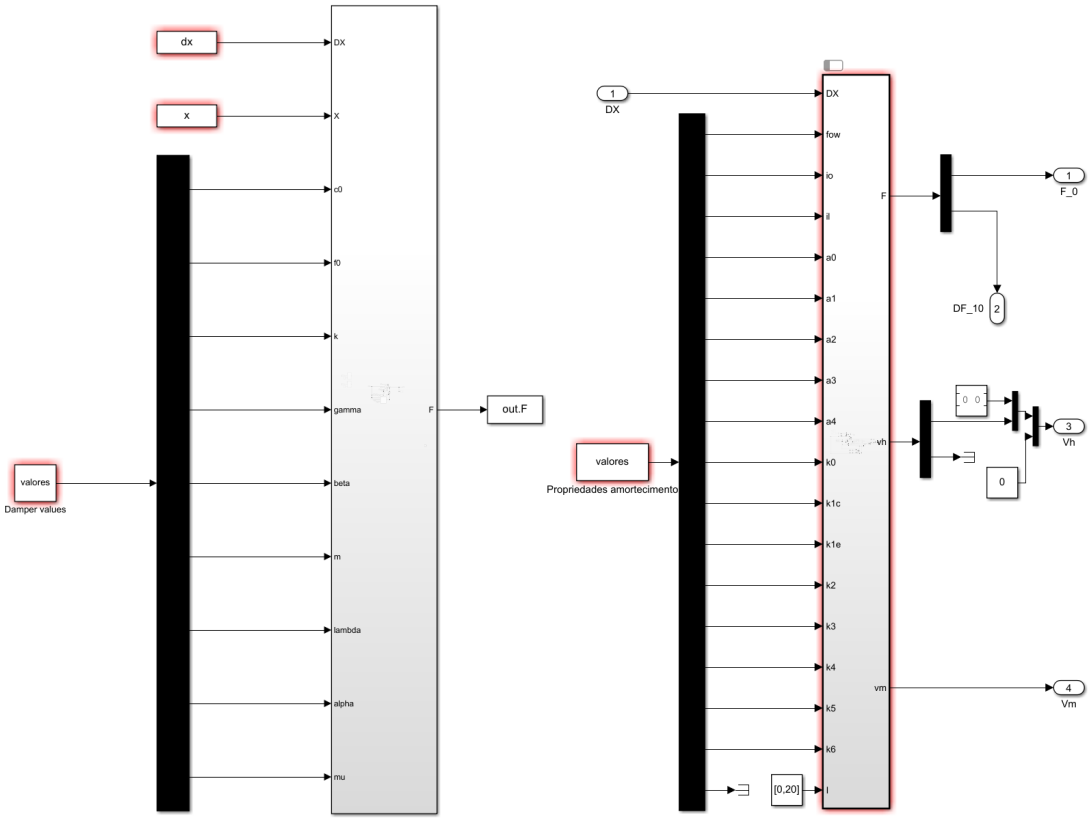

(a) Simulink routine for a generic test bench configuration.

(b) Simulink routine for a generic vehicle configuration.

Figure F.8. Implementation of the two damper test conditions.

For the Bingham damper, the high and low speed blocks are in Figure F.9.

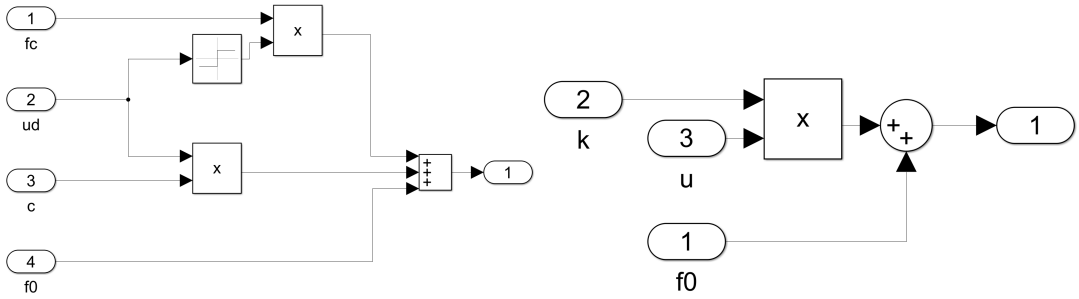

(a) "FD high" block internal diagram.

(b) "FD low" block internal diagram.

Figure F.9. Internal diagrams of the Bingham damper high and low force block.

For the Bouc-wen model, the z block handling the differential equation evolution is shown in Figure F.10

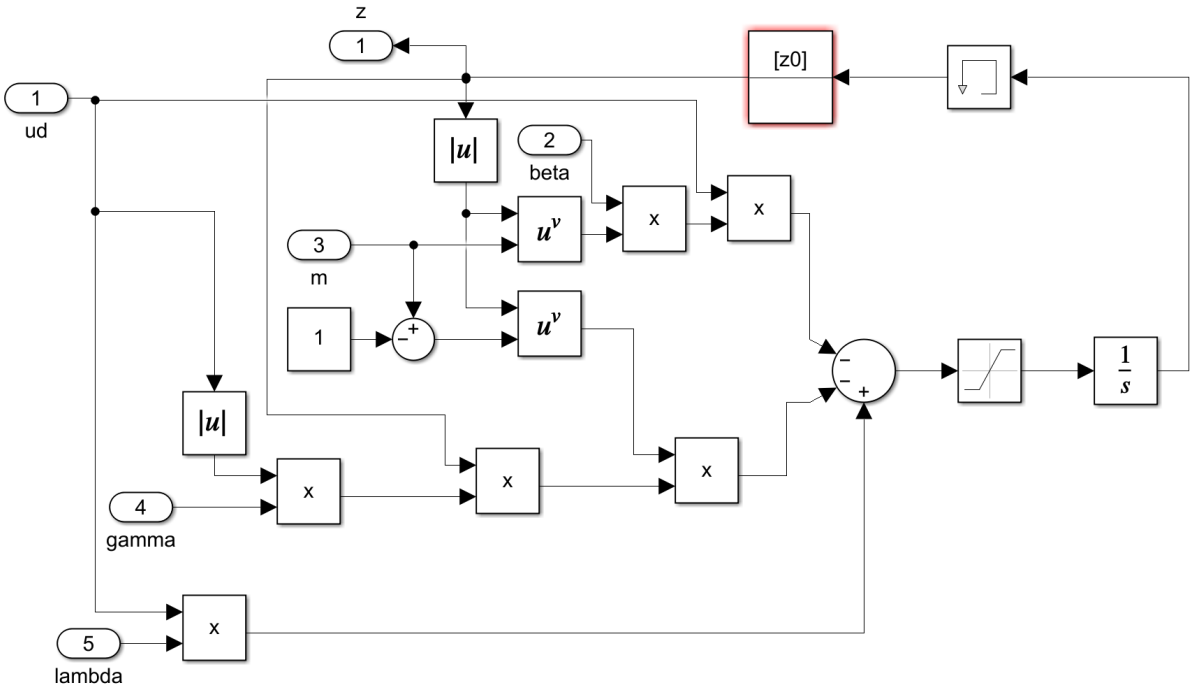

Figure F.10. Internal diagram of the ”z” block, which handles the differential evolution of the z variable of the Bouc-wen model.

The Wang implementation’s Simulink diagrams has been split into sections for ease of view. The sections which were differentiated by color are singled out in Figure F.12 for the green section, Figure F.13 for the red section, Figure F.14 for the yellow section, Figure F.15 for the blue section and Figure F.16 for the orange section.

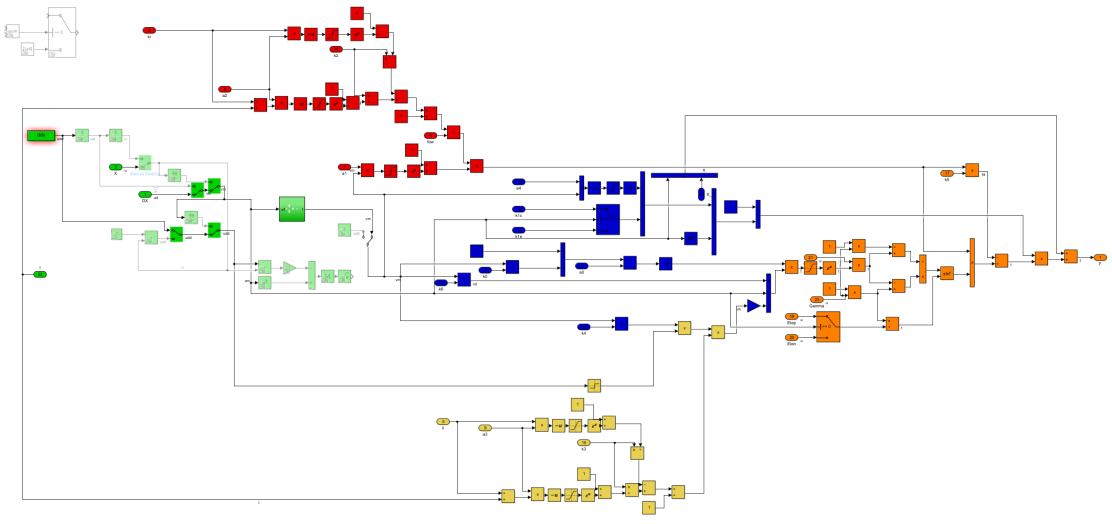

Figure F.11. Simulink routine for the Wang damper model.

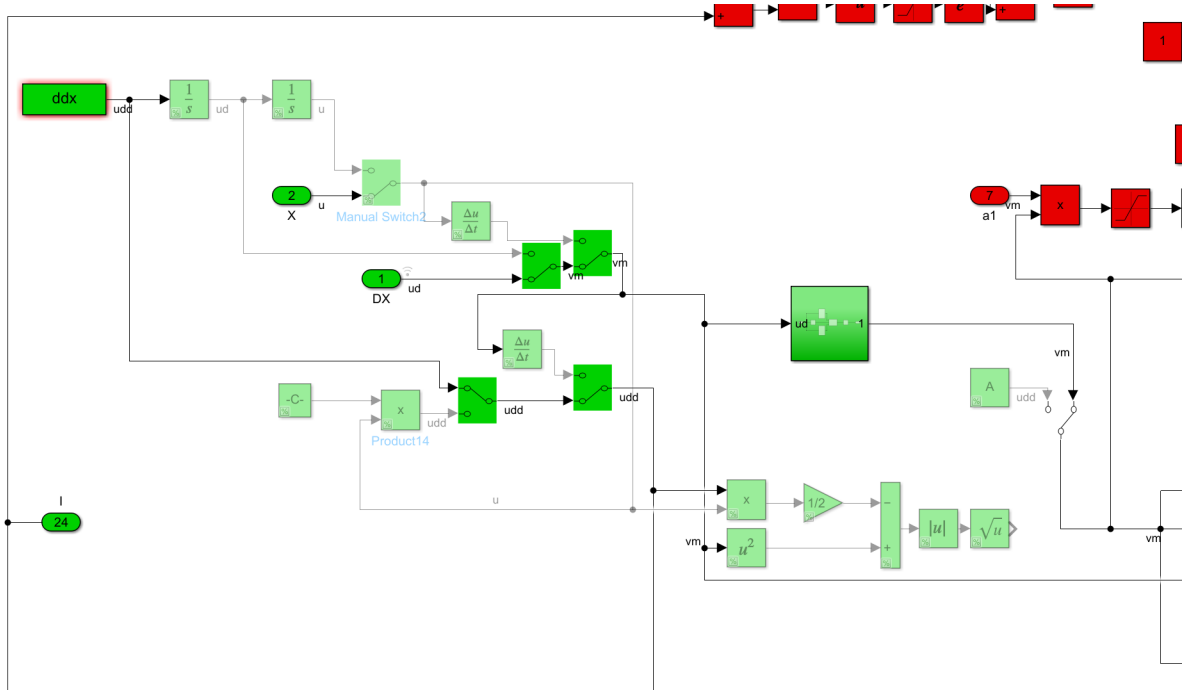

Figure F.12. Zoom of the Simulink routine for the Wang damper model green coded region.

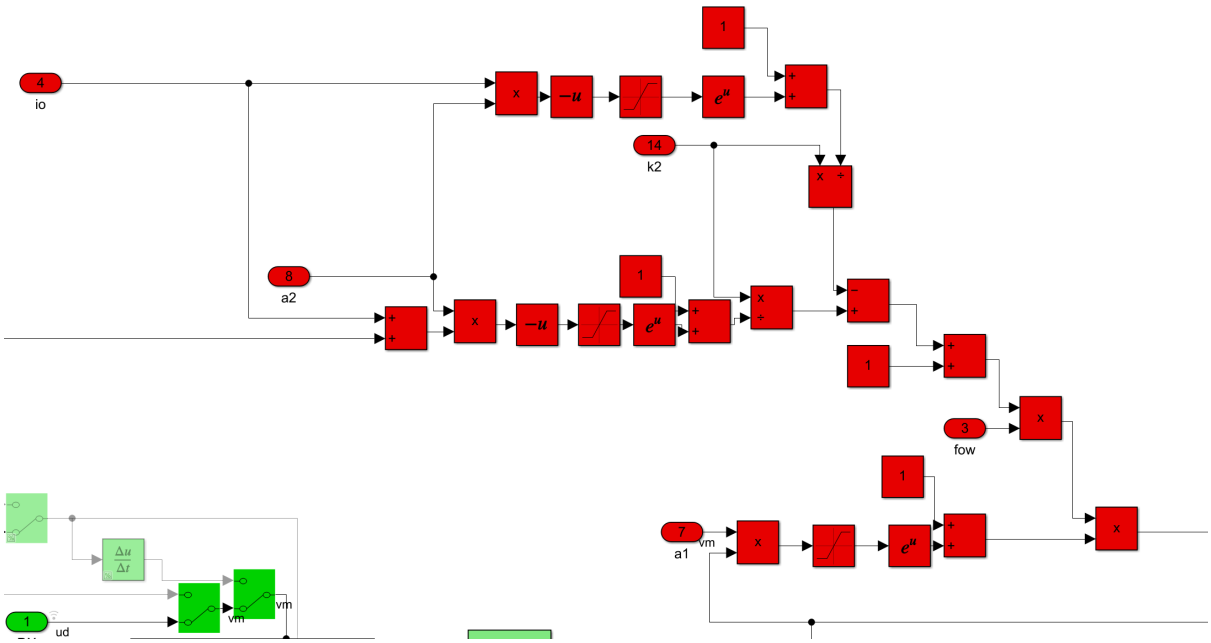

Figure F.13. Zoom of the Simulink routine for the Wang damper model red coded region.

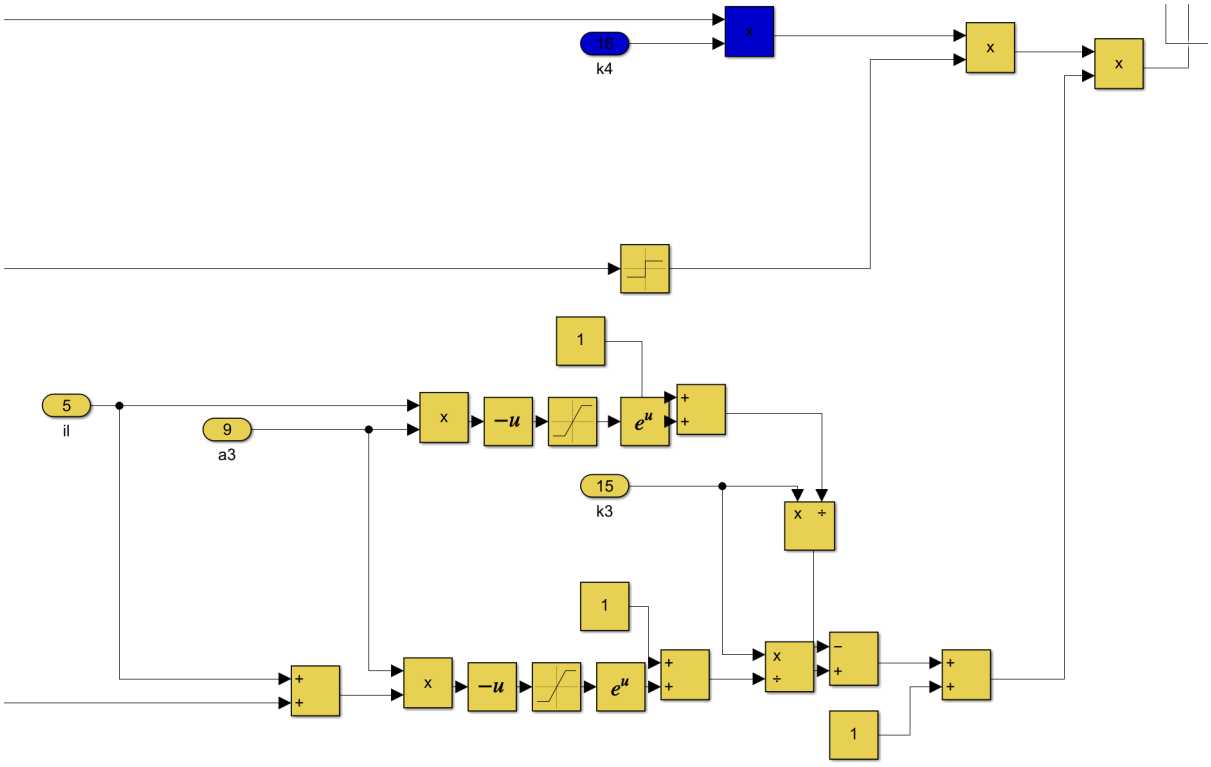

Figure F.14. Zoom of the Simulink routine for the Wang damper model yellow coded region.

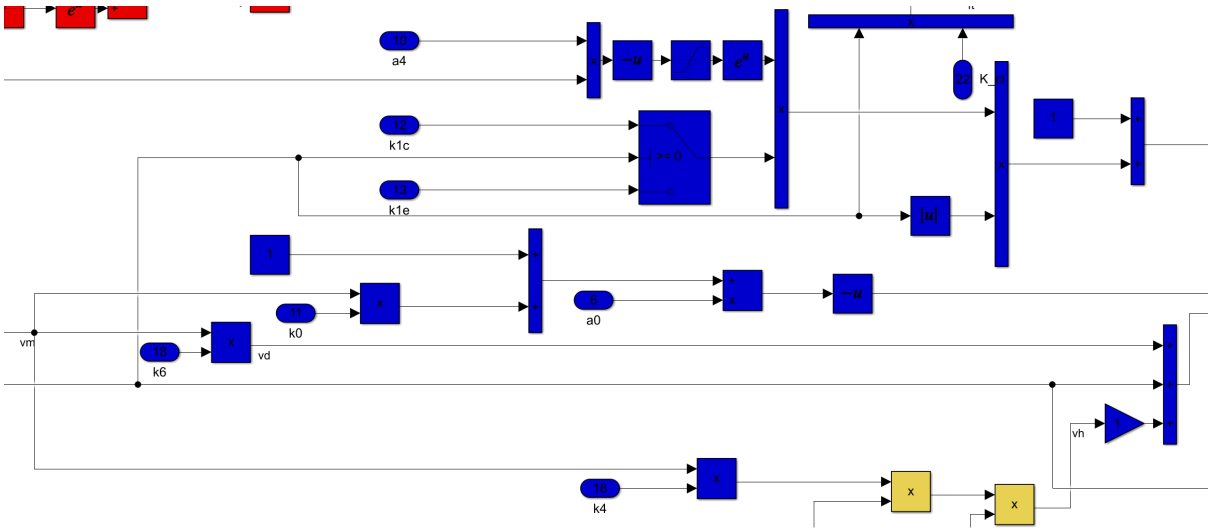

Figure F.15. Zoom of the Simulink routine for the Wang damper model blue coded region.

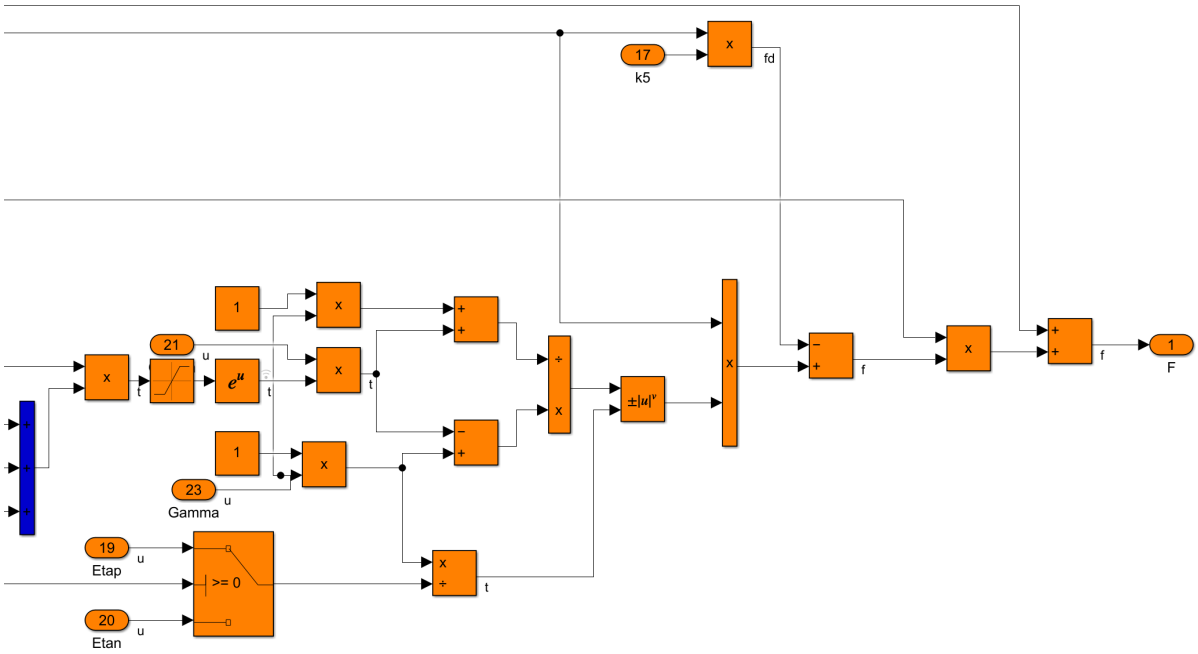

Figure F.16. Zoom of the Simulink routine for the Wang damper model orange coded region.

The green section contain commented blocks. Some of the blocks commented out are simply leftovers from earlier tests, while some determine what version of the Wang damper is being used. This is specifically the case for the V_m section, which can either be directly determined by a harmonic excitation parameter A, the latch mechanism proposed in section 3.2 or the original formulation proposed in its paper. In the diagram shown, the upper block constitutes the new proposed model for V_m, while the lower commented out version is the original formulation and the rightmost constant block A is the velocity from a set harmonic oscillation. This can all be better observed in Figure F.17. The 2nd new v_m proposal is not included in the picture, but can also be seen in Figure F.17.

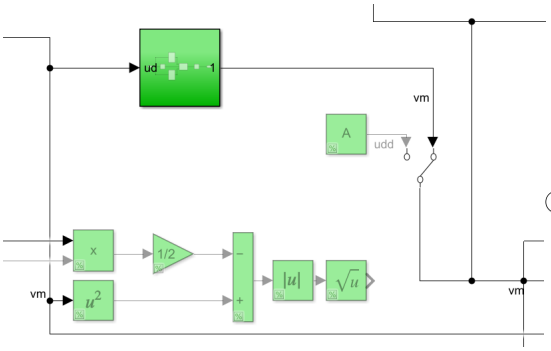

(a) Region which determines the v_m value in the Wang damper model green coded region.

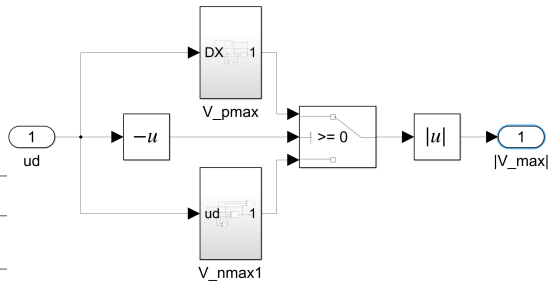

(b) Internal structure of the block for the modified Wang damper V_m calculation process.

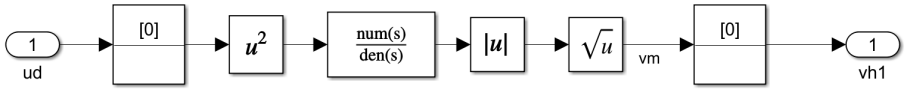

(c) Internal structure of the block for the 2nd modified Wang damper V_m calculation process.

Figure F.17. Details of the V_m calculation process.

The block on the left contain two latches, which are described in Figure F.18.

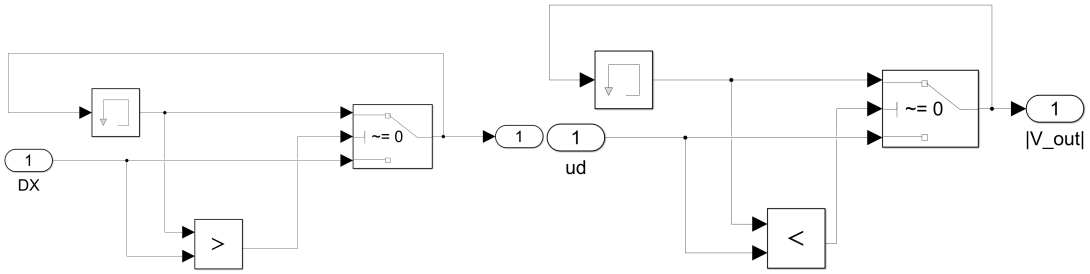

(a) Latch for positive acceleration values.

(b) Latch for negative acceleration values.

Figure F.18. Simulink routine for the first proposed modified v_m calculation technique, which is latch based.

APPENDIX G

APPENDIX: FREQUENCY NORMS CALCULATION

In the process of calculating the genetic optimization, the following codes are employed for calculating the frequency domain response parameters:

- H2.m
- H8.m

where $H2.m$ calculates the H_2 norm and $H8.m$ calculates the H_∞ norm. They can take 1 or more time array domains and return the averaged result in the frequency domain.

APPENDIX H

APPENDIX: FORCE DERIVATIVE $\frac{dF}{d\dot{v}(\dot{x})}$

$$A_A = (1 - k_5) \tag{6.18}$$

$$A_B = O\mathrm{e}^{F_1(\dot{v})} \tag{6.19}$$

$$B_A = \gamma - A_B \tag{6.20}$$

$$B_B = A_B + \gamma \tag{6.21}$$

$$C_C = A_A B_A^{F_4(\dot{v})} \tag{6.22}$$

For the latch v_m model, F_1' and F_2' are described as

$$F_1' = \begin{cases} -\frac{a_0}{(k_0 v_m + 1)} & if \ \ |\dot{v}| < v_m \\ -\frac{a_0\left(1+sgn(\dot{v})k_4(1+\frac{k_3}{1+e^{-a_3(i+I_1)}}-\frac{k_3}{1+e^{-a_3(I_1)}})+k_6\right)}{(k_0\dot{v}+1)^2} & if \ \ |\dot{v}| > v_m \end{cases} \tag{6.23}$$

and

$$F_2' = \begin{cases} exp(-a_4 v_m)\left(\frac{1+sgn_2(\dot{v})}{2}k_{1c} + \frac{1-sgn_2(\dot{v})}{2}k_{1e}\right) & if \ \ |\dot{v}| < v_m \ \& \ sgn(\dot{v}\ddot{v}) > 0 \\ exp(-a_4\dot{v})\frac{(a_4\dot{v}-1)((k_{1e}-k_{1c})|\dot{v}|-(k_{1e}+k_{1c})\dot{v})}{2|\dot{v}|} & if \ \ |\dot{v}| > v_m \end{cases} \tag{6.24}$$

while for the second proposed v_m model, the transfer function model, F_1' and F_2' are described as

$$F_1' = -\frac{a_0}{(k_0 v_m + 1)} \tag{6.25}$$

and

$$F_2' = exp(-a_4 v_m)\left(\frac{1 + sgn_2(\dot{v})}{2}k_{1c} + \frac{1 - sgn_2(\dot{v})}{2}k_{1e}\right) \tag{6.26}$$

$$\begin{aligned} \frac{\partial F(\dot{v})}{\partial \dot{v}} = (B_B^{F_4(\dot{v})})^{-1}[&C_C\left(F_2(\dot{v}) + 1\right) f_t(max(\dot{v}))\left(-F_4'(\dot{v})\ln\left(B_B\right) - \frac{A_B F_1'(\dot{v}) F_4(\dot{v})}{B_B}\right) + \\ &C_C\left(F_2(\dot{v}) + 1\right) f_t(max(\dot{v}))\left(F_4'(\dot{v})\ln\left(B_A\right) - \frac{A_B F_1'(\dot{v}) F_4(\dot{v})}{B_A}\right) + \\ &C_C\left(F_2(\dot{v}) + 1\right) f_t'(max(\dot{v})) + C_C F_2'(\dot{v}) f_t(max(\dot{v}))] + k_{cl}, \end{aligned} \tag{6.27}$$

where all the constants are from the Wang model equations.

ANNEX A

NSGA-II

The code for the NSGA-II was originally developed by Seshadri (2009). Its original code is made available in Matlab's website, while the modified version used in this Thesis is available in the code repository address provided in Chapter 4. The following disclaimer accompanies it:

Due to the complexity of the codes, readers are encouraged to read the documentation available in the Matlab page. The code contained in the GitHub folder has been custom fit for the purposes of the genetic optimization performed in Section 5.2, and may differ from the original code.